There is a need for EU steel producers to gain a scientific understanding across the board of the damage mechanisms inducing ductility break-ups at both the surface and sub-surface of deforming stock during hot rolling, for a range of free machining (FCS) and heat treatable (HT) steels.

These steels, especially as-cast FCS steels, have inherent low ductility, which is conducive to corner cracking.

The main objective of this multi-partner project was to develop a physical understanding of the causes and mechanisms of crack initiation and growth at high temperature and the relatively high strain rate during rolling of low ductility steel long products.

This objective was achieved using a combination of innovative laboratory mechanical and pilot rolling tests, material constitutive modelling, microstructural characterisation, and online defect assessment and detection methods.

Key beneficial or detrimental microstructural and geometrical parameters have been identified covering 'hook type' oscillation marks, cortical zone, mean local area fraction of MnS, Mn/S ratio, cohesive strength of inclusion/matrix, matrix hardening rate, initial solidification structure and surface state (oxidation/embrittlement).

The project outcome concluded on the relevance of large and/or closely spaced MnS inclusions at early stages of void nucleation while small particles (including clustering) will mainly control the fracture event. Likewise, the influence of process parameters, such as reheating time, temperature-strain rate and tensile triaxiality-strain relationships, amongst other a-dimensional parameters, have been identified and accounted for in a range of material models.

The project concludes with practical rolling recommendations and innovative concepts for future work.

EC

KI-NA-23890-EN-S

PACROLP: the prediction and avoidance of cracking in long product hot rolling

EUROPEAN COMMISSION

European Research Area

PACROLP: the prediction and avoidance of cracking in long product hot rolling

Interested in European research?

RTD info is our quarterly magazine keeping you in touch with main developments (results, programmes, events, etc.). It is available in English, French and German. A free sample copy or free subscription can be obtained from:

Directorate-General for Research
Information and Communication Unit
European Commission
B-1049 Brussels
Fax (32-2) 29-58220
E-mail: research@ec.europa.eu
Internet: http://ec.europa.eu/research/rtdinfo/index_en.html

European Commission

Research Fund for Coal and Steel

PACROLP: the prediction and avoidance of cracking in long product hot rolling

D. Farrugia, Z. Husain [1], V. Santisteban, J. Llanos [2], J. Bianchi, P. Vescovo [3],
J. Pera [4], J. Rodriguez-Ibabe, C. Revilla [5], J. Fredriksson [6],
J. Demurger, R. Forestier, B. Kieber [7]

[1] **Corus UK Limited Research —** Development & Technology, Swinden Technology Centre, Moorgate,
RotherhamSouth Yorkshire, S60 3AR, UNITED KINGDOM
[2] **Sidenor I + D —** Barrio Ugarte, 48970 Basauri, SPAIN
[3] **CSM —** Via di Castel Romano, 100, 00128 Rome, ITALY
[4] **Mefos —** PO Box 81297125 Lulea, SWEDEN
[5] **CEIT —** P. M. Lardizabal 15, 20018-San Sebastian, SPAIN
[6] **Imatra Steel Oy An —** Terastehtaantie 1, 55100 Imatra, FINLAND
[7] **Ascometal Creas —** BP 70045, 573001 Hagondange, Cedex, FRANCE

Final report

Directorate-General for Research

*Europe Direct is a service to help you find answers
to your questions about the European Union*

Freephone number (*):
00 800 6 7 8 9 10 11

(*) Certain mobile telephone operators do not allow access to 00 800 numbers or these calls may be billed.

A great deal of additional information on the European Union is available on the Internet. It can be accessed through the Europa server (http://europa.eu).

Cataloguing data can be found at the end of this publication.

Printed in Luxembourg

PRINTED ON WHITE CHLORINE-FREE PAPER

CONTENTS

NOMENCLATURE

SRX, DRX, MDRX	Static recrystallisation, Dynamic recrystallisation, Metadynamic recrystallisation
T	Temperature
t	time
ε	plastic strain
ε_{ond}	damage onset strain under pure tension
$\varepsilon_{fracture}$	fracture strain in pure tension
$\varepsilon_{dyn.}$	threshold for DRX to start
$\dot{\varepsilon}$	plastic strain rate
Z	temperature compensated strain rate
$Q_{def}, Q_{app,SRX}, Q_{app,MDRX}$	deformation and apparent post deformation activation energies
d	grain size
$\sigma_o, \sigma*$	yield and saturation stresses
$S_o, \widetilde{S}$	yield and saturation hardness
$press, p$	hydrostatic pressure (first invariant of stress tensor). Positive under tension.
q	second invariant of stress tensor
m_o, m_s	rate sensitivity exponent at yielding and saturation
$\varepsilon*$	characteristic saturation strain
h_o	work hardening rate
$\Delta\sigma$	amount of stress softening due to DRX
X	recrystallised volume fraction
t_{50}	time for 50% recrystallised volume fraction
$f^\varepsilon, f^\sigma \; f^{Gm} \; f^G$	damage functions as defined in WP7
$\sigma_{matrix} / \sigma_{pp}$	local ratio of matrix/precipitate hot strengths
$\varepsilon_{matrix} / \varepsilon_{pp}$	local ratio of matrix/precipitate strains
κ, E	bulk and elasticity moduli
hc	thickness of the layer removed from the bloom skin
hc0	mean thickness of the original cortical layer
SKIZ	Skeleton by Influence Zones
RPS	Revised plane strain specimen (Gleeble)
HT	Heat Treatable steels
FCS	Free Cutting Steels
HPW:	High Pressure Water descaling
FEM	Finite Element Modelling
CAFÉ	Cellular Automata Finite Element
S,Mn, Bi, Te, Ca	Sulphur, Manganese, Bismuth, Tellurium, Calcium
SPH	Smooth Particle Hydrodynamics
NEL	Natural Element Formulation
L/hm	roll gap shape factor (L : projected length of arc of contact (mm) ; hm : mean stock thickness (mm))
STR, PSR, SPR, PEEQ	Triaxiality, Principal Strain Ratio, Principal Stress ratio, Plastic Equivalent strain
RPS	Revised Plane Strain
GS	Grain size

FINAL SUMMARY

PACROLP: The prediction and avoidance of cracking in long product hot rolling

RFCS Agreement No. RFSR-CT-2003-00002

Period 1 September 2003 – 30 June 2007

1. Background

There is a need by EU Steel Producers to gain a scientific understanding at micro, meso and macro-scale of the damage mechanisms inducing ductility break-up/defects at both surface and subsurface of the deforming stock during hot rolling, for a range of free machining (FCS) and heat treatable (HT) steels [1]. These steels, especially FCS steels have inherent low ductility or ductility through (Fig. 1(a and b).
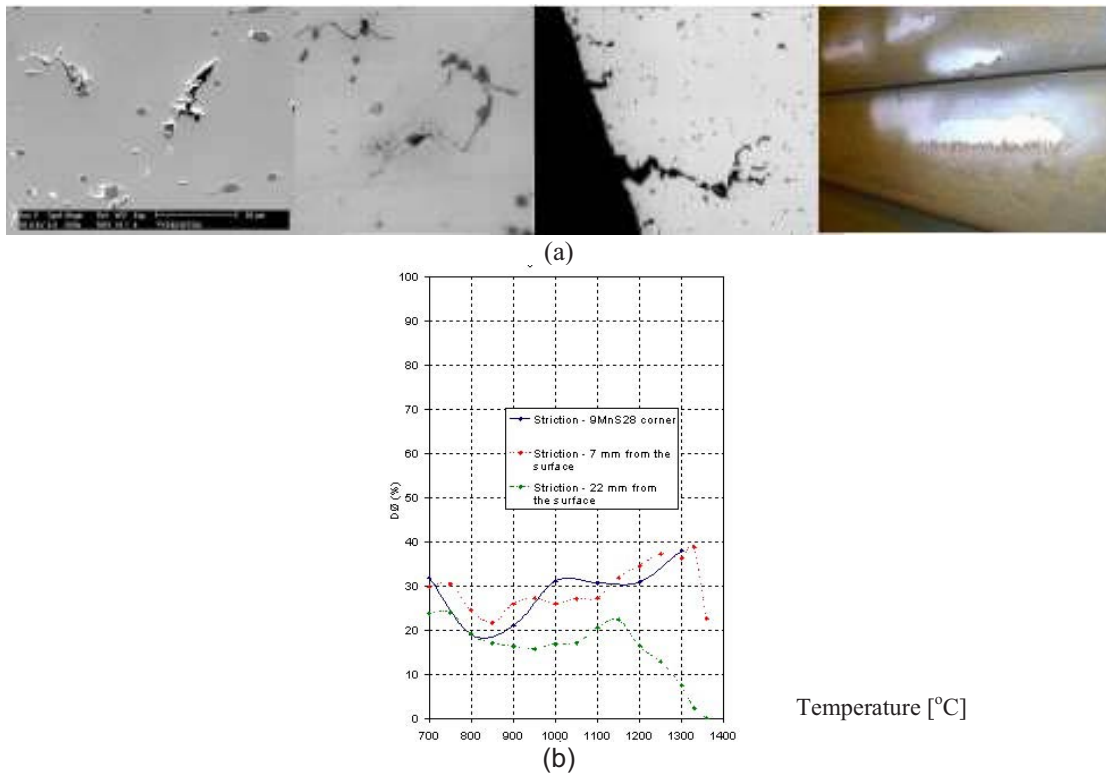

(a)

(b)

Fig. 1(a and b): (a) Micro to macro cracking in FCS steels (b) tensile ductility 9SMn28 (CSM) function of temperature (as-cast conditions)

The area of high temperature ductile damage has not been up to now a major focus of interest at RFCS level and within the scientific community as compared to developments at room temperature and creep/superplasticity regime [2,3]. FCS steels are known to have inherent low ductility, especially lead-substitute (Te, Bi, high S) grades in the as-cast conditions where despite use of tailored rolling processing conditions (high temperature, low roll cooling, minimum or no HPW descaling), ductility break-ups (e.g. corner cracking, etc.) are major causes of yield losses. The problem is further compounded by economical pressures to standardise ingoing feedstock with tight corner radius (6-15 mm) with major consequences on mill pacing (reduced) and hence likely increase of ductility problems mostly at small bar sizes. The trends of combining continuous casting and hot charging, reducing the possibility of surface rectification prior rolling, can also be a main contributor to the risks of surface defects at the early stage of rolling, mostly on coarse cast structures with second phase inclusion, segregations and potential casting defects (blow holes, oscillation marks, etc.). This, together with the potential future implementation of the European legislation

5

(ELVD) to promote lead substitutes in machinable steels (Bi, Te, high S) where new rolling recipes need to be developed due to different thermo-mechanical behaviour is leading to the requirement to identify the most significant parameters affecting ductility during hot rolling of bloom and billets. For heat treatable steels, despite their higher intrinsic ductility, surface quality is of prime importance and presence of shelly, seam type defects is to be avoided. Benefits from such a study may not exclusively come from improved tolerance to minimising risk of onset of cracking using current industrial settings, but the knowledge developed will help optimising pass schedules and designs and finally mill pacing. On a wider front, it will also allow a greater insight into the influence of upstream processes within the bound of the project, i.e. from casting, pacing during reheating inc. discharge temperature with potential associated energy savings and improved roll cooling and finally HPW descaling.

A 7-partner EU project (PACROLP) was therefore set-up with the aim to identify the main mechanisms and parameters (process and products) affecting crack initiation (nucleation) and growth across the physical length scale at high temperature and relatively high strain rate (max $10s^{-1}$) during hot rolling of long products. This objective was met by a combination of laboratory mechanical and pilot rolling tests, material constitutive modelling, microstructural characterisation and finally on-line defect assessment and detection methods for a range of free machining (FCS) and heat treatable steels as shown in Fig. 2.
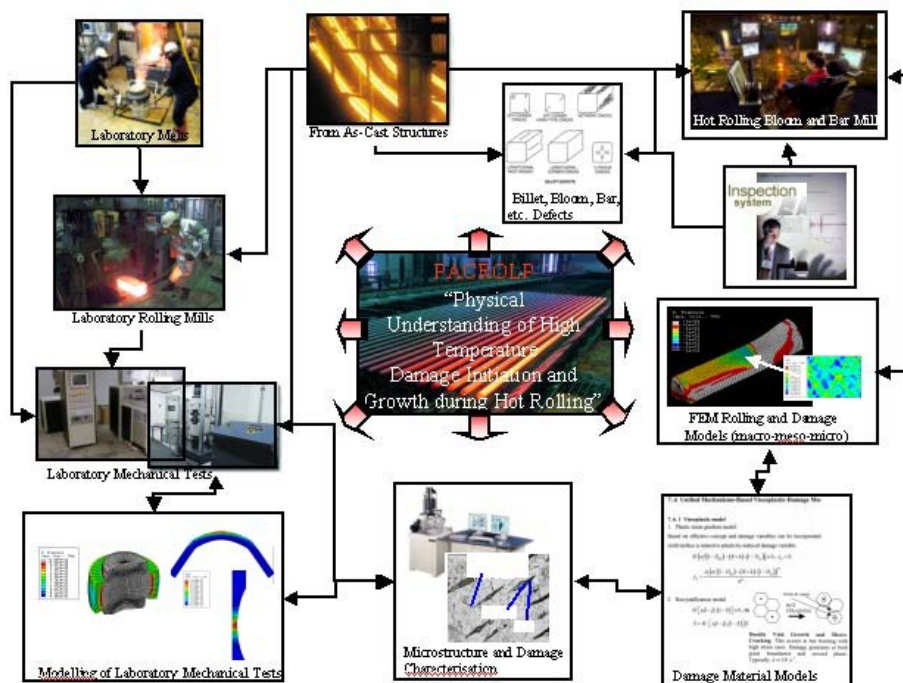

Fig. 2: PACROLP project flow and structure

The conditions tested and simulated are primarily those encountered during cogging/roughing mills of bloom and bar mills (max strain rate 10 s^{-1}, Tprocessing [800-1200°C]), i.e. replicate the transition from as-cast to wrought structure, however the investigation had to cover surface and microstructural characterisation of concast billets/blooms, effect of reheating on material behaviour and finally downstream rolling to finished products (bars, rods). The project was however not set-up nor resourced to study in details the links between continuous casting and rolling with respect to both casting process parameters and prediction of solidification structure inc. inclusion precipitation (this should remain a project on its own merit), but was designed to take account of a range of input cast structures as initial state for studying during rolling the transition between as-cast and wrought microstructures.

The project has benefited from an extensive and complementary mix of steel grades, particularly FCS steels with a range of Mn/S ratio, Pb, S, Bi and Te from both BOS blooms and EAF cast billets (see Section 3 for composition). For the point of view of the detailed ductile damage mechanisms, FCS steels were the prime

focus. HT steels were however investigated by three partners for surface quality, on-line defect detection and rollability testing, and cover a range of bearing (100Cr6), rock drill, Q&T, Ni Cr low C grades. The range of composition available in the Consortium, together with cross testing of specific grades at partner facilities has greatly enhanced the detailed understanding of the effect of microstructure and mechanical-thermal parameters on ductile damage, primarily for FCS steels. Access to industrial mills with respect to defect detection, material acquisition (as-cast, wrought), etc, has also been a major asset in supplying pedigree samples and process data with a clear logistics for material identification and tracking. In addition, the range and expertise on mechanical testing and material characterisation has provided an excellent platform for assessing and ranking effectiveness and applicability domains of conventional and newly developed mechanical tests with respect to strain to failure, triaxiality and overall ductility.

Mechanical testing covered forgeability tests (tensile), compression using a range of conventional and new designs, bending and finally torsion in both monotonic and strain reversal mode. Influence of both dynamic and static recrystallisation, as well as grain coarsening has also been studied, together with the effect of MnS inclusions on FCS steels. Tests carried out were also made on a range of representative sizes of volume/surface samples in both as-cast and wrought conditions. This is important in order to account for initial defects such as concast oscillation marks and the extent/presence of the chill equi-axed zone. Mechanical testing and microstructural characterisation has been extensive and invaluable for the development of constitutive material models. The project is proposing a framework for addressing the multiscale nature of ductile damage (exc. effect of grain boundaries) by adopting a top-down length scale approach via mesoscale ductile damage criteria (post processing), mesoscale fully coupled constitutive models with key state variables, microFEMs for modelling inclusion interactions and finally multiscale CAFÉ models for bridging length scale for damage prediction. Some of these models were applied comparatively using a standard axisymmetric compression benchmark provided by one of the partner (Mefos) as well as being validated where possible with mechanical testing and industrial data. FEM modeling has also been used to derive key strain-stress path data for mechanical testing thus providing a way to develop strain to failure-triaxiality curves, which are key to the understanding of crack initiation and growth. In addition FEM has been used to develop and optimize new sample geometry for mechanical testing with a new revised plane strain (RPS) design tested at two different size scale. The project covered on-line defect detection methods from optical, eddy current to laser ultrasonics. The optical system is working industrially on-line at the Ori-Martin bar mill, an eddy current facility based on the Förster Defectomat® system was trialled at Ovako Imatra whilst the laser ultrasonics EMAT system under development in another RFCS project [4] was assessed during the first half of this project. The project looked at influence of casting (defects, structure), and reheating with respect to reheating time and temperature as shown in Table 3. Knowledge developed was also been put into practice by redesigning/optimising roll passes during roughing of billet and early finishing of rods. Finally the project is proposing a set of detailed but also practical guidance covering both product and process parameters for minimising onset of cracking during rolling. This knowledge is transferable and can be directly exploited.

This project was structured in 11 WorkPackages (WPs) (see Technical Annex Appendix 1) and as shown briefly in Table 1 below. The role, equipment and work accomplished, together with interactions between partners are illustrated in Table 2 and will be further detailed in Section 3 of the this final report.

Table 1: Project structure

Tasks	Title	Partners	Leader
WP1	**Selection of Materials**	all	Corus
WP2	**Selection of thermo-mechanical and rolling conditions**	all exc. CEIT	Sidenor
2.1	selection fo thermo-mechanical conditions with respect to mechanical testing and industrial plant	all	
2.2	Reference of rolling trials to laboratory simulation	all exc. CEIT	
WP3	**Mechanical testing**	all	Corus
3.1	Torsion	CEIT, Ascometal	
3.2	Gleeble/ PSC	Corus, Sidenor, CSM	
3.3	Other tests (e.g. bending)	Sidenor, Imatra	
3.4	Strain path	CEIT	
3.5	FEM Modelling of mechanical tests	CEIT,Ascometal, Corus, CSM, Sidenor	
WP4	**Laboratory rolling**	Corus, Mefos, CSM	Mefos
WP5	**Microstructural characterisation**	all	CEIT
WP6	**Determination of Key parameter sensitivities and establishment of regime maps**	all	Corus
WP7	**Development of damage equations & Constitutive models**	all exc.Imatra	CSM
WP8	**Incorporation of consitutive models in multipass rolling FEM models**	CSM, Corus, Mefos, Ascometal, Sidenor	Ascometal
WP9	**Further development of detection device for hot metal application**	Corus, Imatra	Corus
WP10	**Application of improved reheating and rolling practices to industry**	all, exc. CEIT	Mefos
WP11	**Development of set of guidance for hot rolling without generation of significant defects**	all	Corus

Ductility break-up for the range of steel investigated (primarily FCS steels) is intrinsically complex with many interactions existing between casting, reheating and rolling. To name a few, effect of steelmaking (BOS v EAF route with respect to residual content and their effect on diffusion during reheating (Cu, Sn, etc.)), steel composition re. Mn/S critical index, MnS inclusion types (I, II, III), MnS through thickness and perimeter size/spacing distribution, influence of continuous casting with respect to oscillation marks, solidification pattern, ductility on cooling (ZTT, etc.), cortical zone, intrinsic defects (blowholes, etc.) and surface state, influence of reheating with respect to oxidation, Mn depletion, embrittlement and finally influence of rolling with respect to key process-product thermal-mechanical parameters, all potentially in isolation and/or combination could have significant effects in affecting ductile damage.

Strain and stress paths with respect to triaxiality and principal longitudinal stresses and strains, together with local temperature gradient due to roll gap conduction heat losses are key parameters affecting ductility break-up. Studying the effect of each input factor and their interactions & correlation is beyond the scope of this project. There are major challenges linked to collection and machining of sample pedigree (statistics), type(s) of mechanical tests required, sampling position and initial characterization (non-destructive) of structure, observation of time-position-length scale of relevant mechanisms (nucleation, growth and coalescence of voids/cracks), combined observation of cracking and austenite grain boundaries and effect of softening mechanisms (RX, etc.), etc. Table 3 is an attempt (non-exhaustive) to list known process and product parameters per primary process (i.e. casting, reheating and rolling) affecting ductility with a clarification of those studied within the scope of this project. A summary table with detailed explanation and supporting evidence is presented at the end of the extended summary with indication of range of sensitivities and uncertainties/further work required. This will be further extended and supported in the main section of the final report (Section 3).

Table 2: Role, Equipment and brief summary of work carried out by Partners

Partner	Process coverage	Steel	Main steel codes investigated	As-cast/Wrought	Steel Partner investigated	Steel location investigated	Mechanical testing equipment	Type of mechanical test	mechanical test standard	Process conditions	Specimen size	Product characterisation methods	Modelling	FEM code	Pilot facilities	Industrial / Pilot Defect detection	Investigations/achievements	Industrial Exploitation/benefits
Corus	Scunthorpe BBM C&I bloom rolling roughing block (BOS/Bi-Te route)	FCS, LFCS, FCS-Te, FCS-Bi, LFCS-Bi	FCS (777F), LFCS (339H), tellory+(360M), Bi-FCS (602M), Te-FCS (9252M)	AS/CW	9Mn328 CSM as-cast	Corner, surface, internal	Gleeble, Dilatometer	reversed plane strain (RPS), U-bending, PSC, AnC, DCC, PSC, HC, DCC (dilatometer), tensile (Birmingham U)	yes	880-1000,1200C 0.1, 1, 10s-1, 1200C-30s holding time, argon, air, double hat (50% red, with intermediate reheat 10s max time)	10x15x20mm (RPS, PSC), 100x8mm gauge dia (8mm dia ends), GS4a (tensile), 25x10x16mm (sheared), 10x15 x5 mm (edge) (hexagon), 15x28mm (flying saucer), 24x60mm (double collar)	Optical, SEM, image analysis	A dimensional criteria (str_epr, por, sms&_epr-str, tawel, rabin, etc.), assessment of damage criteria (McClintock, etc.), ABAQUS FEM standard damage models, viscoplastic VUMAT, Oarson standard ABAQUS, microPEMS, global/submodelling ABAQUS, CAFE VUMAT model	ABAQUS	3-High mill (SOR)	Pilot laser EMAT hot detection system (pilot plant)	envelope of processing conditions, role of MnS inclusion and FCS microstructure, new mechanical test for ductility, double hat compression testing, standard for mechanical testing, nucleation/growth curves, constitutive models, assessment of laser EMAT for defect detection, limited pilot rolling, microscale and CAFE FEM, modelling benchmark, overall co-ordination and direction	Corus C&I &CES
Sidenor	Vitoria Three high reversible billet rolling roughing block (EAF route)	FCS, LFCS	9SMnPb36, 9SMnPb36, 9SMnx8, 9SMn36	AS/CW		Corner, surface, internal	Gleeble, Press	tensile, Double necking tensile, 3 point bend	yes	1000-1300C, 10s-1, 60s holding time, vaccum (gleeble)	116x10 (tensile Gleeble), 25x25x127 (3 point bend)	Optical, SEM, Image analysis	FEM rolling simulation + Cockroft-Latham damage criteria	ABAQUS		on-line hot inspection	industrial application and monitoring, macrostructural characterisation, mechanical testing, envelope of processing conditions, influence of casting, influence of reheating, redesign of pass design	Vitoria bar and rod mill
CSM	On-Martin billet rolling (EAF)	FCS-Bi, FCS-HighS	9SMn38, LS30-Bi + additional grades investigated at On-Martin / CSM pilot	AS/CW	9Mn328 pilot mill rolled and as cast specimens provided to partners	Corner, surface, internal	Gleeble (Oulu)	Axisymmetric compression, stress relaxation and tensile	yes	Mech testing, 800 to 1150 °C, 0.1 to 5.5 s-1, Flat Rolling= 960 to 1140 °C core, reduction up to 60%	119x10 diam (tensile Gleeble), 10x7 diam (compression Gleeble), 70 to 10 mm thickness (flat rolling)	Optical + SEM	ABAQUS FEM model with dynamic damage-thermomechanical-microstructure coupling via Oarson and user defined criteria	ABAQUS	2 high flat rolling	barCheck - CCD thermal mapping system (industrial Plant)	on-line defect detection/measurement/assessment/constitute, recrystallization kinetics, microstructure characterisation, role of control zone and process conditions by pilot rolling and mechanical testing on cracking	CSM and On-Martin rod mill
Mefos		ball bearing and two phase steel with # S content	SKF803	AS/CW	rock shell 4H5864 (austra)	Corner, surface, internal	Forging press	axisymmetric compression, RPS (Corus) large scale				Optical + SEM	MSC MARC of rolling and upsetting + dynamic prediction of damage using Cockroft-Latham, mcClintock	MARC	2 high flat rolling + bar rolling (ROR) inc rolling with artificial defects	Visual (pilot plant)	envelope of processing conditions, pilot plant rolling with/without artificial defects, FEM of ROR rolling/upsetting, modelling benchmark test, microstructure characterisation, pass design and reheating influence	Ovako Bar Oy of AB, Imatra, Ovako Steel AB – Hällefors, Swedish Materials Technology, Sandviken
CEIT				AS/CW	LFCS (Corus), Tellor+ (Corus), 9SMnPb30 (Sidenor), 9Mn328 (CSM)	Corner, surface, internal	Torsion	Torsion, interrupted torsion and reverse torsion		1150-1200s (holding time), 800-1190C, 1s-1 (0.1 and 10s-1) up to 16 pass reversal		optical, SEM image analysis inc SKIZ	SKIZ modelling				mechanical testing (torsion, reverse torsion), detailed damage and microstructure and inclusion (MnS, FeS, FeO) characterisation inc. confined surface, SKIZ technique	All partners + EU
Ovako-Imatra	Medium bar rolling	medium carbon, N alloyed, MC Q&T, MC, lowCNiCr, rock drill, 18CrNiMo7	7228, 4737, S073, 6121, 4H564	AS/CW		Corner, surface, internal							TEMPSIMU, temperature modelling during casting			Eddy current/Forster Defectomat® hot detection system + Tiede magnetic particle inspection system	casting, rolling defect analysis, on-line defect detection	Ovako bar Oy AB, Imatra
Accumetal	Accumetal FOS bloom and wire rod	FCS and bearing steel	FCS 32Mn35Pb, FCS-Bi 32Mn65Pb, 100Cr6	AS/CW	9Mn328 CSM as-cast	Corner, surface, internal	forgeability, PSC, torsion	tensile, PSC (unclear), torsion	yes	700-1350C, 1-10s-1 (tensile), 900-1200C (PSC) 1-10s-1, 900-1200C (torsion) 0.4-8s-1	19diac 840x30x80mm (PSC), 6 gauge dia)x100mm (tensile)	Optical, SEM, 3D roughness	post processing damage criteria (Lemaitre, Oyanne, Clauboche)	Forge 2005, Lam3		Ultrasonic, EKEM, on-line hot Eddy Current, SEM	envelope of processing conditions, detailed mechanical testing, comparison ductility by tensile, compression and torsion testing, influence of surface state and oscillation marks, standard for mechanical testing, nucleation/growth curves, microstructure characterisation, influence of reheating, modelling benchmark, uncoupled damage models	Accumetal Lucchina bloom, bar and rod mill

At microscale [3, 5] cracking is due to the nucleation, growth, and coalescence of micro-damage, the cumulative term for micro-voids and micro-cavities, which are formed by various mechanisms during plastic deformation. Different growth speed can be observed depending on microstructure (inclusions and processing conditions). Further inward from the visible cracks the material may still have a high density of micro-damage, which, if over a critical level, can adversely affect material properties. By modelling the accumulation of damage, it should be possible to optimise a rolling schedule to minimise the amount of material containing a high density of damage that must be removed to eliminate defective regions of a rolled product.

2.   Main summary results

Section 2 integrates findings from all the 11 Work packages and has been written in such as way as to provide a concise albeit detailed description of the main factors affecting ductility at high temperature.

Damage takes various forms through the microscopic to macroscopic length scale. Ductile damage usually involves for the triaxiality encountered (<1), nucleation, growth and coalescence of voids in a plastically deforming steel matrix (see Fig. 3). This damage can be further accelerated by the presence of second phase inclusions (non-metallic such as in FCS or heat treatable steels) depending on inclusion spacing/clustering. Potential sites of defect formation during hot working are therefore located:

- Within austenite grains (intragranular fracture)
- At austenite grain boundaries
- At matrix-second phase interfaces
- At second phases, i.e. inclusions

Conditions studied in this project are between 850 -1250°C (above AR$_3$), 0.1 to 10s^{-1} and strain up to fracture.

The microcracking within austenite grains is unlikely at high temperature except at very high strains and has not been observed in this RFCS project (Fig. 4).

Fig. 3 : Micro-Damage mechanisms

Table 3: List of main parameters affecting ductility

Casting

Product	Investigated	Process	Investigated
Oscillation marks (hook, etc.)	yes	Mould level/fluctuation	yes
Depressions (longitudinal, transverse)	no	Secondary cooling	no
Glaciation	no	Superheat	
Cortical (chill) zone	yes	Casting powder	yes
Longitudinal/transverse/facial & spiral cracks	partially	Mould taper	partially
Microstructure matrix (as cast grain size/boundaries, etc.)	yes	Mould zone alignment	
FCS Microstructure MnS inclusions (type, morphology, size, spacing, area, fraction, distribution, etc.)		Mould cooling	
Microstructure other inclusions (FeS, FeO, etc.)	yes	Slag pool	
structure (dendritic, columnar, etc.)	partially	Casting speed	yes
Porosity	yes	Straightening strain	
Incipient cracking (intercolumnar cracks, pin hole/ blowholes)	partially	Spray cooling	
cast feedstock radius	partially	Strand bulging	
AlN precipitation (HT steels)	no	Roller spacing	
zero strength ductility on cooling (ZDT, ZST)	partially	liquid flux infiltration	
Mid ductility temperature on cooling (MDT)	no	Meniscus level velocity	
		Temperature	partially
		Meniscus formation distance	
		quenching	yes
		EMS	partially

Reheating

Product	Investigated	Process	Investigated
Oxidation (grain boundary, effect on cortical zone)	partially	Temperature	yes
Decarburisation	partially	resident time	yes
Embrittlement/Diffusion (Cu, Ni, etc.)	partially	Atmosphere	no
Low melting phase (Pb, Te, Bi)	partially	Scheduling	no
Microstructure (grain size, Mn depletion, etc.)	yes	Pacing	no

Composition

Product	Investigated	Process	Investigated
Al	yes		
Nb	no		
V	no		
P	no		
N	yes		
Mo	no		
S	yes		
Ti	no		
Ti and V	no		
Zr	no		
Cu	partially		
Ni	partially		
Sn	no		
C	partially		
Mn	yes		
Ca	yes		
Si	no		
Noble /tramp elements	partially		
Mn/S ratio	yes		
MnSc	yes		
Pb	yes		
Te	yes		
Bi	yes		

Table 3: List of main parameters affecting ductility (contd.)

Rolling (R)|Thermo-Mechanical Processing (Mechanical Testing MT)|Modelling (M)|Pilot Plant (PP)|Production (P)|Microstructure Characterisation (MC)

Product	Sub-product feature	Inherited (i)/ developed	Investigated	Process	Sub process features	Investigated
1. steel matrix microstructure/structure	grain size (GS)	(i,d)	yes (MT, MC)	temperature	bulk	yes
	grain boundary (GB)	(i,d)	yes (MT, MC)		radial gradient	no
	segregation	(i,d)	partially		perimeter gradient	no
	texture/crystallographic orientation	(i,d)	no		recalescence	no
	porosity	(i)	partially	strain/deformation	equivalent strain	yes (MT,M, PP, P)
	dynamic Rx (DRX)	(d)	yes (MT, MC)		principal strain / ratio	yes (MT, M)
	static Rx (SRX)	(d)	yes (MT, MC)		strain to failure	yes (MT, M)
	cortical zone (CZ)	(i,d)	yes (R,MT, MC, PP)		nucleation	yes (MT, M)
	oxidation after reheating	(i,d)	yes (MC)		strain path (reversal)	yes (MT, M)
	decarburisation	(i,d)	yes (MC)		shear strain	yes (MT, M)
	embrittlement	(i)	yes (MC)	strain rate	mean	yes (MT, M)
	hardening	(d)	yes (M)		variable	no
2. Non metallic inclusions				stresses	triaxiality magnitude	yes (MT, M)
					triaxiality inversion	yes (MT, M)
MnS	type, spacing (inter, surface), area (inc. mean local), size, fraction, orientation	(i,d)	yes (R,MT, M, MC)		triaxiality gradient	partially
	cohesive strength (effect of Pb, etc.)	(i,d)	partially (M, MT)		principal stress / ratio (max, mid, average)	yes (MT,M)
	precipitation re. GB	(i,d)			equivalent stress	yes (MT,M)
	void following nucleation	(d)	yes		linked to strain rate	yes (MT,M)
	cristallographic orientation	(i,d)	no	pacing	time in length of contact	no
	plasticity index/deformability	(i,d)	yes (MT, M, MC)		heat loss roll gap	yes (M)
FeS		(i,d)	yes (MC)		heat loss interstrand/SEE line on roll oxide	partially (M)
FeO		(i,d)	yes (MC)	interpass changes	effect of interpass time, temperature, GS, strain and strain rate on SRX and roll gap conduction/HTC	yes (MT, M)
3. Surface Oxide		(i,d)	partially (MC)	roll cooling	surface chilling	no
4. Roughness/Surface finish		(i,d)	yes			no
5. Critical dimensions	corner radius	(i,d)	no	Edge induced cooling / interpass cooling		yes (PP)
	shape in general (front end, cross, plan)	(i,d)	partially	Descaling	temperature	no
6. Artificial defects		(i,d)	yes (PP)		descalability	no
7. Damage	nucleation	(d)	yes (MT,M, MC)		secondary scale hardness/thickness	no
	growth	(d)	yes (MT,M, MC)	Mill dynamics/entry/delivery/ guiding/pitch line/twist/asymmetry		no
	coalescence	(d)	yes (MT,M, MC)	forward slip		no
	cracking	(d)	yes (PP)	Interstand tension		no
	void welding within roll gap	(d)	yes (M)	Pass design/matching feedstock (linked to triaxiality inversion, etc.)		partially
				Pass design/shape (SO, S, box, etc.)		yes (M,P)

Fig. 4: Main ductile damage observations during mechanical testing (Corus)

Main results of project (WP6) have shown that cracking/ductile damage is influenced or inherited by:

1. Inherited from steelmaking/casting/reheating

1.1 As-cast surface conditions (FCS oscillation marks) (Sidenor I+D). Hook type oscillation marks (1 to 2 mm in depth) can create nucleation sites for crack opening, with their significance greatly enhanced when FeS inclusions and enrichment of Cu, Ni, Sn are present (Fig. 5). Inclusion distribution around the oscillation marks shows a short transition from a large distribution of small inclusions to bigger inclusion but without a reduction in number as it happens in the rest of the surface. This also creates an additional weak point in the oscillation marks.
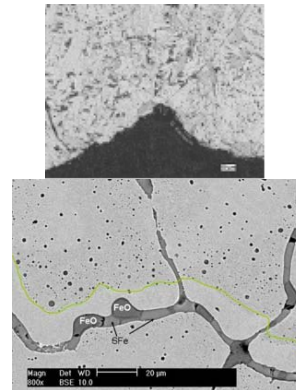
Fig. 5: hook type oscillation and Mn depletion (Sidenor, CEIT)

1.2 Casting and secondary cooling (Rock drill steels 4HS64)

▤ Cracking for this type of steel is usually subsurface, particularly close to corner edge of bloom/billet. Casting parameters and abnormalities in the secondary cooling of blooms are important factors influencing crack development as ductility for this type of steel was only partially affected by reheating and rolling conditions. Casting secondary cooling was simulated at Mefos Pilot mill by a sequence of reheating, cooling and rolling to promote AlN dissolution/precipitation in as-cast structure and study effect of excessive secondary cooling and recalescence. Despite the extensive matrix of trials, **no cracking could be detected** (Fig. 6)

which showed the excellent ductility of this grade and the unlikeliness to promote cracks during rolling. Detailed microstructure characterisation reveals formation of bainite, tempered martensite and pearlite at edge corner and potentially cracks in primary grain boundaries. Cracking was also limited during axisymmetric upsetting and only appear during cooling of front side in scaled RPS specimen (Fig. 7 and Section 3).

▣ **Influence of mould taper** The major risk of appearance of these cracks is for steel grades with a carbon content of 0.28-0.40 % in combination with a small mould taper of the mould (Fig. 8) [6,7]. The amount of taper will also be affected by wear. Peritectic phases as well as fluctuations in the mould level results in irregular shrinkage, which also affects the crack development.

▣ Experience at Imatra shows that the **upper corners of blooms** are more **sensitive for crack development** and that cracking intensity is increasing at the end of the casting process. The use of water quenching did however not improve cracking. So the defects are probably created before the quenching step and might be caused by abnormalities in the secondary cooling of blooms.
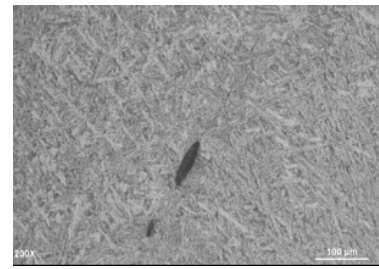
Fig. 6: Pilot simulation trial of secondary cooling during casting (Mefos- rock drill steel) – SEM microstructure

Fig. 7: Large scale deformed Corus RPS specimen (cooled side) (Mefos)
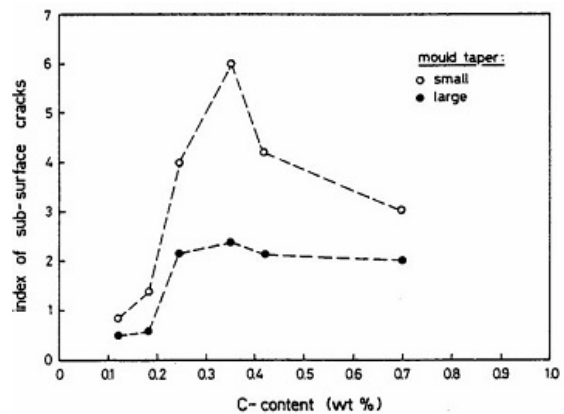
Fig. 8: Cracking index during casting function of C content and mould taper

1.3 Cortical zone (thin equiaxed zone obtained from casting/solidification due to rapid solidification) with thickness ranging from 5 to 15mm provide an effective barrier against opening of sub-cortical pre-existing casting defects and improve ductility. This was assessed by pilot rolling (CSM), PSC/forgeability and RPS tests (Ascometal, Corus). Thinning (2-4 mm) of cortical zone via oxidation and reduction has to be minimised, the potential asymmetry close to billet/bloom edge can also reduce protection (see Fig. 9(b)). In addition, work by CSM has shown the effect of removing cortical thickness on ductility breakup and crack opening together with effect of temperature (Fig. 10). This not only
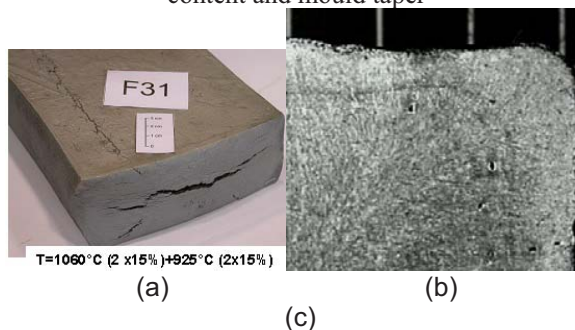
Fig. 9(a-c): (a) Removal of cortical zone during rolling , (b) cortical zone, and (c) effect of oxidation (CSM, Corus)

combines effect of solidification structure but also MnS spacing/size.
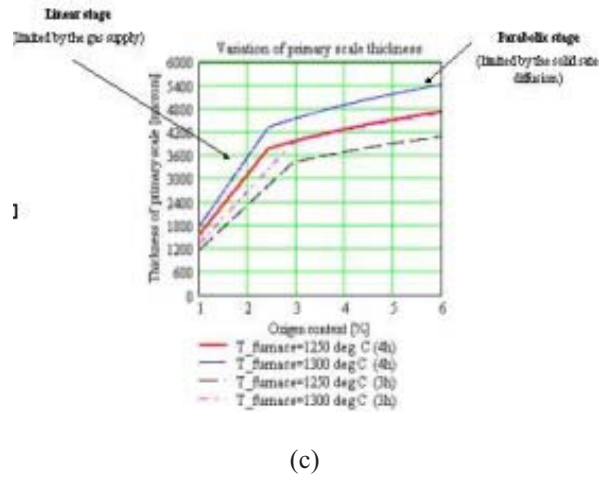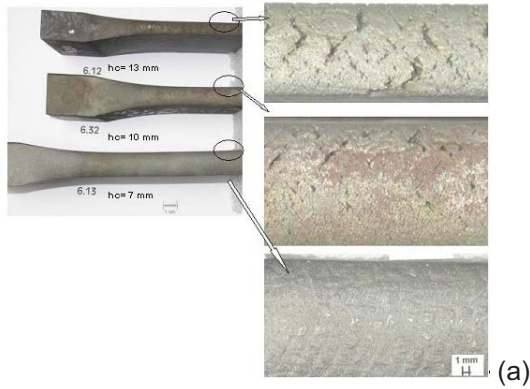
(a)

(b)

Fig. 10(a and b): crack opening after 60% reduction function of (a) remove cortical depth hc at T = 960°C (b) temperature for fixed hc = 13 mm 9SMn28 steel (CSM)

1.4 Steelmaking process route (BOS v EAF) will induce different level of residuals (tramp elements (Cu, Sn, Ni)) which role is to increase hot shortness / embrittlement during reheating via grain boundary diffusion (see Fig. 11).

(c)

Fig. 9 (a-c): (a) Removal of cortical zone during rolling, (b) cortical zone, and (c) effect of oxidation (CSM, Corus)
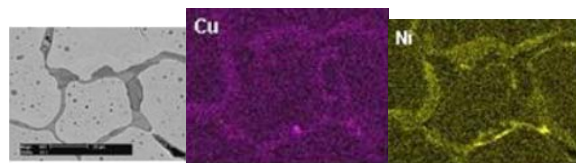
Fig. 11: Type of residuals studied (CEIT)

15

1.5. Influence of AlN (rock drill steels)

High values of [AlN] will increase amount of surface defects. In rock-drill steel Al is used in combination with N to promote fine-grain formation during solidification. Cracking (both length- and crosswise of differing severity) can occur during rolling if AlN precipitation is not controlled as experienced by Inexa Profil, Lulea (see Section 3).

1.6 Austenite Grain structure

▤ FCS Resulphurised steels have limited grain growth/coarsening at temperature considered (<1220°C), therefore DRX and SRX will be rapid at low critical strains. This has implication on crack resistance, re. path for crack propagation when coupled with a high fraction of inclusions (inc. triple points) (see Fig. 12). At high temperature, low strain rate, grain boundary sliding will also be promoted at high triaxiality, low strain (See RPS CSM steel).

▤ Nucleation of new grains seems to be independent of the presence of inclusions.

▤ A mixture of large (3000 microns) and fine grain size (case of rock drill) can reduce ductility.

▤ SRX in double hit RPS testing seem to be beneficial following reduction/damage at low temperature but further promote cracking if damage at high temperature has already been promoted. This was also confirmed by multipass laboratory rolling by CSM (see also [8]).

▤ SRX, DRX kinetics was experimentally measured by CSM-Oulu University using stress relaxation technique with equations shown below. This was done in collaboration with the Group of Prof. P. Karjalainen and Dr. M. Somani at Oulu University [9]. The softening behaviour was incorporated into damage Constitutive models (see Section 2 and WP 7). GS will affect onset and magnitude of DRX.

MDRX: $t_{50} = 2.43 \cdot 10^{-3} . \dot{\varepsilon}^{-0.784} . \exp(57000/RT)$

SRX: $t_{50} = 1.2 \cdot 10^{-11} . \dot{\varepsilon}^{-0.134} . \varepsilon^{-2.8} . D^S \exp(176500/RT)$

$s = 2.13 . D^{-0.105}$

(a)

(b)

(c)
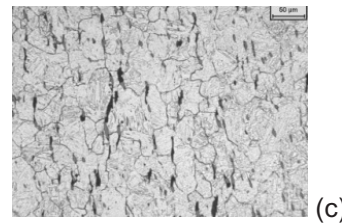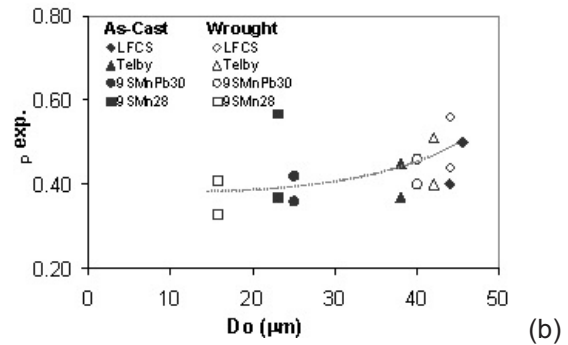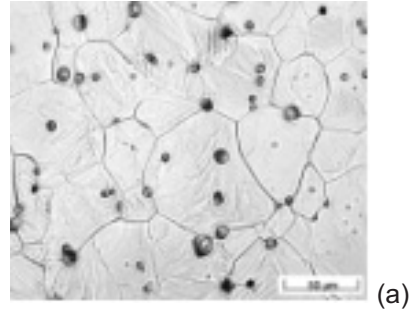
Fig. 12(a-c): (a) Grain size following coarsening, (b) Effect of GS on peak strain (p exp), and (c) effect of SRX (CEIT, Corus)

1.7 Strength-Ductility steel matrix

▨ For a given FCS steel grade, there is no change in matrix hardening behaviour brought about by a change in MnS inclusion size.

▨ It has been found that as-cast structures for some FCS steels, particularly leaded steels have an higher intrinsic as-cast strength than in wrought state (longitudinal) (see Fig. 13)

▨ In the range 1150-900°C, the peak flow stress of FCS increases with the decrease of temperature (Fig. 14), with a well-defined trend (activation energy Q = 324,000 kcal mol^{-1} °K^{-1}) and a definite slow down of that trend below 950°C [9]

▨ Ductility in as-cast conditions is lower than in longitudinal wrought (DR) condition (verified by tensile, torsion and compression testing) (Fig.15).

▨ Transverse ductility in wrought FCS is not too dissimilar to as-cast structure in view of the elongation of the MnS inclusions in the rolling direction (anisotropic properties) (see Fig 15).

▨ **Ductility is lower below the cortical zone** and at bloom/billet inner position assuming all other factors equal due to increased coarseness of inclusions (Fig. 16). Ductility at surface is more affected by inclusion location/spacing, variable adverse thermo-mechanical conditions and other factors such as pre-existing defects, oxidation, embrittlement and cortical zone thickness. When cracking is nucleating at surface, growth is easier due to clustering/small inclusion cluster and adverse thermal-mechanical regime (see 2). Cracking will be dependent on thermal-mechanical factors acting in the three principal directions.

▨ Increase of fracture strain should be expected as strain hardening of the steel matrix increases (at higher strain rate).

▨ Decreasing gradient of plasticity between inclusion and matrix reduces strain partitioning as shown in microscale FEM triaxial deformation (Corus) (Fig. 17). Figure 17 models at micro-scale two globular 3D MnS inclusions and their interactions with the matrix. On the left, high strain gradient is predicted due to the mismatch of plasticity between inclusion and matrix. This is not the case when the index of plasticity is similar.
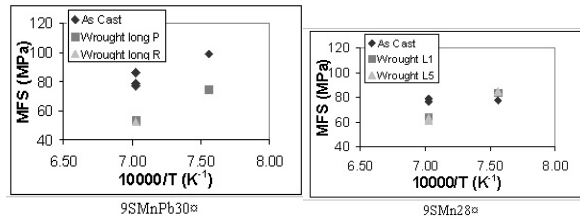
Fig. 13: Steady state stress versus temperature (CEIT)
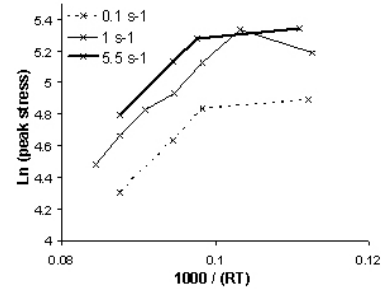
Fig. 14: Peak flow stress function of temperature (CSM)
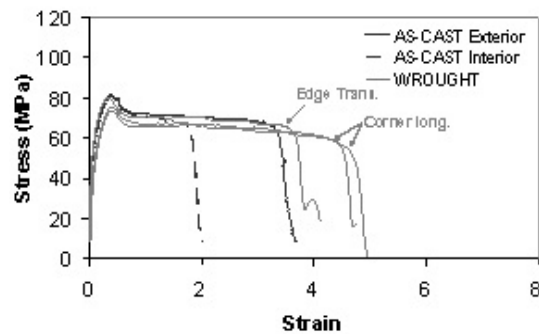
Fig. 15: torsional ductility (CEIT)
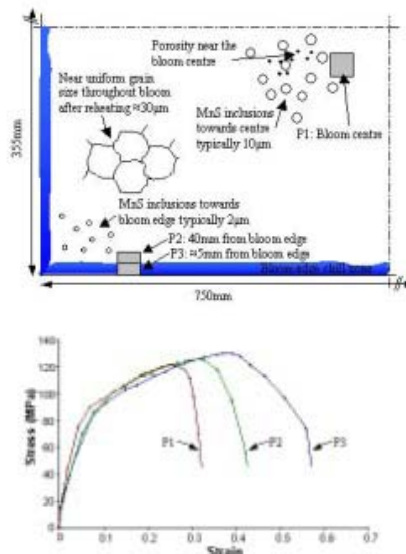
Fig. 16: Ductility FCS 1100°C 10s-1, tensile testing) versus position (Corus-Birmingham)
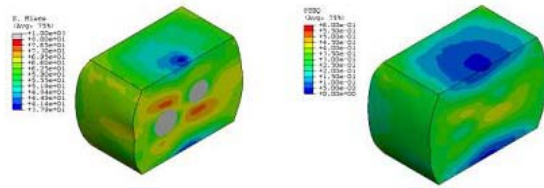
Fig. 17: 3-directional straining microFEM with hard inclusion/soft matrix (left) and hard inclusion/hard matrix (right) (Corus)

1.8 Non-metallic Inclusion (CEIT, Corus, CSM, Sidenor, Ascometal)

▤ Mn/S ratio plays a significant role in increasing ductility (and avoiding phases such as FeS). The critical MnS index as calculated by Alvarez et al [10] should be greater than 1. This is also confirmed by Nicholson et al [11] relating Mn/S of FCS and Leaded FCS steels, to rolling temperature/ductility (Fig. 18). A Mn/S ratio (>4) should be aimed at, although in this project, a Mn/S ratio as low as 2.6 was tested (CSM 9MnS8).

▤ MnS inclusions can be of three different types (although a fourth type also exist), but **type I (globular)** is mostly expected for the types of FCS steels studied (See Fig. 19). Pure or duplex (Oxide-Sulphide) can precipitate but will have opposite plasticity properties. In general, MnS have a high plasticity similar to other inclusions such as silicates, but behaviour is non-linear and overall plasticity index is less than 1 (see Fig. 20 and [12-14]) at high temperature. Small inclusions do not deform (less than 1.5 microns) in view of the increase of interfacial energy and their overall contribution to the matrix deformation (see Section 3). Larger inclusion stringer found in direction of rolling in wrought structure will change the ductility between longitudinal and transverse direction (anisotropy).

▤ Different level of de-oxidation (rimmed/semi-killed v killed steels) depending on level of Al. will generate different type of MnS inclusions. Type I MnS are expected (high O_2 content, with low S solubility). Pure and duplex eutectic MnS (MnS-MnO) can however be formed with expected different plasticity properties. Silicate and alumina can be present acting as nuclei. The MnS inclusion often has varying amounts of other elements, for instance Cr. Calcium often added to melt will modify MnS inclusions and generate CaS which is less ductile than MnS inclusions. Plasticity index will be changed function of inclusion type, strain and temperature.

▤ MnS (FCS) inclusions tend to precipitate on

Estimated rolling temperatures for free-cutting steels
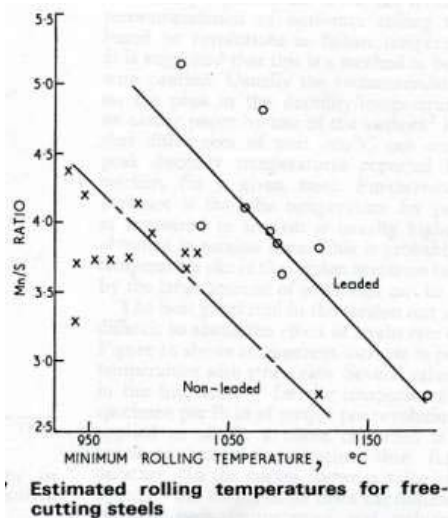
Fig. 18: Mn/S ratio v rolling temperature[9]
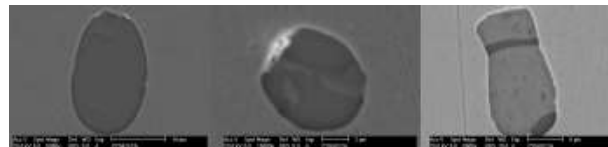
Fig. 19: MnS type and morphology (Corus)

18
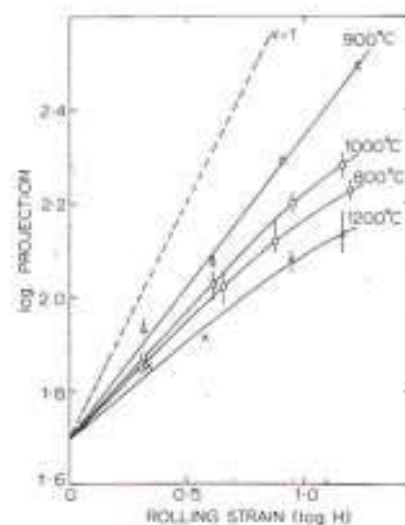
grain boundaries (60%). This ratio increases as DRX/SRX is enhancing path for intergranular cracking (Fig. 21).

▣ MnS size distribution varies from surface (edge) to centre by a factor greater than 10. Inclusion diameter (detected) is ~ 1-1.5 microns at surface (Figs. 22-23).

▣ The main factor influencing nucleation, growth and coalescence and hence ductility is size and spacing, which can be related to a mean local fraction (using SKIZ technique [15] see Fig. 24) or diameter to spacing ratio (Fig. 25). A ratio of s/d < 2 (s: spacing, d; diameter) enhances strain concentration [16]. Ductility is therefore sensitive to mean local area fraction of inclusions (MLFI) (Fig. 26, similar to Edelson et al [17]). Closer inclusion spacing (coupled with less deformable inclusions) will lead to stress and strain network as shown in micro-FEM analyses (Fig. 27). This is further confirmed by Paliwoda [16]. MnS inclusion clustering plays a larger role during growth and coalescence. Triaxiality will also play a key role and its influence will be linked to MLFI and plasticity of inclusions (see 2).

▣ A size effect in fracture due to void/inclusion requires a critical strain and stress ratio to be achieved in relation to the inclusion/void spacing or mean area fraction.

▣ Bi-modal distribution of second phase inclusions (primary sulphides and secondary oxides or carbides) can create additional strain concentration and potentially change the behaviour to void sheet mode cracking (under high triaxiality) (see side wall RPS results).

▣ Inclusion shape and morphology can also play a role in further enhancing strain concentration or impingement depending on direction of straining. This has been demonstrated by micro-FEM analysis, however effect is less than size and spacing ratio.

▣ Crystallographic orientation of MnS (cubic structure) also plays a role and its effect is not well understood although preliminary studies have been initiated at Oxford (under direction of Corus) showing that nucleation is more dependent on the MnS orientation and resolved shear stress than the austenite steel matrix (see way forward Section 3).

▣ Localisation of flow will occur between and around inclusion tips with potential secondary oxide/inclusion playing a key role. Slight porosity (as-cast) will also contribute to decrease fracture strain.

▣ Reducing void/inclusion fraction should increase fracture strain.

▣ From Thomason [18], for inclusion greater than 1 micron, the critical stress for decohesion at interface has to reach a critical stress equal to the

Fig. 20: MnS plasticity index [7]
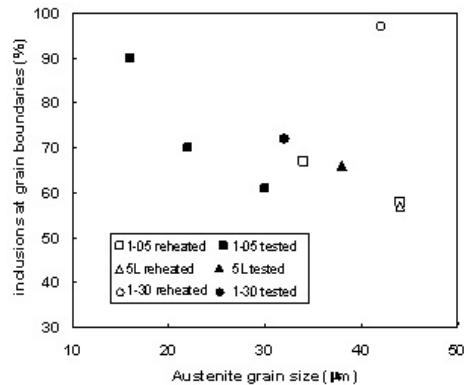
Fig. 21: MnS precipitation v RX/GB (CEIT)
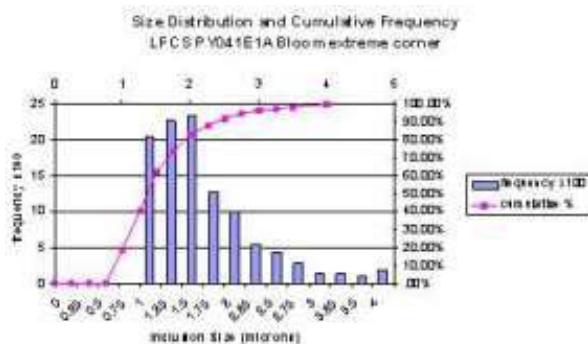
Fig. 22: Frequency/histogram plot of MnS diameter (surface) (Corus, CEIT)
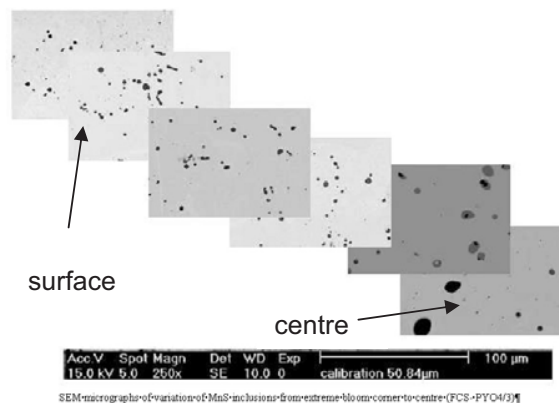
Fig. 23: MnS inclusion size variation function of position (Corus, CSM)

equivalent stress supplemented by the mean stress (hydrostatic pressure) [19,20]. This neglects the stress increase brought about by smaller inclusions (less than 1 micron) on dislocation gliding (i.e. influence of particle radius). As shown in 2, maximum principal stress is 30% greater than equivalent stress (Fig. 28). A critical **120 MPa** may be required for decohesion at Interface (2mm below surface of RPS specimen). **This is in good agreement with tensile stress in Fig. 16 following maximum load.**

▤ Pb, Te, Bi precipitates often at inclusion tips lower cohesive strength. These are low melting phases (350°C for Pb) and microscopic behaviour at high temperature is not well understood. Pb for instance will become liquid/gaseous, enhancing the capillarity effect and influencing the bonding strength of the steel matrix/inclusion interface [21]. During strain reversal in torsion, Pb precipitation was different in as-cast and following strain reversal (see Fig. 29). MnS inclusions could be assumed to be fully voided or associated with a low interfacial strength A contradictory behaviour is therefore present by adding Pb to improve machinability at room temperature, whilst deleterious effect occurs at high temperature due to the low melting. However LFCS have a higher ductility than Bi and Te, therefore easy nucleation does not necessarily translate to easy growth and coalescence of crack mostly at high temperature where matrix strain repartition can exit together with creation of voided structures which do not coalesce (see Fig. 30). Interfacial strain/stress will be developed as demonstrated by Eshelby theory of the order of the elasticity moduli [22].

▤ Orientation and morphology of MnS inclusions will also play a role in affecting strain partitioning (Fig. 31). Inclusions are not perfectly globular and tend to be oriented parallel to compression (and rolling) direction. Eccentricity of inclusion will increase as the ratio between the max and intermediate principal stress increases.

1.9 Oxidation and decarburisation (ball bearing steel)

Formation of Fayalite and decarburisation layer (up to 100 microns) coupled with precipitation/embrittlement at grain boundary and presence of Cr oxide inclusions reduce ductility during rolling (Fig. 32). This is further discussed in Section 2 with respect to **reheating temperature and residence time.**
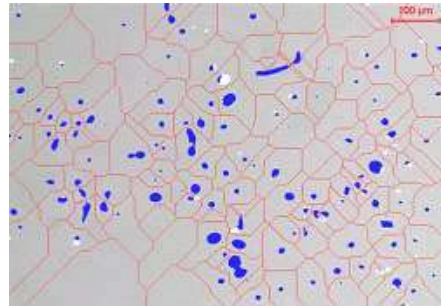
Fig. 24: SKIZ technique and influencing zone (CEIT)
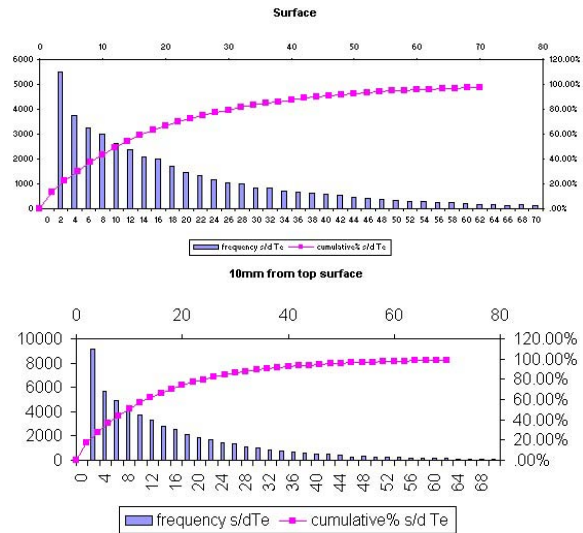
Fig. 25: s/d ratio from surface to 10mm below bloom surface (Corus) S; spacing, d: mean diameter MnS inclusions
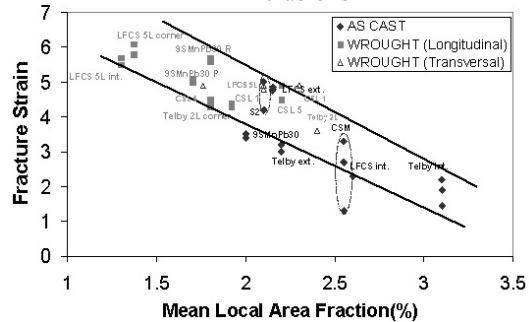
Fig. 26: Torsional fracture strain v MLFI (CEIT)
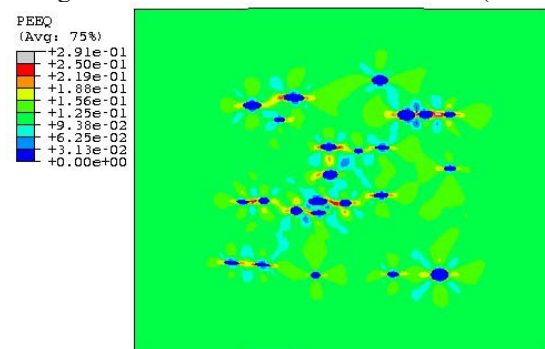
Fig. 27: micro-FEM for strain partitioning (uniaxial test) (Corus)
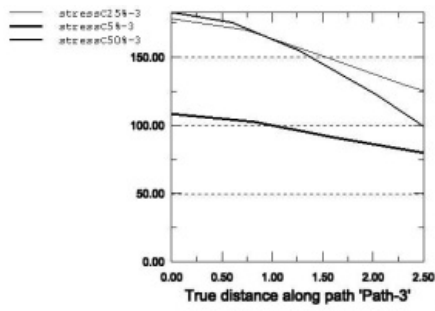
Fig. 28: critical stress for decohesion at MnS particle (Corus)
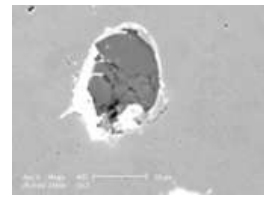
Fig. 29: Pb precipitation following strain reversal in torsion (CEIT)

Fig. 30: FCS voided structure (tensile) with limited coalescence (Corus-Birmingham)

(a)
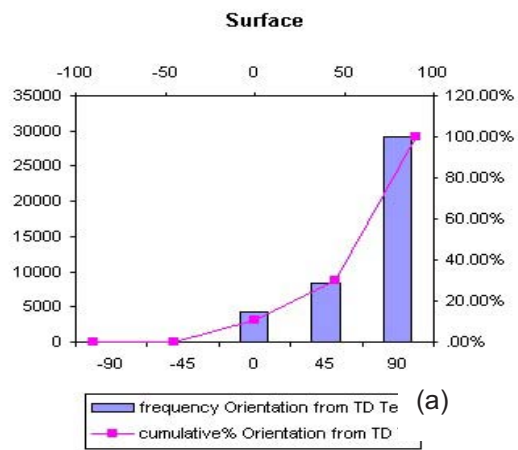
Fig. 32: Oxidation/decarburisation layer (bearing steel – 1180°C – 60 min Mefos)

(b)
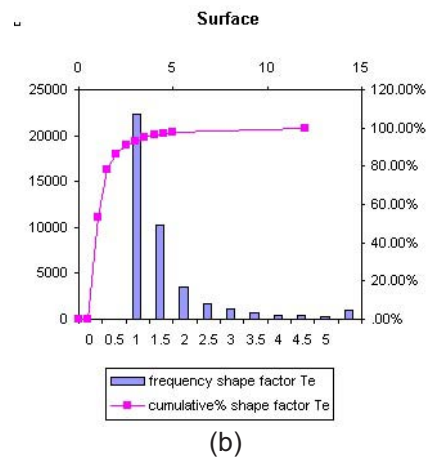
Fig. 31:(a and b): Orientation (a) and shape factor (b) MnS - Te-steel (Corus)

21

2.1 Inherited from Rolling

2. 1.1 Influence of thermal-mechanical parameters (rolling, mechanical testing)

During rolling in primary mills (cogging, roughing), the bloom/billets corners undergo a complex regime of triaxiality (STR) and principal stress ratios (PSR) (see definition of these ratios in Section 3) depending if and when the corner is brought into contact with the roll pass profile (function of schedule and matching cast billet/bloom roll profile fillet radii). In addition, temperature gradient (~200°C) due to roll gap conduction can be experienced at the surface or corner with rapid recalescence at exit of pass due to the heat capacity of the feedstock and slow pacing. Concast feedstock tends to present a fuller initial section profile with corner fillet radius between 6-15 mm. Detailed analysis of the triaxiality and PSR ratios reveal that two regimes can be present in the roll bite, with or without inversion of triaxiality. This triaxiality inversion is in the longitudinal direction but closer look reveals that an inversion is also present through the stock thickness or along a radial cross section path (Fig. 33(a-d)).

The magnitude of the triaxiality is less than 1 varying between 0.1 to 0.5 in absolute term and 1-1.2 for the tensile principal stress ratio (PSR). This level of triaxiality is also present in later passes, e.g. round-oval (see Ascometal Section 3), although the structure will have greater intrinsic ductility as shown by Sidenor (Fig. 33(e)). These values have been used as guidelines for the mechanical tests. Rolling is therefore very sensitive to additional local/non-local parameters (surface/subsurface) and to a certain extent strain hardening due to the low level of triaxiality. As triaxiality increases as demonstrated by Bandstra [23], fracture strain is drastically reduced but independent of any further rise of tensile triaxiality. Strain hardening has major effect in increasing ductility at high triaxiality (>2). Within the material, depending on geometry and pass schedule/reduction, triaxiality (str) inverts some 5 mm below surface in the through thickness direction with the principal stress ratio spr at around 10 mm. So depending on magnitude, if the cortical zone is not thick enough, there will be further possibility for subsurface cracking depending on strain rate/temperature. This is further affected by heat losses due to roll gap conduction and cooling affected zone (CAZ) due to diffusivity (see Fig. 33(f)). This is dependent on projected length of contact, speed and oxide scale thickness (typically 4 to 10 mm cooling affected zone by roll gap conduction).

- ▤ Key mechanical parameters (see Section 3 for definitions) are:

- Triaxiality STR (> 1/3) in bi-directions
- principal stress ratio SPR (> 1)
- principal strain ratio PSR (> 1.5)
- principal average stress SPR$_{av}$ (until mid principal stress becomes negative)
- SPRmax/SPRmin
- principal stress ratio/triaxiality (>1) SPR/(1-STR) as developed from Argon and Le Roy [19, 20]
- principal stresses (I, II, III) (worse case if all tensile) (linked to triaxiality, inclusion spacing and inclusion/void shape)
- equivalent strain (linked to strain at rupture, dislocation density, strain concentration/partitioning due to inclusions)
- temperature
- strain rate
- strain path
- integrated damage criteria either based on principal average stress (see range of criteria in Section 3) used in conjunction with integrated nucleation criterion based on triaxiality (Fig. 34) or developed part of this project (CSM, f$^{\sigma}$).

These parameters (strain, strain rate, temperature) are intrinsically linked to the metallurgical phenomena such as DRX and SRX.

All quantities are defined as instantaneous and integrated (time or strain path integral).

In addition strain reversal was also studied with respect to ductility and effect of recrystallisation. All parameters have been calculated by FEM and used in combination with mechanical testing and rolling data.
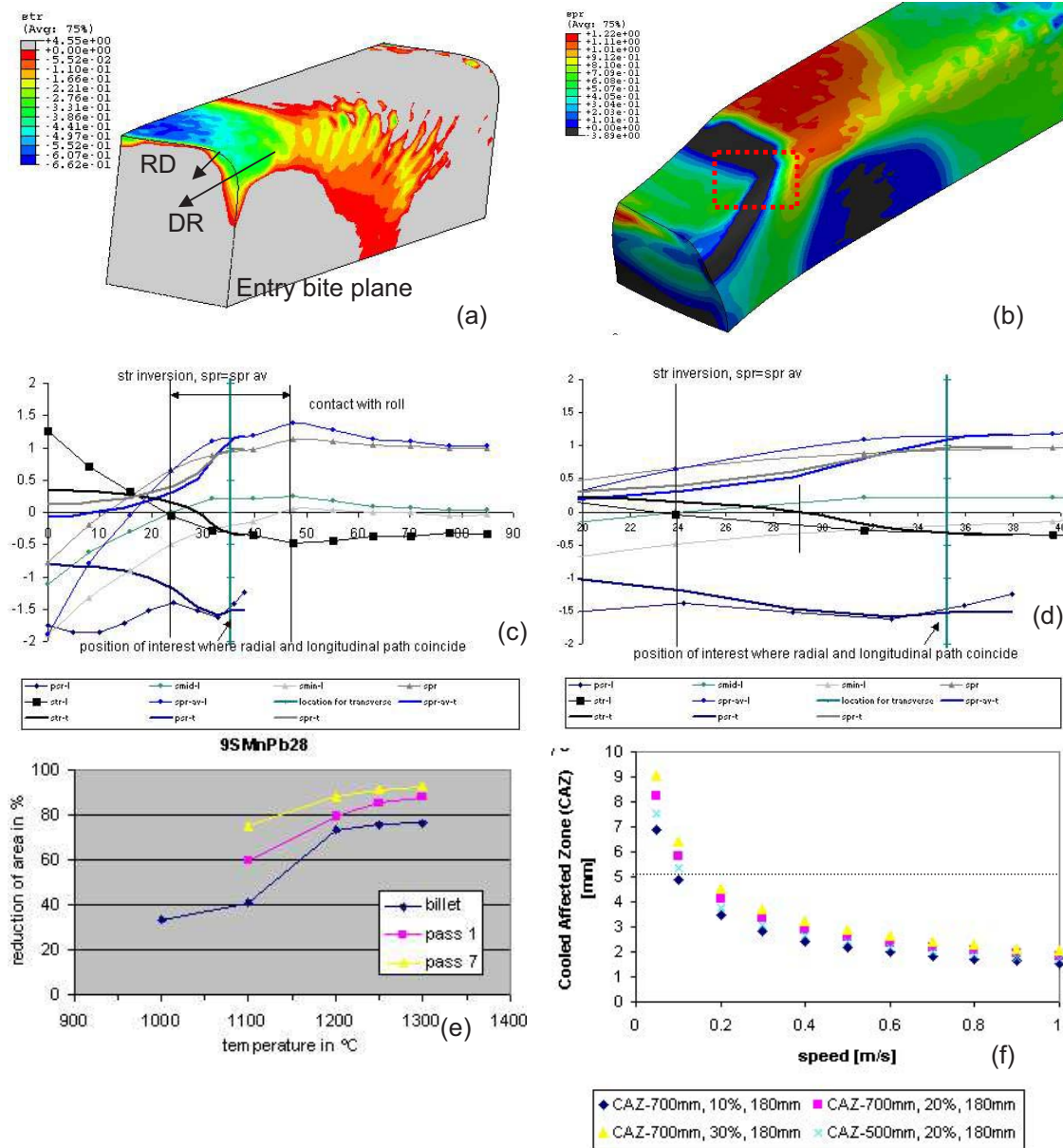
Fig. 33(a-e): triaxiality and SPR inversion (Corus) (a-d), ductility increase (tensile) function of rolling reduction (Sidenor) (e) and heat affected zone (cooled) due to contact (Corus) (f)

23
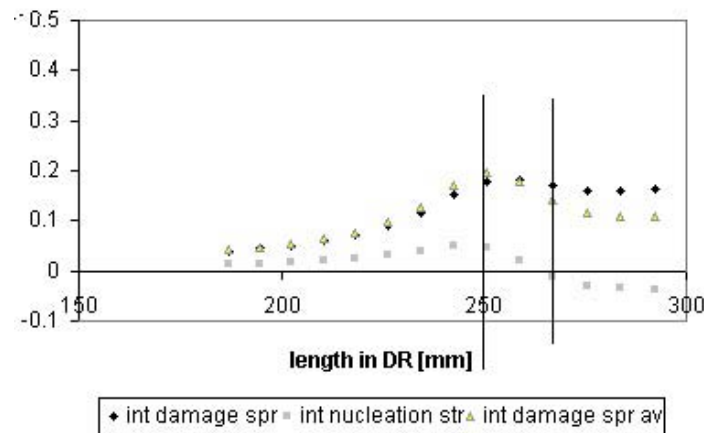
Fig. 34: Integrated longitudinal damage and nucleation criterion at feedstock edge during rolling. At inversion of triaxiality, corner is in contact with roll

Mechanical testing has proven invaluable in understanding key damage mechanisms and through the work of some of the Consortium partners, who managed to develop a standard guideline for mechanical testing (see Section 3), the key mechanical tests used, developed and selected were:

- Torsion (CEIT, Ascometal)
- Tensile testing (Ascometal, Sidenor, CSM, Corus)
- Compression (PSC inc. curvature (Ascometal) and novel geometries (RPS with tapered angle, etc) (Corus), Mefos (axisymmetric and large scale Corus RPS)
- Bending (U-bending (Corus), 3-point bending (Sidenor))

Mechanical testing was used to test steels of interest (FCS, HT) in controlled conditions (strain, strain rate, temperature, spatial position) to assess and extract information on:

- strain to fracture (tension, compression, torsion)
- nucleation or onset of damage (see fig.38) by coupling FEM results of triaxiality-strain to observation of initiation of void/cracking
- recrystallisation kinetics (torsion, stress relaxation)
- incremental observation of nucleation, growth and coalescence of crack
- influence of cortical zone
- influence of spatial position of MnS inclusion (size, spacing)
- derivation of stress-plastic displacement information following necking for fitting damage model (tension)
- derivation of mean local area fraction of MnS
- influence of strain reversal on fracture/damage
- influence of double hit/recrystallisation-recovery mechanism on crack growth/coalescence

At mesoscale, Interaction of triaxiality-equivalent strain is fundamental to nucleation and growth, mostly with presence of second phase particle (interface MnS/steel matrix influence). Coalescence is more function of principal stress direction and strain, exc. all microstructure effects. Therefore cracking can proceed beyond triaxiality inversion and will be dependent solely on principal stress, dislocation density (strain), microstructural features (second phase inclusion, spacing, etc.) and intrinsic ductility of matrix. This has been observed in RPS mechanical testing (crack up to 3 mm for 50% reduction) and tensile testing. Triaxiality-strain at rupture changes according to mechanical testing as per Rice & Tracey evolution [24]. **Strain at rupture increases as triaxiality reduces**.

- Torsion has null or quasi-null triaxiality, therefore strain at rupture is high. This test is designed for studying high shear, softening mechanism and intrinsic ductility of matrix and inclusions. It was observed that the test is sensitive to inclusion spacing and mean local fraction as strain at rupture

24

varies from 2 to 6 (see Fig. 19) depending on grades and location tested (FCS only). However this test is not representative of induced cracking during rolling (due to triaxiality), despite the fact that plasticity is imposed from surface. Mode studied is a shear mode of ductile failure, where crack grows at 45 deg to principal stress.

- Tensile testing or forgeability test except if interrupted will generate data at rupture (same as torsion) but test is negative with respect to triaxiality (0.6 +), except if interrupted tensile is carried out from uniform deformation/maximum load where triaxiality is 1/3. Nucleation will therefore be rapid and test is dominated by growth as triaxiality gradient increases rapidly prior to coalescence (last part prior to fracture) and is always tensile. It is known that for large triaxiality (> 1) strain at rupture becomes less sensitive (see [23]). Tensile triaxiality is also generated from centre of specimen so does not involve surface effect. The only way of changing triaxiality is to adopt an approach similar to Bridgman [25] via notch/gauge length size.

- Tensile testing is however very useful for assessing ductility trough. Strain at rupture is very sensitive to small change of triaxiality close to the rupture, as shown in Figs. 36 and 37.

- Compression testing such as PSC and RPS are good tests for studying onset of cracking by generating the correct magnitude of triaxiality/strain to rolling at surface/subsurface (See Section 3). Maximum triaxiality generated is around 0.4-0.5 depending on taper. Triaxiality is also fairly constant, so growth at constant triaxiality can be studied and derived for a longer period of time (or strain path). This is useful in deriving nucleation curves function of strain rate and temperature. These tests can be scaled up to large scale as demonstrated by Mefos using the Corus geometry (see Fig. 7) and adapted to give a triaxiality-strain path. The inversion in triaxiality is through thickness except for pure PSC.

- Compression testing by axisymmetric compression under high friction creates damage zone, which are maximum at the equatorial plane with a fracture orientation between 45 to 50o to the direction of the maximum principal strain (see Mefos, Corus and benchmark).

- 3-point bending tests as carried out by Sidenor are valuable with respect to the surface/volume aspect of the feedstock, however 3-point bending subjects the structure to high level of shear bands (different to pure bending). 4-point bending is preferable.

All mechanical tests studied by FEM are shown in Fig. 62.

It is possible and necessary to use a range of tests with some interpolation to reconstruct fully nucleation/onset of cracking curves. This is shown in Figs. 37 and 38.
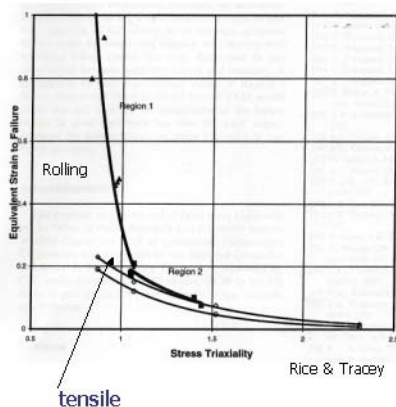
Fig. 35: Triaxiality – strain to rupture [17]   Fig 36: strain to rupture (FCS 9SMn28 CSM grade) v triaxiality (Ascometal)
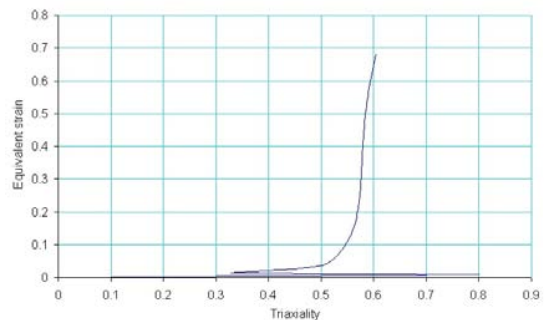
For the range of steels and conditions studied (strain rate, temperature), a reasonable comparison can be drawn-up between PSC, RPS, forgeability and torsion testing (Fig. 38). It is clear that at low or quasi-null triaxiality, the strain to fracture variation is large and function of shear damage (strain) and microstructure. As triaxiality increases, strain to fracture reduces and is more representative of a normal mode of cleavage fracture, thus exposing more the interface properties of the steel microstructure and inclusions. In reality for the mechanical test studied, a mix ductile fracture might be encountered with

crack void growth closer to 60° (mix mode between 45 and 90°). Inclusions spacing/grain boundary (GB) orientation will also play a key role as being the weakest crack growth path (rather than intragranular cracking).
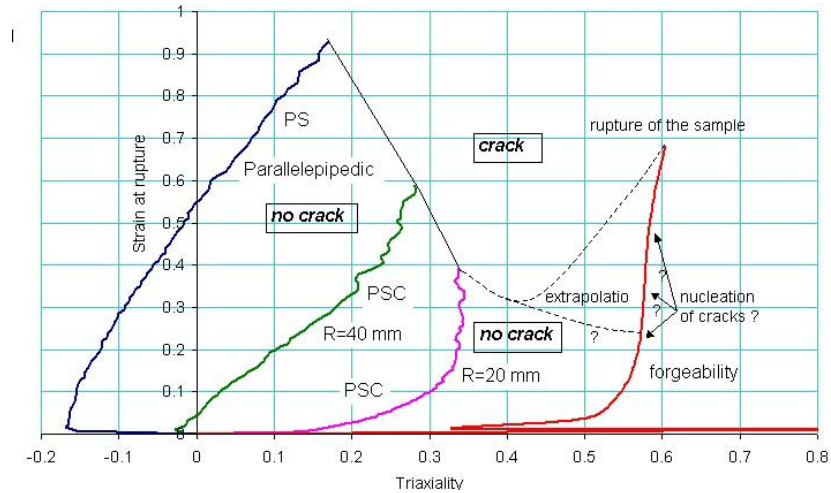
Fig. 37: CSM 9SMn28 grade strain @rupture versus triaxiality for both PSC (inc. curvature) and forgeability (tensile)
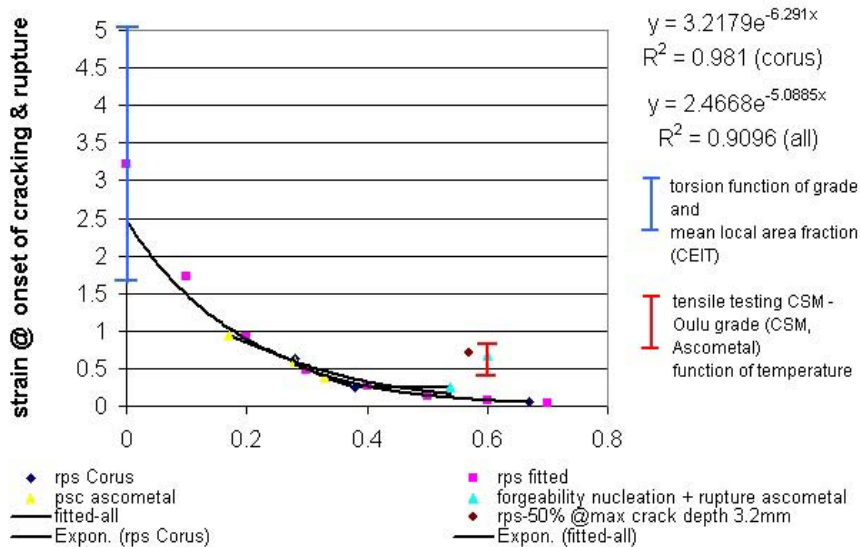
Fig. 38: Overall comparative study of nucleation and failure (Corus, Ascometal, CEIT and CSM) – FCS steels

At high temperature differences exist between PSC and forgeability tests with respect to strain at rupture (Fig. 39). Figure 39 is in fact a mixture of strain representing superficial cracking (lower strain) and strain at rupture via tensile test failure. It is believed that at high temperature, the tensile test is more sensitive to the intrinsic ductility of the matrix and the void volume fraction (coalescence part reduced), being also a test where cracking grows in to out. This requires initial central fracture and growth/coalescence of cracks to sub-critical regions in the process of microvoid nucleation and growth. Thus rapid fracture is indicative of large void volume fraction and/or reduced increment of plastic deformation to explain the cup and cone fracture path. In this case, no excessive shear bands are created. The PSC test is a test where ductile failure is mainly controlled by nucleation, i.e. once microvoids are nucleated, only small void-growth strains are required to bring about the conditions for microvoid coalescence by plastic limit load failure of the intervoid matrix. This is typical to steels with high volume fraction of second phase and where hard and strongly bonded inclusions exist. It is also a test more prone to effect of oxidation, embrittlement and depending on strain rate, grain boundary cracking (at non-contacting surfaces). **Thus compression testing can be considered as a non-**

destructive test for crack observation as cracking is initiated at surface (equatorial free surface). A different mode of cracking has also been observed at high temperature (1200°C) low strain rate (0.1 s^{-1}) in the RPS test where cracking becomes parallel to the maximum principal stress (Fig. 40, outlier points). This is in agreement with McClintock [26], who also observed that for material with close inclusion spacing, normal fracture does not occur but wide cracks tend to open on planes parallel rather than normal to the maximum stress. This is also indicative of effect of minimum hardening and influence of grain boundary cracking. This may also explains the differences with tensile testing. The principal strain criterion proposed by Oh [27] is in good correlation with crack depth/width (See Section 3).
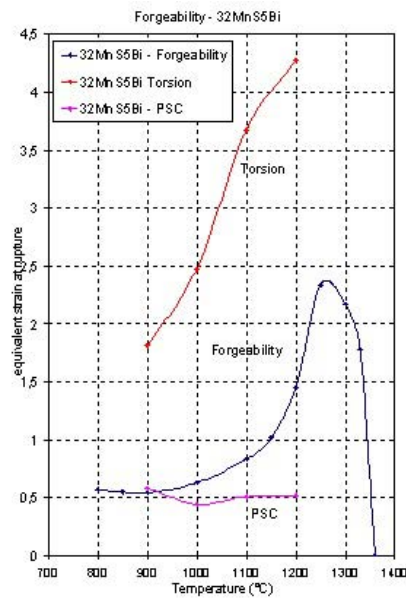
Fig. 39: Superimposition "strain at rupture", PSC, torsion and forgeability
(Ascometal 32MnS5 Bi grade)
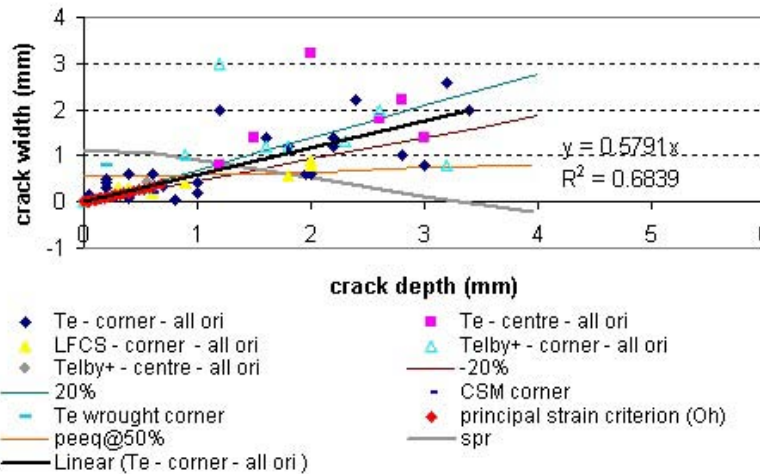
Fig. 40: crack depth v width RPS specimen for main FCS grades tested (Corus)

Further evidence of influence of inclusion spacing in lowering ductility is shown in Fig. 41 where a comparison between Ascometal forgeability tests and CEIT torsion testing on high Sulphur CSM grade is made. Tensile ductility at high temperature is drastically reduced compared to Bi-grade in Fig. 39. As mean local area fraction increases, ductility in torsion, tension and compression is reduced by the fast coalescence process brought about by reduced inclusion spacing and potentially increased particle/matrix bonding. This was confirmed by CEIT during torsion testing of 9SMn28 (CSM grade) of wrought structure where no decohesion could be observed (See Section 3). This is linked to interface strength of inclusion/steel matrix.

Leaded steel have a weak cohesive strength due to Pb effect and therefore have a higher ductility in as-cast conditions (all other factors equal).
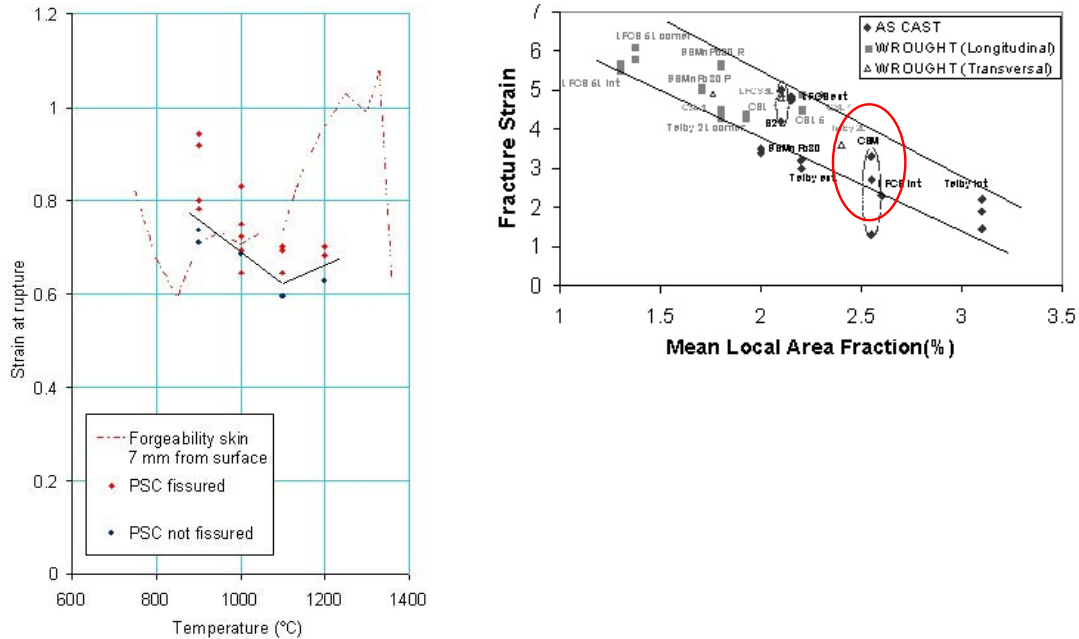
Fig. 41: 9SMn28 (CSM grade) tensile, PSC (Ascometal) and Torsion (CEIT) results

At microscale, the influence of triaxiality-and inclusion spacing has been studied with microFEM models (Corus). Specific biaxial testing with various triaxiality settings (from 0.7 to 1.7) has been imposed. The objective was to predict strain increase due to inclusion impingement compared to far field strain (no inclusion interaction). Influence of inclusion hardness v matrix has also been studied. Debonding and crack growth has also been studied by incorporating a Gurson- Tvergaard type porosity model (nucleation and growth [28]) within the microFEM either at the MnS inclusions to represent low nucleation site for debonding (for instance assuming Pb is precipitating) or within the matrix (see below). Strain tends to concentrate at tip of MnS inclusions with small interaction between different clusters (see Fig. 42).

28
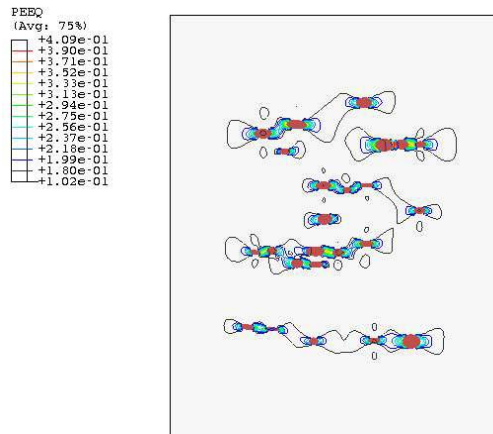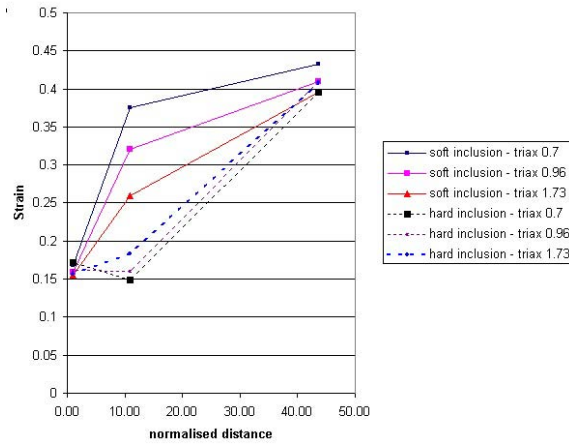
Fig. 42: Bi-axial 2D microFEM of matrix/inclusion interaction function of hardness of inclusion, spacing and triaxiality. Normalised distance represents the ratio of decreased spacing

The closer the inclusions, the greater the strain concentration is developed (up to x3). When inclusions are softer than the matrix (taking into account matrix hardening), more interactions between the various inclusion clusters are developed, i.e. less strain concentration is predicted. The triaxiality has a greater effect when the interspacing of inclusion increases to a given threshold with an inverse predicted behaviour between hard and soft inclusion. As triaxiality increases, strain tends to be less concentrated at soft inclusions, which are less closely spaced. For closely spaced inclusions s/d<2, the spacing between inclusions is the most significant parameter affecting strain concentration, as triaxiality and hardness of inclusion have little effect.

Strain increase due to inclusion impingement and hardness is shown further in Fig. 43. As inclusion hardness increases, strain concentration increases. Similarly as mean local area fraction increases, strain concentration increases, and this will reduce ductility.
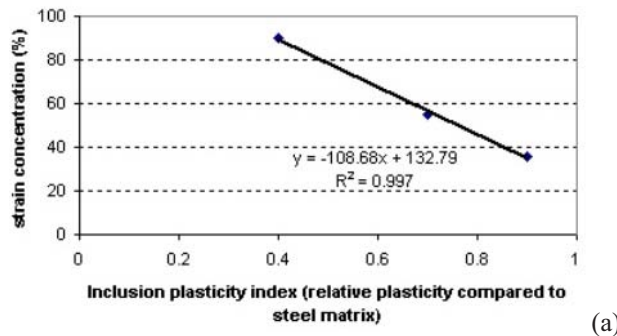
(a)

(b)
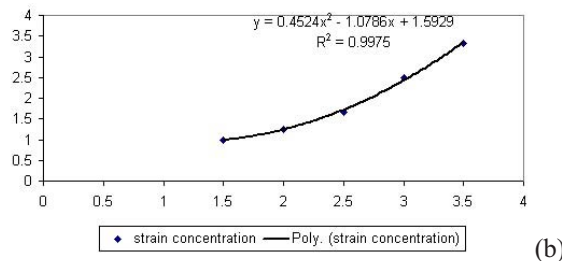
Fig. 43(a and b): Strain increase due to inclusion hardness for a given distribution (a) and spacing (b) (mean local fraction fitted from CEIT torsion experiment)

Decohesion, strain concentration at inclusion tip and rotation are also demonstrated in the next series of microFEM models for a range of MnS plasticity indexes and steel matrix strengths (Fig. 44). Uniform strain field and no decohesion is predicted when the ratio between inclusion and matrix plasticity is close to 1. As MnS inclusion plasticity decreases, deformability of inclusion increases and strain partitioning is more localised within the inclusion. Figure 45 shows interaction between two inclusions with decohesion. As the deformation increases, dead zones are created above inclusions (see [12, 29]), strain concentration is still located at inclusion tip but interference between inclusions reduces as deformability of inclusion increases. This explains to a certain extent the improved ductility of wrought structure as inclusion spacing increases.
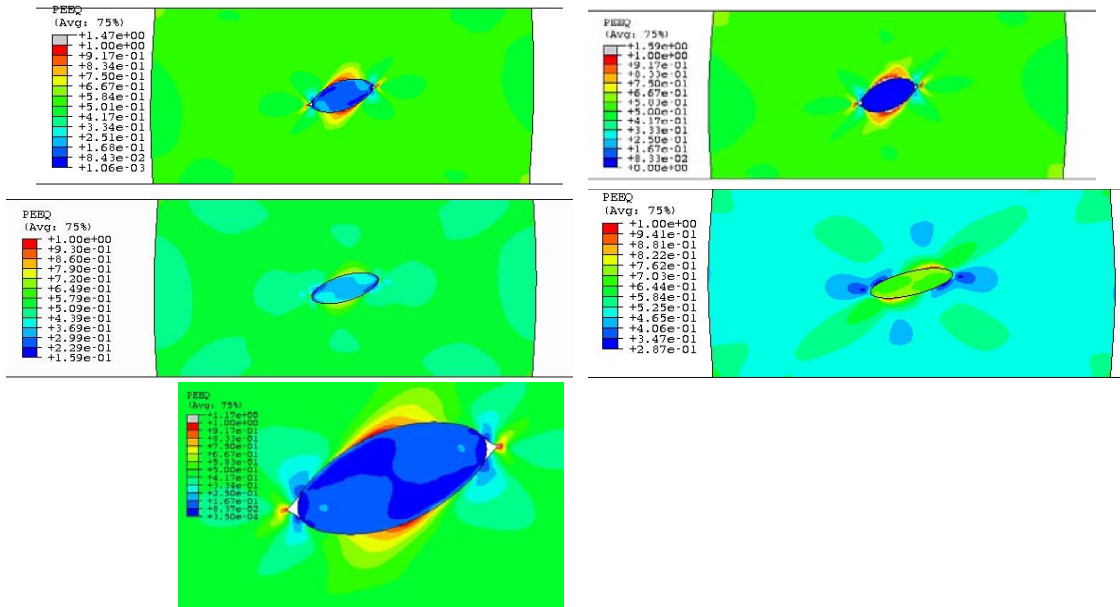
Fig. 44: Equivalent strain and decohesion predicted in compression due to inclusion/matrix plasticity ratios (Corus)
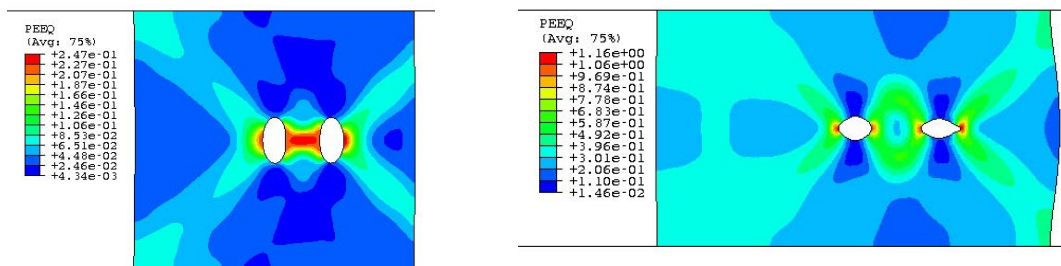
Fig. 45: Equivalent strain and inclusion/matrix interaction during compression for two inclusions (Corus)

Figure 46 shows microFEMs carried out to investigate nucleation around inclusion tips. A Gurson model was fitted to the matrix with hard inclusions, which was then submitted to a tensile test.
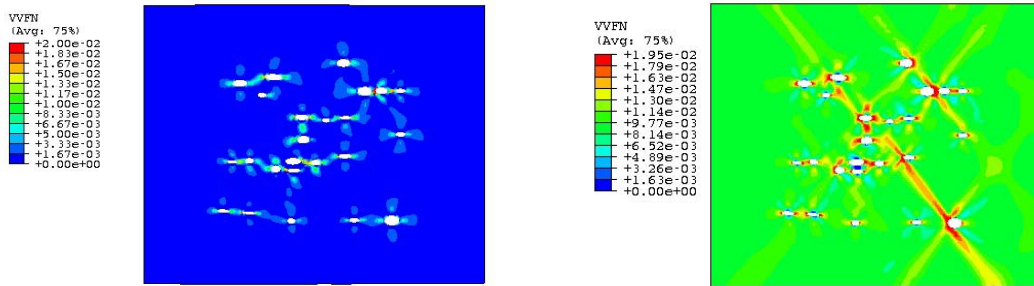
Fig. 46: Void Volume Fraction predicted at tip of inclusion during tensile loading. Larger inclusion and more closely spaced see larger nucleation (case of hard inclusion, relatively soft matrix). Nucleation is also promoted by other microstructural features as shown in right figure where a relative density in matrix less than 1 has been imposed (Corus)

Influence of strain rate and temperature

A complex effect of strain rate and temperature exists which is related to softening mechanisms occurring during deformation as well as hardenability of matrix/inclusions. Forgeability tests are routinely carried out at strain rate above 5 s^{-1}. It is the Consortium opinion that it is preferable to set-up strain rate conditions close to the process being studied. Figure 47 shows variation in ductility function of strain rate and temperature. As detailed in Section 3 and illustrated in Fig. 40, opposite cracking mode has been observed at high temperature and low strain rate with low temperature deformation during RPS testing (Corus). This was also confirmed by studying effect of RX at interpass time, where RX at high temperature low strain rate show a negative effect on nucleation/ductility. Specific work by CEIT could not precisely identify the trends during torsion, due to maybe presence of internal defects. The curves obtained are presented in Fig. 47 (right). Work by CSM show two effective branches depending on Zener Hollomon (strain rate) parameter. This is confirmed on CSM grade 9SMn28 at low strain rate where ductility is low.

31

(b)

(d)
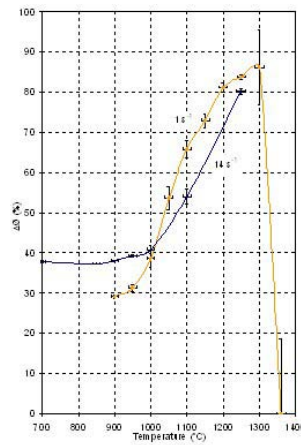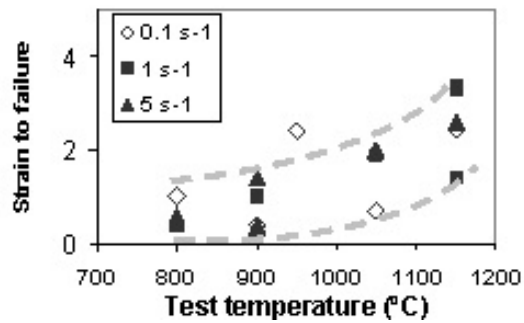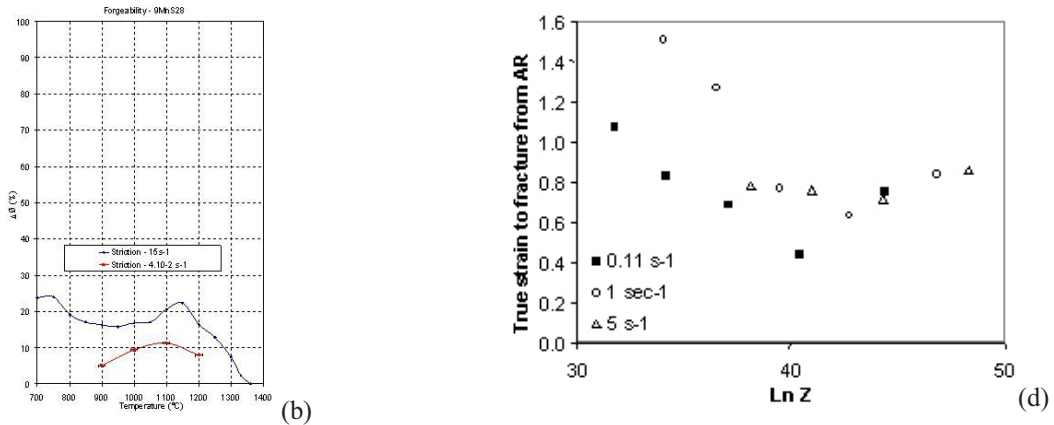
Fig. 47(a-d): Influence of strain rate and temperature during forgeability (a) 32MnS5Pb (b) 9SMN28 (Ascometal), torsion (CEIT) (c) and tensile testing (CSM) (d) - 9SMn28 (CSM grade)

Influence of strain path (CEIT)

An extensive study of strain path effect (reversal) in torsion was carried out by CEIT. Varying factors such as strain per pass (0.25 to initiate DRX), holding time (0 to 5 s), number of reversals (up to 16) followed by monotonic deformation, etc, were investigated (Fig. 48). The conclusion of this detailed work shows that large MnS inclusions are more affected by the strain path (central location of bloom and billet) and in all the tested conditions show voids associated. In addition, when samples of LFCS and Telby steels (Corus steels) were tested, after the reversal a high number of inclusions appear globular and surrounded with Pb, Bi and Te, whereas in monotonic test inclusions are elongated and Pb, Bi, Te appear emanating from the corner in the direction of deformation. This effect could potentially modify the cohesion between MnS inclusions and matrix, and reduce further ductility.
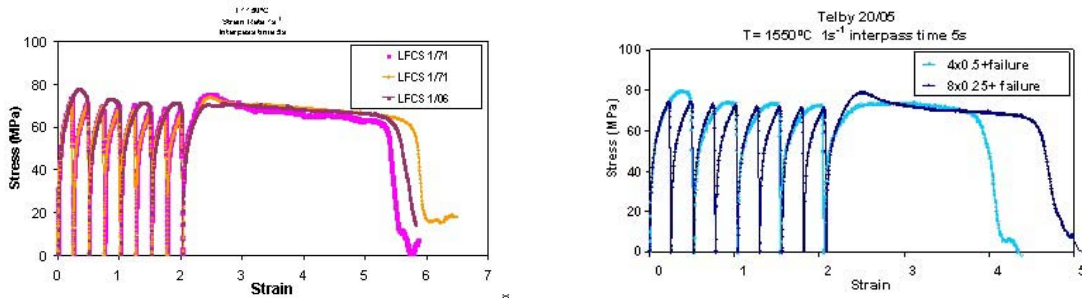
Fig. 48: Influence of strain path (reversal) effect on LFCS and Telby+ steels (up to 8 reversals) (CEIT)

Influence of austenitisation & pacing

- **FCS steels**

A complex trend has been observed, with somewhat conflicting results. Austenitisation temperature, prior deformation, in forgeability tests does not seem to have a significant influence on ductility compared to the austenitisation time. Within the temperature range studied (< 1250°C), minimum grain coarsening occurred, hence no major change to the microstructure. Austenitisation time seems however detrimental during tensile testing as shown in Fig. 49 below. Plant observation shows quality billet index function of resident time and temperature. It shows that for a given billet section and grade, a range of resident time and discharge temperature is required to minimise temperature gradient and improve ductility during rolling. Therefore the reheating time has to be considered together with the temperature because bars rolled with a good discharge temperature can have a poor quality due to short residence time.

32
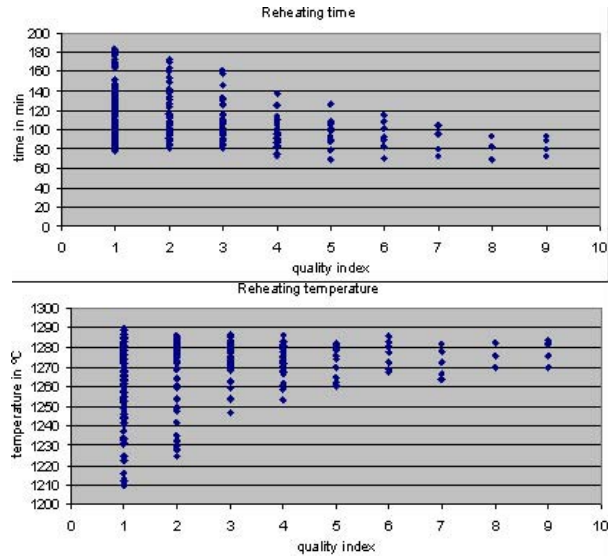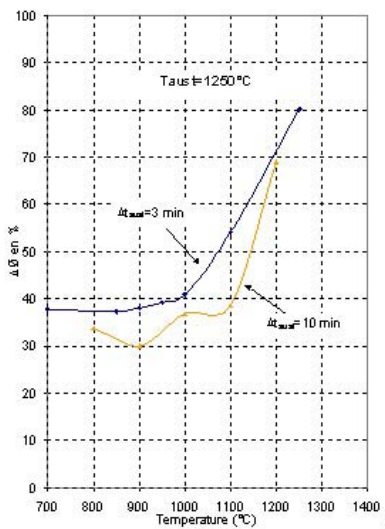
Fig. 49: Influence of austenitisation time (tensile test) prior deformation (Ascometal) and resident time/temperature during reheating of EAF billet production (Sidenor)

- **Ball bearing steel (Mefos)**

Frequency of cracking was dependent on reheating time with longer reheating times at higher temperature promoting decarburisation (up to 100 microns in depth), Fayalite formation (above 1177°C) and precipitation of Cr oxide and GB embrittlement. These factors have all negative influence on ductility.

Influence of surface state: Surface state, contrary to initially thought (and also compared to warm/room temperature deformation), has not a profound influence on reducing ductility as shown by Ascometal (PSC test 9SMn28, 0.53 v 0.57 (machined) strain @rupture at 1000°C), however "real" surface state in production are often associated with oxidation/embrittlement, etc. and therefore surface state should be considered as potential catalyst for crack initiation. This is further compounded by the length scale issue brought about by proximity of inclusions to surface as well as reducing effective barrier of cortical zone (see Fig. 50).
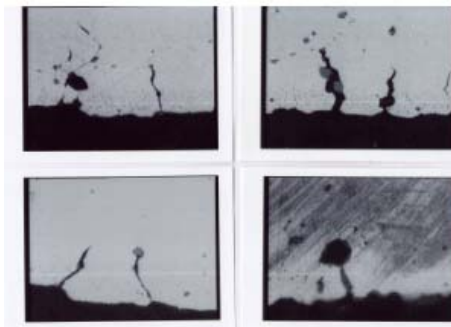
Fig. 50: Effect of inclusion closed to deforming steel surface (Corus, Te-FCS steel)

CSM has quantified the effect of cortical zone thickness on cracking index by carried out, in the laboratory rolling mill, experiments with various decorticated surface layers. This is summarized in Fig. 51 which also shows elongation of inclusions with temperature. Below 7 mm removal of surface, cracking increases.

33
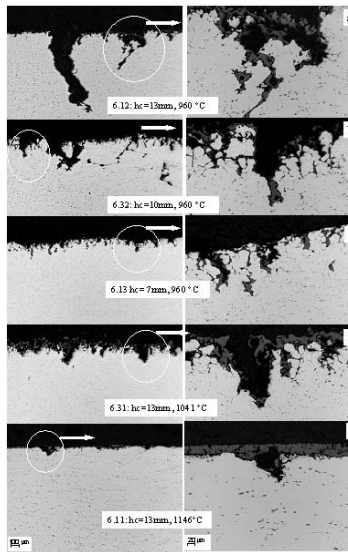
Fig. 51: Effect of cortical zone and temperature on cracking 9SMn28 (CSM)

This is further illustrated in Fig. 52 below which shows the variation of the mean crack dimensions function of temperature and cortical zone thickness.
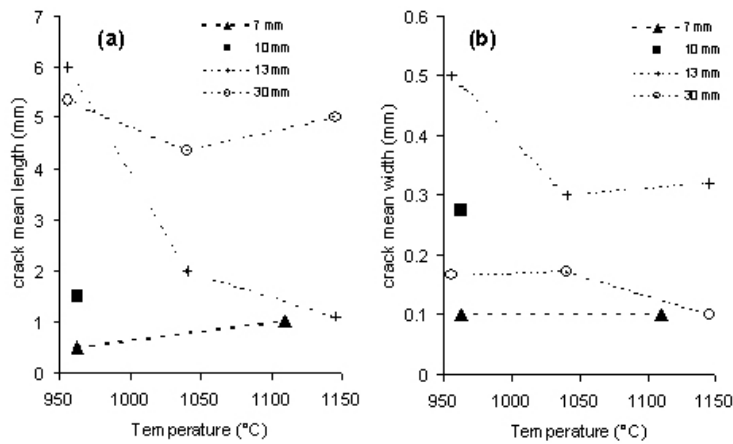
Fig. 52: mean dimensions of crack (length, width) in CSM 9SMn28 Laboratory rolling experiments (CSM)

Influence of pass design: primary rolling in box-box H/V configuration reduces propensity for cracking compared to diamond/gothic passes. This was verified by Corus, Sidenor and Mefos and implemented by Sidenor. Optimisation of pass radius in wire rod plant at Ascometa-Fos has been undertaken based on minimization of triaxiality. This modification is scheduled to be implemented shortly in the plant (Fig. 53).
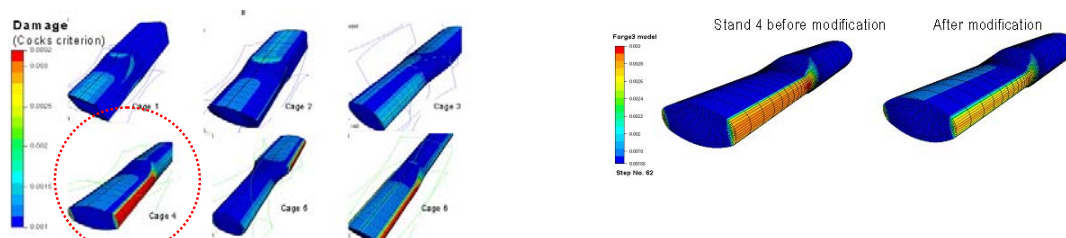
Fig. 53: Pass design optimisation based on project delivery (Ascometal Fos)

- **Influence of Strain, cortical zone and positioning within bite**

Laboratory mill experiments carried out by CSM have quantified the effect of positioning on onset of cracking function of cumulative reduction (Fig 54). Cracking and subsurface cracking start to occur at a reduction of 50%, i.e. at a longitudinal position of 31 mm from entry bite.
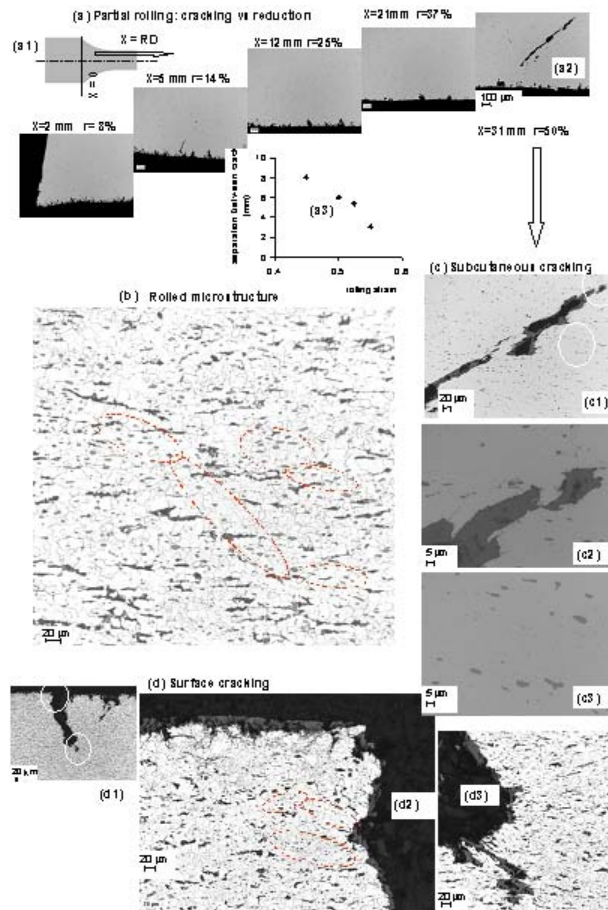
Fig. 54: Influence of cortical zone, bite positioning, strain/triaxiality on cracking 9SMn28 (CSM)

35

- **Influence of dynamic recrystallisation and thermal gradients**

Thermal losses, L/hm (mean roll gap factor <1) and dynamic recrystallisation kinetics can create a regime of non-uniform strains, which will be more prevalent at subsurface, as indicated by the FEM modelling carried out by CSM in Fig. 55 (see dashed circles) produced with the incremental formulation described in[66] and the constitutive model in Table 17. Therefore cycles of DRX, SRX at interpass which are linked to pacing will include a regime of either annihilation of strains energy or accumulation which will have an effect at surface/subsurface of the deforming feedstock, subjected to triaxiality inversion and tensile principal stresses. Of particular interest is the development of high strains (encircled) at the feedstock cross sectional edge. The highest values of this local strain are near and above the predictions for 60% nominal thickness reduction in the flat rolling experiments that CSM carried out, which showed the profuse defect formation (see Section 3). Such strain localisation extends to the neighbourhood of the preset defect area and constitutes a danger for its propagation towards the surface when crossing the tensile stress state on exiting the roll gap.
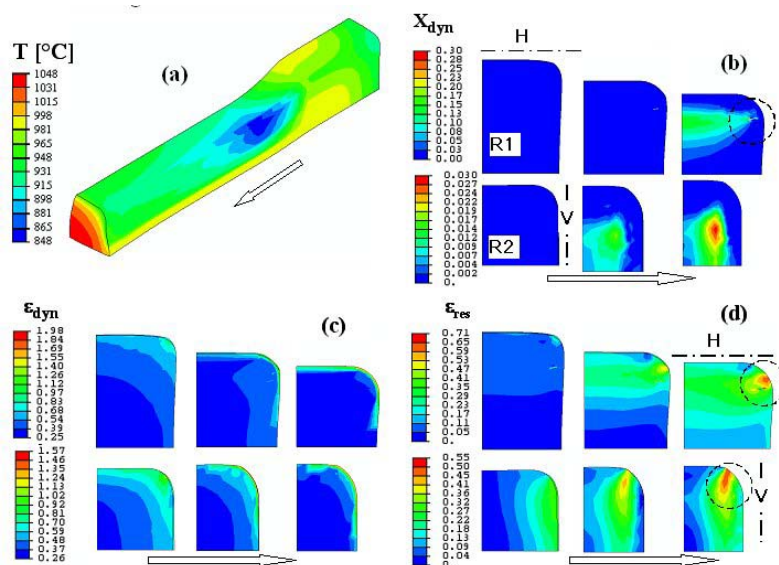
Fig. 55: Influence of thermal losses and dynamic recrystallisation on non-uniformity of strains 9SMn28 (CSM)

- **Final ductile cracking theory (WP6-8):**

Ductile damage has been investigated across the length scale function of casting, reheating and rolling/deformation parameters.

- **Nucleation** at mesoscale (exc. microstructure) is a strong function of triaxiality and strain, and requires a given level of triaxiality for void initiation at a given strain (> 0.33 in tension). This threshold triaxiality increases as strain reduces, however different mode of ductile fracture may be imposed/observed, therefore it is important to fix the triaxiality-strain curve(s), which bear a similitude to the rolling process. Triaxiality should not be strongly affected by temperature and to a certain extent strain rate. These (triaxiality-strain) are therefore the external process parameters to be considered, which are function of deformation, pass geometry, matching billet-roll fillet, etc. during rolling. Length scale effect via inclusion spacing, diameter, morphology, index of plasticity plays a role in changing the strain concentration and distribution at and around the inclusion/matrix interface. Composition and type of FCS grades will have different cohesive interfacial strengths between MnS inclusions and matrix, but little change in strain hardening behaviour (except some differences between as-cast and wrought but this is believed to be a secondary effect). Nucleation is therefore dependent on triaxiality, plastic strain (dislocation density) and second phase inclusion (spacing/diameter, plasticity (mean local area fraction) and to a certain extent shape). A necessary condition for nucleation is that **a critical value of normal stress must be exceeded at the**

inclusion-matrix interface which is function of dislocation density (strain) and triaxiality (or mean stress) (see [19, 20]). Two modes of nucleation exist, continuous nucleation or discontinuous nucleation where initial cavitation occurs on large or elongated inclusions followed by a second step of nucleation at higher strains. The later has been observed in torsion and compression (RPS, double collar (see Fig. 56 below)). Larger particles introduce damage easily in the initial deformation process; this is then followed by smaller particles which will then control the fracture event, mostly if closely spaced. A minimum str of 0.15 - 0.2 is required for nucleation at high strain (see Fig. 38). A low nucleation strain (say 0.05) can be assumed for leaded steel. Nucleation precedes growth and was studied in detail in various mechanical testing (see Section 3, Fig. 38 and Fig. 56 below).
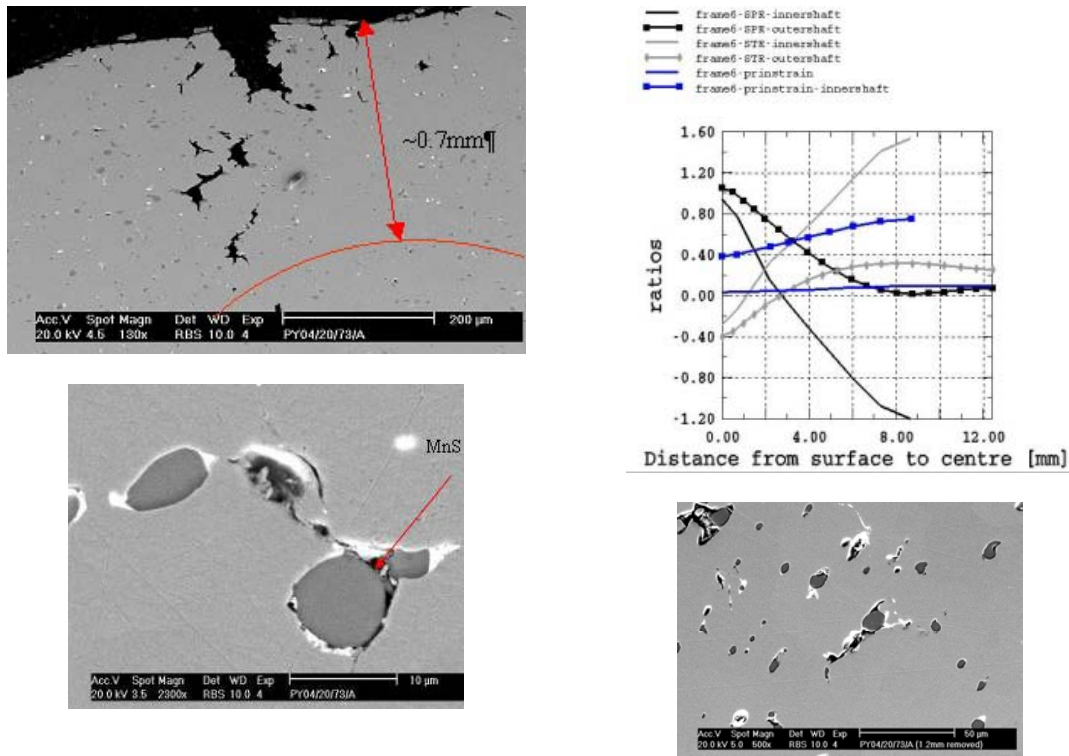
Fig. 56: Double collar compression test equatorial plane showing damage + internal nucleation/decohesion ahead of crack tip (Corus)

- **Growth of voids or void linkage** can be rapid (case of compression testing, irrespective of strain rate), slow (case of torsion testing) or "normal" depending on the volume fraction of second phase inclusions, inclusion spacing and mean diameter (mean local inclusion) as well as strain and triaxiality. This is evident in torsion where fracture via growth and coalescence is slow (high fracture strain, null triaxiality) and for instance in the case above of the double collar test outer ring (Fig. 56) where the local strain is not high enough despite triaxiality inversion at ~1 mm from external surface. Depending on triaxiality, different mode of growth can theoretically be observed during rolling (LT, LW, TW (L: longitudinal, T: Thickness, W: Width or Transverse) when the triaxiality is greater than 1/3. As triaxiality increases, the various mode of growth reduces. Compression testing is ideal for determining microvoid nucleation strains. **The key for slow/rapid growth is the extent of triaxiality/mean principal stresses and strain for reaching other sub-critical stages in the microvoid nucleation and growth sequence ahead of the initiated crack**. This was observed in RPS testing where cracking can proceed ahead of the inversion triaxiality assuming enough strain is present. This is somewhat opposite to the tensile test where triaxiality is always tensile. There is also an inverse dependence of fracture strain on tensile stress transverse to inclusion/void. It is fair to say that in all the calculations made, no consideration of the triaxiality change at the crack tip has been considered but as shown by McClintock (see [26]) values can reach 5.36 in plane strain processes. Strain hardening also plays a key role in retarding fracture,

together with structure cleanliness in reducing growth but extreme purity is required to improve ductility significantly. **Linkage occurs when the largest inclusion dimension is of the order of the mean spacing (see Fig. 56). Therefore growth can be rapid when s/d<2 (s: spacing, d; diameter). This may explain why edge cracking can be promoted due to a large fraction of small inclusions, potentially closely spaced and submitted to adverse processing conditions, which will then dictate the fracture behaviour**.

- **Coalescence** occurs when the dynamic recovery processes cannot accommodate the rate of plastic deformation under adverse principal and/or shear stresses. Strong association with the maximum principal stress and/or average principal stress (if greater than max principal) is present and needs to be taken into account. There is less dependency on triaxiality. In addition mean local area fraction, GB, etc. plays a key role at microscale. The ratio SPR/(1-STR) as derived from [19,20] is a relevant normalised criterion for coalescence (see Section 3). Influence of strain rate and temperature are also key in changing the mode of coalescence from 90 degree to principal stress direction to parallel mode. At low strain rate, high temperature, grain boundary cracking has been observed which is also linked to an index of plasticity ratio between inclusion and matrix being maximum. These mechanisms are schematically represented in Fig. 57 below. Fracture loci as defined by Le Roy [19] to simple stress state (uniaxial axisymmetric and plane strain) are shown in Fig. 58 (case of spheroidized steel). It can be shown that as the ratio between maximum principal to mid/min ratio gets closer to 1, nucleation is promoted at stress closed to yield. As the min principal stress becomes compressive, higher critical stress for decohesion is required above the equivalent stress.
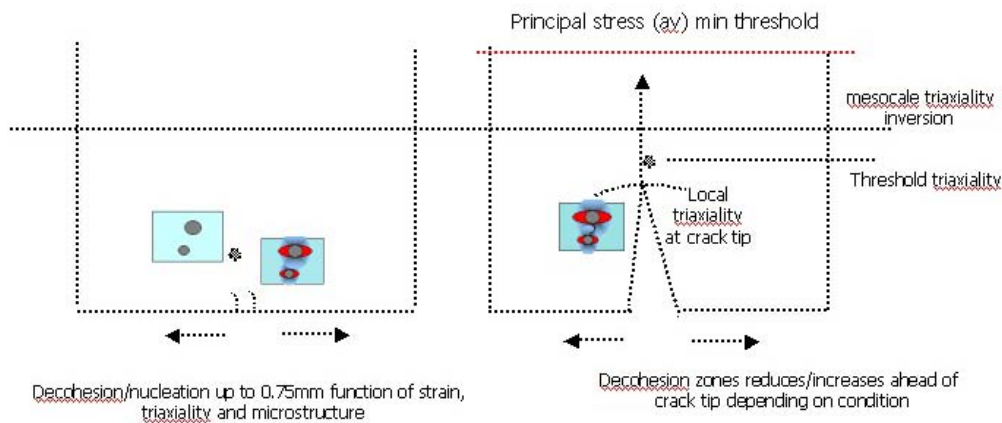
Fig. 57: Schematic representation of ductile damage (FCS) observed in RPS testing (Corus)
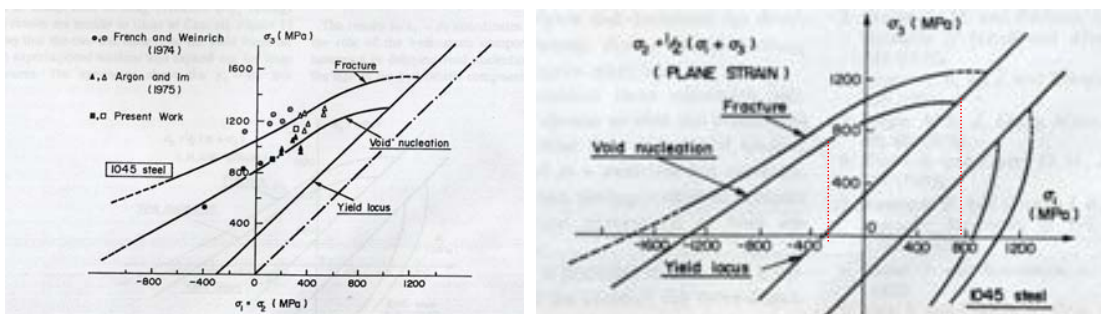
Fig. 58: Fracture loci (nucleation/fracture) v yield loci in stress space – axisymmetric (left), plane strain (right) [18]

- **Applicability of Models (WP7-8):**

A series of models have been developed and are presented in Section 3. A top down multiscale approach has been implemented part of this project and is summarised in Table 4 below.

Table 4: Model framework (see also Table 2)
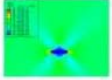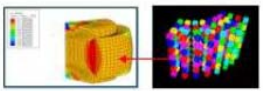
Type	Scale	Details
Criteria (time/strain integral of triaxiality/strain), e.g. Oyane, Chaboche/Lemaitre, Cocks, Cocroft, etc.	Macro (mm and above) + microstructure parameters (Field Variable)	Calibration/ Easy implementation $i_c \equiv \int_\Gamma \frac{p}{\sigma} d\overline{\varepsilon}$
Constitutive models	Meso (sub mm)	Gurson/Tvergaard, In-house
Constitutive models	Meso + internal state (sub mm)	In-house/BirminghamU-based on dislocation density
MicroFEM (in-house) of inclusion interaction + micro-mechanics (polycrystal plasticitymodelling -Oxford University)	Micro (microns)	Global FEM/ submodel Displacement
CAFE (Sheffield University collaboration)	Meso/Micro	

Figure 59 shows applicability of some of the constitutive models developed to multistand bar rolling (Ori-Martin) with particular emphasis on the principal-equivalent stress ratio f^σ which predicts both expansion of the preset defect within the stock cross section, as well as new non-negligible damage areas departing from the main rolling surface. Therefore, full defect generation can result either from new onset of damage at surface and/or coalescence due to debonded/microvoided subcutaneous defects.

It is shown (Section 3) that the f^σ model best predicts the observed edge cracking. The important improvement over the original Cockroft-Latham [35] index used in this project is the coupling of the damage function with consolidation and material properties sensitive to material degradation. Figure 60 shows applicability of more simple criteria to rolling by Mefos and indicate the practical effect of using such criteria for identifying regions at risk of damage due to underfilling of groove.
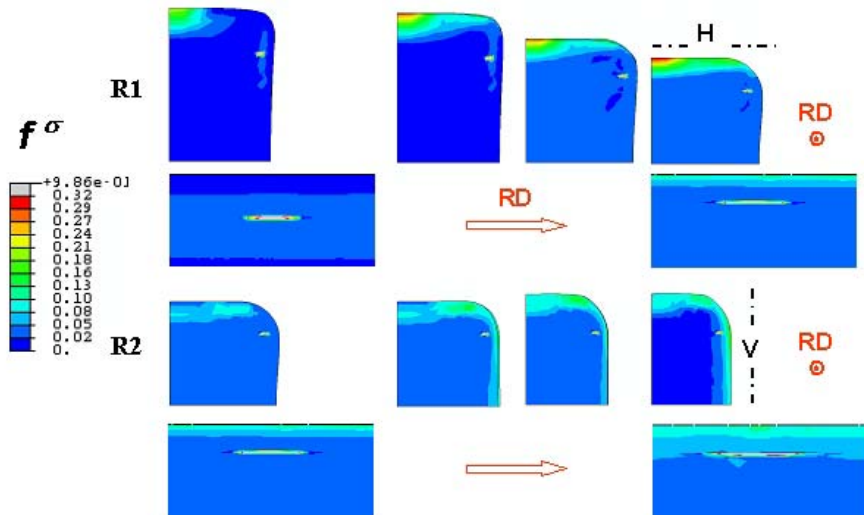
Fig. 59: Damage modelling bar rolling (Ori-Martin first two stands) (CSM)

39
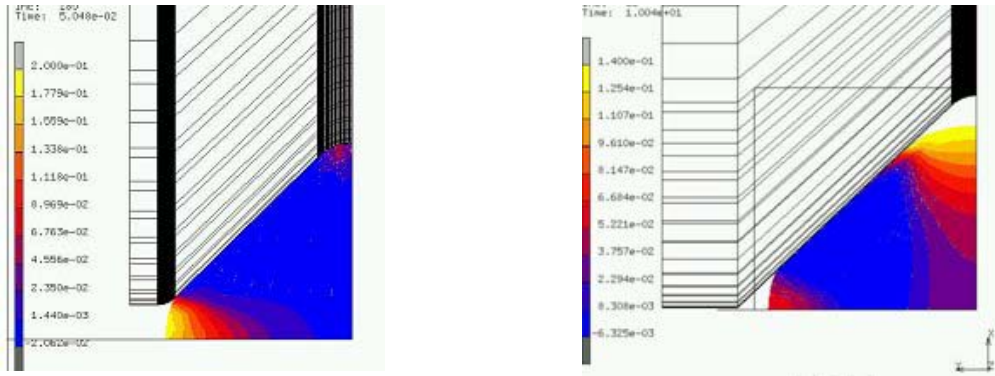
Fig. 60: Cockroft-Latham damage criterion applied to square bar rolling showing under-filled regions (right) (Mefos)

The project looked also at applicability of various existing damage criteria and their suitability to predict correctly where growth rate might occur. Figure 61 shows computed theoretical damage growth rates for some of the models considered, highlighting the increase of growth rate as triaxiality increases (greater than 1/3), however care should be taken as applicability for instance of the Rice and Tracey growth model [30] to the Corus RPS test does not seem to fit observed experimental findings in terms of localisation of cracks (growth is mostly predicted at side surface as being driven by maximum tensile triaxiality). Also large differences exist at low triaxiality where for instance cavity growth rate can be potentially suppressed when a compressive triaxiality of $-\sigma/3$ can be imposed (mean stress = 0). Triaxiality based only growth models therefore may not be accurate enough as being mostly developed for tensile testing [31-34].
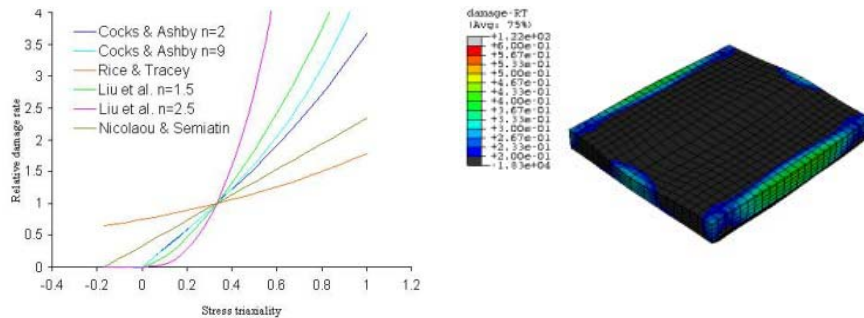
Fig. 61: Test of various damage growth models and application to RPS showing incorrect growth location regions (Corus-Birmingham)

- **Cross validation of Models (WP7-8):**

An uniaxial compression test with conditions supplied by Mefos (high Coulomb Friction 0.4, flows tress data 20MnCr5 steel) was selected as a benchmark for comparing some of the damage models used and developed. Modelling tests were to replicate one of the compression tests carried out by Mefos (see Section 3) with an initial cylinder geometry of 46 by 46mm (height to diameter ratio) deformed to 21 mm. Owing to the intrinsic ductility of the rock drill steel, only one experimental case shows evidence of damage for the conditions tested (950-1150°C) and strain rate (1.5 s^{-1}). Repeat of these conditions on a dual-phase steel with high Sulphur content showed the detrimental effect of Sulphur as cracking increased. Figure 62 shows computed discrete results of principal stress, triaxiality and strain ratios as well as regions for damage initiation and growth (across length scale) computed by Mefos (using Marc software, Cockroft-Latham [35] and Oyanne [36] criteria), Corus (using a range of normalised criteria, "standard" ABAQUS damage models [37, 38], meso/multiscale constitutive models developed with Birmingham University [39] and finally models adapted from CAFÉ modelling [40]) and Ascometal (using Forge 2005 and Lemaitre damage model [41]) (see also details in Section 3). It should be stated that none of the damage models were calibrated to this steel composition (see also ref [42]) and for most of the simple criteria did not include any microstructure information (only

40

strain/stress based). However, the study is still relevant comparatively with respect to initiation/extent of damage zones predicted and show that all models predict correctly regions of onset of cracking. No models currently developed is accurate enough to take account of the multiscale (length and time) nature of ductile damage, therefore a multi-step approach from simple criteria to more detailed modelling is recommended.

(a)

(b)

(c)

(d)

(e)

(f)

(g)

(h)

(i)

(j)
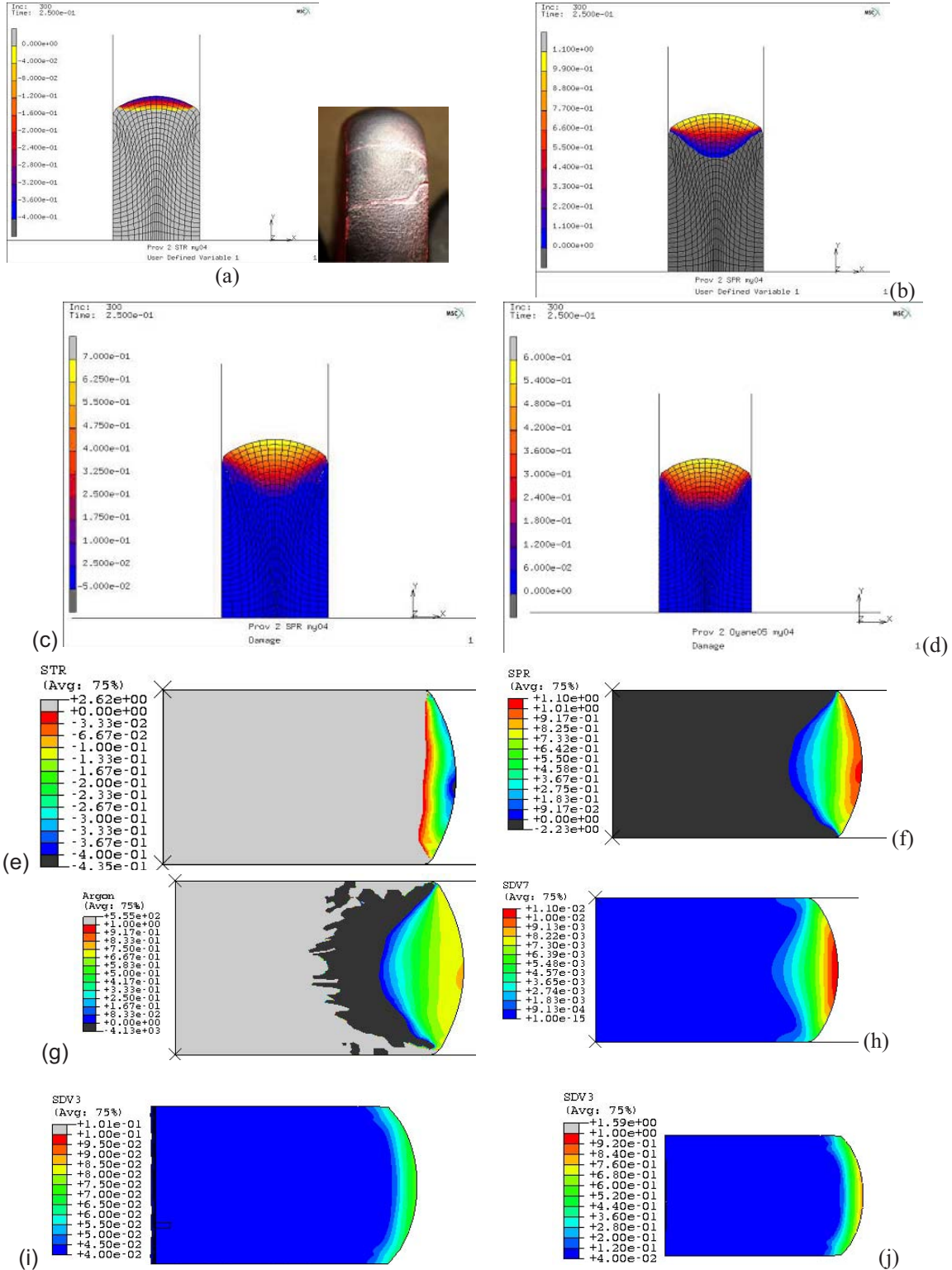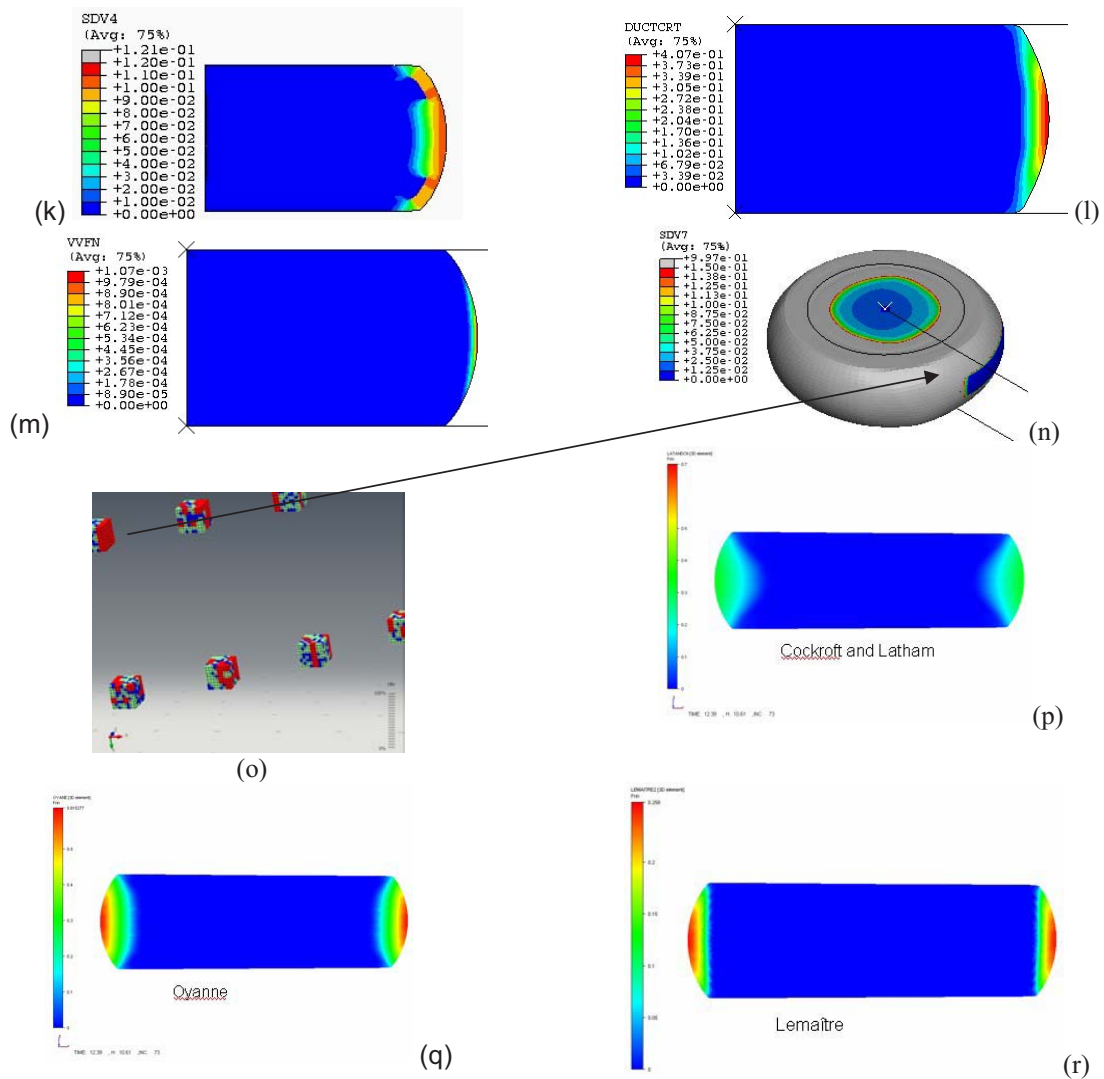
Fig. 62(a-r): Comparison Mefos (Marc®), Corus (ABAQUS®) and Ascometal (Forge2005®) - Axisymmetric compression isothermal, strain rate 1.5 s⁻¹. (a) Mefos STR (b) Mefos SPR (c) Mefos Cockroft Latham (d) Mefos Oyanne damage (e) mesoscale Corus STR (f) mesoscale Corus SPR (g) mesocale Corus SPR/(1-STR) (h) Constitutive VUMAT model 1 (Corus) damage plasticity viscoplastic (i) Constitutive VUMAT model 2 (Corus) damage inclusion low inclusion density (s/d > 2) (j) Constitutive VUMAT model 2 (Corus) damage inclusion high inclusion density (k) Constitutive VUMAT model 2 (Corus) damage coalescence high inclusion density (l) Ductile damage ABAQUS ® "standard" model (no user-subroutine but include nucleation/growth [38]), (m) Gurson nucleation model Corus, (n, o) CAFÉ model Corus with ductile behaviour (CAFÉ cells ductile damage (red), blue (inclusion)), (p) Ascometal Cockroft Latham (Forge 2005®), (q) Ascometal Oyanne damage model , (r) Ascometal Lemaitre (2) (Forge2005®)

Ideally in view of the change of stresses and strains over time and potential changes in direction due to rotation, integral quantities of stress and strains are preferred and these are taken into account in the formulation of the constitutive models (See Section 3).

- **On-line detection methods (WP9)**

Three on-line detection methods were used/trialed during this project with methods ranging from CCD optical measurement (CSM/Ori-Martin), eddy-current (Ovako Imatra) and finally EMAT laser ultrasonics (Corus) (Fig. 63). Prototype to production systems were used with the CSM/Ori-Martin

being an industrial patented system installed since 2004 at Ori-Martin plant (see [43]) (H/V Stand4/5 intermediate mill), the Imatra-Ovako system was a new system trialed for a small tonnage (720 t) on the medium bar mill, with finally the Corus system being a prototype laboratory equipment developed in another RFCS project [4] and tested during the first 18months of this project on a moving hot billet. Two systems are aimed at surface detection, whilst the Corus prototype is aimed at both surface and bulk.

The on-line defect detection system used in the Project by CSM is a registered product [43] of a joint venture between CSM and Ori Martin. It has two heads that continuously screen four 'faces' of the rolling stock, and detect, count and capture images of every suspected defects. These are filtered by the system to discard rolled scale images and confirm the open cracks. The main display screen gives the position of each defect along both the length and width of the projection of the hot rolled bar and information on their opening status. Each defect is codified, stored and can be examined individually as shown in the bottom rows of Fig. 61. For steels of interest 9SMn28 and LS30-Bi, defects detected were localized type defects, very shallow, elongated in the case of LS30-Bi steel (pre-rolled grade with few surface defects). Profuse edge generation defects, which are deeper and open in the case of as cast 9SMn28 steel, were also detected.

An Eddy Current surface defect detection system was installed temporarily at Ovako Imatra's medium bar mill in May 2007. The unit was a commercial system (Defectotherm T60) by German Company Institut Dr. Förster GmbH & Co. KG and was aimed at surface detection of round bars between 22 to 25 mm diameter. The unit was successful in detecting tail-end overlapping and roll groove wear but no other surface detects for the tonnage and grade rolled (representing 20% of production) were detected as surface quality was not an issue.

A hybrid Laser-EMAT (ElectroMagnetic Acoustic Transducer) system that involved taking a university prototype and developing it for use on hot, moving steel was implemented at Corus. The system was demonstrated to work successfully on hot moving steel in the pilot plant rolling mill at 800°C. The EMAT system could be used for finding internal defects, in addition to surface defects at a resolution of 1 mm. EMATs are better receivers of signals than laser interferometer and probably more adapted to rough and exposed surfaces.

Fig. 63(a-c): On-line detection equipments/prototypes used & tested (a) CSM-Ori-Martin optical production system 9SMn8 (b) Ovako Imatra Production trial of Eddy Current system (c) Corus Laser-EMAT prototype system
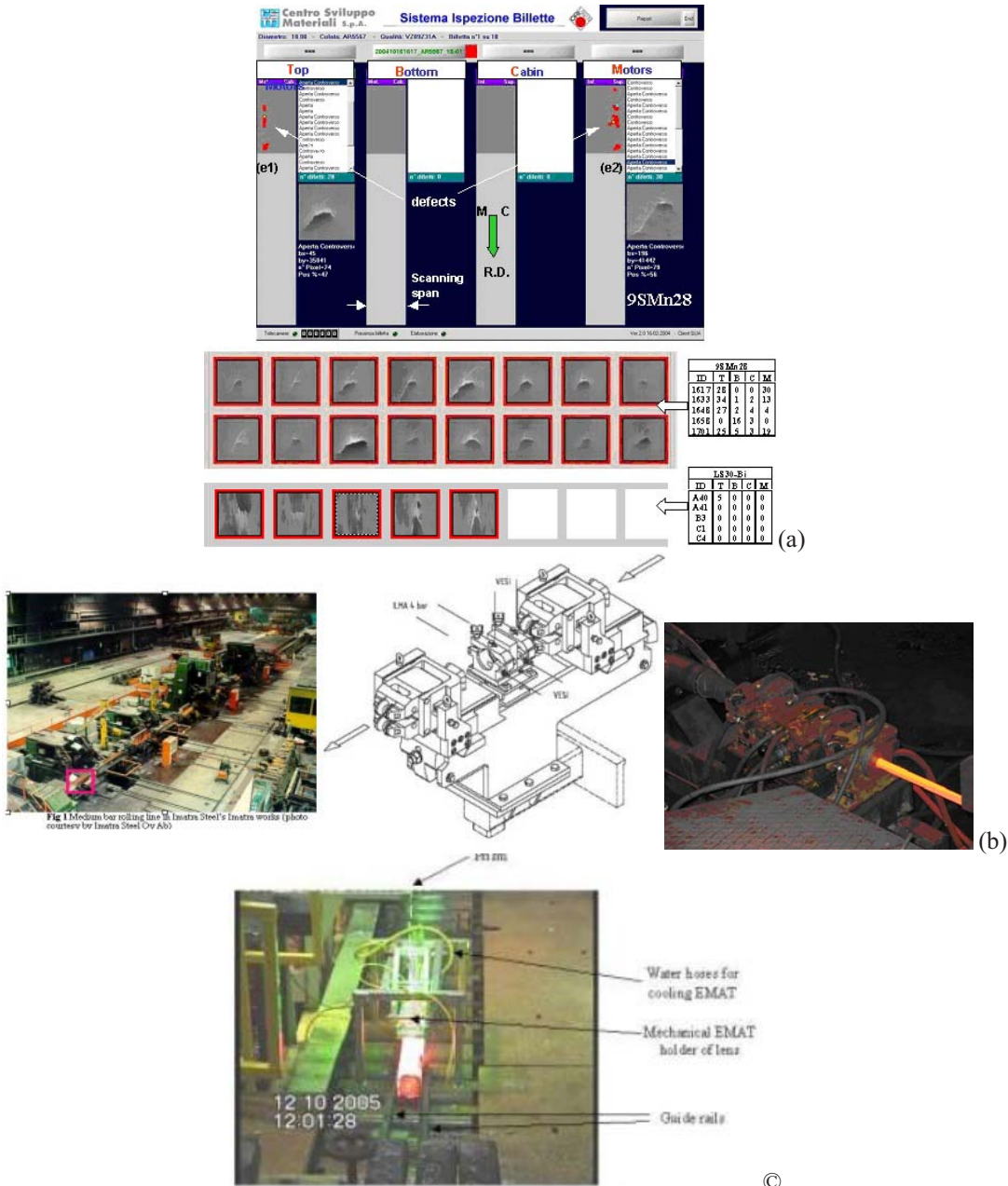
- **Exploitation and impact of the research results – Final guidance and sensitivity (WP11)**

The effect of key process and product parameters as presented in Table 3 have been studied in detail for a range of FCS steels and heat treatable steels, although for the later the understanding across the length scale was not fully assessed, partly due to their relatively good intrinsic ductility. Table 5 is therefore a summary of all key parameters versus processes and length scale and their relative effect on ductility. Parameter dependency is in relation to their effect on ductility during the rolling process, but this may not be necessarily absolute as far as the through process is concerned. An example of this is for instance the cortical zone, this is considered to be an independent parameter during rolling but a dependent parameter in casting as being linked to steel composition, solidification regime and caster conditions. On the other hand, strain during rolling is considered as a dependent variable function of reduction, pass

design, etc. Table 5 gives also an indication of the degree of confidence of the project findings as complexity and further understanding remains in linking interactions of key input factors for specific grades. For instance, rolling a Te-FCS will require different processing conditions to a Pb-FCS steel as being less sensitive to temperature (see Ascometal Fig. 39 and Section 3 results). Some of the detected defects appear to originate form either new damage at rolling surfaces or as the result of their coalescence with either existing microvoids or DRX-activated matrix debonding in the subcortical layers. The difficulty resides that without FEM modelling, it is difficult to estimate the local strain acting at surface/subsurface. **Due to H/V rolling and changes in roll gap shape factor, edges are not always submitted to large strains, as larger strains can be induced at subsurface. Also the reduction/elongation of the cortical zone** will be non-uniform, depending on amount of free spread and localised reduction. It was assessed that for 5 roughing passes with 90° turn, the cortical zone could be reduced by 50%. Comments are also added where appropriate when parameters have to be considered in combination or interaction. A brief guide to methodology of damage assessment and application on mill is also summarise below and further detailed in Section 3. Guidance with respect to suitability of mechanical testing to simulate rolling conditions and ductile damage is summarised in Table 6 and Fig. 64. These tables have to be read in conjunction with the Section above and Section 3 illustrating in more detail the effect of key input factors.

- **Exploitation and impact of the research results – Methodology for damage assessment and minimisation in rolling mills – Guidance (WP11)**

A series of steps are proposed to list the key parameters/actions to undertake for assessing damage issues with the view to minimise effect during rolling.

1. Assess temperature – time in reheating furnace.
2. If defect present, track defect location/position to key pass/input feedstock (use of FEM or other methods is recommended).
3. Check roll cooling (minimise without inducing thermal fatigue/roll wear).
4. Assess primary descaling conditions (oxide scale during rolling should be maintained ductile).
5. Assess steel grade composition (for FCS, check if Mn/S critical ratio is greater or less than 1) and check additions of Pb, Bi, Te, etc. as these will change the cohesive strength between inclusion and matrix.
6. Calculate primary reheated oxide scale thickness (see Fig. 9).
7. Assess cortical zone thickness (from previous metallurgical quantification of as-cast or as-cast reheat chilled zones function of grade, feedstock size, casting process, etc.) or via model.
8. Assess/measure surface temperature (surface) and any non-uniformity across perimeter.
9. Calculate mean strain rate.
10. Assess thickness affected by cooling versus thickness of cortical zone based on mill pacing, length of contact.
11. Check groove filling (avoid underfilling).
12. Check from available data extent of ductility trough (tensile test data).
13. Assess/predict recovery temperature at interpass time.
14. Calculate bulk strain (without FEM) based on pass schedule, simple roll design software or if available discrete strains through the stock cross section by FEM (preferred option).
15. Calculate all normalised criteria for mechanical assessment (STR, SPR, PSR, SPR/(1-STR), PEEQ). Check regions where STR>0.2, SPR> 1, PEEQ>0.2, etc.
16. Couple simple damage criteria (Lemaitre, Ghosh, Oyane, McClintock, etc.) and assess critical location.
17. Check SPR, STR inversion function of position in roll bite and product.
18. Check SRX/DRX with the use of kinetics Avrami equations.
19. Check with available nucleation curves (strain function of triaxiality (STR)) (see Fig. 38).
20. Optimise pass reduction to minimize STR/strain. This will have a significant effect for low ductility steels such as Te or Bi-FCS.
21. Improve/optimise casting/reheating conditions prior to redesign critical passes. Optimise inclusion spacing (small and largely spaced) by inclusion modification (La, CA additions, cooling, etc.).
22. Check Mn/S ratio and oxidation conditions- minimise oscillation marks (hook type).

23. Redesign pass schedule, matching ingoing feedstock to pass profile and minimise open spread. Check mill pacing.

Constraints are ingoing cast feedstock (overall dimensions, corner radius, cortical zone) and mill pacing (mostly for continuous mill). In case of reversing roughing, more options are therefore available for modifying to a certain extent pacing (strain rate, recovery, etc.). In summary, assuming a range of ingoing reheated cast structure to the rolling process (cogging, roughing), it is key to optimize temperature and strain rate as well as deformation and triaxiality. For most of low ductility steels, maintaining the surface temperature as uniform and as high as possible during the first rolling stands by avoiding both water cooling and adverse descaling conditions (britte scale) whilst using appropriate rolling speeds, should be beneficial (e.g. Pb-FCS steels). Increasing microalloying to reduce propensity for DRX, and reducing the local strain at rolling stock edges by designing and maintaining during their life adequate roll profiles should be aimed at for harder to roll grades (Te-FCS). Figure 65 is a summary of the key parameters affecting damage regime map. As triaxiality increases, strain to failure decreases (for triaxiality less than 1). Damage initiation is reduced as strain rate increases mostly at high temperature. In the presence of a thick cortical zone, surface damage is drastically reduced, but subsurface (sub-cortical boundary) may still be present. An example of regime maps for 9SMn28 as-cast steel is shown on Figure 66 following normalization of crack dimension at maximum value of temperature and cortical zone (T = 960 °C, hc = 13 mm). **Decreasing damage risk is pointed by arrows. Results show the influence of the stress state and corresponding damage predictions using the models developed by CSM (See WP7-8).**

Table 5: Effect of the tested parameters on the ductility. "+" means that an increase of the parameter improves the ductility, "–" means that an increase of the parameter decreases the ductility, "±" means that an increase of the parameter can either improve or decrease the ductility, "C" means acting as catalyst and "0" means no influence of the parameter on the ductility

Processes	Parameters	Length Scale	Dependency I : Independent D : Dependent	Effect on hot ductility	Comments	Confidence	Further work
Casting	Oscillation marks	mm	D	C,0	In combination with oxidation or changes to local microstructure (inclusion distribution – short transition between small and large inclusions) in oscillation marks	high	
Casting	Excessive cooling during casting		I	-	Affects Heat treatable steels		
Casting	High level AlN		D	-	Affects Heat treatable steels		
Casting	Pb, Bi, Te	µm	I	-	Affects FCS steels- Pb less effect than Te, Bi	High	cohesive strength/precipitation
Casting/ rolling	Roughness	sub-mm	I	C,0	In combination with oxidation, etc.	High	
Casting	Cortical zone	mm	I	+	A min thickness is required (7 mm)	High	Theoretical prediction of chilled zone would be beneficial together with through process variation
Casting	MnS Inclusion spacing	µm	I	+	Link between spacing and diameter	High	Prediction of MnS precipitation/spacing- optimisation of spacing
Casting	MnS diameter	µm	I	-	Same as above via s/d ratio		
	MnS Mean local fraction	µm	D	-	Determined by SKIZ	High	
	Spacing/ diameter ratio	µm	D	+	If s/d >2.7 (threshold), inclusions are independent	High	
	MnS Type	µm	I	+-	Type I pure and eutectic studied	Medium	Eutectic MnS MnO to be studied, re. melting temperature
	MnS Plasticity ratio with matrix	µm	D	-	Plasticity assumed from Literature and effect studied by FEM	Medium	More work required as plasticity is affected by type and eutectic composition
	MnS Cohesive strength	µm	D	+-	No data available at high temperature	Low	More research needed on effect on Pb, Te, Bi
Reheating	Austenitisation temperature		I	±		Medium	More research needed
Reheating	Austenitisation duration		I	-		High	

Processes	Parameters	Length Scale	Dependency I : Independent D : Dependent	Effect on hot ductility	Comments	Confidence	Further work
Reheating	Embrittlement	μm	D	-	Effect of tramp elements (EAF), FeS, Mn depletion zones	High	
Reheating	Oxidation	μm –mm	D	-	Effect of Fayalite, reduction of cortical zone, reoxidation (inc MnS)	High	
Rolling	Temperature		D	±	Depends on strain rate, pacing , roll cooling and oxide scale	Medium/ High	
	Temperature gradient		D	-	Affects sub-critical cortical zone	Medium	Perimeter and radial gradient to be studied in more detail
Rolling	Strain rate		D	±	Depends on temperature, but generally higher strain rate increases ductility mostly at high temperature. Minimum ductility shifts to lower temperature (or higher Z) when higher strain rates are applied	Medium/ High	
Rolling	Triaxiality STR	μm –mm	D	-	Depends on strain for nucleation/growth, above 0.33 negative effect	Medium/ High	Inversion and gradient to be studied
Rolling	Strain (equivalent PEEQ, principal PSR)	μm –mm	D	-	Above a threshold, depends on triaxiality. Matrix hardening is beneficial, low strain can promote voiding under tensile stresses as matrix cannot © local deformation. Too high strain is also detrimental, promoting DRX and damage mostly at low temperature (should be below critical strain for DRX)	Medium High	More work required at effect of strain at inclusion level
Rolling	Principal Stress (max, mid, average) SPR	μm – mm	D	-	Above a ratio, further affected by max and mid principal stresses being tensile. Dependent on principal/triaxiality ratio	High	
Rolling	Pass design box		I	+	Box pass recommended	High	
Rolling	Strain path		D	0-	Depends on inclusion size		
Rolling	Recrystallisation SRX	μm	D	+-	Depends on temperature and pre-existing damage zones. At high temperature, negative effect	Medium	More double hit deformation required
Rolling	Recrystallisation DRX	μm	D	-	Depends on temperature and pre-existing damage zones, reduces grain size and crack arrest, creates through thickness non-uniformity	Medium/ High	
Rolling	Grain size	μm	+		Grains size small in as-cast structure, promotes DRX.	Medium	Link between grain size and grain boundary cracking
Rolling	Grain Boundaries (GB)	μm	I		Grain boundary sliding may be reduced due to pinning effect of inclusions, thus enhancing GB cavitation	Low/ Medium	
Rolling	MnS crystallographic	μm	I	+-	Interfacial stress is determined by crystallographic	Low	More work using polycrystal

Processes	Parameters	Length Scale	Dependency I : Independent D : Dependent	Effect on hot ductility	Comments	Confidence	Further work
	Orientation		D		orientation of MnS. The austenite matrix grain orientation affects slip		plasticity and EBSD
Rolling	Oxide scale	µm-submm	D	+-	May further promote crack opening if brittle, although insulation effect is beneficial	Low/ Medium	
Rolling	Mill pacing	mm	I	+	Function of bar size in continuous mill- should be beneficial up to a given threshold	Medium/ High	
Rolling	Roll cooling	mm	I	-	Promotes surface chilling and heterogeneity surface/subsurface (see fig	High	
Rolling	Pass radius matching	mm	I	+	Increase matching of feedstock to groove pass radius minimises adverse tensile stresses and triaxiality inversion in bite	High (although not studied)	
Rolling	Descaling	mm	I	+-	Depends on nature of scale and brittle transition. May further increase propensity for opening/surface steel extrusion between scale fragments	Medium (not studied)	
Rolling	Spread		D	-	Open spread is to be minimised	high	

Table 6: Summary of applicability of mechanical testing to high temperature ductile damage and rolling

Type of tests	Tensile triaxiality	Principal stress ratio	Principal strain ratios	Comments
Tensile, U-bend	High (STR > 0.5) (min 1/3)	High SPR>2	High (>2)	Test dominated by medium to high triaxiality. Standard test for damage, Damage initiated from centre
Hexagon, octagon	Low (<0.2)	Low-Medium	Low-Medium	High shear, low volume fraction under tensile triaxiality, inversion of triaxiality during test
flying saucer, plane strain with/without curvature, double collar, revised plane strain	Medium (0.2<STR<0.5)	Medium (1< SPR>2)	Medium (<2)	Close to rolling with (flying saucer, inner ring double collar, PSC) or without inversion. Inversion of triaxiality on front face of plane strain. Traixiality can be changed function of curvature. Damage initiated from surface. Ideal test for nucleation/growth
Upsetting	Low (within 0.5 mm from surface)	Low-Medium Tensile up to 3 mm from surface	Low-Medium	High shear and inversion of triaxiality ratio during deformation
Torsion	null	Null if no axial stress imposed	Shear strain	High shear
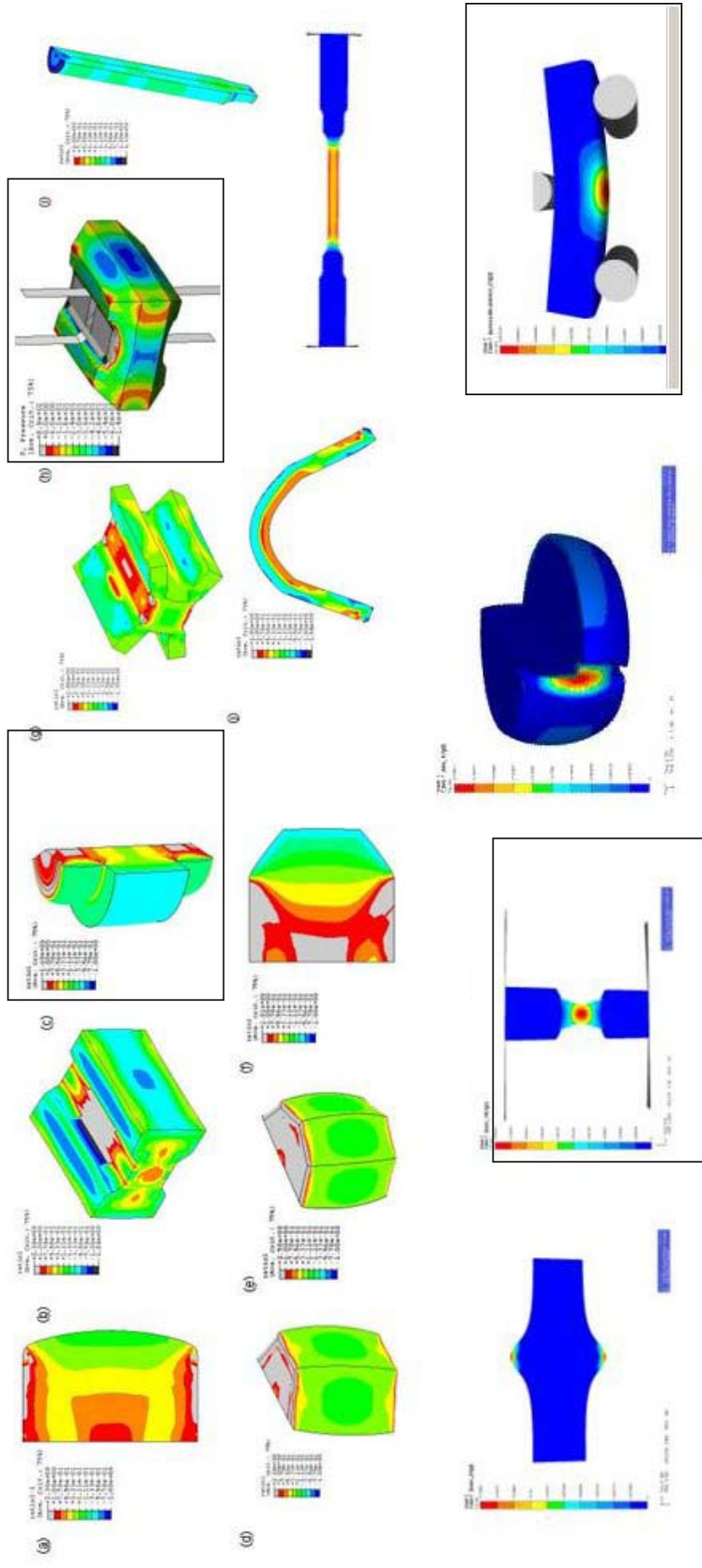
Fig. 64(a–o): Assessment of a range of mechanical tests (standard + new) for ductile damage carried out by Partners: triaxiality plots (Corus) (green to blue negative triaxiality, i.e. tensile at 33% reduction in height) – (k to o) damage plots (Ascometal)

(a) Upsetting (with friction) (Mefos) (b) Plane strain without curvature (Ascometal) (c) double collar (Corus) (d) hexagon compression (Corus) (e) octagon compression (Corus) (f) flying saucer (Corus) (g) double-T plane strain (Corus) (h) revised plane strain (Corus) (i) tensile (Corus, Ascometal, CSM) (j) U-bend (Corus) (k) torsion/tension (CEIT) (l) SICO Gleeble test (m) tensile (n) crack limit index test (o) 3-point bending (Sidenor)

51
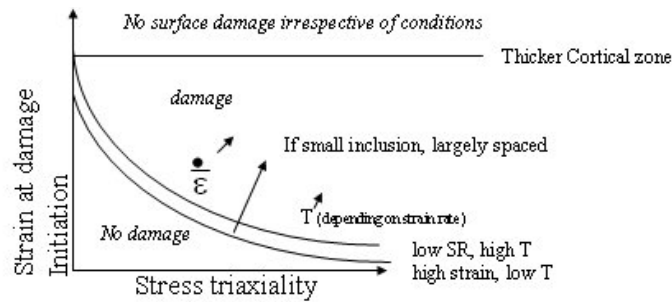
Fig. 65: Regime map for damage initiation
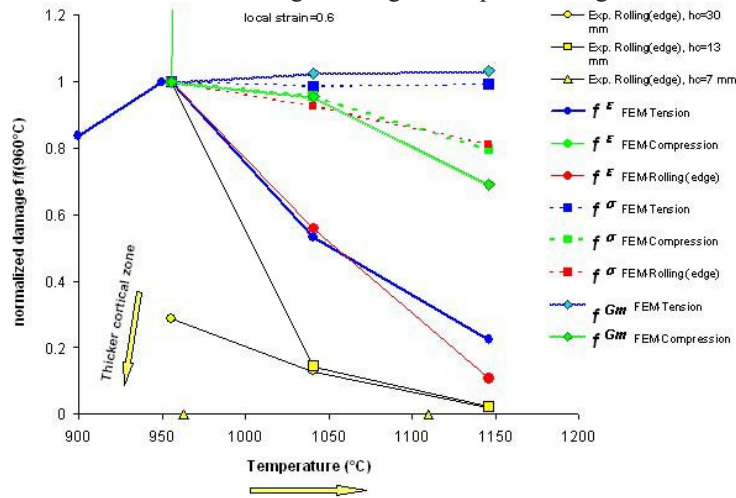
$$f = \frac{total\ defect\ area}{total\ area}$$

Fig. 66: Regime map for as-cast steel 9SMn28 (benchmark) (CSM)

- **Exploitation and impact of the research results – Main Conclusions**

➢ A summary of the main parameters and their sensitivities is proposed in Table 5 with through process parameters dealing affecting the surface/subsurface state and the length scale.

➢ Guidance as to minimize onset of damage at high temperature is illustrate above with step by step check points. This involve a combination of process data, analysis tools (FEM) and mechanical testing.

➢ Thicker cortical uniform zone, coupled with reduced tensile triaxiality (less than 0.33) and principal stresses (one or two direction), increasing pacing in relation to temperature and a range of strain are the major parameters to influence the rolling operation and the subsequent hardening/softening.

➢ The project has been extremely innovative and challenging in ranking all mechanical tests and their suitability to rolling. Compression test with curvature or inclination coupled with tensile testing is the best combination of testing for developing a thorough understanding of the mechanisms of damage.

➢ A refined ductile theory taken into account spatial distribution of inclusions is proposed, this is coupled with a multi-scale approach for modeling.

➢ Large and closely spaced inclusions initiate damage earlier, however may not necessarily explain the process of surface corner cracking, only to the point where some of these inclusions can act as primary catalyst to nucleation, mostly when close to surface. Overall the inclusion size is small at surface due to solidification/crystallization; volume fraction can be high with a ratio, spacing to diameter small. This creates adverse effect to rapid growth and coalescence, compounded by the fact that reduced thickness of chilled zone and adverse thermo-mechanical parameters are acting on the structure. This affects generally 10mm from surface of stock where triaxiality, principal stress ratios, heat zone affected by roll gap conduction and asymmetry brought about by DRX can play a key role.

52

- Surface oxidation, and MN depletion (low Mn/S ratio) can further promote formation of FeS which linked with high density of small inclusions and/or oscillation marks can create a catalyst for damage initiation and propagation.
- The length scale aspect is critical to the understanding of the increase of strain concentration and partitioning brought about by inclusions which are less deformable by matrix. Increasing asymmetry between plasticity index between inclusions and matrix increase stress/strain concentration which will be acting at the particle interface.
- The cohesive strength at particle interface is key to easy nucleation but may not translate automatically to growth as the mean local area fraction (SKIZ) or spacing to diameter ratio dominates the mode of fracture.
- The project has gone a long way to increasing high temperature ductile damage but also has highlighted areas for further work and main challenges (See below).

- **Further Work, Recommendations and Challenges**

In view of the multiscale nature of the mechanisms inducing ductile damage during high temperature, the following recommendations for future work are highlighted below:

- Promote use and implementation of Damage Mechanics (DM) within Production/Roll design.
- Further develop on-line NDT with thermo-mechanical processing data storage so as to have a complete process and product history of a particular cast.
- Further develop and apply characterisation techniques such as FIB to build a more spatial (3D) representation of damage
- to build a more spatial (3D) representation of damage
- Develop techniques for quantifying austenite grain boundaries and damage without need for quenching through transformation or reaustenitisation.
- Develop and apply NDT during mechanical testing for allowing easy test filtering (damage/no damage) and easier and faster post metallurgical characterisation. Experimental characterisation of damage and its evolution are certainly both a weakness and an interesting field of work. Characterisation of damage and calibration of models is a challenge.
- Assess evolution (through process) of cortical zone and relate to defect initiation.
- Assess in more details extent of non-uniformity of process/product conditions.
- Develop a complete library of nucleation curves function of strain rate and temperature and microstructure for critical grades using a range of mechanical test geometries [44]. A full detailed understanding of nucleation is required as current science is lacking.
- Develop incremental understanding of in-situ damage using for instance X-ray tomography in terms of kinetics of crack growth and coalescence v recovery processes [45] (Fig. 67).
- Apply and further develop nano-indentation methods and obtain relevant data of nano/micro hardness of inclusion/interface properties and cohesive strength.
- Develop a simple damage criterion plug-in for linking state variables with damage integrated outputs. Assess further sensitivity and integrity of these simple models. Augment accuracy via incorporation of microstructural features such as MnS spacing (see Section 3). Calibrate models.
- Further develop length scale models taking into account microstructure/second phase inclusion clusters (e.g. CAFÉ modelling), cohesive zone modelling, and polycrystal plasticity (Fig. 67, see also Section 3). Submodelling should be further developed and use for detailed constitutive models (Fig. 69). Self-Consistent Strain local models for distributed phases can easily be interfaced in the current FEM rolling simulation at selected locations enhancing the predictive capabilities of the resulting multiscale modelling. Models of casting should be linked to reheating/rolling models for transferring or mapping key microstructural features as state variables.
- Develop alternative non-continuum theories (inc. thermodynamic state) and modelling approach. Meshless methods (NEL, SPH) can be a good candidate for studying crack growth and coalescence.
- Assess applicability of Molecular Dynamics simulation for dislocation hardening/impingement around inclusions, i.e. the dynamic response of material [46].
- Develop detailed understanding of void/crack healing.
- Improve on knowledge of sensitivity of key input factors and extent of asymmetry/plastic instabilities and develop further knowledge of interactions.
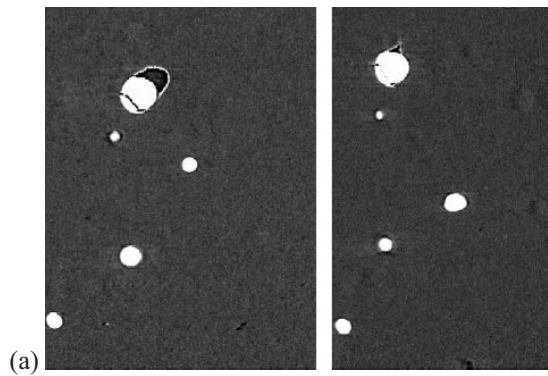
Fig. 67: X-Ray tomography from [44]
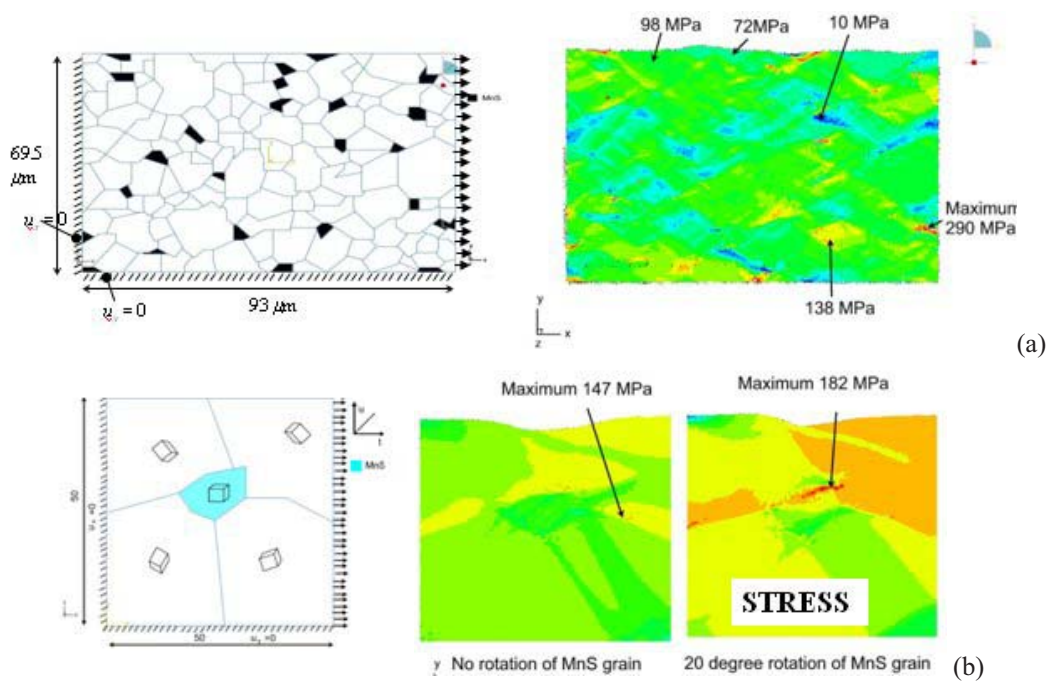
Fig. 68(a and b): (a) Polycrystal 2D FEM model (Corus-Oxford University) meso (austenite grain size and MnS inclusions) – Micro (MnS surrounded by 4 austenite grain size)
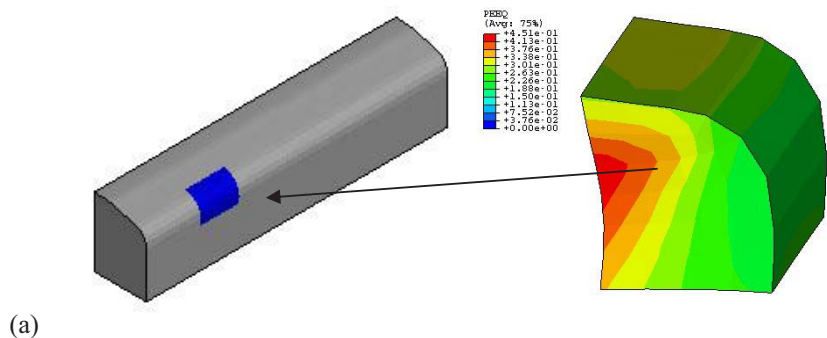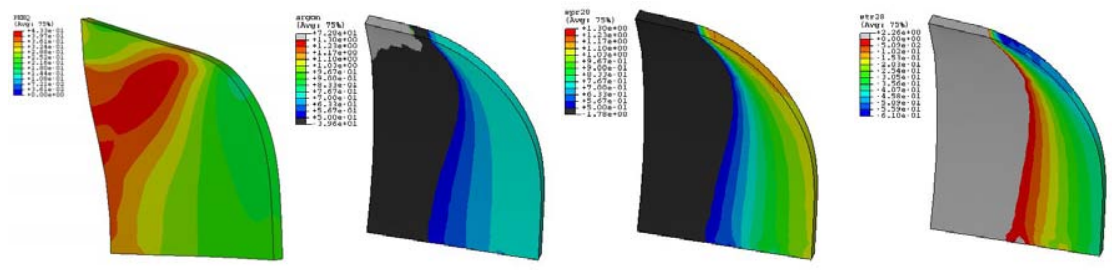
Fig. 69(a-e): (a) Global FEM model with view of global partition (equivalent strain) (b) Remeshed and analysed FEM submodel of partition (equivalent strain) (c) SPR/(1-STR) (d) SPR submodel (e) STR submodel

3. Scientific and technical description of the results

3.1 Objectives of the project

The drive towards higher contribution steels with improved machinability (in the case of free cutting steels) and higher surface quality and consistency, together with the potential future implementation of the European legislation (ELVD) to promote lead substitutes in machinable steels (Bi, Te, high S) is leading to a requirement for improved understanding and control of as-rolled surface quality, most critically for steels which have low ductility and a narrow temperature range for defect free rolling. This is also true when processing heat treatable, bearing, forging but also stainless steels (austenitic, ferritic, duplex).

One of the main objectives of this proposal is to gain a scientific understanding at micro, meso and macro-scale of the damage mechanisms inducing ductility break-up/defects at both surface and central regions of the deforming stock during hot rolling, for a range of known low-ductility steels. The project is focused on BOS and EAF route free cutting steels with various lead substitutes (Bi, Te, etc.), and Mn/S ratios (varying between 2.6 to 7.0), but also heat treatable, bearing and forging steels, under a variety of processing conditions. The approach adopted is based on a combination of mechanical testing, microstructural characterisation methods, pilot and production rolling mill trials, and finally material constitutive and modelling techniques.

3.2 Comparison of initially planned activities and work accomplished

All the Tasks within each of the Work-Packages illustrated in Table 1 have been completed in line with the Project Gantt Chart (Fig. 70) and the 4-month granted extension at beginning of project. Five Consortium meetings were held at each of the partner sites. Although the project started late due to awaiting RFCS approval, the objectives were completed according to the Technical Annex of the contract which can be found in Appendix 1 and extended summary.

This project did not exceed the overall budget and the project costs from each of the partners were approved after the submission of the mid-term report. Final, audited cost claims are being submitted.

The technical collaboration between partners has been excellent and covered:

- Steel quality and supply (WP1): CEIT has been testing Corus, Sidenor and CSM steels in both as-cast and wrought conditions.
- CSM supplied Corus and Ascometal as-cast billet high sulphur FCS steel for testing using the various standard and new mechanical tests developed.
- Mefos has worked closely with Ovako Imatra for testing at laboratory scale Rock drilled as-cast steel.
- Mechanical testing (WP3). Testing methods have been assessed within the Consortium and guidance produced (see Table 6, Fig. 64 and WP3). The revised plane strain test developed by Corus has also being tested at a larger scale by Mefos.
- Guidance/review of methods for microstructural characterisation, identification of key damage and microstructural parameters, and development of regime maps has being jointly developed.
- Collaboration on modelling benchmark between Mefos, Corus and Ascometal was set-up to assess applicability of models (See Fig. 62).

Fig. 70: Gantt chart and Main Achievements

Tasks	Title	Partners	Leader	Task achieved
WP1	Selection of Materials	all	Corus	✔
WP2	Selection of thermo-mechanical and rolling conditions		Sidenor	✔
2.1	selection fo thermo-mechanical conditions with respect to mechanical testing and industrial plant	all		✔
2.2	Reference of rolling trials to laboratory simulation	all exc. CEIT		✔
WP3	Mechanical testing	all	Corus	✔
3.1	Torsion	CEIT, Ascometal		✔
3.2	Gleeble/ PSC	Corus, Sidenor, CSM		✔
3.3	Other tests (e.g. bending)	Sidenor, Imatra		✔
3.4	Strain path	CEIT		✔
3.5	FEM Modelling of mechanical tests	CEIT, Ascometal, Corus, CSM, Sidenor		✔
WP4	Laboratory rolling	Corus, Mefos	Mefos	✔
WP5	Microstructural characterisation	all, exc. Mefos	CEIT	✔
WP6	Determination of Key parameter sensitivities and establishment of regime maps	all	Corus	✔
WP7	Development of damage equations & Constitutive models	all exc. Imatra	CSM	✔
WP8	Incorporation of constitutive models in multipass rolling FEM models	CSM, Corus, Mefos, Ascometal, Sidenor	Ascometal	✔
WP9	Further development of detection device for hot metal application	Corus, Imatra	Corus	✔
WP10	improved reheating and rolling practices to industry	all, exc. CEIT	Mefos	✔
WP11	guidance for hot rolling without generation of significant defects	all	Corus	✔
Reports				

3.3 Description of activities and discussion

3.3.1 WP1: Selection of materials

The project has focused on FCS and HT steels in as-cast and wrought state from both BOS bloom and EAF billet routes as described in Table 2. The as-cast 9MnS28 CSM steel was used as a mechanical testing/damage benchmark across CSM, Corus, Ascometal and CEIT.

- **Free-cutting steels (FCS)**

Corus UK covered 5 as-cast and wrought FCS steels of interest. Two x 1 tonne bloom sections (W x H X L: 750 x 355x 500 mm) were obtained from each strand of the bloom 750 caster, together with 7 x 1m length rolled 140 mm square billets for each of the quality. All as-cast blooms were pre-machined to bars (two ingoing square bar sizes, 52 x 52 and 68 x 68 mm) according to semester report [47]. In addition the benchmark 9SMn28 CSM steel was studied using RPS testing.

Sidenor I+D have been focusing on a range of FCS, LFCS and Bi-steel. FCS and LFCS have however been the main grades of interest. The Mn/S ratios vary between 3.91 and 4.70. Analysing heats 26264 9SMnPb28 and 26540 9SMnPb30, the sulphur content is similar, 0.260% and 0.302%, however the manganese content sets the difference, 1.100% and 1.420%. This means Mn/S of 4.23 and 4.70. This situation has given the opportunity to study the influence of Mn and Mn/S ratio.

CSM has focused on a low C FCS with high S content (0.42) and a low Mn/S ratio of 2.6 for grade 9SMn28.

CEIT has studied a range of FCS, LFCS and Telby+ steels from Corus, together with LFCS from Sidenor I+D as well as the 9SMn28 FCS CSM steel.

Ascometal has added two FCS to their existing portfolio of bearing steel in order to further develop and tune their existing damage modelling criteria. Composition included a FCS and a Bi-FCS steel. They also studied the 9SMn28 benchmark CSM steel.

58

Table 7 details the various composition of all FCS steel considered, together with Mn/S and Mn/S critical index ratios as defined by [10]:

$$MSCindex = \frac{(Mn/S)}{(Mn/S)c}$$

$$(Mn/S)c = 1.345 \cdot S^{-0.79}$$

. . . (3. 1)

The MSC index (Manganese-Sulphur-critical), defined in Equation (3.1) denotes the susceptibility to hot shortness and cracking during solidification/deformation for non Ca- treated as-cast FCS steels through the formation of low melting interdendritic liquid FeS, if the ratio of (Mn/S)/(Mn/S)c is less than 1. This critical value depends on S content, provided there is no diffusion of Mn and S in the solid during solidification.

In view of the Al content used for de-oxidation (semi-killed steels), type I globular MnS monotectic and eutectic are expected as per classification of Sims and Dahle [14].

Table 7: FCS steel Partner matrix

Group	Type	Code	Cast Code	Mn/S	MnS Index	C	Si	Mn	P	S	Cr	Mo	Ni	Al	N	As	B	Co	Cu	Nb	Pb	Sn	Ti	V	Bi	Ca	Sb	Te
Corus	FCS	773F	15532	3.16	0.93	0.07	0.003	0.98	0.059	0.31	0.014	0.002	0.022	0.001	0.0073	0.003	0.0001	0.006	0.028	0.001	0.0001	0.002	0.0008	0.003	0.002	0.0001	0.001	0.001
Corus	LFCS	539H	14984	3.76	1.05	0.072	0.002	1.09	0.057	0.29	0.017	0.002	0.02	0.001	0.0108	0.003	0.0001	0.004	0.013	0.001	0.31	0.003	0.0005	0.003	0.001	0.0003	0.001	0.002
Corus	Telby+	360M	16653	3.61	1.19	0.06	0.002	1.3	0.066	0.36	0.023			0.001	0.0086	0.004	0.0001	0.005	0.025	0.001	0.25	0.003	0.0004	0.003	0.068	0.0002	0.002	0.015
Corus	Bi-FCS	602M	18485	3.68	1.00	0.07	0.004	1.03	0.063	0.28	0.024	0.002	0.028	0.001	0.0094	0.004	0.0001	0.005	0.064	0.001	0.007	0.003	0.0003	0.002	0.077	0.0002	0.001	
Corus	Te-FCS	9252M	29367	5.52	1.45	0.36	0.18	1.49	0.015	0.27	0.025	0.003	0.02	0.002	0.0079		0.0001		0.012		0.001	0.004	0.0006	0.002	0.001				0.007
Sidenor	FCS	9SMn30		4.41	1.23	0.079	0.02	1.28		0.29									0.001			0.002		0				
Sidenor	LFCS	9SMnPb28		4.23	1.08	0.08	0.02	1.1		0.26										0.24	0.003		0				
Sidenor	LFCS	9SMnPb30		4.70	1.35	0.08	0.002	1.42		0.302										0.23	0.004		0				
Sidenor	Bi-FCS	9SMnBi30		4.57	1.24	0.073	0.004	1.28		0.28								0.001						0.03			
CSM	FCS	LS30Bi		7.00	1.57	0.3	0.11	1.54	0.14	0.22			0.0009						0.0004				0.002	0.004	0.09			
CSM	FCS	CSM4108		5.73	1.46	0.28	0.15	1.49	0.14	0.26			0.0009						0.0004				0.002	0.004	0.06			
CSM	FCS	CSMBi1000		7.00	1.57	0.3	0.11	1.54		0.22			0.0009						0.0004				0.002	0.004	0.05			
CSM	FCS	CSMBi1500		7.00	1.57	0.3	0.11	1.54		0.22			0.0009						0.0004				0.002	0.004	0.15			
CBIT	FCS	9MnS28 Z09Z2		2.62	0.98	0.09	0.02	1.1	0.08	0.42	0.18	0.09	0.22					0.2	<0.005			<0.005	0.11					
CBIT	FCS	S2		3.34	0.93	0.07		0.97		0.29																		
Ascometal (NEW)	LFCS	32MnS5Pb		4.88	1.27	0.335	0.186	1.297	0.014	0.266	0.163	0.058	0.127						0.152			0.022	0.01			0.01		0.008
Ascometal (NEW)	Bi-FCS	32MnS5Bi		4.72	1.25	0.35	0.196	1.279	0.01	0.271	0.11	0.041	0.088						0.145			0.003			0.046	0.01		0.011

Figure 71 shows in more details the Mn/S and Mn/Sc ratios ranging from 2.6 to 7.0. Figure 72 shows the absolute variation in key elements (e.g. Pb, S) content.
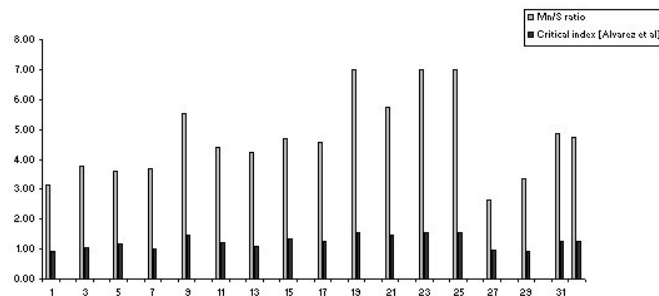
Fig. 71: Mn/S and Mn/S critical index ratios
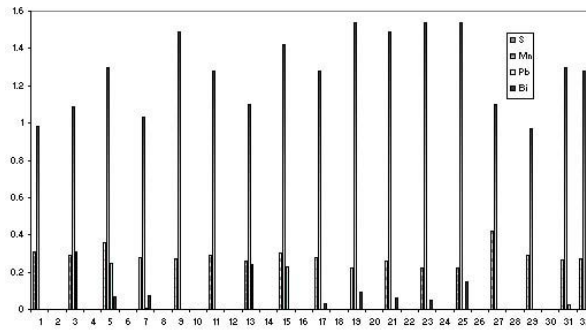
Fig. 72: Absolute variation in key element content within Partner FCS mix

- **Bearing – heat treatable steels**

Mefos: Mefos has focused its investigations on ball-bearing steels, rock-drill steel grade and dual phase with different S content.

Ascometal: Ascometal has initially focused on bearing steel billets 100Cr6, rolled from bloom prior to studying FCS steels.

Ovako-Imatra: Imatra has been focusing on heat treatable low alloy steels, type 18CrNiMo7.

A summary of all current grades is shown in Table 8.

Table 8: Bearing and heat treatable steel Partner matrix

		Type	Code	Cast Code	C	Si	Mn	P	S	Cr	Mo	Ni	Al	N	As	B	Co	Cu	Nb	Pb	Sn	Ti	V	Bi	Ca	Sb	Te
Alloy/heat Treatable steels	Mefos	ball bearing	SKF803		1	0.25	0.35			2.5																	
		microalloyed	S355J2G3		0.13	0.43	1.27																0.07				
		Rock drill steel	Imatra steel		0.244	0.26	0.63	0.08	0.023	1.27		2.91						0.156									
		dual phase with S			0.017	0.3	0.9	0.008	0.023	25		6.9						0.156										
	Imatra	case hardening	18CrNiMo7		0.2	0.25	0.7			1.3	3.83	3															
		Precipitatiton hardening	imaform		0.06	0.25	0.9	0.025	0.08	1.3						0.003											
		Q&T	C40 (V-1649)	5073	0.46	0.3	0.75	0.04	0.035	0.25	0.06	0.25											0.11				
		Q&T	42CrMo4 (PMS.A.5.56)	6121	0.43	0.25	0.8	0.04	0.04	1.1	0.17	0.4															
		Precipitatiton hardening/ Hot forging	38MnSiVS6 (C38+N)	7228	0.38	0.57	1.35	0.025	0.027	0.2		0.3											0.11				
		Rock drill steel	16CrNiMo7 (4HS64)	4737	0.225	0.25	0.7	0.02	0.015	1.3	0.24	2.9															
	Ascometal	bearing	100Cr6		0.934	0.227	0.341			1.38		0.122															
	CSM	spring	55Cr3		0.55	0.31	0.78	0.007	0.002	0.76	0.02	0.07						0.1	<0.005					<0.005	<0.005		

3.3.2 WP2: Selection of thermo-mechanical and rolling conditions

3.3.2.1 Envelope of processing conditions

The envelope of processing conditions (strain, strain rate, triaxiality, etc.) integrated four production plants ranging from Bloom and Billet Mill (BBM) roughing stand (Corus C&I Scunthorpe), billet and rod mill (Sidenor Vitoria 3 high reversing rougher), Ori-Martin billet mill and finally Ascometal-Fos bloom, billet and wire rod mill. Figure 73 shows the various layouts and on-line production defect detection systems. These conditions were then used to define the design space for mechanical testing.
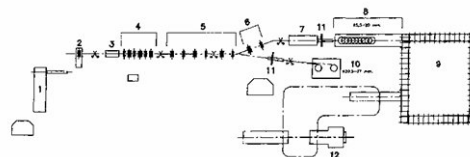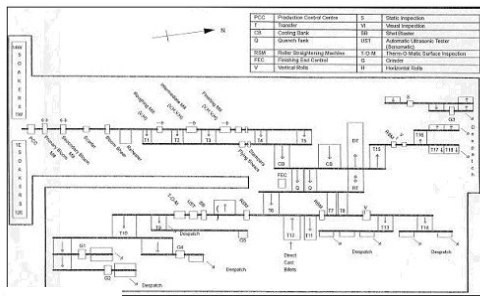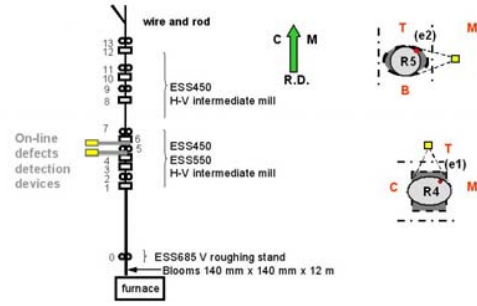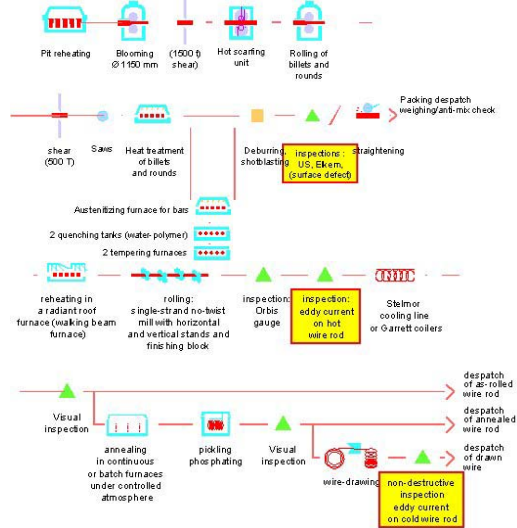
Fig. 73(a-d): Main plant layouts (a) BBM Corus Scunthorpe (b) Vitoria mill Sidenor (c) Ori-Martin Billet mill (d) Ascometal-Fos bloom, billet and wire rod mill

The Corus Bloom and Billet mill at Scunthorpe is a semi-continuous mill, rolling to close tolerances BOS initial ingots (750 x 355) to semis ranging from square billets (up to 160 mm sq) to rectangular blooms (up to 275 mm sq) and narrow slabs (up to 470 mm wide). The primary mill was the main focus of this project in order to study the transition from as-cast to wrought structure, particularly at bloom corner. Full assessment of schedules (413, 468) with respect to L/hm, triaxiality, strain, principal stresses was carried out and presented in mid term report [47]. Figure 74 illustrates key features of the schedules studied which were used as input to mechanical testing conditions. It is interesting to notice the state of inversion of triaxiality as discussed in Section 2 (Fig. 74 (e)). Triaxiality inverses during the pass when corner is brought into contact with roll at some normalised distance of the projected length of contact, creating a pattern of tensile, compressive then tensile triaxiality at exit bite. If no contact is developed, the triaxiality will remain tensile. The gradient during this inversion is important together with the absolute difference of the inversion. In the case shown the triaxiality evolves from -0.5 to 1.6. The time-integral of triaxiality will also play a key role and is dependent on pacing/strain rate. More details can also be found in [48].
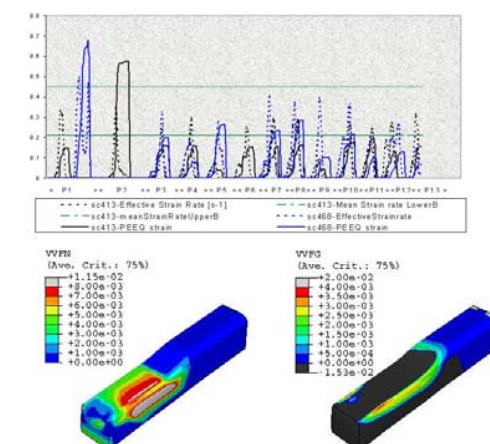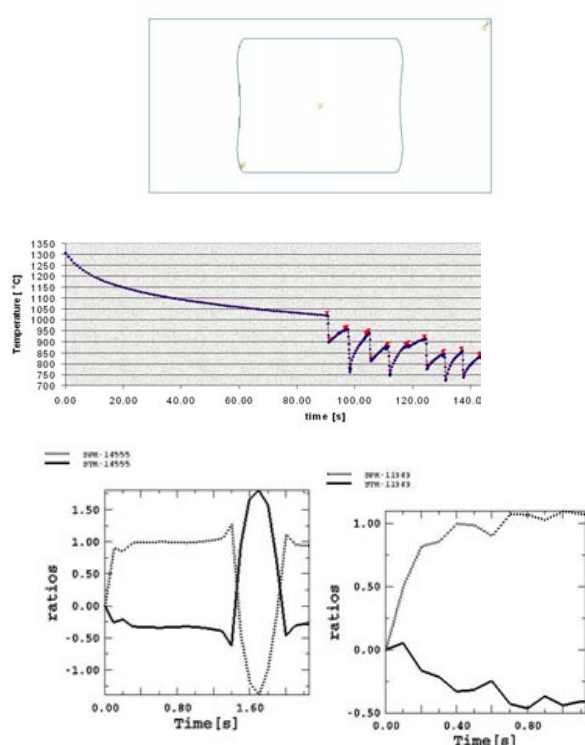
Fig. 74(a-e): Main BBM thermo-mechanical conditions sc413 and sc468 (Corus) (a) Defect tracking from input BOS 750 ingot (b) strain rate and equivalent strain @corner © Temperature evolution corner (FEM) @ low rpm (d) predicted nucleation and growth of cavity/porosity for pass12 (initial density 0.98) (e) triaxiality, principal stress ratio SPR evolution during two BBM passes

The SIDENOR wire rod rolling mill at Vitoria produces wire rod and bar in coil from 5.5 to 37 mm, mainly aimed to the automotive industry. The mill layout (Fig. 73(b)) consists of a walking beam furnace (75 t/h), a three-high roughing mill, an intermediate mill (14 H/V stands), a finishing block (10 H/V stands) and two finishing areas: 2 Garret coilers with three cooling stations (rod diameter >18 mm) and an EDC system (rod diameter 5.5 - 18 mm). Several controlled cooling processes are possible to achieve In the EDC, depending on the steel grade to be rolled and on the requested properties for the customer. Main focus of this project has been on the roughing block. Calculations of strain, strain rate (prior to FEM analysis) were made with the software WICON. The calculated values are shown in Table 9. Mean strain rate are between 5.89 s^{-1} and 12.7 s^{-1}. Three different thermal profiles through the roughing process have been simulated for different initial temperatures (1200ºC, 1225ºC and 1250ºC).

The Ori-Martin billet mill has been the focus of investigation by CSM for rolling a range of FCS from 140 mm square billets. As-cast and wrought billets were rolled and monitored via the use of the on-line detector system [43]. Typical reductions are ~27% with temperature of 1065 °C. Both LS30Bi and 9MNS28 as-cast were monitored and used for mechanical testing and laboratory flat rolling with different reductions and reheating/soaking times.

Table 9: Sidenor Vitoria Roughing block processing conditions

Pass no.	Groove shape	Reduction (%)	Strain	Strain rate (s^{-1})	Temp 1 (ºC)	Temp 2 (ºC)	Temp 3 (ºC)
1	Diamond	17%	0.19	7.29	1200	1225	1250
2	Diamond	14%	0.16	6.53	1189	1213	1237
3	Diamond	22%	0.25	9.27	1177	1200	1223
4	Diamond	10%	0.10	5.89	1163	1185	1207
5	Square	20%	0.23	9.45	1147	1168	1189
6	Box-Oval	26%	0.31	12.70	1127	1147	1167
7	Round	19%	0.21	9.86	1105	1124	1142
	Average	18%	0.21	8.87	1158	1180	1202
	Maximum	26%	0.31	12.70	1200	1225	1250
	Minimum	10	0.10	5.89	1105	1124	1142

Table 10: CSM Ori-Martin billet mill processing conditions for LS30Bi grade

ID	General conditions	Furnace Temp. (°C)	RH time (h:min)	Stand N°	Surface Temperature (°C)	Area red (%)	Exit rolling speed (m/s)	Roll diameter (m)	On line defect detection system	Intermediate stock cuts for inspection
A40	• No pressurised water descaling. • Water cooling in R0 still on • Reheating time extended artificially • Rolling till final rod diameter 16 mm	1171	4 : 12		1167				10 detections 5 open cracks near bar head, upper face, at R4 exit	Exit R7 Exit R13 Final bar 16 mm diameter
				R0	1157	20	0.9	0.609		
				R1		23.1	0.185	0.510		
				R2		17.2	0.223	0.560		
				R3	1091	22.4	0.288	0.440		
				R4		21.9	0.369	0.417		
				R5		27.1	0.507	0.448		
				R6		23.5	0.664	0.438		
				R7		27.3	0.912	0.404		
A41	• No pressurised water descaling. • Water cooling in R0 still on • Reheating time extended artificially • Whole rolled bar cut after R7	1171	4 : 17		1163 , left to cool down in the run out table for 1' 26"				4 detections 0 defects	Exit R7
				R0	1065	20	0.9	0.609		
				R1		23.1	0.185	0.510		
				R2		17.2	0.223	0.560		
				R3	1021	22.4	0.288	0.440		
				R4		21.9	0.369	0.417		
				R5		27.1	0.507	0.448		
				R6		23.5	0.664	0.438		
B3	• No pressurised water descaling. • Water cooling in R0 still on • Standard reheating time • Rolling till final bar diameter 8 mm	1177	2 : 30		1169				1 detections 0 defects	Exit R7 Exit R13 Final rod 8 mm diameter
				R0	1153	20	0.9	0.609		
				R1	1158	23.1	0.281	509		
				R2	1135	17.2	0.34	560		
				R3	1093	22.5	0.439	440		
				R4	1108	22.1	0.563	417		
				R5	1119	27.1	0.773	448		
				R6	1052	23.5	1.011	438		
				R7	1093	27.2	1.389	404		

Finally the Ascometal Fos plant Bloom, billet and wire rod mill was studied in detail with the use of FEM to map strain, strain rate and triaxiality. This is in addition to the statistical analysis of defects from bloom and wire rod which is detailed in the next section. The FEM modelling based on LAM3® software was isothermal and assumed full recrystallisation. Steady state predictions of strain, strain rate and triaxiality were made along the streamline where damage was predicted to be maximum. These are detailed below in Fig. 75 for the first 6 passes of the bloom/billet mill. In total 18 passes (Bloom) and 8 passes (wire rod) were studied. Transition from as-cast to wrought will occur during bloom rolling.
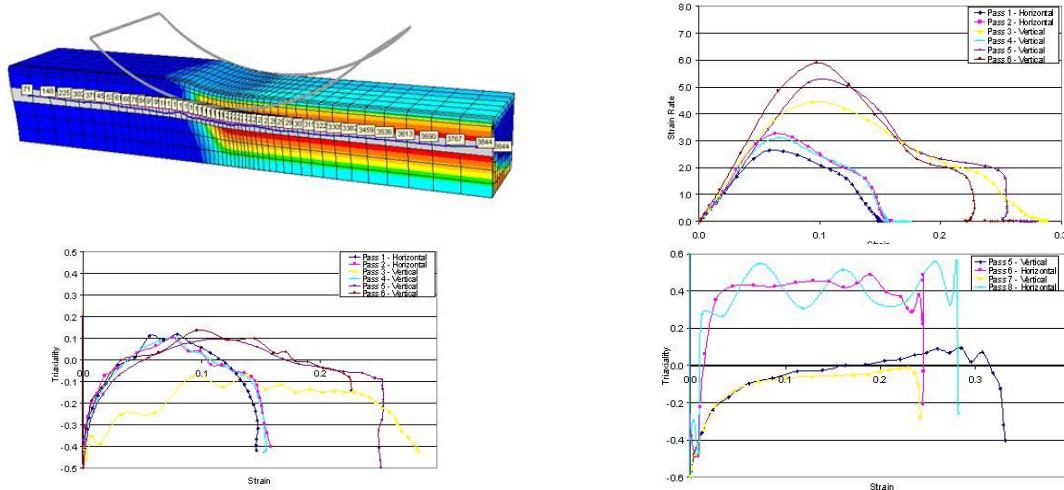
Fig. 75(a-d): Lemaitre damage plotted on streamline (b) strain rate Bloom passes 1-4 (c) triaxiality Bloom passes 1-4 (d) triaxiality wire rod passes 5-8

It can be observed that the strain rate, in the area, where predicted damage should be maximum, is between 2 and 8 s⁻¹. Within each pass, the accumulated strain is between 0.15 and 0.3. The sign of the hydrostatic pressure changes from a positive value to a negative value at the location where the damage criterion is maximum during a rolling pass, sometimes the state remains compressive. The higher values

of triaxiality (0.4/0.6) are reached at passes 4, 6 and 8 of the wire rolling mill and are typically 0.1 during bloom and billet rolling.

In summary conditions to be tested during mechanical testing are as follows:

- Temperature [800-1250°C]
- Strain rate [0.1 -10s^{-1}]
- Strain [0-0.6]
- Tensile triaxiality < 1

3.3.2.2 Defect production analysis

Most partners have focused their effort in identifying type of defects through the various stages of rolling via either access to on-line detection systems (e.g. CSM Ori-Martin, Ascometal Fos), statistical analysis via plant database systems (Ascometal, Ovako Imatra) or visual inspection.

Figure 76 shows defective material after first pass for a 9SMnPb36 bar rolled at the Vitoria Plant (Sidenor). This shows cracks in open region and subsurface, predominantly in regions of open spread. The distribution of MnS and Pb as shown in the micrograph does not show major differences between faces, corners, subsurface, half radius or centre. Cracks tend to initiate at areas of free spread where tensile stresses will be acting. Opening of the oscillation marks at the left corner in the area of free spread and tensile stress can also be noted. In the micrographs of the cross section of the opened oscillation marks, oxide and FeS have been detected. Detailed visual inspection showed that opening of oscillation marks occur during Pass 3 (diamond pass).
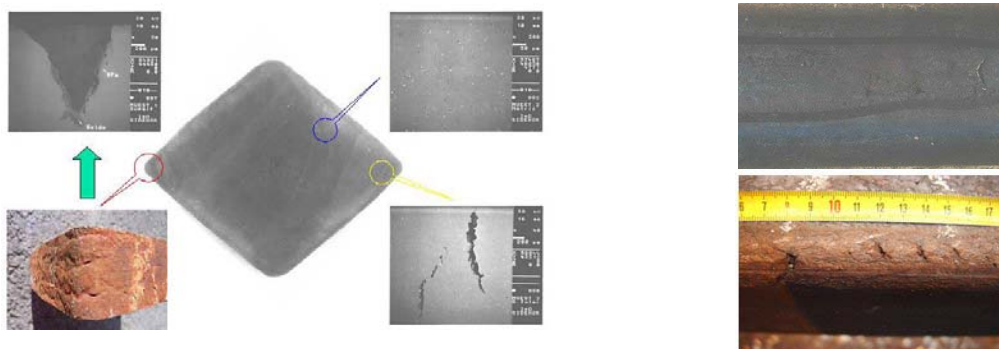
Fig. 76(a and b): (a) cracking at Vitoria Sidenor 9SMnPb36 after first pass
(b) cracking (oscillation marks) after pass 3

Other examples of defect analysis and detection are shown in Fig. 77 taken from the on-line detection system installed between stands R4 and R5 of the Ori-Martin billet mill. Tailored experiments at standard/low rolling temperature (1170°C and 1065°C) but also large resident time were carried out for a range of material (medium C- Bi wrought, as-cast high S). For the medium C steel in wrought conditions, the absence of significant cracking generation in these industrial trials (**out of 5 feedstocks rolled, only one of them developed a minimum number of defects)** can be attributed to the use of a bar already roughed, with no sharp edges, without geometric as-cast defects and not fully recreated as-cast conditions in spite of the long soaking. Increase cracking risk was however deduced [47] when rolling temperature was reduced at RO stand and shorter resident time were used. Ori Martin rolled also five 140 mm x 140 mm as-cast blooms 9SMn28 intentionally at 1040°C to induce profuse defect generation and its detection by the on-line system. Although elongated, the defects were more round than in the previous material and certainly deeper and affected the bar top surface at stand R4 exit. Defects were concentrated in one top-lateral surfaces edge (e1) of R4 and (e2) of R5. Although taken from two different viewpoints, it can be seen either the expansion of the affected zone, the increase in the number of defects.
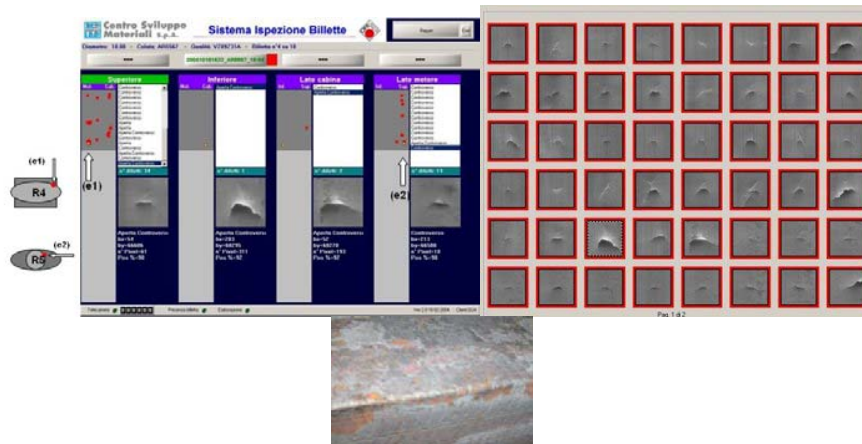
Fig. 77: Example of cracks detection by the on-line system-9SMn28 –
Initial as-cast billet with oscillation marks (Ori-Martin-CSM)

These conditions (mostly Sidenor) are to be put in the context of bar rolling where a comparative study for a similar area reduction has shown that square/diamond pass promotes region of tensile triaxiality at entry, within and exit of bite compared to a box pass (Fig. 78).
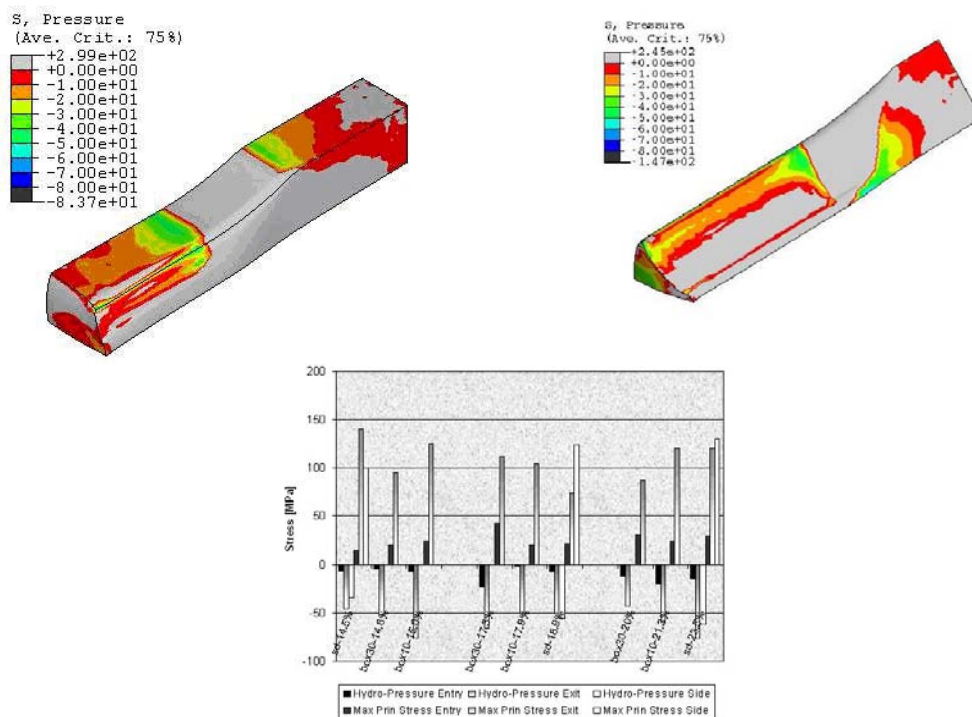
Fig. 78(a-c): (a) box pass 10^0 shoulder angle (b) square diamond pass (c) Laboratory Mill – RollDesign 2 (Corus [48]) - Bar chart showing magnitude of FEM tensile hydrostatic pressure and maximum principal stresses predicted at three key feedstock positions for square-diamond, square-box 10° and finally square-box 30° – Ingoing bar size: 52 sq mm, sharp corner. Area reductions varying from 14.5 to 23.5%.

Ascometal has carried out a statistical analysis from the surface inspection databank of Ascometal Fos/s/mer Plant taking into account 2 years production rolling for a given customer. At FOS, 3 devices are used for the surface inspection on billets and wires on the production plant (see Fig. 73(d)):

- An ELKEM infra-red thermography on billets and round bars after the rolling mill.
- an eddy current system on hot wire after the wire rolling mill.
- an eddy current system on cold wire after wire drawing.

Main defects encountered on the final wire product are shell type defects (Fig. 79) which have two origins, either from pre-existing defect (not detected/enhanced during rolling) or due to decohesion around inclusions. SEM analysis was used in support to this investigation and confirms origin of defects either from inclusions (MnS, TiN, Aluminate) or from refractory/casting powder and exogenous or endogenous inclusions. These defects can occur prior or during hot rolling of bloom/billet or during rod rolling. The former is often linked to decarburisation. It was found that 100Cr6 bearing steel grade inclusions have lower volume fraction than FCS steels so nucleation/growth/coalescence will be reduced during rolling. This was also verified during mechanical testing and therefore redirected Ascometal research towards FCS steels. Different trends with no obvious correlation were however found. Large diameters tend to have more defects than smaller feedstock, after bloom/billet rolling, more defects were observed arising from ingot head or foot. This was opposite to rod rolling where increasing level of defects were found originating from billets coming from ingot middle. As defects when detected after bloom/billet rolling is removed/repaired, little correlation through the process can be made.

Fig. 79: Defect of 2-3 mm (shell or fish scalling) – 100Cr6 (Ascometal)

Finally Ovako-Imatra focused their research in assessing the temperature profile through casting and quenching as well as performing a detailed statistical defect analysis through casting/reheating and rolling at their medium bar mill following a major revamp/capital investment. The analysis included different grades (S355J2, 18CrNiMo7, C38D+N, C40E, 42CrMo4, etc.) with approximately 5000 bars per month of data and the following defects (Fig. 80) [47]:

- seam
- scratch
- crack, length > 1 m
- spiral crack
- crack, length < 1 m
- overlapping
- indent
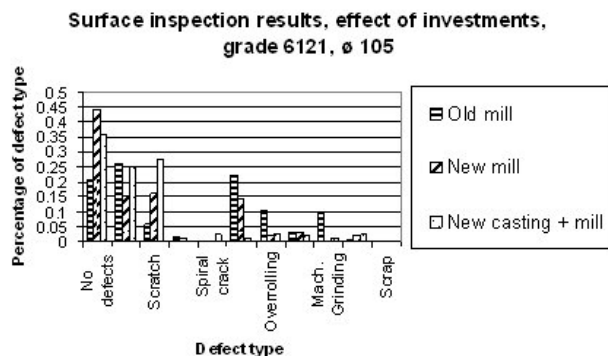
Fig. 80: Surface inspection results, effect investments, Grade 6121 (Ovako-Imatra)

Thermal simulations were also run to assess quenching efficiency and potential for formation of AlN precipitation v Ms start. In addition Imatra has carried out extensive industrial trials to collect information on defects/cracks for sensitive grades such as 18CrNiMo7. A typical edge edge cracking

defect is shown in Fig. 81 (originated from bloom corner). Crack depths are between 1 to 3 mm with width up to 5 mm. Length varies between 200 - 300 mm, typically one defect in a bar. A decarburisation zone can be clearly seen with subsurface defects induced by loss of ductility due to low Mn and high Ni. Yield of individual casts of this steel grade are sensitive to casting/strand conditions inc. link casting/secondary cooling.

Fig. 81: A typical crack in a 135 mm diameter round bar (left) optical microscopy showing crack and decarburisation (right) (Ovako-Imatra)

3.3.3 WP3: Mechanical testing

One of the main objectives of this proposal is to gain a scientific understanding across the length scale (micro, meso and macro scale) of the damage mechanisms inducing ductility break-up/defects. Defects detected during rolling coupled with mechanical-thermal analysis are not sufficiently informative to gather that understanding and start developing more physical models, which account for microstructural features. Mechanical testing has the main advantage if reproducing rolling conditions to test material in controlled conditions/atmosphere with improved consistency and tracking of sample location/orientation. Therefore, mechanical testing has been the major focus of interest and developments in order to derive a range of data (e.g. flow stress, strain @ rupture), properties (Grain size, RX) but also to identify the main mechanisms for onset (nucleation), growth and coalescence of cracks. A range of tests has therefore been used, some being conventional (tensile, torsion, compression), others being more specific and innovative to capture specific rolling strain path and surface effects. FEM analysis was used as a mean to determine the strain-stress path during deformation, as well as comparing effectiveness of all mechanical tests studied. This resulted in a detailed ranking and guidance of mechanical tests (see Table 6 and Fig. 64). FEM was also used to design and optimise new geometries which improved the range of information and damage mechanisms acting in a single test deformation. Most of the mechanical testing was carried out for studying FCS steels in view of their increase inclusion density, although monotonic uniaxial and large scale RPS tests were carried out by Mefos on HT steels. Both monotonic with/without triaxiality inversion and strain reversal (torsion) capturing the wide range of triaxiality-strain values (see Fig. 38) were studied.

The main mechanical tests studied and applied were:

- Tensile testing up to fracture for ductility assessment function of temperature and strain rate and position within bloom/billet to investigate MnS inclusion size/spacing. This test promotes damage at inner sample and covers a high range of triaxiality (> 0.33). Ideally it should be interrupted but this was not achieved. (CSM-Oulu, Ascometal, Sidenor, Corus).
- Torsion testing with/without strain reversal to investigate shear behaviour and shear damage at high strain, including effect of dynamic recrystallisation and inclusion spacing. Effect of reversal for various pre-strain and interpass times has also been investigated to check effect of H/V rolling configuration. As mentioned in Section 2, this is a test involving surface effect and nearly constant strain rate (no necking). Null or quasi-null triaxiality is present during testing (CEIT, Ascometal).
- Compression with a range sample of geometry, single/double hits, deformation pattern (plane strain, axisymmetric), size and sample orientation/location. (all except Sidenor, Ovako-Imatra).
- Stress relaxation compression tests to determine onset of recrystallisation (MDRX, SRX) (CSM-Oulu University).
- Bending in either U or three-point bending of large scale specimens allowing study of large surface/volume ratio and oscillation marks (Corus, Sidenor).

Some of these geometries/tests are illustrated in Fig. 82 .

1000ºC

1300ºC

58

Ø10   Ø9,9   M 10×1,5

15   10

Tipo B

116

(a)

(b)

880 C/19mm

(c)

(d)

(e)

(f)

(g)

2A   3A   4A

(h)

□ 0.05

0.8<Ra<1.25

30º   5   8   Ø6   6

100   -0,1
12-0,05

(i)

cutting map

22   18

20,72

30

25

19,08   R40

22   30

deformed surface

19,08

19,08   80

(j)

69

(k)

(l)
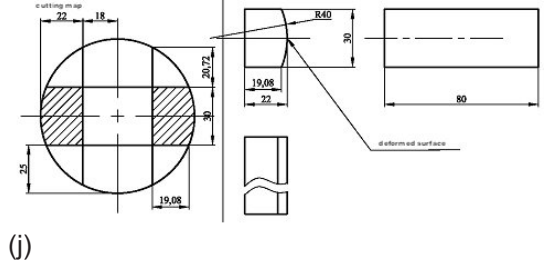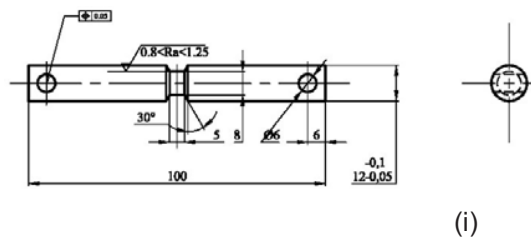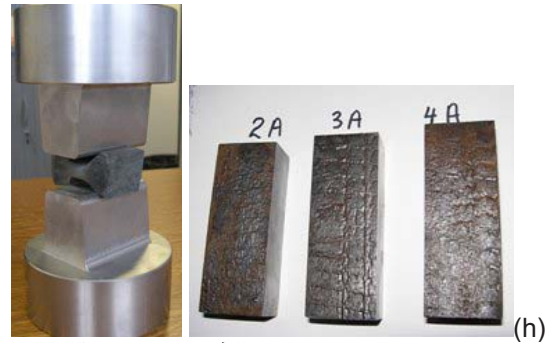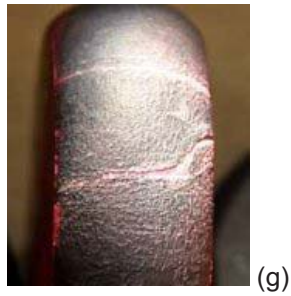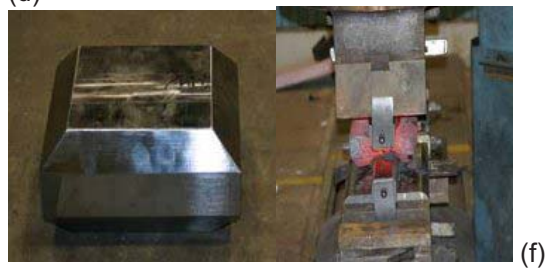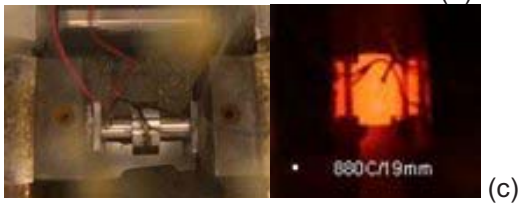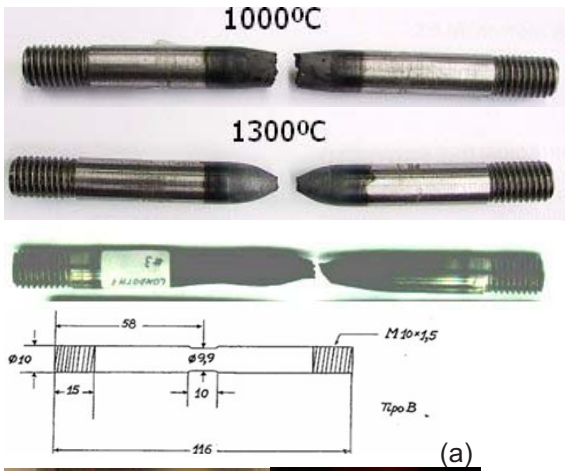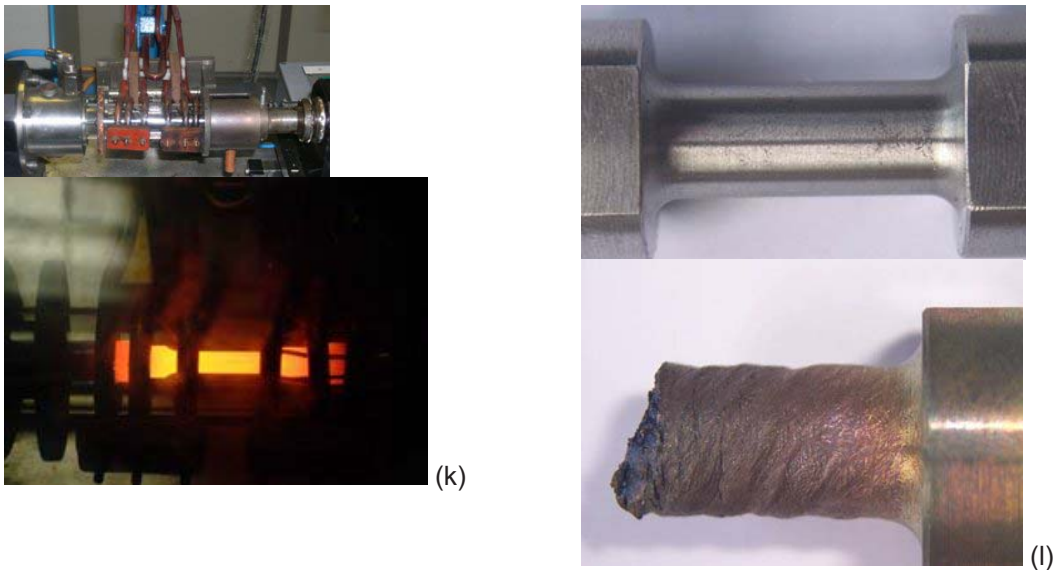
Fig. 82(a-l): Examples of mechanical tests used and developed
(a) Gleeble tensile testing inc. double necking test (Sidenor) (b) 3-point bending large scale (Sidenor)
(c) Gleeble Double Collar specimen (Corus) (d) U bend Gleeble test (Corus) (e) Gleeble range of
mechanical test used including new RPS geometry (Corus) (f) Large scale Corus RPS specimen (Mefos)
(g) Uniaxial compression (Mefos) (h) PSC test (Ascometal) (i) Tensile forgeability (Ascometal) (j) PSC
with curvature (Ascometal) (k) torsion (Ascometal) (l) CEIT Torsion

3.3.3.1 Sample position/machining

FCS mechanical testing has been the major focus of this project in view of the inherent low ductility of these grades. HT steel mechanical testing was carried out by Mefos (upsetting compression) and to a certain extent Ascometal on 100Cr6 steel (torsion, PSC).

Care was taken by all partners to machine specimens from key location within the bloom or billet. Tracking of position and orientation of samples from initial feedstock has been essential as material was sent in both as-cast and wrought to partners such as CEIT and one of the key objective was also to study the influence of spatial distribution of inclusions through the material. Where possible, repeatability was assessed to cover the statistics of inclusion distribution and mechanical test variability. Variability will be inherently linked to machine compliance and type of test. Compression testing may therefore induce more variability due to sample holding and initial positioning. Figure 83 illustrates some of the location/position. **Surface, subsurface and central (or near central) location of bloom and billet has been the main regions of interest for mechanical testing**. Specimen size was also covered from Gleeble type of samples (min 6 mm) (tensile, compression) to large scale 3-point bending specimen. This is illustrated in Table 2 and further discussed below in the Summary of this workpackage. Gleeble testing specimen are taken as near to the surface as possible in order to take into consideration not only the material ductility (e.g. MnS), but also the influence of the solidification structure and oscillation marks**. Rectangular prisms for compression are therefore exposing more surface state than cylindrical specimens (tensile, torsion) and this is combined with the fact that fracture will be induced by surface/subsurface effect.** For instance in Fig. 83(e), RPS specimens were machined from original machined bloom bar (see Fig. 83(c)) by skimming a maximum of 2 mm of the surface from the bloom. The front plane of the RPS samples (taper) are machined further 3 mm from the top face, therefore the mid point tapered face elevation is 5mm below top face. The maximum distance (at mid taper point) from original bloom surface is worse at position 4 and equal to 6 to 7 mm from both surfaces (top/side) of bloom. Positions 1 and 3 are better with respect to testing the influence of the cortical zone being from one side of top surface/side 2 mm from original bloom.
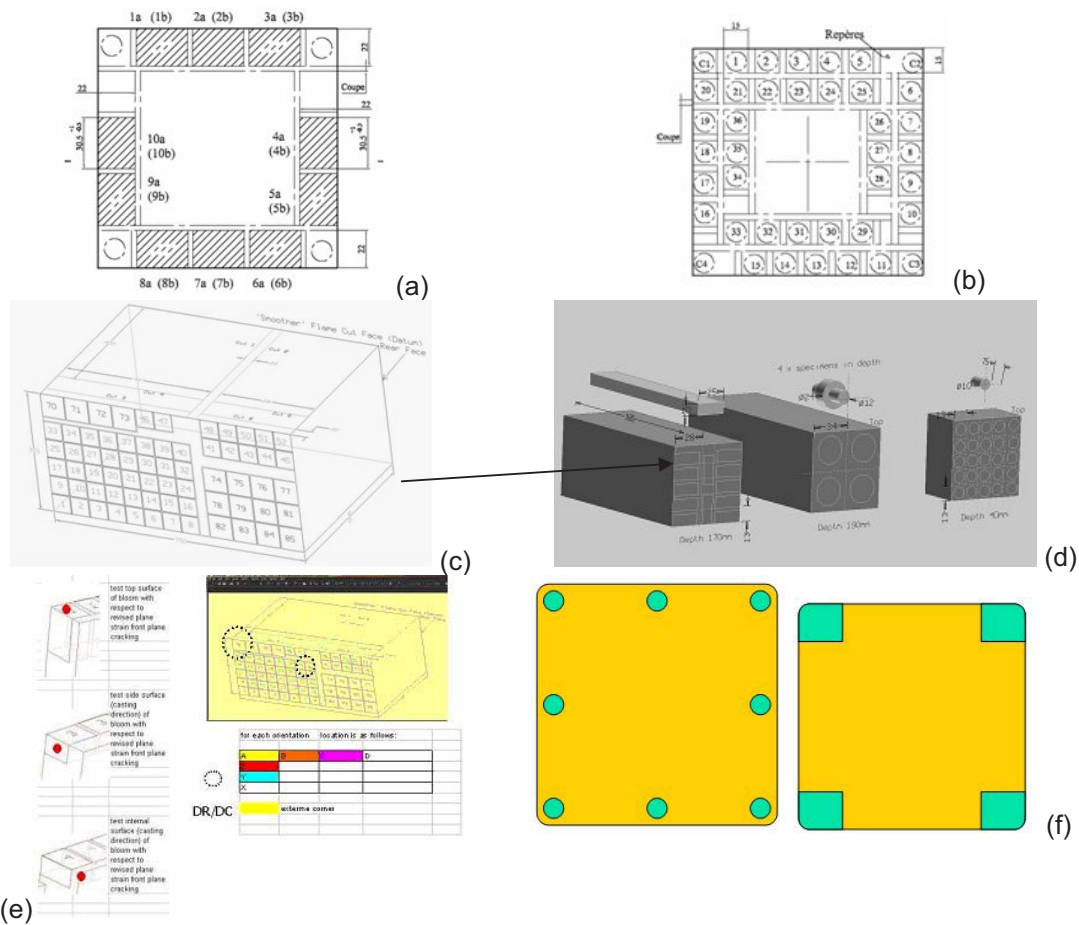
Fig. 83(a-f): Examples of machining/tracking of mechanical specimen position (a) PSC test (Ascometal), (b) Forgeability test (Ascometal) (c) Bloom 750 bar specimen (Corus) (d) Gleeble U-bend, double collar and axisymmetric compression specimens (Corus) (e) Gleeble Revised Plane Strain (RPS) tests with location (A,B,C,Z,Y,X) and orientation tracking (1,3,4) from direction of casting (Corus - red dot mid front plane) (f) Gleeble tensile specimens and 3-point bend (Sidenor)

Mechanical testing was also used in combination with detailed characterisation techniques (optical, SEM, etc.) which required further machining and polishing, thus further increasing variability/uncertainty mostly when dealing with MnS inclusions. Therefore, the approach adopted was only able to develop a 2D representation of damage. More advanced techniques (e.g. tomography, FIB, etc.) are therefore required to develop a more complete spatial representation. Attempts were made using thermal etching to design tests for observing both prior-austenite grain size and damage without need for re-austenitising the structure or quenching heavily through transformation (additional distortion/transformation stresses). This is a field for further development as identified in extended summary.

3.3.3.2 FEM analysis of mechanical tests

FEM modelling of all mechanical tests available within the Consortium, together with new test geometries has been carried out in parallel with experimental testing and as a mean to design and optimise new shapes. This was done to position and compare suitability of a given mechanical test to rolling conditions, where triaxiality is less than 1, strain at corner between 0.1 to 0.6 and temperature varying from 850 to 1250°C. This was shown in the extended summary in Fig. 62 and further illustrated below for some specific tests (Figs. 84 and 86). Strain paths of triaxiality allowing reconstruction of triaxiality-strain plots up to observed experimental fracture have been computed from the FEM simulations. Detailed analysis of FEM results function of position, plane of observation combined with

a series of deformation tests has allowed to build-up an incremental picture of the damage mechanisms. This has been realised for compression testing for varying strain deformation at a given temperature. Without any NDT equipment installed on mechanical testing machines, the only way of identifying damage is to perform tests in varying decreasing deformation (compression) or interrupted mode (tension). FEM results indicated that for the geometries considered (*red square*), **the double collar, U-bend, HCLI, flying saucer, RPS, tensile forgeability, PSC test with curvature, 3-point and U-bending with finally torsion** (for high strain/recrystallisation) should be experimentally tested amongst the Consortium facilities. The key criteria used for cross comparison of mechanical tests and suitability for rolling are explained below. In addition, distance under which key criteria are relevant (i.e. tensile) have been computed at a single relevant location function of strain path or using a path plot at a particular plane of interest showing variation from surface to centre for instance (see Fig. 85(c)). These are further explained for one specific test, the revised plane strain test developed by Corus. Figure 87 shows variation of STR function of deformation at specimen surface. It can be shown that for most tests the surface triaxiality STR can be either tensile through the total deformation or invert at some critical deformation (hexagon, double collar inner ring).
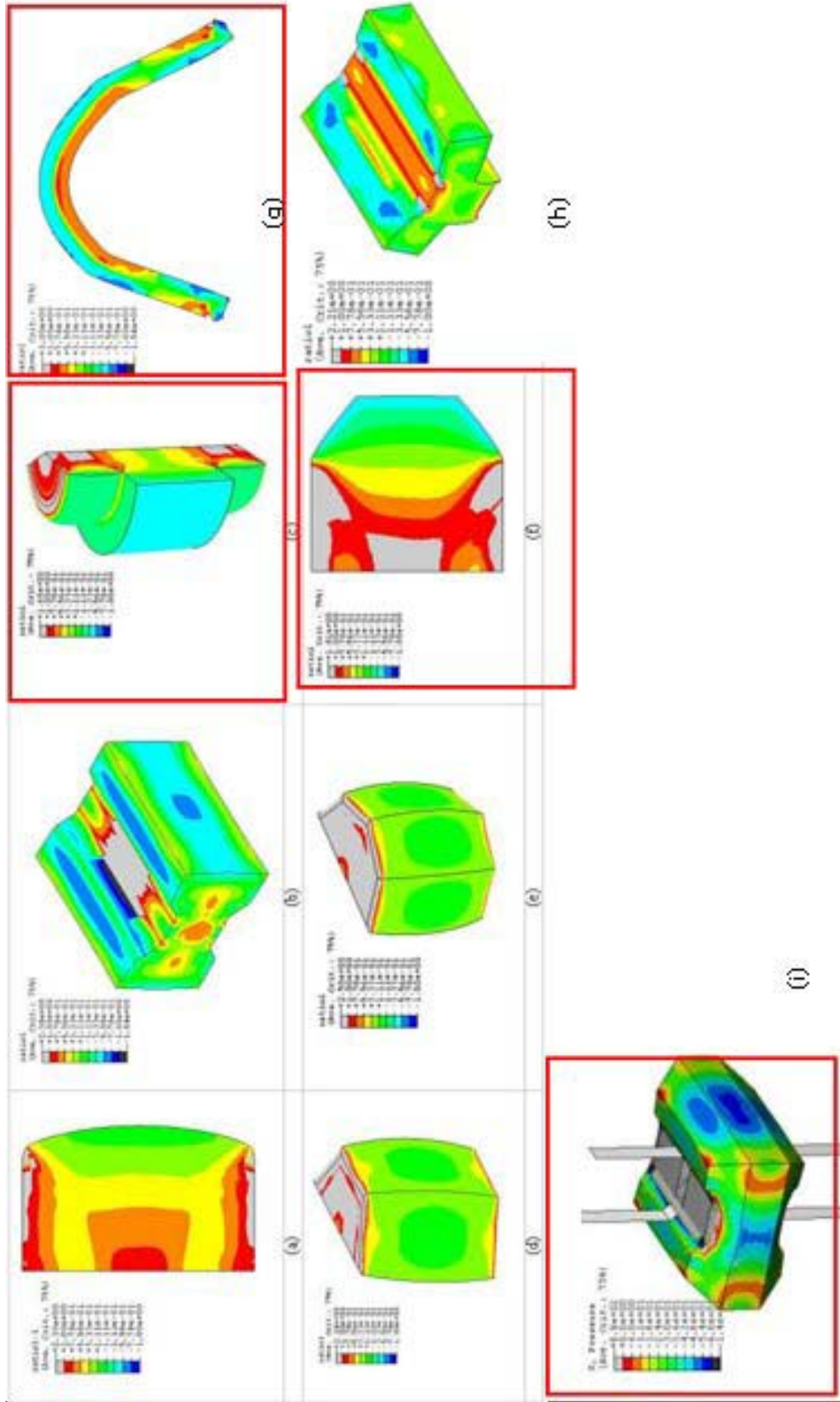
Fig. 84(a-i): Mechanical test FEM simulations showing triaxiality (STR) for reduction/extension in height of 33% (green to blue indicates negative triaxiality, i.e. tensile state) (a) uniaxial with friction, (b) plane strain, (c) double collar, (d) hexagon, (e) octagon, (f) flying saucer, (g) U-bend (h) single-T, (i) RPS (Corus)
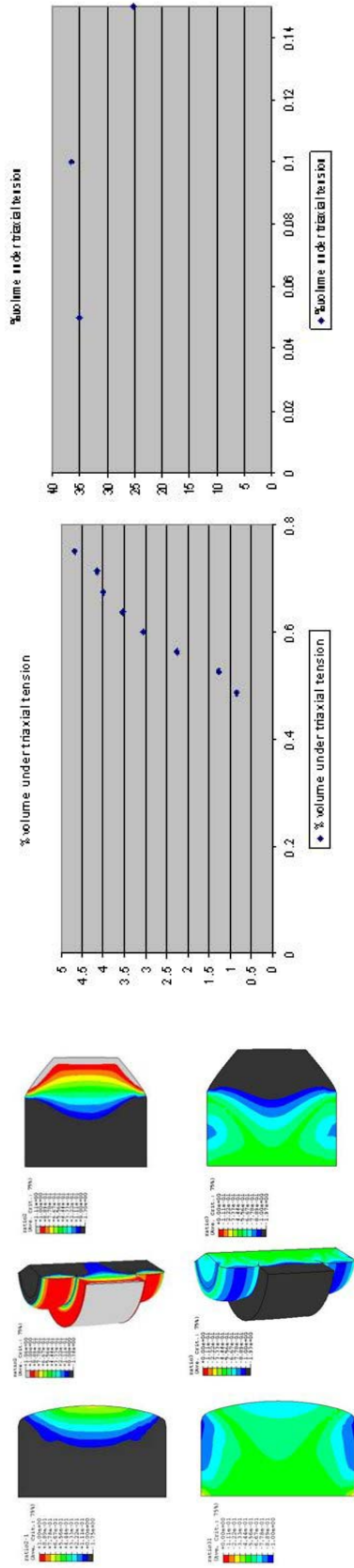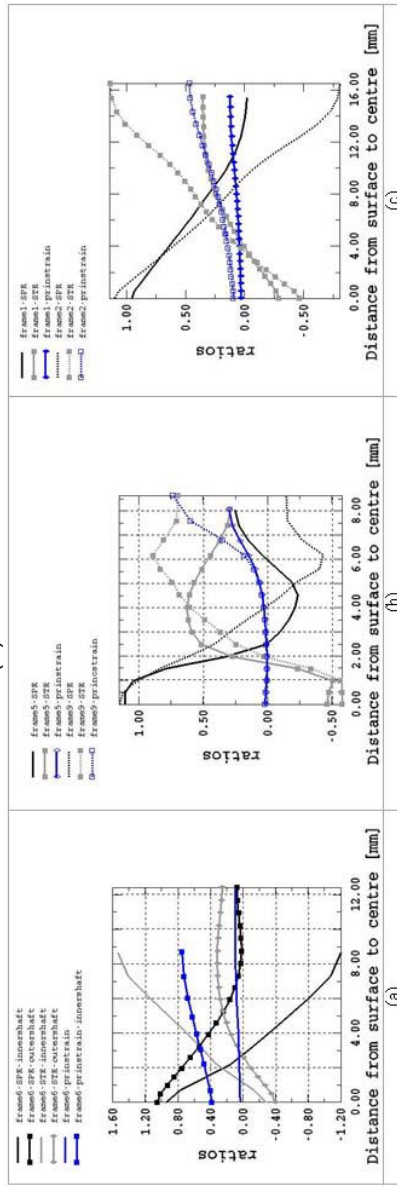
Fig. 85(a-c): Mechanical test FEM simulations showing (a) principal stress ratio (SPR) (Top row) and principal strain ratio (PSR) (bottom row) for reduction / extension in height of 33% (black: compressive state) uniaxial with friction, double collar and flying saucer (b) extent of volume under tensile state uniaxial and flying saucer compression (c) Path plots of relevant STR, SPR and PSR ratios (uniaxial (a), plane strain (b), flying saucer (c)) (Corus)
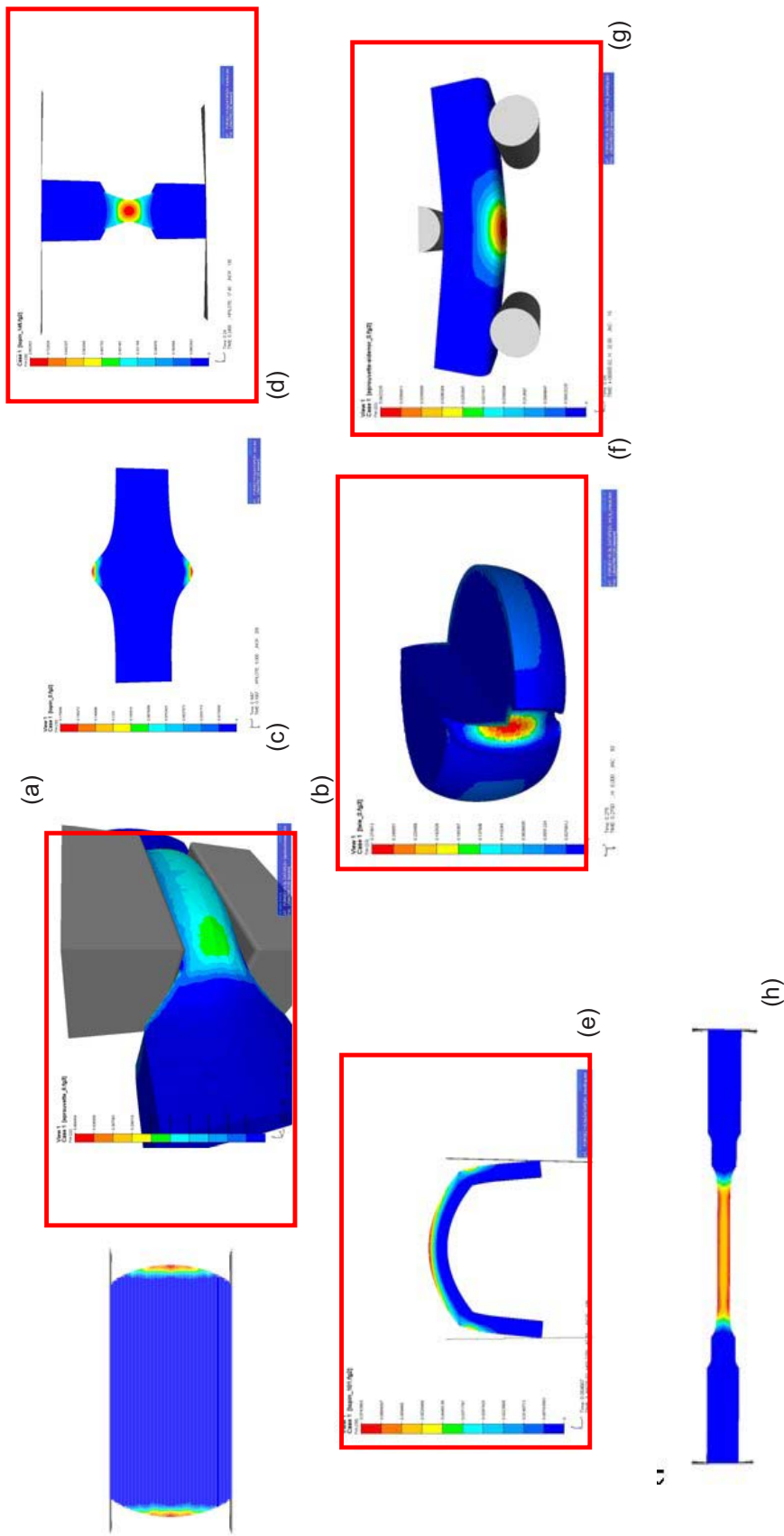
Fig. 86(a-h): Mechanical test FEM simulations showing ductile damage (Lemaitre damage model [41]) for uniaxial compression (a), PSC (b), Sico test (c), tensile 9(d), Ubend (e), crack Limit Index(f), 3 point bending (g) and) and torsion/tension (h) (Ascometal)

Similarly, STR will change sign through the depth (radial) of the sample during reduction (see analogy rolling Fig. 33). These are important criteria which will be further detailed later.
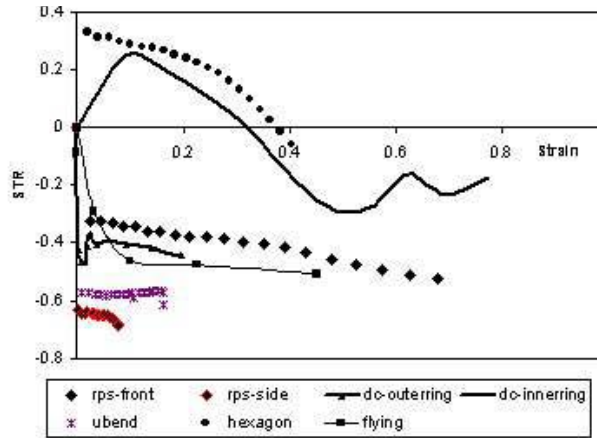
Fig. 87: maximum variation of triaxiality STR function of deformation/strain at surface position (Corus)

- **Key mechanical a-dimensional criteria for mechanical testing (and rolling)**

Key normalised criteria have been applied/defined to quantify:

- the magnitude of the stress triaxiality ratio during testing

$$STR = -\frac{1}{3} \cdot \frac{\sigma_{ii}}{\sigma_m}$$ . . . (3.2)

A negative STR indicates a state of tensile triaxiality as σ_{ii} is equal to trace (σ_{ii}). σ_m is the equivalent stress.

- the magnitude of the tensile principal stress ratio (>0) (σ_{III} is the longitudinal principal stress)

$$SPR = \frac{\sigma_{III}}{\sigma_m}$$ . . . (3.3)

- The magnitude of the mid principal stress ratio (SMID)

$$SMID = \frac{\sigma_{II}}{\sigma_m}$$ . . . (3.4)

- The magnitude of average principal stress

$$SPRav = SPR + SMID > SPR$$ . . . (3.5)

- the magnitude of max-min principal strain ratio

$$PSR = \frac{\varepsilon_{III}}{\varepsilon_I}$$ . . . (3.6)

The lower and more negative this ratio is, the greater principal tensile strains are developed.

- the instantaneous magnitude of normalised tensile mechanical work which promotes ductile damage (PEEQ is the integrated equivalent plastic strain).

$$TMWD = SPR * PEEQ \qquad \dots (3.7)$$

- the magnitude of the Mises - octahedral shear stress ratio.

$$MOSSR = \frac{\sigma_m}{\frac{\sqrt{2}}{3} \cdot \sigma_{yy}} \qquad \dots (3.8)$$

- the magnitude of the max principal stress to the hydrostatic stress ratio.

$$MHS = \frac{\sigma_{III}}{\sigma ii} \qquad \dots (3.9)$$

- Modified Argon [19] criterion.

$$Argon = \frac{PSR}{1-STR} > 1 \qquad \dots (3.10)$$

- Simple damage criteria (type Cockroft-Latham).

$$TMWD_{int} = \int SPR.d\varepsilon \qquad \dots (3.11)$$

3.3.3.3 Summary of mechanical testing

- **Information extracted from mechanical tests**

Mechanical testing was used to test steels of interest (FCS, HT) in controlled conditions.

- (strain, strain rate, temperature, spatial position) to assess and extract information on:
- strain to fracture (tension, compression, torsion).
- nucleation or onset of damage (see fig.38) by coupling FEM results of triaxiality-strain to observation of initiation of void/cracking.
- recrystallisation kinetics (torsion, stress relaxation).
- material hot strength.
- incremental observation of nucleation, growth and coalescence of crack.
- influence of cortical zone.
- influence of spatial position of MnS inclusion (size, spacing).
- derivation of stress-plastic displacement information following necking for fitting damage model (tension).
- derivation of mean local area fraction of MnS.
- influence of strain reversal on fracture/damage.
- influence of double hit/recrystallisation-recovery mechanism on crack growth/coalescence.

3.3.3.3.1 FCS steel mechanical testing (all partners except Mefos, Ovako-Imatra)

- **Monotonic Deformation**

(a) Bending

(i) 3-Point bending (Sidenor)

The objective of this test is to force the original surface of the billet to crack due to any discontinuity in solidification cracks, oscillation marks and embrittlement/oxidation. These are large samples integrating a wide distribution of surface and subsurface features. The conditions for this test are shown in Table 11. The position of the specimens from the billet is shown in Fig. 83(f). In order to quantify the results of the test, a cracking index has been used as shown in Fig. 88.

Table 11: 3-point bending conditions (Sidenor)

Specimen size (mm)	25 x 25 x 127
Furnace atmosphere	Industrial conditions
Heating time (min)	Industrial conditions
Heating temperature (°C)	Up to1200
Test temperature (°C)	Pirometric measurement
Lower rollers diameter (mm)	20
Lower rollers length (mm)	80
Lower rollers distance (mm)	84.5
Upper roller diameter (mm)	20
Upper roller length (mm)	35
Strain rate (mm/s)	100
Piston stroke (mm)	28-32
Angle (°)	80-90

0	cracks free
1	some cracks
2	a lot of cracks
3	severe cracks
4	very severe cracks
5	fracture
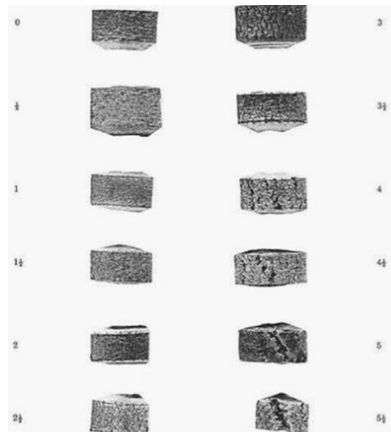
Fig. 88: 3-point bending cracking index

The results of the hot three point bending tests show two types of behaviour regarding oscillation marks (Fig. 89). Hook type oscillation marks are more prone to cracking under 3-point bending. In order to differentiate oscillation marks and intrinsic ductility of material in 28329 9SMn30 (Mn/S = 4.6), material corresponding to half radius near the corner of the billet was tested. No cracking appears in the adjacent half radius sample.

Fig. 89: (left) 3-point bending cracking of oscillation mark (hook type) – (right) Damage at corner and subsurface (no cracking)

(ii)   U-bending (Corus)

Corus has developed the Gleeble U-bending test (Fig. 89) using machined plates of 165 mm length, 25 mm width, 10 mm thickness with notch at mid length in order to concentrate resistive heat and ensuring symmetry of deformation. Tests were conducted only on Bi-FCS cast steel (PY04/29) up to fracture at 850°C and stroke of 0.3 mm/s. Figure 90, shows the fracture profile of the specimen at a stroke of 48.4 mm. The triaxiality, principal stress ratio and the argon modified criterion predicted by FEM is also shown. Figure 90 shows clearly the development of the tensile zone over and along the top level of the neutral axis. This test, due to its geometry allows in principle a wider range of inclusion content/shape/frequency to be studied, however it has proven to be difficult to ensure complete symmetry due to issues regarding positioning in the Gleeble machine/Jaws. Also this test is expensive to run with respect to material and by notching at half length, reduces regions of interest. This test was therefore not pursued further, despite some of the information obtained at fracture, **re. triaxiality 0.6, strain 0.13, SPR> 1.**
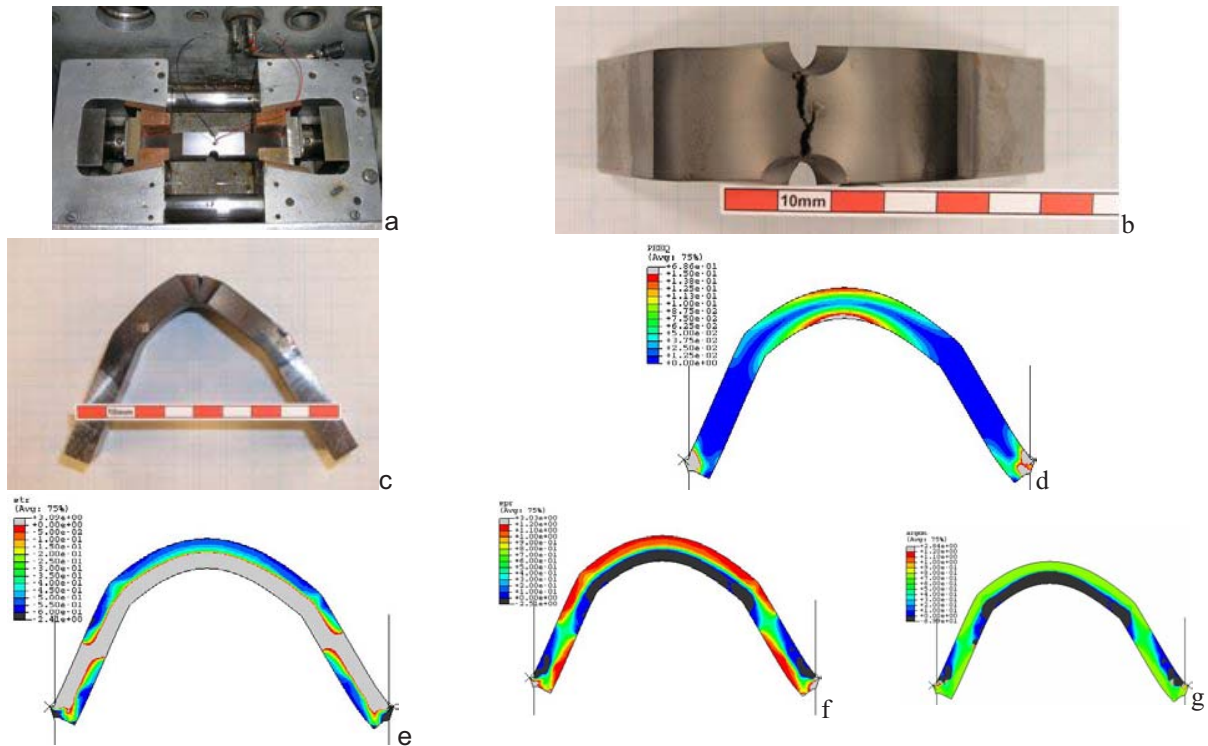
Fig. 90(a-g): (left) 3-point bending (a) undeformed specimen in Gleeble (b,c) cracked specimen (d) FEM equivalent strain (e) STR (f) SPR (g) Argon modified criterion (Corus)

(b)   Tensile/Forgeability (Ascometal, CSM/Oulu, Corus, Sidenor)

(i)   Forgeability curves (Ascometal)

Ascometal carried out a programme of tensile testing on the steels shown below

	100Cr6	32MnS5Pb	32MnS5Bi	9SMn28 (CSM)
Forgeability	16 samples 900-1200°C 1 and 10 s^{-1} constitutive data	15 samples 700 to 1350°C, 10 s^{-1} 20 samples for the parametric study (Temperature, austenising time, strain rate)	15 samples 800 to 1350°C 10 s^{-1}	15 samples 800 to 1350°C @ surface, 7 and 22 mm below surface

Results are shown below for all steels in Fig. 91 showing reduction in diameter versus temperature. It can be observed that for the temperature considered in this project, 100Cr6 bearing steel has excellent

ductility compared to the FCS. The low ductility of 9SMn28 is attributed to being in as-cast conditions. The ductility of the samples extracted at 22 mm from the surface is significantly lower that the ductility of the sample extracted at 7 mm from the skin of the billet. **These tests show that the cortical zone has a better ductility than the inner part of the billet, mostly at high temperature. As expected also, the ductility of Bi-FCS is lower than that of Pb-FCS (see trough). A strain @ rupture of 0.5 for Bi steel is derived up to 950-960°C.**
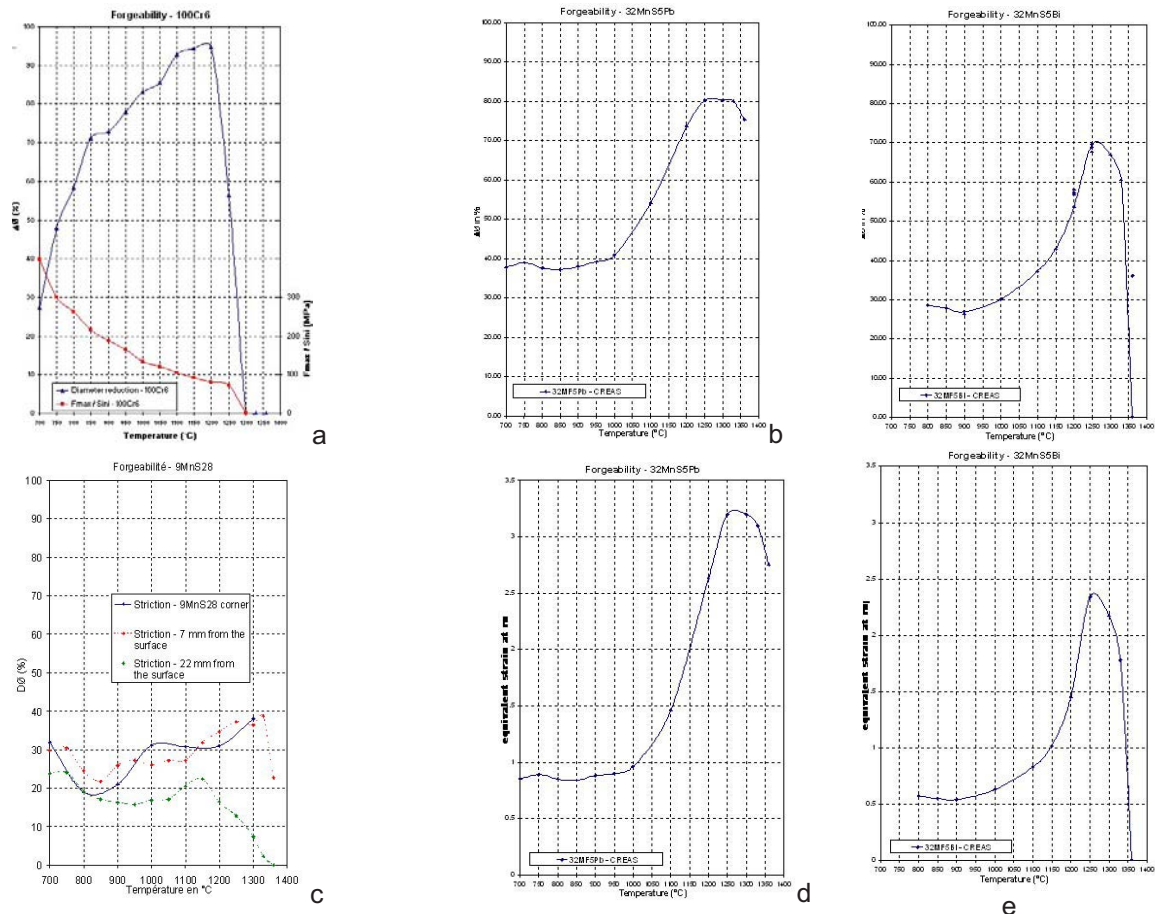
Fig. 91(a-e): Forgeability curves for 100Cr6 (a), 32MnS5Pb (b), 32MnS5Bi (c) and benchmark grade 9SMn28 (d) recomposed FEM strain at rupture 32MnS5Pb (e) recomposed FEM strain at rupture 32MnBi

(ii)   CSM/Oulu University - 9SMn28 benchmark steel

Tensile specimens (10 mm diameter x 110 mm length with 10 mm M15 threads) were reheated at 10°C/s to 1150°C, held 2 minutes for soaking, then cooled at 5°C/s to the deformation temperature. As shown in Fig. 92, ductility (reduction of area at fracture) is lowest around 960°C. Ductility is in general lower at the lowest strain rate (0.11 s^{-1}) with no major differences at the higher strain rates. **The minimum ductility shifts to lower temperatures (i.e. to higher Z, see Table 12) when high strain rates are applied.** The strain to tensile peak from elongation exhibits a relative maximum around 960°C (Fig. 92(b)) and is minimum at 800°C. These results suggest that damage is not only controlled by ductility, but also by the onset of damage near the strain to peak (nucleation). This is a criterion which has been used in the construction of one of the damage function examined in WP7. All mechanical tests were carried out in zones outside central or corner material.
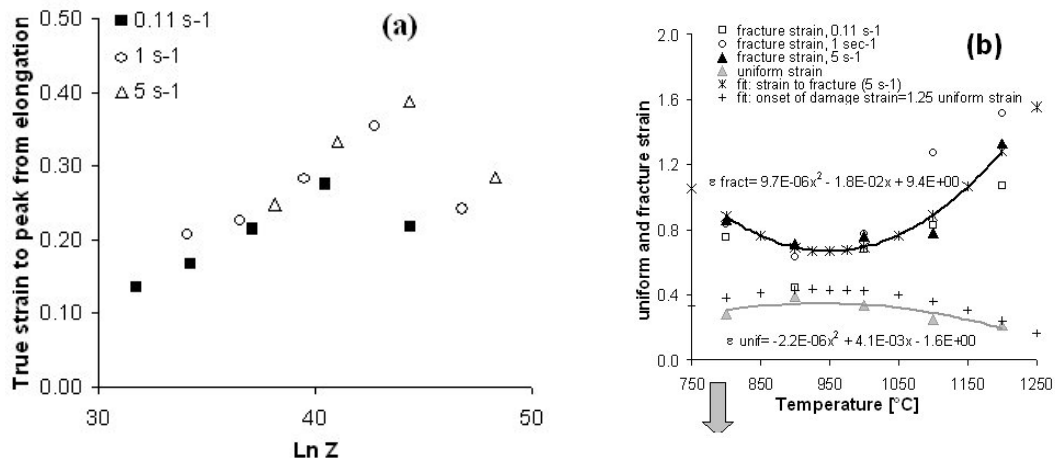
Fig. 92(a and b):Tensile test 9SMn28 (a) strain to peak function of Zener Hollomon (b) strain to fracture function of temperature

(iii)   Corus – Birmingham University LFCS, Telby+

Tensile testing at Birmingham University has also been carried out on Telby and LFCS steels. Stress/strain data following necking (maximum load) have been extracted to derive stress-displacement (flow stress) and fracture energies which were used as input to the "standard" damage ABAQUS evolution model (see WP7). From tensile testing (Fig. 93), it can be observed that ductility is worse for the Telby FCS steel and that also ductility is reduced at bar 22 (towards centre of bloom). This is consistent with findings from other partners (see CEIT, CSM and Ascometal). Telby+ Gleeble tensile samples were also taken respectively from 5, 40 mm and near bloom centre (outside porosity region) and flow stress to fracture is shown in Fig. 93(d). LFCS seems to be more sensitive to temperature than the Telby+ (Fig. 93(c)).

(a)

(b)

81

(c)

(d)
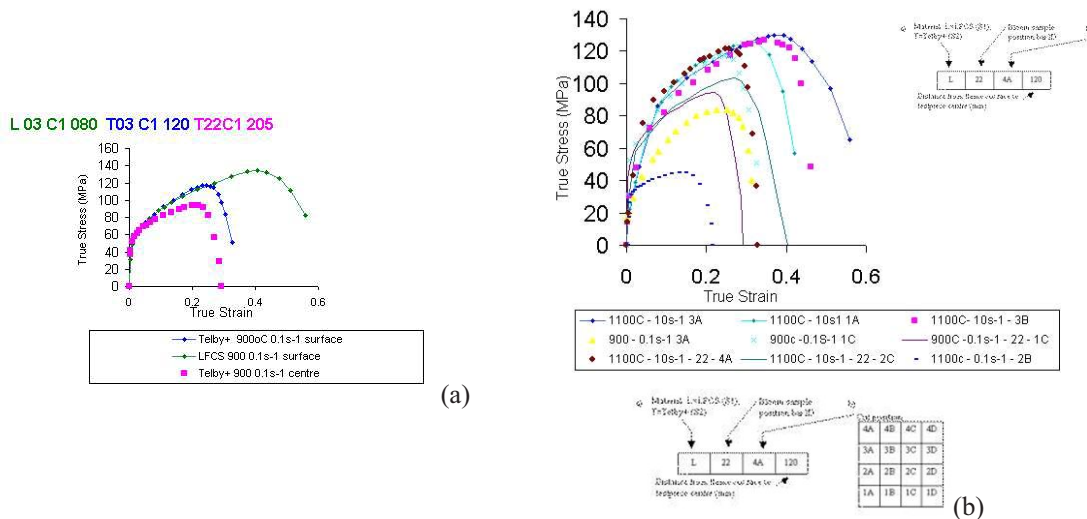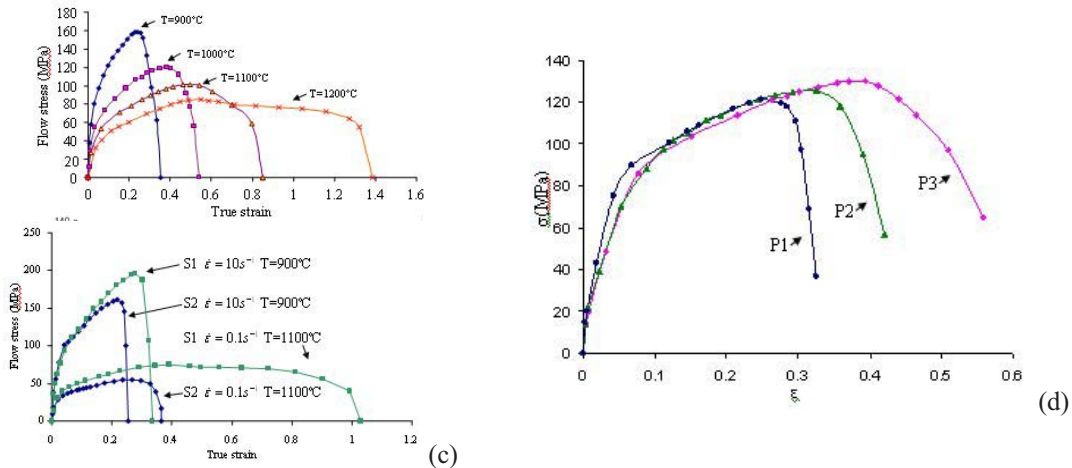
Fig. 93(a-d): Extract from tensile flow stress data (Birmingham-Corus) for Telby and LFCS (bar 03 and 22) (a) stress-strain data surface/centre (b) Telby+ stress-strain @ various positions (c) LFCS flow stress data function of temperature ($\dot{\varepsilon} = 1.0s^{-1}$) (d) Telby+ Flow stress variation function of positioning from centre (P1) to surface (P3) $T = 1100°C$, $\dot{\varepsilon} = 10s^{-1}$

(iv) Sidenor - 26564 9SMnPb28, 26540 9SMnPb30 and 28329 9SMn30

The objective was to evaluate the ductility of the subsurface of the as-cast material without effect of surface cracks or oscillation. Test conditions are shown below:

Specimen size (mm)	116 x 10Ø
Heating cycle	On heating
Atmosphere	Vacuum
Heating speed (ºC/s)	10
Maintenance time (s)	60
Test temperature (ºC)	1000, 1100, 1200, 1250, 1300
Strain rate (s⁻¹)	10

Ductility results (Fig. 94) show as expected a dependency of ductility with temperature for this specific strain rate (high) and similar to CSM results, show a trough towards lower temperature with typical as-cast ductility of 30%. The presence of Lead decreases the ductility further, however at 1300ºC the reduction of area is similar in all three cases. The leaded heats with similar sulphur but different manganese content have a similar ductility, but a different behaviour is observed. In the case of the higher manganese composition (26540 9SMnPb30) there is a continuous increase of ductility. The lower manganese leaded steel (26564 9SMnPb28) shows a change in ductility from 1200ºC.
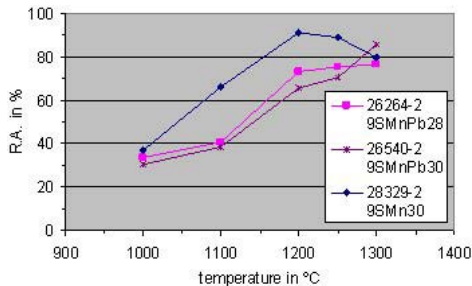
Fig. 94: Ductility curves for 26564 9SMnPb28, 26540 9SMnPb30 and 28329 9SMn30

Ductility of faces and corners at 1250ºC has also been compared (see Fig. 95 and Fig. 83(f)). In most of the cases the ductility at sub- corner is worse than the ductility of the face.
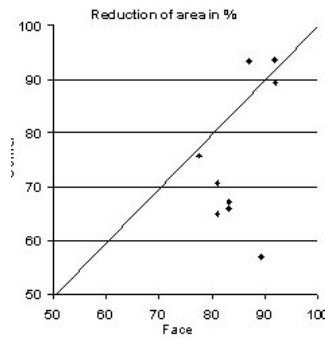
Fig. 95: Ductility curves 9SMnPb28 corner versus face of billet

(v)   Sidenor - Double necking tensile testing 26564 9SMnPb28

Gleeble double necking testing using hot jaws practice with stainless steel instead of copper jaws has been carried out to assess if fracture is caused by ductility breakup or if there is the additional influence of the oscillation marks. For double necking testing, the tensile specimens are machined from the billet corners as near to the surface as possible with the caution of removing surface oxidation and irregularities. Figure 96 shows the computed stress-strain curve at both subsurface and corner. A momentary stress fall at the beginning of the ductile zone in the case of samples from billet corner can be observed, however the reduction of area continues only in one section which seems to indicate that double necking effect has not been found in this material.
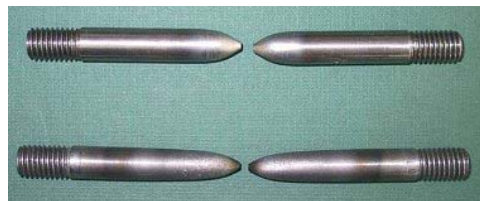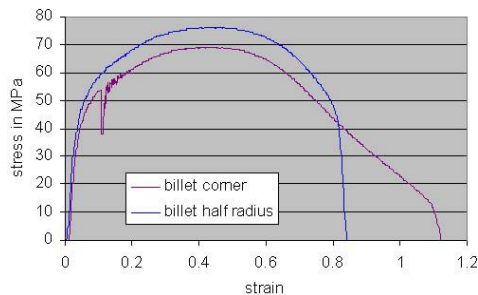
Fig. 96: Strain-stress curves of double necking test. 9SMnPb28 (Sidenor)

(c)   Compression (Ascometal, CSM/Oulu, Corus, Mefos)

(i)   Ascometal – PSC/PSC curvature - 32MnS5Pb - 32MnS5Bi- 9SMn28 steels

Ascometal carried out a programme of compression testing as summarised below. The aim was to determine onset of fracture and compare via reconstruction by FEM, triaxiality-strain curves. Specific PSC with curvature from round feedstock (wire rod in wrought conditions) was also carried out. Study of roughness and presence/opening of oscillation marks on CSM 9SMN28 has also been carried out.

	100Cr6	32MnS5Pb	32MnS5Bi	9SMn28 (CSM)
PSC test	2 samples 900°C 700 mm/s	4 samples 1130°C 700mm/s 6 samples 900°C 700 mm/s profilometer analysis metallurgical analysis	4 samples 1130°C 700 mm/s 6 samples 900°C 700 mm/s profilometer analysis metallurgical analysis	20 samples 900-1000-1100- 1200 °C 700 mm/s test of different sampling from a billet profilometer analysis - metallurgical analysis parametric study

Figure 97(a and b) shows results of PSC tests on 32MnS5Pb –and 32MnS5Bi plotting reduction (upsetting rate) function of temperature. There is clearly an improvement of ductility or resistance to cracking as temperature increases (case of Pb grade). This is not the case for the Bi grade which shows a relative independence to temperature. The CSM as-cast grade shows a trough at 1100°C.

83
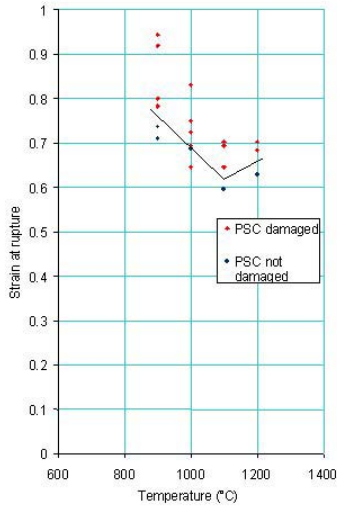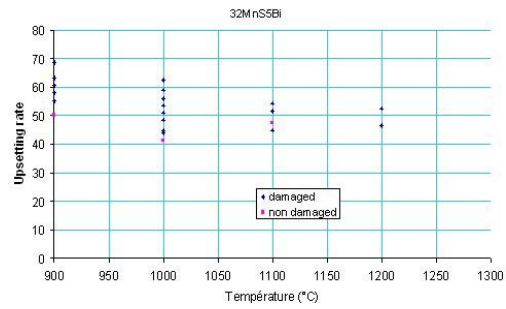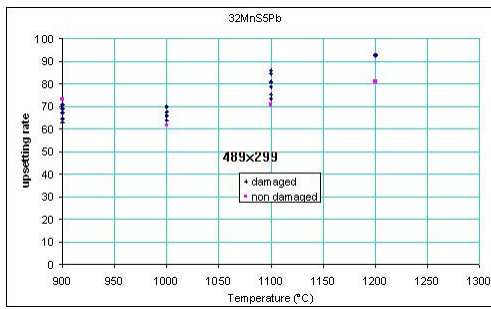
Fig. 97: PSC tests 32MnS5Pb, 32MnS5Bi and 9SMn28 (Ascometal)

(ii)   RPS (Corus) – Te-FCS (surface, centre, as-cast-wrought), LFCS (corner), Telby+ (corner), 9SMn28 CSM (4a. 4b, 4z corner))

A revised geometry to the standard plane strain test as used in standard Gleeble thermo-mechanical simulator has been designed [44]. The geometry can be composed of one to four tapered faces at specific inclination (say 10 to 60°) to promote required level of triaxiality-strain ratios. It was shown that a standard rectangular prism with faces in contact with anvils cannot promote ductility break-up under normal tensile mode (only shear mode and at high strain). By machining inclined front and bottom faces (within the plane strain compression plane, as denoted by the first taper index), together also with side faces (second index), one can generate two states of stress-strain conditions, i.e. mid triaxiality and strain together with high triaxiality-low strain regions within a single test as shown in Figures 4 and 5. Path plots of interest will therefore be at mid front (path3) and side horizontal (path2) mid planes as indicated by the dashed lines. This is further illustrated in Fig. 98, where for 45° degree front inclination, str -0.4, SPR~1.1 with tensile principal stresses (max, mid) acting from 17% deformation.

(a)

(b)

84
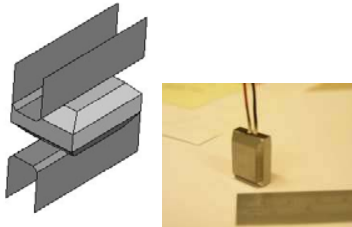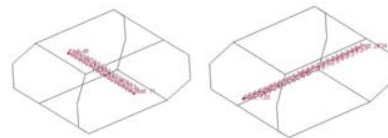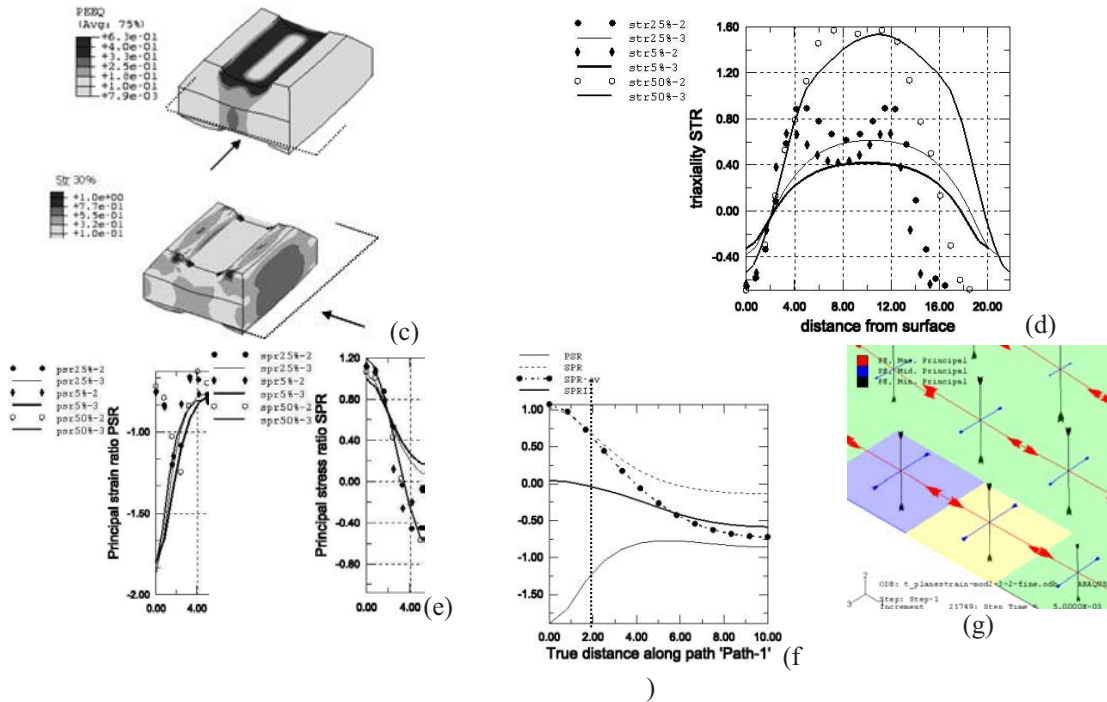
Fig. 98(a-g): RPS FEM analysis showing set-up (a) path plots (2 and 3) (b), strain and triaxiality (c), triaxiality at mid equatorial plane (paths 2 and 3) (d) and various ratios (PSR, SPR, etc.) (e, f) principal stress at 17% (g) principal strain tensor at 5% deformation (limit capped to 0.1)

Testing has been on Te-FCS as-cast corner and centre bloom at respective positions (a,b,c,y,z) and orientations 1, 3 and 4 (See Fig.82(e)), wrought Te FCS (4a, 4b, 4z), Telby+ as-cast corner (1a, 3a 4a) and finally as-cast LFCS (a, b, z) and orientations (1, 3 and 4). Conditions ranged from 0.1 to 10 s^{-1}, 880, 1000 and 1200°C and 5 to 50% reductions. The RPS deformation plane has been oriented according to 3 directions. For the centre testing, bars 31 and 32 were selected, located above the potential central porosity area (see black circle).

Figure 99 shows measured depth and width of cracking for various steels and conditions/position. The grade shows worse ductility, followed by Telby+, then LFCS and CSM grade. For similar conditions tested, bloom centre ductility is low. At low strain rate (0.1^{s-1}), cracking starts to occur at low reduction (5%) with the larger cracks occurring at high temperature. At the lower temperature tested, 880°C, a reduction of 10% is required with more cracking irrespective of orientation/position occurring from 25% reduction. The CSM grade in position 4 at corner (A, B and Z) shows extremely good ductility at the two temperatures tested (880 and 1000°C). Similarly the Te wrought structure shows little sign of cracking (except one case at 1200°C). Overall position 4A is worse at corner, with ductility improving away from extreme corner. For near centre material, ductility does not seem to be dependent on spatial location within the distance of the machined bar tested. For LFCS, 30% reduction at 880°C is required to initiate cracking (str = 0.39, peeq = 0.31 (surface)).

(a)
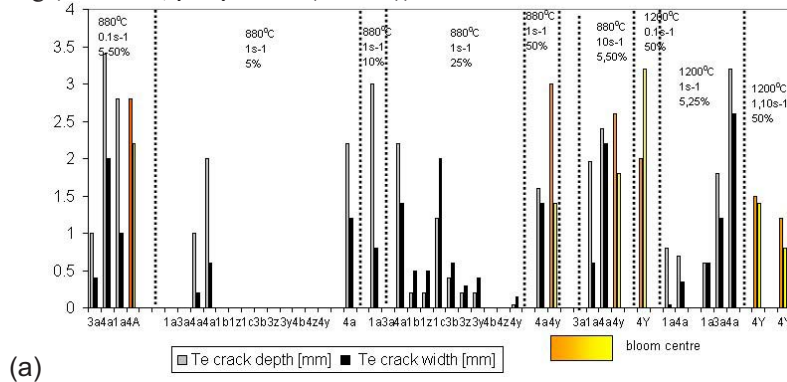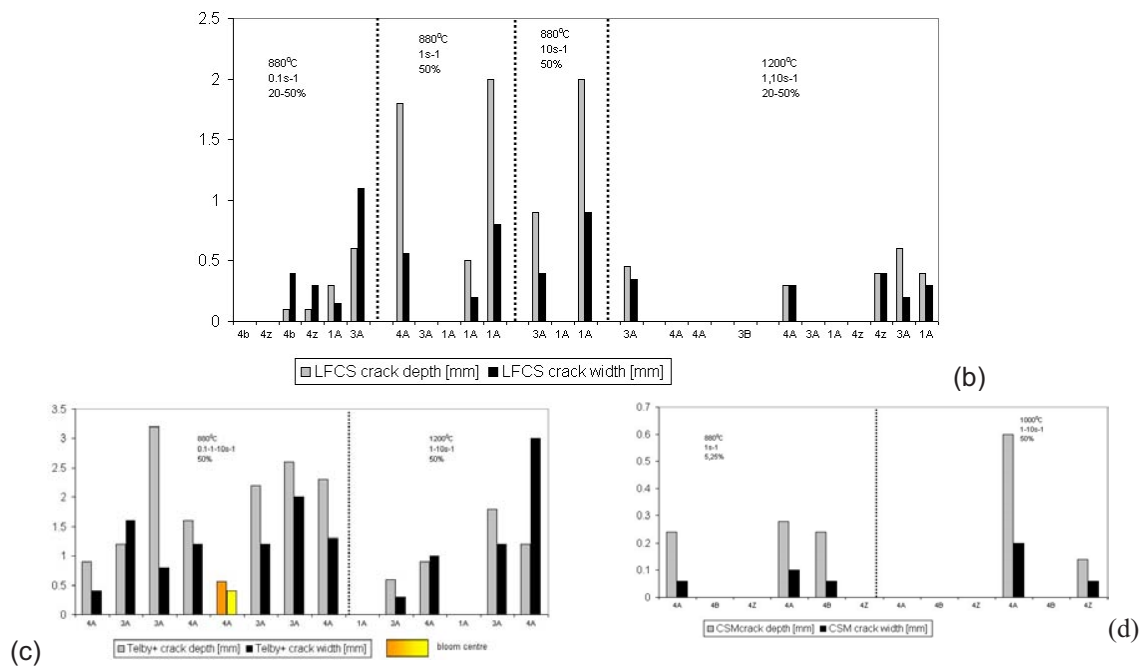
Cracking (e)

LFCS 30% - 880°C –1s-[1]- str 0.39 – peeq 0.31

LFCS 50% - 1200°C – 1s-1 – str 0.52 – peeq 0.69

Te 20% - 880°C – 1s-1 – str 0.37 – peeq 0.18

Te wrought 1200°C -5%- 1s-1

Fig. 99(a-e): RPS measured crack analysis (a) Te as-cast (b) LFCS as-cast (c) Telby+ as-cast (d) CSM 9SMn28 as-cast (e) summary cracking

Analysis of crack depth v crack width is shown in Fig. 100(a) for all tests with additional criteria plotted such as principal strain ratios [27], etc. Overall normal behaviour is observed, i.e. cracking is perpendicular or normal to the max direction of principal stress (hoop) at the coalescence stage. An inverse behaviour (see Te centre) can however be observed mostly at high temperature 1200°C, where crack width is greater than depth, i.e. mode of cracking is parallel to max principal stress. It can be observed that the trend follows the ratio of the max principal strain to min principal strain ratio with similar correlation factor. Figure 99(b) also integrates results from typical rolling passes. It is clear that cracking is promoted if points lay below the RPS line.
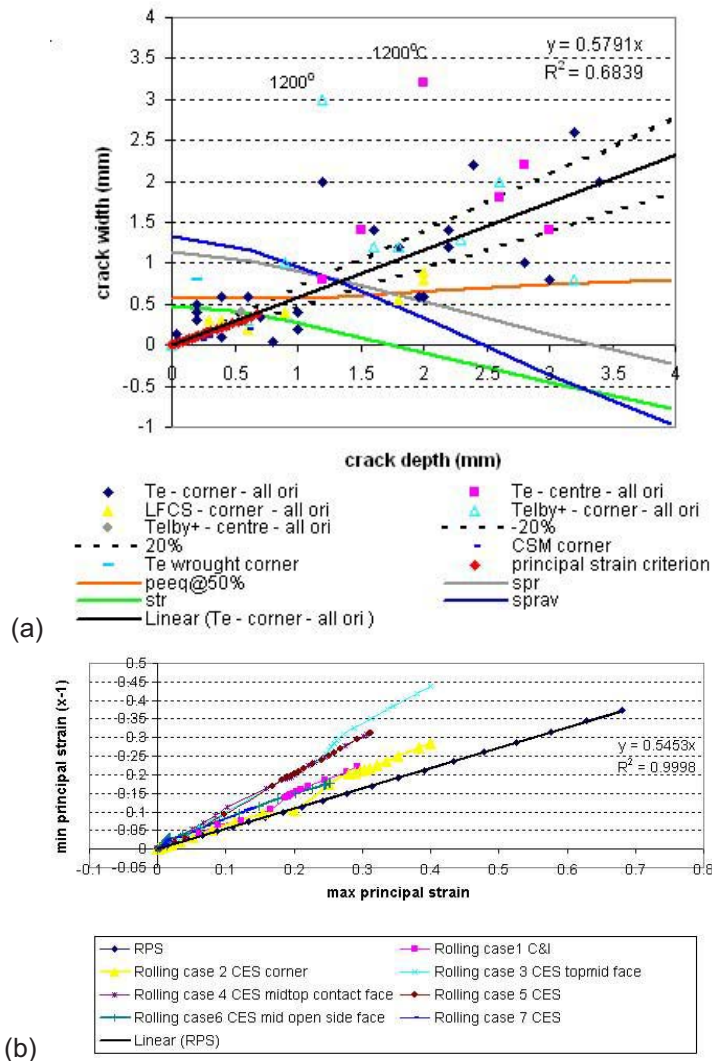
Fig. 100(a and b): (a) RPS Crack assessment for all steel tested (b) Principal strain v min principal strain during RPS and Rolling (box passes scenarios).

(iii)   Additional compression testing (Corus) – Double collar (Telby+ corner)

Figure 101 shows the double collar test deformation and heat input into the section, as the sample is continuously deformed between the Gleeble anvils/jaws at a speed of 0.22 mm/s ($5.10^{-3}\,s^{-1}$). Cu jaws were used at this stage, together with a controlling thermo-couple on the inner shaft of the double collar test.
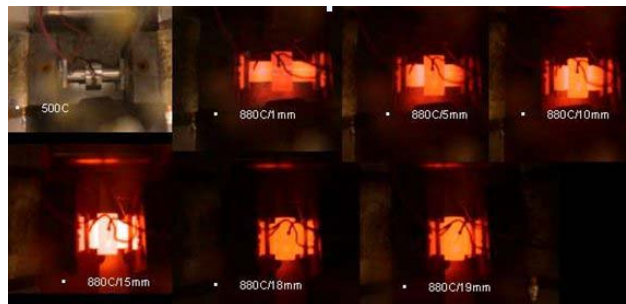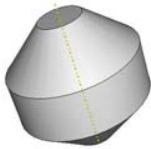
Fig. 101: Gleeble Double collar specimen (Corus)

Other compression testing (flying saucer, hexagon, etc.) is detailed in Fig. 5 (see also Fig. 87 for strain paths).

Tapered uniaxial " Flying saucer"	15 (max. diameter) x 28 (height)	New test developed to promote hoop tensile stress.	
Hexagon	5 (edge length) x 10 (diameter) x 15 (height)	New test developed with h/D=1.5. Potential study of shear fracture on inclined planes leading from straight edge and lateral fractures. Same comment as plane strain for bloom/surface representation.	

(iv)   Double collar thermal etching (Corus)

Dilatometer experiments using polished double collar axisymmetric specimens (Fig. 102(a)) have also been carried out with the view to use thermal etching technique to reveal prior austenite grain size and cracking. The specimen (max length 10 mm) is being deformed in a dilatometer in vacuum using the thermal etching technique. Bi-FCS has been used (bar 29/70) for this series of preliminary tests. The thermo-mechanical treatment initially used is shown in Fig. 102(b). Polished double collar samples (see Fig. 102(a)) are reheated to 1200°C for 30 s then slow cool to deformation temperature (1000°C), prior to main deformation of ~50% at 1/s. The sample is subsequently cooled to ambient (slow cooling through transformation). This test permits to capture the grain structure and potentially damage zones in one test, avoiding therefore re-austenitisation.
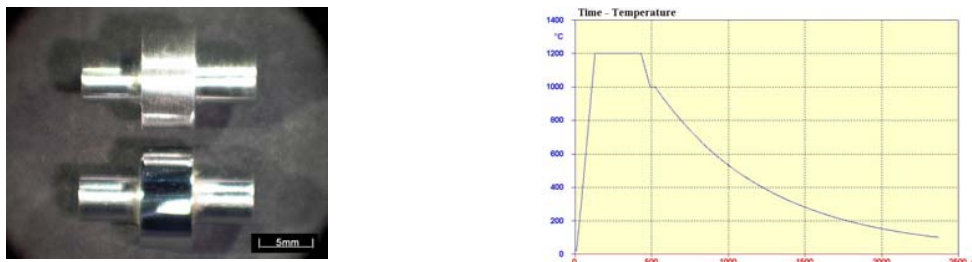
Fig. 102(a and b): (a) Polished double collar sample (b) thermo-mechanical profile (Corus)

(v)   Compression testing (CSM/Oulu)

A series of compression tests were carried out on 9SMn28 at various temperature and strain rate (Fig. 102). These data were used for fitting the constitutive model (continuous line).
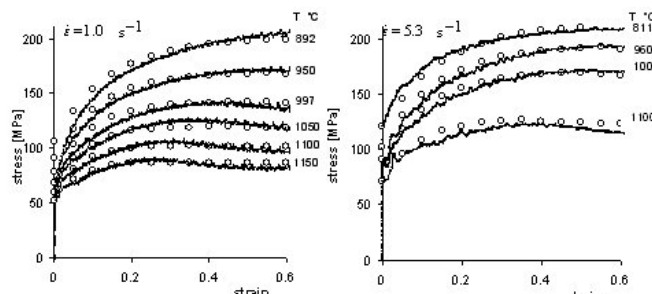
Fig. 103: CSM/Oulu Compression testing - true stress-strain data 9SMn28

(d) **Torsion (CEIT, Ascometal)**

(i) **Torsion (CEIT)**

Two different types of torsion tests have been carried on five free cutting steels qualities in both as-cast and wrought conditions:

- Torsion tests to failure at different temperatures and strain rates (evaluation of ductility measured as ε_f).
- Interrupted torsion tests (evaluation of damage evolution).

The specimens were machined from different locations. A summary of the tests is shown below.

Table 12: Summary of deformation applied in interrupted torsion test at 1150ºC and 1 s^{-1}.

Strain	0----0.5----1----1.5----2----2.5----3----3.5----4----4.5----5----5.5
S2	x x x x x ε_f
Corus LFCS 1/05	X x x x ε_f
Corus LFCS 1/30	x x x x ε_f
Corus Telby 20/05	x x x x ε_f
Corus Telby 20/30	X ε_f ε_f ε_f
Sidenor 9SMnPb30	x x x ε_f
CSM 9SMn28	ε_f x Xε_f

The thermal/mechanical profile is shown below in Fig. 104.
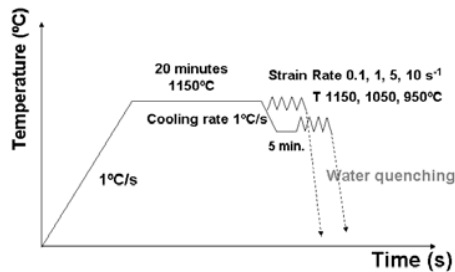
Fig. 104: Thermal cycle profile of monotonic torsion test

Examples of $\sigma-\varepsilon$ curves obtained at different temperatures and strain rates are shown in Fig. 105.

(a)

(b)
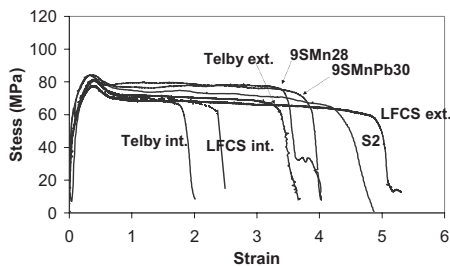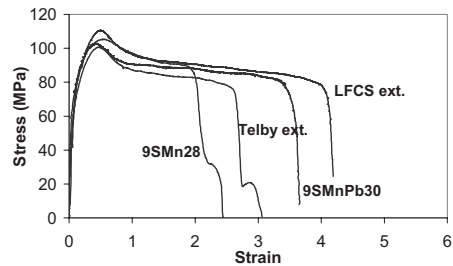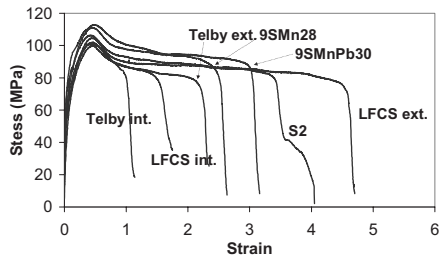
Fig. 105(a-c): Flow curves from torsion tests at (a) 1150ºC and 1 s⁻¹, (b) 1050ºC and 1 s⁻¹ and (c) 950ºC and 0.1 s⁻¹

In all the cases, the curves show a peak stress followed by softening and a steady state region, typical of the occurrence of dynamic recrystallisation. Comparing the different curves, there are significant differences in ε_f values depending on the steel grade. When LFCS and Telby steels are compared, it results that the addition of Bi and Te has a deleterious effect on ductility. Furthermore, the tests done with samples machined from external (05) and internal (30) areas of the blooms, in both LFCS and Telby steels, indicate that the lower ε_f values correspond to the inner regions (less numerous and larger inclusions). The higher values of ductility correspond to 1150ºC and 1 s⁻¹. A summary of fracture strain obtained by interrupting and quenching samples is shown in Table 12 above.

Increase in ductility in the wrought condition can be observed in Fig. 106 compared to as-cast results, irrespective of temperature. In the case of LFCS and Telby steels, the samples taken from the corner are slightly more ductile than those from the interior. On the other hand, the ductility of samples taken in the transversal section is very similar to those measured with specimens from the as-cast material, except for the CSM 9SMN28 grade.

1150ºC Tested temperature 1050ºC
Corus LFCS steel
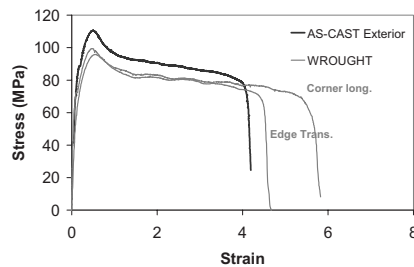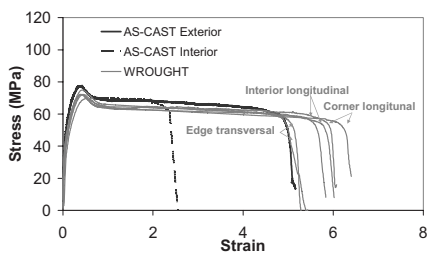
Corus Telby+ steel
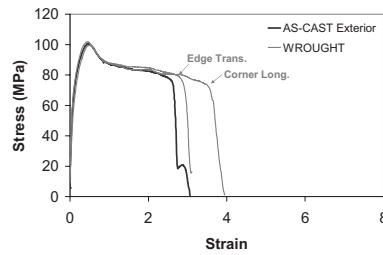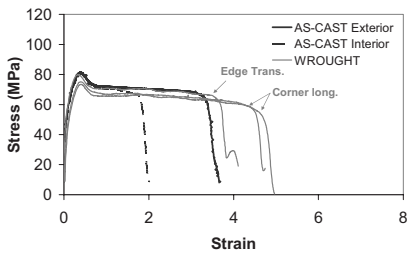
Sidenor 9SMnPb30 steel

CSM 9SMn28 steel

90
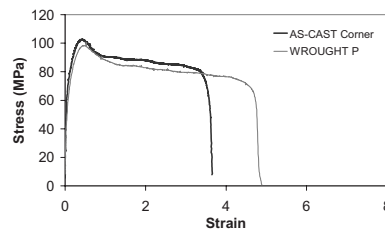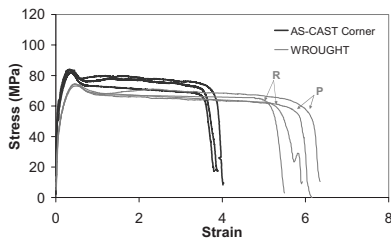
Fig. 106: Comparison of ductility between as-cast and wrought state at different positions at 1 s^{-1}

(ii)   Torsion (Ascometal)

The following tests were carried out as shown below. Torsion was used to assess strain @ rupture as well as providing stress-strain data for fitting constitutive models (see example 100Cr6 Fig. 105(b)).

	100Cr6	32MnS5Pb	32MnS5Bi	9SMn28 (CSM)
Torsion test	16 samples 900-1200°C 1 and 10 s^{-1} constitutive data	8 samples 900-1000-1100-1200°C 7.4 and 0.36 s^{-1} strain at rupture	8 samples 900-1000-1100-1200°C 7.4 and 0.36 s^{-1} strain at rupture	

Strain at rupture obtained for different temperatures and different strain rates were recorded for both Bi and Pb grades (Fig. 107(a)). These tests highlight a ductility trough for decreasing temperatures for the 32MnS5Bi. In addition, the ductility seems to be slightly better for the higher strain rates. Results obtained with the 32MnS5Pb were more difficult to interpret due to inherent ductility of this grade (thermocouple broke prior rupture therefore tests could not be exploited). Constitutive models were also fitted on all grades (Fig 107(b)) using an inverse analysis module Tormatic [52]. Tormatic is based on the Fields and Backofen theory [53].
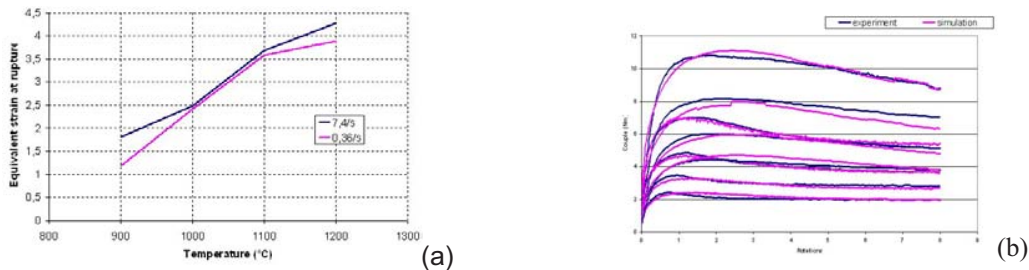
Fig. 107(a and b): (a) Equivalent strain at rupture obtained for the 32MnS5Bi from torsion tests
(b) Examples of constitutive model fitted to torsion torque/twist data (100Cr6)
according to procedure [52]

(e)   Strain path (reversal torsion testing) (CEIT)

Strain reversal tests have been carried out under hot torsion mode with steels LFCS 1/05 and 1/30, Telby 20/05 and 9SMn28. The objective of the multipass strain reversal test was to evaluate the influence of strain path on the damage evaluation in comparison to monotonic conditions. In the tests one pass is given at a defined strain (ε_{ip} = 0.25 or 0.5) followed by a certain holding time (t_{ip} = 0 or 5 s) before applying the same strain value in the reverse direction. This procedure is repeated, modifying the total number of passes (4, 8 or 16) and the time between passes. After the application of the last pass, the samples were water quenched in order to analyse the microstructural damage. Temperature and strain rate have been maintained constant during all the process at 1150ºC and 1 s^{-1}, respectively. Analysis of critical strain for DRX was carried out prior to strain path experiments. ε_c = 0.3 critical strain at onset of dynamic recrystallisation (RDX) (obeying the relationship, $\varepsilon_c = a \cdot \varepsilon_p$ (a = 0.76 in these steel grades)), was assumed (case of LFCS steel), 0.28 for Telby).

91

Figure 108(a) shows an example of flow curves corresponding to 4 passes in LFCS 1/05 (ext.) steel. By the shape of the curves it can be concluded that 5 s between passes is enough time for a completely matrix softening through static recrystallisation (SRX). The same occurs in the case of LFCS 1/30 (int.) and Telby 20/05 (ext.) steels, but regarding 9SMn28 heat, as can be seen in Fig. 108(b), neither $t_{ip} = 5$ nor 10 s are enough time for a complete softening.
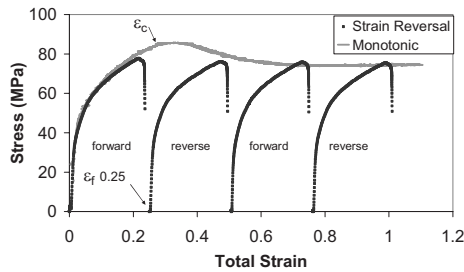
Fig. 108(a): Flow curve of strain reversal test with 4 passes, $t_{ip} = 5$ s $\varepsilon_{ip} = 0.25$, T =1150ºC and 1 s^{-1} (LFCS 1/05)
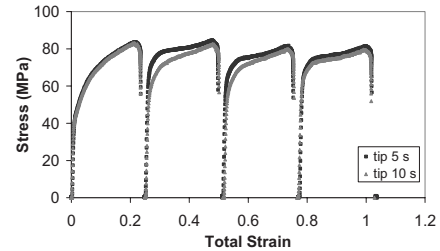
Fig. 108(b): Influence of interpass time in the stress-strain curves, $\varepsilon_{ip} = 0.25$, T=1150ºC and 1 s^{-1} (9SMn28)

Metadynamic recrystallisation occurs when the prestrain exceeds the critical strain for DRX (e.g. 0.5).

Flow curves of tests with no holding time between passes are shown in Fig. 109(and b). At those conditions, the effect of reversing the strain during the deformation becomes more evident than in the case of $t_{ip} = 5$ s with complete SRX between passes. Just after the first reversal the Bauschinger effect [54-57] is observed, the stress rises to reach a stress level lower than the pre-stress, followed by a "yield stress plateau" as a result of a decrease of the work hardening rate. After the plateau the stress begins to increase again because of strain hardening. The length of this plateau depends on the previous applied strain, the higher is the previous strain the longer is this plateau. It is possible to define two different parameters as can be seen in Fig. 109(a): ε_{plat} is the region with constant stress values [58] and ε_{BAUS} is the strain necessary, after the reversal, to reach the maximum stress (σ_f) in the previous pass. Another parameter is β_σ, the drop of tension observed after the reversing [59].
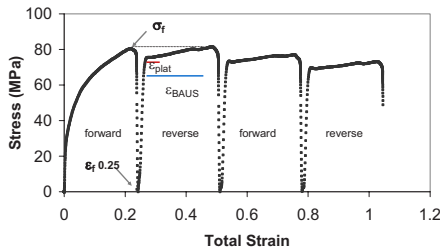
Fig. 109(a): Flow curves of strain reversal test of LFCS ext with no interpass time and $\varepsilon_{ip} = 0.25$
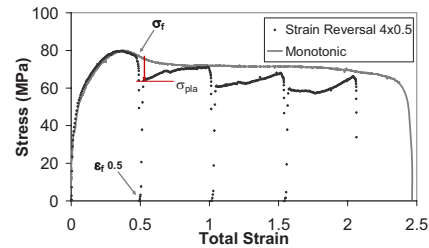
Fig. 109(b): Flow curve of strain reversal test of LFCS int with no interpass time and $\varepsilon_{ip} = 0.5$

Finally, another series of tests were carried out to evaluate the influence of the previous strain path in the final ductility. The specimens were tested with 4, 8 and 16 reversal passes followed by an additional monotonic pass until failure happened as shown in Table 13 below and Fig. 110 (last pass). No major influence can be observed on the LFCS as-cast external surface.

Table 13: Multipass strain reversal test followed by monotonic test until failure (T = 1150ºC and 1 s^{-1})

Steel	Nº passes	Strain per pass ε_{ip}	Interpass time t_{ip} (s)	ε_f
LFCS 1/71 Exterior	4+1	(4 x 0.25)+Failure	5	3
	8+1	(8 x 0.25)+Failure	5	3.2-3.5
	16+1	(16 x 0.25)+Failure	5	2.9
	8+1	(8 x 0.25)+Failure	0	4.2-3.3
LFCS 1/06 Ext.	4+1	(4 x 0.5)+Failure	5	3.2
LFCS 1/30 Int.	16+1	(16 x 0.25)+Failure	5	1.1
	8+1	(16 x 0.25)+Failure	5	1
LFCS 1/31 Int.	8+1	(8 x 0.25)+Failure	0	-
	4+1	(4 x 0.5)+Failure	5	0.5
Telby 20/05 Ext.	8+1	(8 x 0.25)+Failure	5	2.4
	4+1	(4 x 0.5)+Failure	5	2
9SMn28	16+1	(16 x 0.25)+Failure	5	1.9
	8+1	(8 x 0.5)+Failure	5	1.5
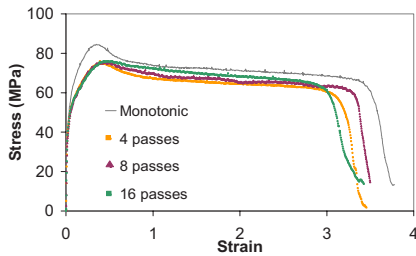
Fig. 110: LFCS external Comparison of the final failure between monotonic test and samples with 4, 8 and 16 previous strain reversal passes

Effect of sample positioning (MnS size) has also been studied in strain reversal torsion test. Figure 111(a and b) shows final failure between monotonic tests and reversal for both external and internal LFCS as-cast structure. Little effect of reversal at external surface compared to internal where inclusions are larger. Low interpass time reduces strain to failure.
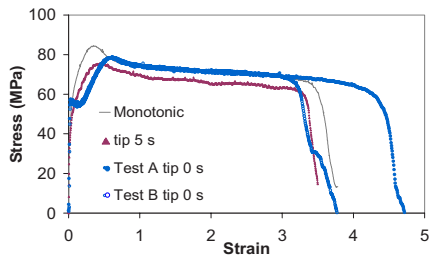
LFCS exterior (a)
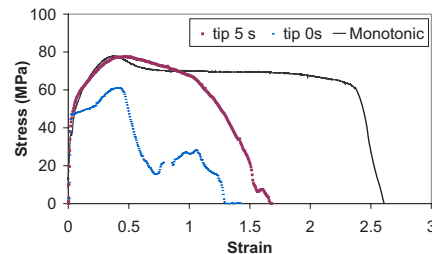
LFCS interior (b)

Fig. 111(a and b): Comparison of final pass stress-strain curves between a monotonic test and samples with 8 previous strain reversal passes considering different interpass times

Ductility of LFCS external steel seems not to be affected if the strain per pass is higher (0.5) whereas samples from LFCS interior and Telby steels show a reduction in ε_f in the case of 4 reversals @0.5 strain (Fig. 112). This probably means that the damage in inclusions after 4 passes (4 x 0.5) is higher than in the case of 8 x 0.25, and therefore damage is numceated faster as strain increases during each reversal (above the DRX). **This also confirms that multiple cycle of DRX has a negative influence on damage. Mostly as inclusions are large (Fig. 112).**
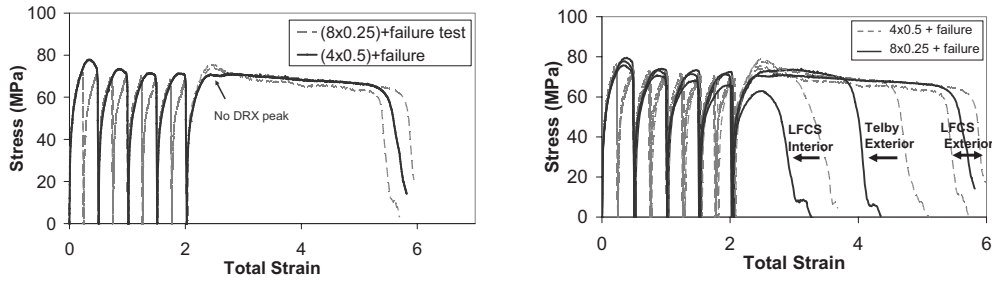
Fig. 112(a) Strain reversal curves of LFCS ext. steel, with ε_{ip} = 0.25 or 0.5, followed by final failure (1150ºC and 1 s⁻¹)

Fig. 112(b): Strain reversal curves, ε_{ip} 0.25 or 0.5, followed by final failure (1150ºC and 1 s⁻¹)

In summary, samples taken from the exterior of the bloom LFCS, with smaller MnS inclusions, show less influence of the previous strain path in the final ductility. On the other hand, at the same conditions of number of passes, ε_{ip} and t_{ip}, the final ductility of the different steel grades shows the same tendency that in the case of single monotonic tests. That is, LFCS ext. shows the higher ductility followed by Telby ext. and finally LFCS int. **Therefore this again confirms that larger inclusions are more affected by the deformation.**

(f)   Stress Relaxation test for recrystallisation kinetics 9SMn28 wrought (CSM, Oulu University [9])

Specimens were reheated at 10°C/s to 1150°C, held 2 minutes for soaking, cooled at 5°C/s to the deformation temperature and then deformed up at two strains 0.2 and 0.6 at temperature in the range of in the range 1150 – 900°C. The deformation was followed by stress relaxation. These data were used to determine the time for 50% volume fraction of metadynamic (MDRX) and static (SRX) recrystallisation defined below:

$$MDRX: \qquad t_{50} = 2.43 \cdot 10^{-3} \cdot \dot{\varepsilon}^{-0.784} \cdot \exp(57000 / RT)$$

$$SRX: \qquad t_{50} = 1.2 \cdot 10^{-11} \cdot \dot{\varepsilon}^{-0.134} \cdot \varepsilon^{-2.8} \cdot D^S \exp(176500 / RT) \qquad \ldots (A3.12)$$

$$s = 2.13 \cdot D^{-0.105}$$

where T is the temperature in °K and D the grain size in microns.

These data have been used to assess recrystallisation kinetics during billet rolling at Ori-Martin (Table 14) and have been incorporated into Constitutive damage models.

Table 14: Recrystallisation kinetics prediction Ori-martin plant (CSM)

Stand	AR [%]	Speed [m/s]	Nominal conditions on entry			Computed status on stand entry				pass			
			Tc [°C]	Ts [°C]	Interstand time [s]	Xc	$\varepsilon_{res,c}$	Xe	$\varepsilon_{res,e}$	$\varepsilon_{dyn,c}$	$\varepsilon_{dyn,e}$	ε_c	ε_e
R0	22	0.78	1049	1030	Furnace-R0= 5	0	0	0	0	0.63	1.14	0.37	0.90
R1	20	0.16	1042	940	R0-R1=7.2	1.0 SRX	0	1.0 SRX	0	0.32	1.32	0.38	0.74
R2	21	0.20	1046	930	R1-R2=7.3	1.0 MDRX	0	1.0 SRX	0	0.31	1.09	0.35	0.53
R3	20	0.34	1048	931	R1-R2=8.1	1.0 MDRX	0	0.9 SRX	0.07	0.35	1.04	0.58	0.94
R4	29	0.35	1051	935	R1-R2=5.4	1.0 MDRX	0	1.0 SRX	0	0.31	1.03	0.68	0.98
						1.0 MDRX	0	1.0 SRX	0				

(g) **Double hit RPS compression testing (Corus) – Te, Telby+ and LFCS steels**

Double hit compression testing (26 tests) using the RPS specimen geometry has been carried out to study the influence of static recrystallisation on healing on damage. A series of tests involving total deformation up to 50% were carried out at both 880°C and 1200°C with interpass time up to 10 s on both Te, telby+ and LFCS as-cast structure. Strain rates involved covered the range of 0.1 and 1 s^{-1}. Compression schedule is shown in Fig. 113 and involve pre-heating/soaking to 1200°C for austenitisation/homogeneisation, cooling to deformation temperature (880°C case only), reheating to 1000°C to promote RX (RX case only when deforming at 880°C), then cooling/deforming at 880°C for the second hit.

Forced air cooling was also used to check structure after first hit. Two hits of 20% each were carried out and compared with a single deformation of 36%. Two hits of 29% each were carried out and compared with a single deformation of 50%.
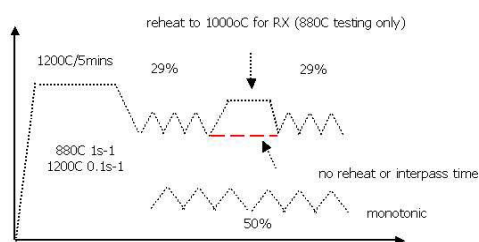
Fig. 113: Double hit RPS compression schedule
(Corus)

Microstructural results are shown in WP5 but it was concluded that large interpass time at high temperature can be detrimental to further crack opening and is further accelerated as temperature increases and strain rate decreases.

3.3.3.3.2 HT steel mechanical testing (Mefos, Ascometal)

(a) **Uniaxial compression testing (Mefos) Rock drill 4HS64– Dual phase (inc. high Sulphur)**

Upsetting trials were performed in the open-die forging press at MEFOS as no cracking was achieved during rolling for the rock drill steel (see WP4). Cylindrical specimens of 46 mm diameter, 46 mm and 69 mm length were cut-out from round bars of rock-drill steel from Sandvik Materials Technology. Conditions for rock drill steel were as followed (Table 15).

Table 15: Upsetting conditions Rock drill 4HS64 (Mefos & benchmark model)

Trial 4HS64				Initial length	Final length	Measured dimensions				
No	Material	Dia-meter	Furnace-temp	L0	L1	Outer diam	Inner diam	Remark	Strain	Strain rate
1	Rock-drill	46	950	46	21	69,8	61,2		0,78	1,57
2	Rock-drill	46	1050	46	21	70,2	61,2	(a) Two visible cracks	0,78	1,57
3	Rock-drill	46	1150	46	21	70,8	61,7		0,78	1,57
11	Rock-drill	46	950	69	23	82,7	71,8		1,10	1,19
12	Rock-drill	46	1050	69	23	82,9	72,3		1,10	1,19
13	Rock-drill	46	1150	69	23	83,2	72,2		1,10	1,19

Conditions for dual phase steel high sulphur are shows below (Table 16). Those for the dual phase steel with lower S content were carried out on cylinders of initial height of 55 mm (reduced to 26 or 27 mm). Little cracking occurred, except for one trial at 1050°C (bar 22). In total 21 tests were carried out.

Table 16: Upsetting conditions dual phase (Mefos)

Upsetting trial No 2, may 2007					Initial length	Final length	Measured dimensions	
Trial								
No	Material	Pos	Diameter	Furnace temp	L0	L1	Outer diam	Inner diam
51	Two-phase, S+	"3"	46	950	46	21	70,4	60,8
52	Two-phase, S+	"3"	46	1050	46	21	73,4	61
53	Two-phase, S+	"4"	46	1150	46	21	73,2	62
54	Two-phase, S+	"4"	46	950	46	21	78	67,6
55	Two-phase, S+	"5"	46	1050	46	21	74,1	64
56	Two-phase, S+	"5"	46	1150	46	21	74,3	64,4
57	Two-phase, S+	"3"	46	950	69	23	82,7	72
58	Two-phase, S+	"4"	46	1050	69	23	84,3	74,5
59	Two-phase, S+	"5"	46	1150	69	23	86,3	73,8
61	Two-phase		46	950	46	21	71,7	61,8
62	Two-phase		46	1050	46	21	72,5	61,2
63	Two-phase		46	1150	46	21	73,2	61,4
64	Two-phase		46	950	69	23	85,7	74,2
65	Two-phase		46	1050	69	23	83	70,4
66	Two-phase		46	1150	69	23	85,1	72,9
No	Remarks:							
51	Very rough surface, tendency towards cracking.							
52	Rough surface. Several cracks, one of them large.							
53	Rough surface. Several large cracks							
54	Rough surface. Some small cracks							
55	Rough surface. Several small cracks							
56	Rough surface. Several deep cracks							
57	Rough surface. Some small cracks							
58	Rough surface. Several deep cracks							
59	Rough surface. Some small cracks							
61 - 66	Smooth surface without cracks							

Visible cracking only occurred on one of the test-pieces, see Fig. 114(a). The calculated max value of the Cockroft-Latham cracking criteria for trial no 2 is 0.45.

Fig. 114(a and b): (a) Rock drill upsetting compression trials – case 2
(b) dual phase higher sulphur (Mefos)

(b)   Large scale Corus RPS compression testing (Mefos) (rock drill 4HS64)

Six pieces of diamond shaped geometry dimension 200x150x100 mm were machined according to Corus design (Fig. 115) and in one of the pieces (piece no 1) a thermocouple was inserted. The pieces were heated in a laboratory furnace to 1260°C. The corners of the pieces were spot cooled on one corner with high pressure water during 65 s to a temperature of 600°C below the surface. Only half of each test-piece sample was sprayed and the other half remained as uncooled reference. Then they were reheated, slowly cooled and upset to different final heights according to the schedule in Table 4. Cracking occurred for all test-pieces on the cooled end of the test-piece. No cracking occurred on the uncooled end. It can be seen that the geometry of the test-piece ends changes with the cooling applied. When only heavy cooling is applied before the forging stroke the typical 45 degree cracking pattern for cold material appears, see Fig. 115(b-e). When the testpiece is reheated or slowly cooled before

forging, the end-material is more ductile. The cracking pattern changes to a point geometry. The crack reaches to around 10 mm inside of the material.

Piece	Spot cooling	Reheating	Cooling in Kaowool	Final dimension	Cold side cracks
1	X			40 mm	Complete 45° crack
2	X			50 mm	Complete 45° crack
41	X	5 min		40 mm	Big crack - mid edge
42	X	5 min		40 mm	Minor crack - mid edge
43	X		10 min	40 mm	Half 45° crack
44	X		10 min	50 mm	Small point crack -edge

Fig. 115(a-e): (a) RPS large scale specimen (b, c) front and length cut Piece 2
(d,e) front and length cut Piece 41 - rock drill 4HS64 (Mefos)

(c)   PSC testing 100Cr6 steel (Ascometal)

Two PSC tests using the press shown in Fig. 81(h) were carried out on 100Cr6 steel according to conditions described below

Test number	Temperature (°C)	Grade	Cast	Shim high (mm)	Heading speed (mm.s^{-1})
PSC9	900	100Cr6	69524	6.5	700
PSC10	900	100Cr6	69524	12.5	700

As for the HCLI test, the PSC test did not generate any cracking on surface sample.

(d)   Hot Crack Limit Index (HCLI) 100Cr6 steel (Ascometal)

This test (see Fig. 85(f)) has been initially selected in view of its similarity to rolling with respect to strain and triaxiality (Fig. 116).
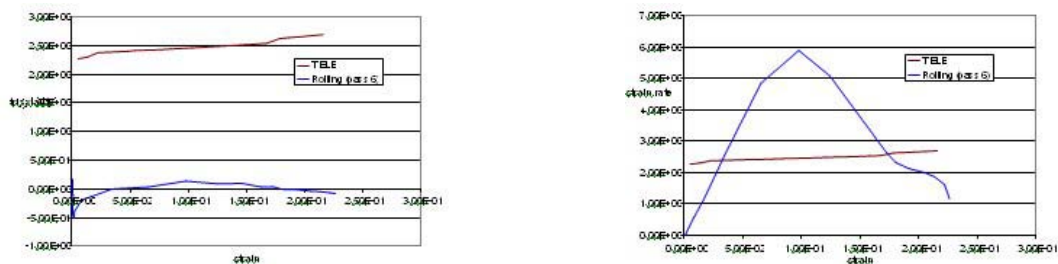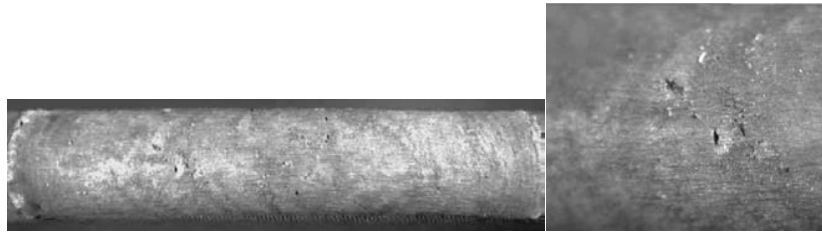
Fig. 116: HCLI test 100Cr6 (Ascometal)

Test Number	Temperature (°C)	Grade	Cast	Shim high (mm)	Heading speed (mm.s^{-1})
TEL7	630	100Cr6	81530	2	700
TEL8	630	100Cr6	81530	2	700
TEL9	630	100Cr6	81530	2.1	350
TEL10	630	100Cr6	81530	2.1	700
TEL11	830	100Cr6	81530	2.1	700
TEL12	830	100Cr6	81530	2.5	700
TEL13	830	100Cr6	81530	2.5	700
TEL14	830	100Cr6	81530	2.5	700
TEL15	830	100Cr6	81530	2.9	700

Even though this test induces a large triaxiality, it was necessary to reach a high strain (higher than 200%) in order to observe superficial cracks. This is not surprising since the 100 Cr6 grade does not contain a high fraction of inclusions (which are nucleation sites for damage). The probability to find such inclusion distribution or defect close to the skin is very low on a laboratory sample. It is therefore difficult to use this grade for developing damage criteria. Ascometal concluded that the 100 Cr6 steel grade was not very sensitive to cracks without the presence of an external and initial defect that increases the local stress and therefore focused their subsequent effort and resource on FCS steels.

(e)   Torsion testing 100Cr6 steel (see description within FCS Torsion testing) (Ascometal)

3.3.4   WP4: Laboratory rolling

3.3.4.1 Study of effect of cortical (chilled) zone - LS30Bi and 9SMn28 steels (CSM)

Experiments were made on the reversible laboratory Danieli mill (475 mm roll diameter) to investigate conditions leading to cracking under flat rolling conditions (Table A.1). Both surface and bulk temperatures were recorded during reheating (bulk only)/rolling following removal of primary oxide scale. Cracking in these flat rolling experiments was only observed for deformations of the order of 60%, value which although globally unrealistic can be achieved locally at stock edges during bar rolling. Two steel compositions were studied (see WP1), wrought LS30Bi and the benchmark grade as-cast 9SMn28.

- **LS30Bi:** various decorticated medium C Bi steel feedstock was rolled according to conditions shown in Table A.1. Effect of reduction and temperature was studied and showed that at 30% reduction, no cracking could be induce for the range of temperature (inc. trough) considered. Increasing reductions up to 50% to worsen edges, no cracking again could be induced. Looking at effect of holding time and very high reduction, extending reheating/soaking times (Bi22-Bi23) resulted in excessive Bi diffusion and losses, producing the typical granular network on the stock surface (Fig. 117(b)). However, the rolling even at heavy 60% reductions to induce critical conditions at the edges did not produce severe cracking (Bi22-Bi23, Fig. 117(d)). This result contrasts with the cracking under similar rolling conditions (Fig. 117(c)) but after a shorter 50' reheating at 1100°C and shows the worsening of workability due to hot embrittlement induced by the presence of Bi. It is interesting to note that almost no defects were found in the industrial mill at similar thermal conditions, and this can be attributed either to the different tensile/compressive cycles underwent by the feedstock along the bar rolling line or to its pre-rolling status (WP1). The

defects always appeared in the edges and at the faces retaining the original cortical structure and never on the machined surfaces, included the one being rolled (Fig. 117(a)).
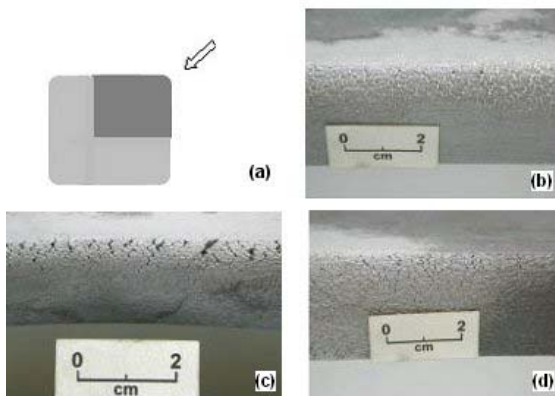
Fig. 117(a-d): Experimental flat rolling of LS30 feedstock: (a) geometry used; (b) effect of extended reheating (Bi23, 5 h at 1200 °C) prior to rolling and (d) after rolling at 1048 °C, 60 % reduction; (c), rolled at 1025 °C, 70 % reduction after 50' at 1100 °C reheating.

- **9SMn28**: different cortical zones down to the complete elimination of its original casting thickness (hco of mean value 5 mm) were trialed. This had also the result of exposing different MnS particle/grain sizes to the surface to be rolled. Cracking was investigated by visual inspection of the rolled specimens, metallographic analysis of selected areas and for the Set 2 experiments by using X-rays screening of the whole bar that detects defects wider than 0.25 mm.
  - Set 1 experiments use the original as-cast cortical zone and two reheating temperatures 1190 and 1110°C. The 2-3 rolling passes at temperatures ending in a range from 925 to 1011°C with reductions from 20 to 40% did not produce any cracking.
  - Set 2 experiments were based on removing the original chilled zone by 4 mm leaving 1 mm of original cortical zone in one to and 8 mm from the surface. Two reheating temperatures 1050°C and 1190°C were used and the specimens rolled at 960°C (corresponding to the low ductility temperature under tension) and at 1110°C in single passes of 15 and 25 % reduction. The aim was to detect whether in the previous experiments cracking had occurred and closed because higher reduction or consecutive passes, but the results were also negative.
  - Set 3 experiments were made on bigger stocks having the cortical zone completely removed, exposing the columnar dendritic zone and larger MnS particles to the rolling surface. They were heated to 1090°C with intermediate reheating after two 15 % reductions. The experiment showed profuse surface crack formation on one side of the rolled surface but no edge cracking, for rolling at temperatures ending in a range from 980 to 1027°C (Fig. 118). The zigzag line pattern of these defects and its location on an area that had been under the rolling pressure suggests one of the weak dendritic regions of the as-cast bloom was exposed.
  - Set 4 were 60% partial rolling experiments, made after removing a layer hc from the as-cast bloom skin to leave several thickness of cortical zone but also its complete elimination. Reheating temperatures from 1100°C to 1190°C were used and the nominal rolling temperature was achieved by varying the holding time prior to rolling, with resulting core temperatures between 960°C and 1150°C and surface temperatures 900 to 1040°C. The results show:
    - (i) The worst cracking appeared after removing hc=13 mm onwards. Both edge (Fig. 10(a)) and rolled surface (Fig. 118(a)) cracking are very sensitive to rolling temperature, the greater generation occurring at 956°C, in agreement with the low tensile ductility results at this temperature (Fig. 92(b)).
    - (ii) The cortical thickness and its uniformity, together with small sized MnS precipitates has a drastic effect in crack prevention. For a given rolling temperature, the thicker the cortical zone (Fig. 10(a)) the lower the edge cracking risk.
    - (iii) Both rolled surface and edge cracking appeared in conjunction with the starting of the lateral spread (Figs. 118(a) and 54). Given the absence of cracking in the previous set experiments, the results is attributed to higher influence of tensile stresses at the roll exit and edges for the larger 60% reduction.
    - (iv) Edge defects were in general short and deep and their type similar to the ones detected in the industrial line.

(v) Defects on the rolled surface developed as short lines, they appeared transversal to the rolling directions, were very shallow (Fig. 118(a)) and none of them developed a full line pattern like in the Set 3 experiments. The comparison of conditions at nearly equal hc removal of 13 - 15 mm from Sets 3 and Set 4, also suggests that interpass recrystallisation in the multipass first case has worsened cracking. This is in agreement with double hit RPS testing.
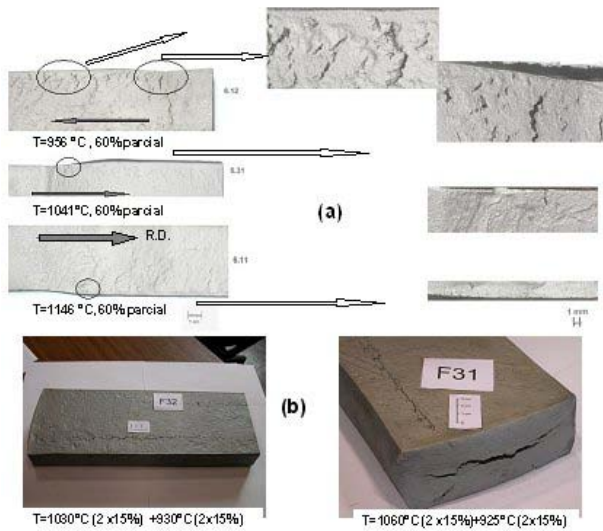
Fig. 118(a and b): Effects of temperature on rolled surface cracking of fully decorticated 9SMn28 steel blooms; (a) hc=30 mm, 60 % reduction one-pass partial rolling and (b) 4-passes x 15% full rolling

3.3.4.2 Study of effect of reheating time – ball bearing (Mefos)

Round bars were heated in Mefos laboratory reheating furnace for different times (up to 300 min) at 1100°C and 1180°C respectively. This was to study effect of delays which tend to increase the amount of surface cracking in industrial conditions. These bars were rolled in the continous 3-stand mill, however no cracking could be induced, despite internal oxidation (up to 0.1 mm) and decarburisation to a depth of 90 microns (Fig. 119). The aim was also to promote fayalite formation at temperature above 1177°C. The program Steeltemp was used to that effect for calculating temperature profile in the furnace [60]. These results show that the rock-drill steel has a very high ductility despite the presence of Cr oxide, decarburisation and oxidation at surface. It was concluded that the industrial reheating atmosphere is key to promoting embrittlement which is difficult to replicate in a Laboratory furnace.
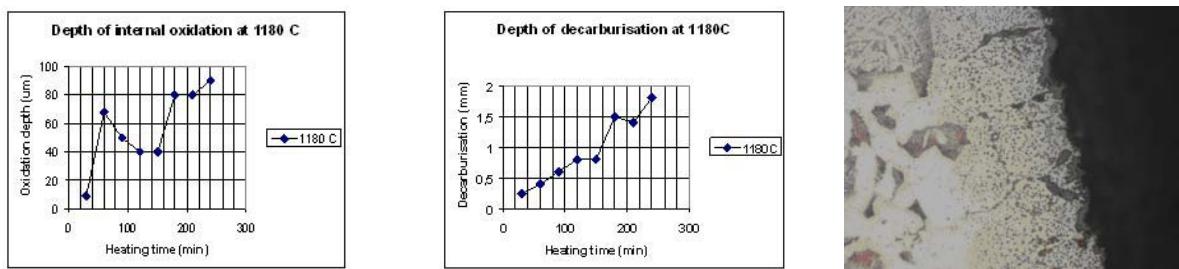
Fig. 119: (from left to right) Depth of internal oxidation and decarburisation as a function of heating time, with oxide precipitation (Cr oxide) and oxidation (extreme right)

3.3.4.3 Study of effect of heat treatment/thermal history on bloom surface– ball bearing 4HS64 (Mefos – Ovako Imatra)

4HS64 as-cast blooms from Ovako Imatra (310*370 mm) were obtained and prepared (machined into 4 pieces) to study effect of thermal history at bloom surface induced by secondary cooling, AlN precipitation and reheating on the casting machine. All samples were reheated to 1280°C. This was considered as starting point for the as-cast structure. And sufficient to dissolve AlN precipitates. Water cooling at the beginning of casting line was simulated by pressurised water spraying (180 bars). Spray was aimed at the corner and its' surrounding as indicated in Figs. 6 and 120. Each bar was then rolled in two passes between flat rolls. The surface temperature was measured with a radiation-pyrometer before the second pass and the rolling force in each pass was recorded. After the trials, the trial-bars were shot-peened and investigated using dye-penetrant method. However, no cracks could be detected on any of the trial-bars. The surface was rough with, in some cases, quite large irregularities. Manual grinding was then performed on the edges but no cracks could be detected.

Fig. 120: Mefos rolling trials of machined corner billets

In summary no cracking could be achieved even if the corner was cooled to below 600°C

3.3.4.4 Open square-oval-round – 3 high mill – Bi FCS (Corus)

Laboratory tolling on the experimental 3 high pilot mill was carried out using as-cast Bi-FCS 602M (PY04/29) steel (roll design1). Both 65 and 52 mm^2 bars were used from bloom surface (65 mm^2) and subsurface (52 mm^2). Furnace temperature was set to 1280°C, drop-out temperature at 1220°C and in all cases a reheating time of 120 min inc. 60 min soak was used.). Bars were rolled through an open square sequence with apex angle of 98/96° creating a rhombus section after 6 passes (Pocket P5 to P10, see Fig. 121). Cracking (transverse and longitudinal) could be observed only on two bars (40a and 40b), at exit of pass P11 and P15 (final round). All sections were etched and visually inspected
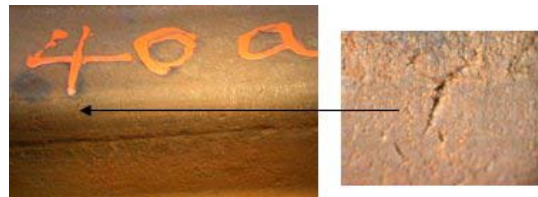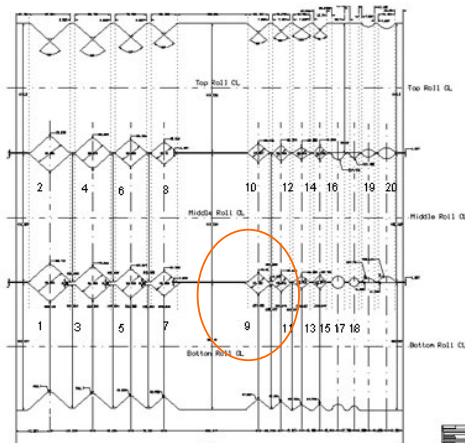
Fig. 121: Corus laboratory rolling trials – Bi –FCS steels – cracking at Pass 11

3.3.4.5 Laboratory rolling artificial defect –ball bearing steel - SKF803 (Mefos)

Trials with artificial cracks were conducted on ball bearing steels being rolled in the Laboratory bar mill at Mefos. Typical v-shaped crack were inscribed on 20 mm round bars which were rolled at 1000°C 1 m/s in two passes (Round-oval and then barstard round following 90° turn). The trials were designed as for the artificial crack to be positioned in the groove opening of the bastard-round pass. No further crack nucleation/growth could be promoted due to the presence of the artificial defect. FEM analysis was also conducted to check the Cockroft Latham damage value due to the presence of an artificial crack (Fig. 122).

Fig. 122(a and b): (a) Artificial V crack on round bars rolled at Mefos in two passes
(b) final crack after two passes (c) FEM damage (CL) after first pass

3.3.5 WP5: Microstructural characterisation

Characterisation has been carried out on:
- Solidification as-cast structure inc. oscillation marks.
- Assessment of grain size and grain boundary.
- Assessment of cortical zone.
- Detailed inclusion characterisation function of grades, feedstock and position, this involved of size distribution, mean size and number of MnS particles per unit area function of position, orientation, shape.
- Wrought structure.
- deformed structure following mechanical testing.
- deformed structure following rolling (laboratory, production).
- structure after reheating (HT steel).

Techniques involved: thermal etching, sulphur prints, optical, SEM, FEG-SEM, image analysis via use of SKIZ technique [15] and profilometry.

3.3.5.1 As-cast Structure FCS

All partners (Except Mefos and Ovako-Imatra) have characterised the bloom/billet as-cast structure with respect to cortical, columnar/dendritic and equiaxed zones. Figure 123(a) from CSM (case 9SMN28 steel) is a good representation of typical structure encountered. Cortical (chilled) zone varies from 5 to 10 mm. Figure 123(a) shows typical porosity at billet centre with associated voids and the presence of incipient cracks, which have been emphasised in white. These were as long as 20 mm, laying mainly along the diagonals of the section where dendritic grains growing at orthogonal directions meet each other. They were not oxidised, run along interdendritic boundaries and were arrested at about 7 mm from the bloom skin. Oscillation marks microstructure is shown in Fig. 123(b) with the three types identified.
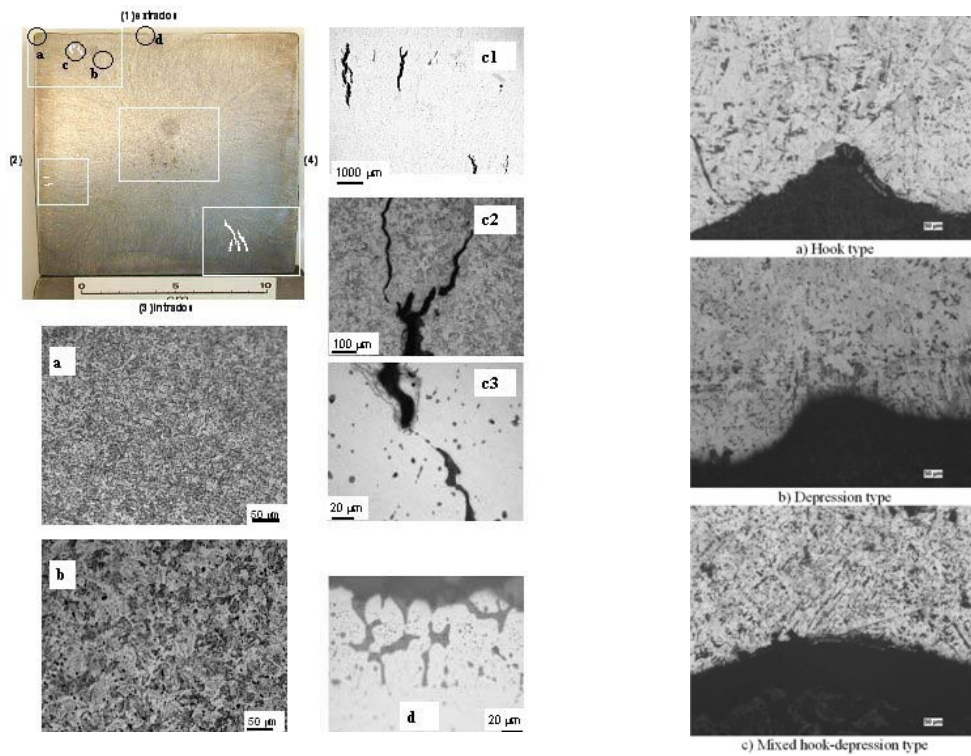
Fig. 123(a and b): (a) Solidification structure of 9SMn28 as-cast blooms: details
of grain size and incipient cracking on a section transversal to casting (CSM)
(b) Oscillation marks microstructure (Sidenor)

3.3.5.2 As-cast austenite grains and grain boundaries

Resulphurised steels show a limited grain growth when compared to other steels due to large amount of inclusions (although not very fine). Austenite grain size distribution is typically between 30 to 60 microns at standard reheating practices (max 1250°C) with a variation through thickness (larger grain size at billet core). Grain growth experiments were conducted to ascertain prior-austenite grain size following reheating/soaking. Figure 124 shows experiments carried out by Corus on Telby+ (PY04/20, bar 73 (bloom surface)) as-cast steel, for three austenitising temperatures of 950°C, 1200°C, and 1300°C. Initial as-cast grain size will affect recrystallisation kinetics (dynamic + static), as well as the ratio between inclusion size/distribution and grain size/boundaries. **The majority of the inclusions (>1 μm) are located at grain boundaries.** After reheating at 1150ºC, in steels LFCS 1/05, LFCS 5L, Telby 20/05, Telby 2L, 9SMnPb30 and 9SMn28 between 48 and 60% of the inclusions are located at grain boundaries, approximately half of them corresponding to triple points (Fig. 124(b-d)). In contrast, in the case of steel LFCS 1/30 and Telby 20/30 (inner parts of the bloom) 98% of the inclusions are at grain boundaries, with a fraction of those located at triple points between 78-80%.

103
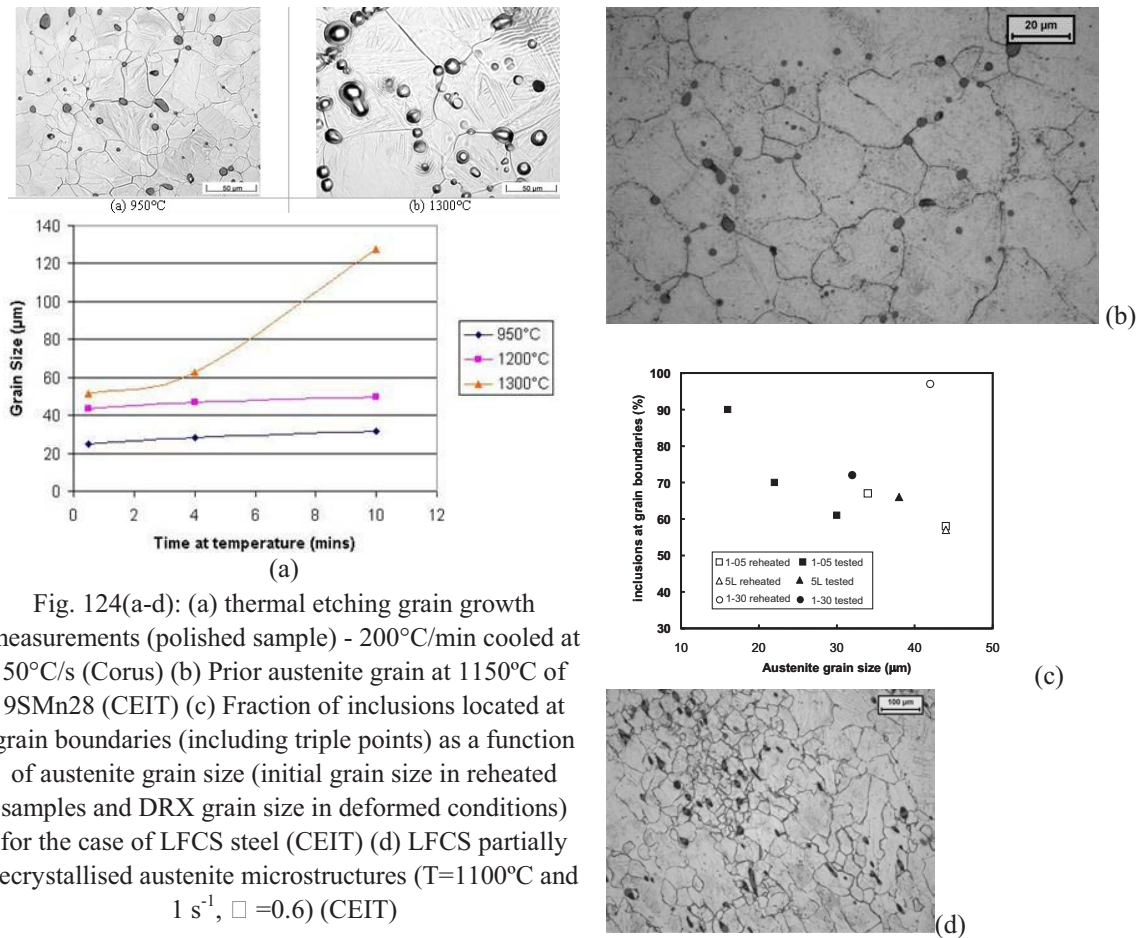
Fig. 124(a-d): (a) thermal etching grain growth measurements (polished sample) - 200°C/min cooled at 50°C/s (Corus) (b) Prior austenite grain at 1150ºC of 9SMn28 (CEIT) (c) Fraction of inclusions located at grain boundaries (including triple points) as a function of austenite grain size (initial grain size in reheated samples and DRX grain size in deformed conditions) for the case of LFCS steel (CEIT) (d) LFCS partially recrystallised austenite microstructures (T=1100ºC and 1 s^{-1}, $\square$ =0.6) (CEIT)

3.3.5.3 Inclusion characterisation in as-cast FCS

Inclusions coarser than 1 micron were characterised by the various Partners. For the steels considered (semi-killed), type I globular MnS inclusions are present in either monotectic or eutectic (MnS-MnO) form (see Fig. 19). Some complex biphasic inclusions can also form such as MnO·Al$_2$O$_3$·CaO (case of S2 and 9SMn28 Sidenor steel). A comparative view is shown in Fig. 125. Volume fraction of Pb inclusions has been also measured. In general, Pb appears as isolated particles or surrounding MnS inclusions. In the case of Telby grade Pb, Bi and Te have been quantified together.
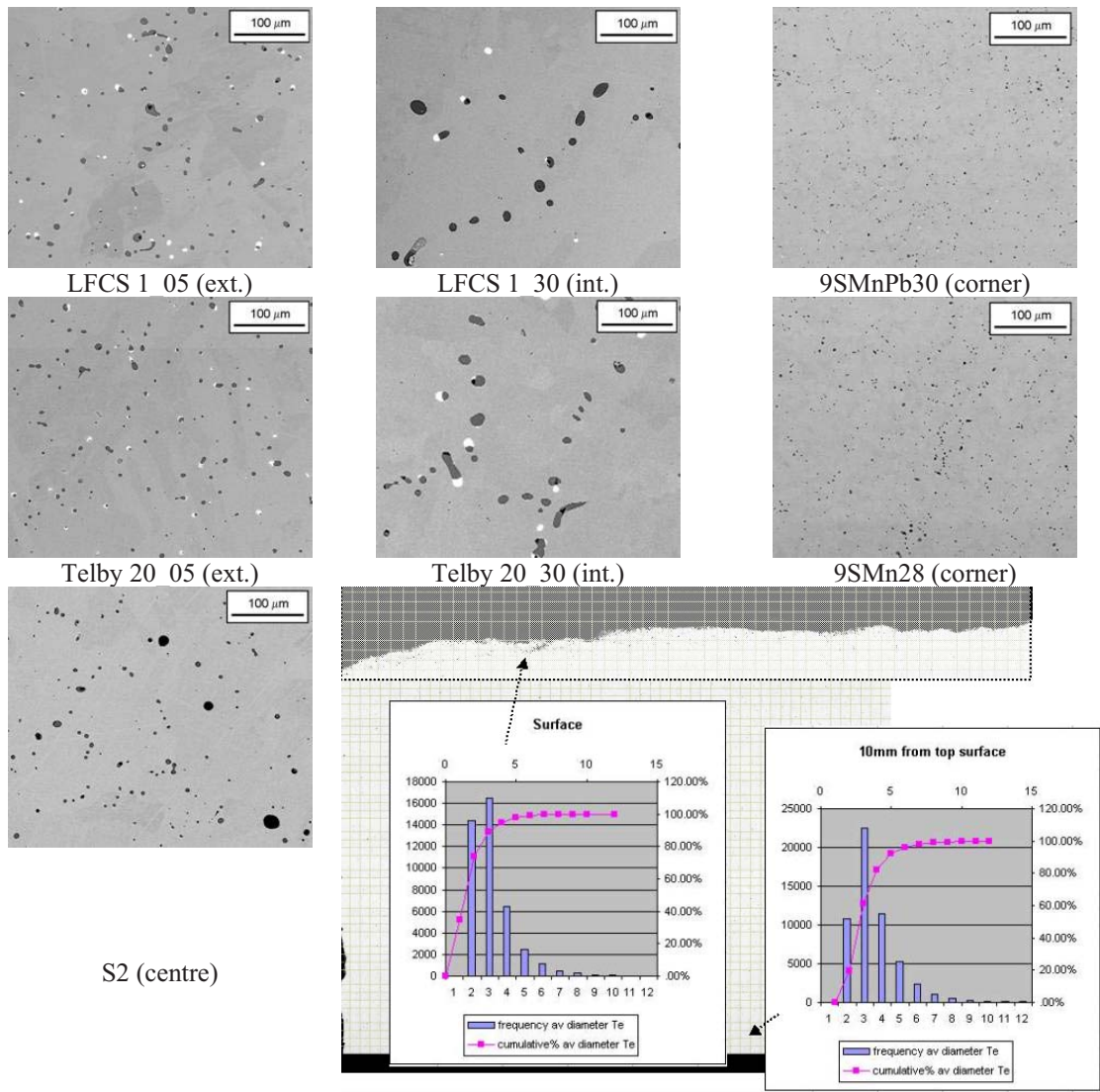
Fig. 125: MnS inclusion distribution in as-cast steel (CEIT, Corus Te-FCS)

Second-phase distributions were also characterised by using the skeletisation by influence zones (SKIZ) [15]. This technique consists of a tessellation of a planar region into cells based on the location of the inclusion centre. For 2D dimensions, each cell contains one inclusion, so that all points within this region are closer to the centre of the enclosed particle than to the centre of any other inclusion. The resulting tessellation is an aggregate of cells or influence zone whose dimensions are determined by the spatial arrangement of the particles. The sides of the cells are obtained from a set of perpendicular bisectors dividing the line segments that join each enclosed particle with neighbouring particles. Following this technique different parameters such as local area fractions, mean near and nearest neighbour distances between particles can be quantified. Figure 126 shows application of this technique on key FCS steels. Table 17 summarises key parameters which quantify the characterization of MnS inclusions. It shows significant differences in MnS inclusion mean size, ranging from 1.8 μm for the case of 9SMnPn30 steel to 8.8 μm in LFCS 1/05 (int.). On the other hand, the volume fraction shows less variation ranging from 1.3 to 1.8%. Therefore large differences in the number of inclusions per mm^2 are present for each specific grade. **Small influence zones are a reflection of inclusion clustering which is a key parameter for growth and coalescence of crack.** Local area fraction is defined as the ratio between the inclusion area and its corresponding influence zone area. High values of local area fraction are related to agglomerations of larger inclusions. The local area fraction values are between 1.3 and 1.7 times larger than the average value. The largest differences correspond to steels **LFCS 1/30 and Telby 20/30**, both samples taken from the inner part of the bloom.
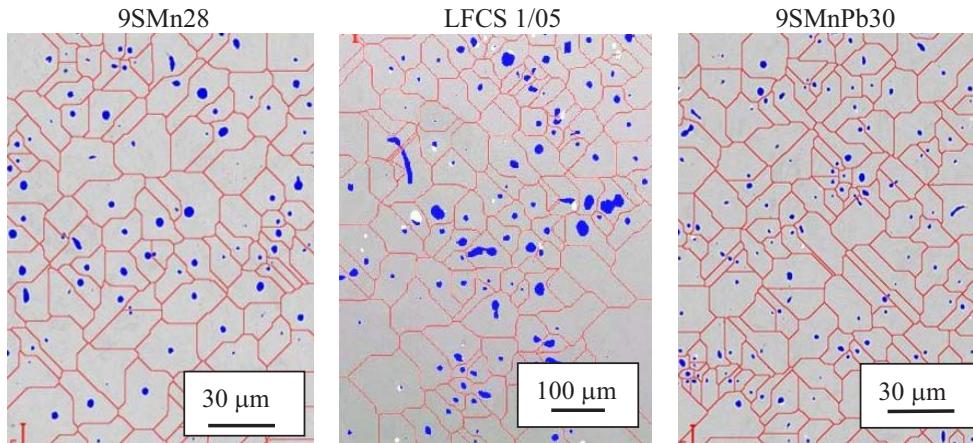
Fig. 126: Example of influence zones of the inclusion distribution in as-cast steels

Table 17: Characterisation of MnS inclusions by the SKIZ technique [15]

Steel	Mean size (µm)	Aspect ratio	Inclusion number per mm²	%fv MnS	%fv Pb	Mean Eq. diameter influence zone (µm)	Mean local area (%)	Mean nearest neighbour distance (µm)	Mean near neighbour distance (µm)
S2	3.7 ± 0.1	1.7 ± 0.1	1035 ± 60	1.4 ± 0.1	-	31 ± 0.6	2.1 ± 0.1	15.6 ± 0.4	33.4 ± 0.5
LFCS 1/05	4.2 ± 0.1	1.6 ± 0.1	760 ± 40	1.6 ± 0.1	0.3 ± 0.06	35 ± 0.7	2.1 ± 0.2	17.6 ± 0.5	36.3 ± 0.6
LFCS 1/30	8.4 ± 1	1.7 ± 0.1	220 ± 50	1.4 ± 0.2	0.3 ± 0.13	73.6 ±1.6	2.6 ± 0.3	33.8 ± 1.2	80 ± 1.6
Telby 20/05	4.2 ± 0.1	1.6 ± 0.1	900 ± 50	1.8 ± 0.1	0.4 ± 0.02	33 ±0.5	2.2 ± 0.1	17.6 ± 0.4	32.7 ± 0.5
Telby 20/30	8.6 ± 0.6	1.8 ± 0.1	310 ± 60	1.8 ± 0.2	0.3 ± 0.05	61.3 ±1.3	3.1 ± 0.2	32.2 ± 0.8	64.0 ± 1.2
9SMnPb30	2.1 ± 0.1	1.8 ± 0.1	4100 ± 700	1.3 ± 0.04	0.12 ± 0.14	15.5 ± 0.3	2.0 ± 0.1	7.6 ± 0.2	16.4 ± 0.3
9SMn28	2.3 ± 0.05	1.6 ± 0.1	3400 ± 200	1.5 ± 0.03	-	18 ± 0.4	2.6 ± 0.2	9 ± 0.3	19 ± 0.4

Other parameters that can be quantified with the SKIZ technique is the near neighbour distance, defined as the average distance between an inclusion and all those inclusions whose influence zone bounds its zone, and the nearest neighbour distance that is the shortest interparticle distance. Three different groups can be identified. The first group corresponds to steels 9SMn28 and 9SMnPb30 where smaller and more abundant inclusions were observed. Intermediate results correspond to samples with medium values of number and size inclusions, that is, S2, LFCS 1/05 and Telby 20/05, and finally, the longer distances were found in samples from the inner areas of the bloom with largest inclusions and minor number of particles per unit area (LFCS 1/30 and Telby 20/30). Values of mean near distance are double of nearest neighbour distance (Figs. 127-128).
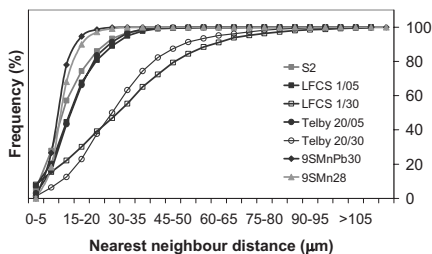
Fig. 127: Cumulative frequency of the nearest neighbour distances (CEIT)
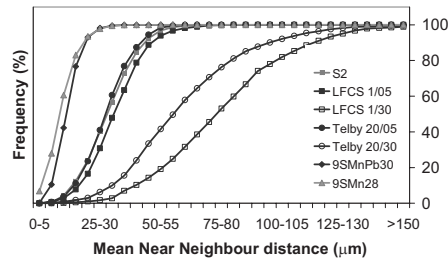
Fig. 128: Cumulative frequency of the mean near neighbour distances (CEIT)

Figure 129 summarises outcome of ductility versus mean local area fraction.
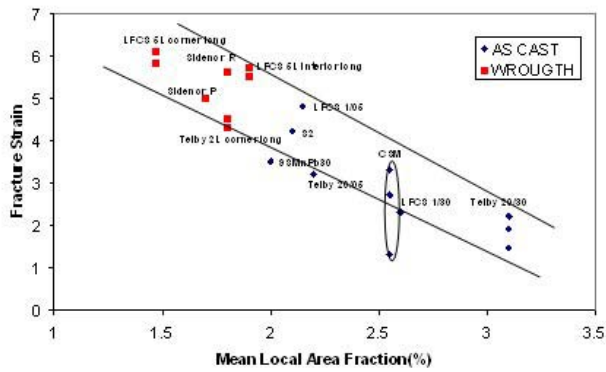
Fig. 129: Ductility (torsion) function of mean local area fraction (as-cast and wrought FCS) (CEIT)

Typical inclusion through-thickness profile is shown in Figs. 130(a and b) below. This should be combined with Figs. 22, 23, 25, 26 and 31 of the Extended Summary which give detailed information of cumulative plot of size, area, shape and orientation of inclusions in as-cast structure. At billet corner of the cortical zone (9SMn28 grade) MnS mean size is of 1-2 microns, with a very fine and homogeneous dispersion (T1). Their size increases towards the bloom centre, with values as large as 15 microns in the central porosity area (T6-T7). The heterogeneity of their distribution also increases towards the centre. The MnS precipitates are rather globular and decorate solidification grain boundaries. The central porosity reveals voids as large as 100 microns (Fig.130b).
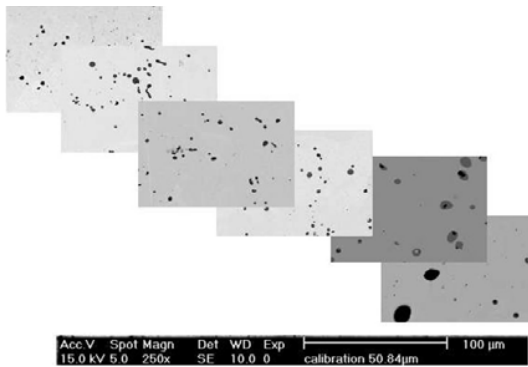
Fig. 130(a): LFCS steel (Corus) spatial distribution
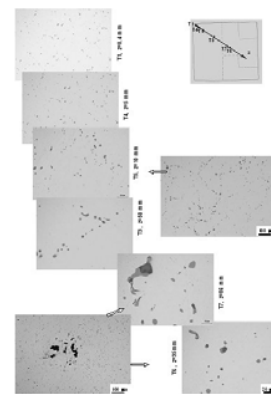
Fig. 130(b): 9SMn28 steel (CSM) spatial distribution

Similar results were obtained by Sidenor (Fig. 131). The range of concentration is large varying between 1657 inclusions/mm^2 and 3116 inclusions/mm^2 for 26540 9SMnPb28 and 1172 inclusions/mm^2 and 2871 inclusions/mm^2 for 28329 9SMn30. Spacing to diameter ratio was also assessed by Corus-Birmingham and shown in Fig. 132. This is a critical parameter which has been input into the constitutive model presented in WP7/Appendix2 and relates to Fig. 93(d).

Fig. 131: 26264 9SMnPb28 (Sidenor) distribution (corner/face)

Material location	Inclusion area	Mean inclusion diameter (d_{inc})	Mean distance between inclusion centres (l_{inc})	Sample size # Inclusions	$\left(\dfrac{d_{inc}}{l_{inc}}\right)^3$
P1	2.5%	15.2μm	41.8μm	1071	0.13
P2	2.8%	6.9μm	20.5μm	1002	0.11
P3	2.2%	3.1μm	10.1μm	2650	0.094

Fig. 132: Spacing to diameter ratio ω (Corus- Birmingham)

3.3.5.4 Characterisation of ductile damage mechanical testing (as-cast, wrought)

Each partner has characterised damage following mechanical testing. Damage characterised is intragranular (see page 6) with decohesion/nucleation at inclusion/matrix interface as well as grain boundaries (high temperature). New gauge length characterisation procedure [65] as the one by CEIT for torsion testing has been applied.

- Torsion testing (CEIT)

In this procedure all the specimen gauge length is considered (approx. 15 mm) taking 40 micrographs (x600) along its central region (in the subsurface plane). On each micrograph the void volume fraction (%fv) is measured with the help of image analysis software. Examples of the measurements obtained with S2 (CEIT) and LFCS 1/05 steels are shown as a function of the applied strain in Figs. 133-134. At low deformation levels the damage is scarce and appears homogeneously distributed along the specimen. The void volume fraction increases with applied strain. Finally at a deformation level close to failure (ε_f) the damage along the sample is higher, with evidence of the localisation of damage in some specific regions of the specimen.
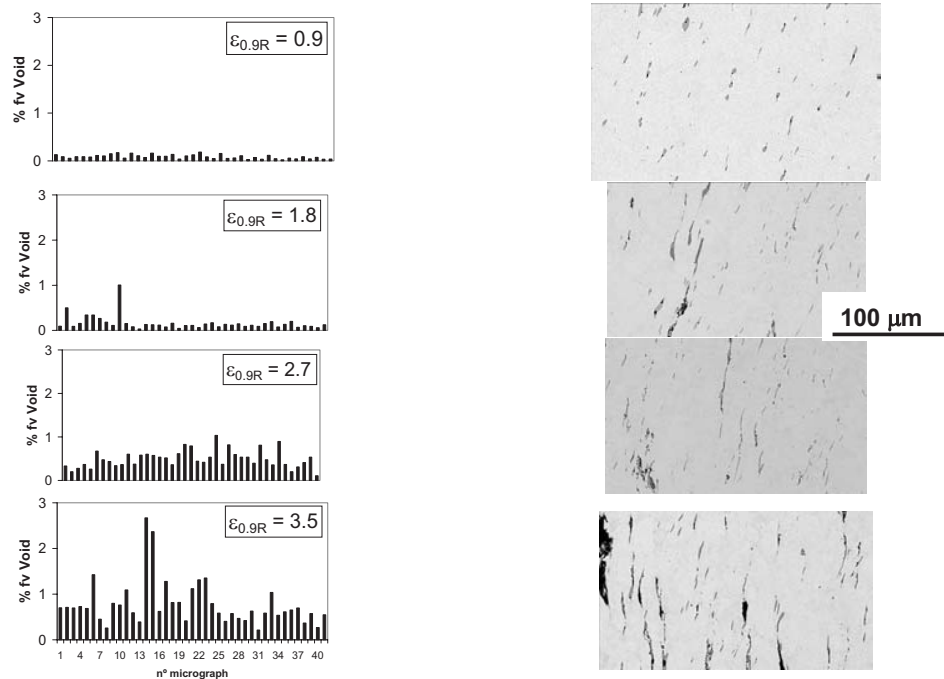
Fig. 133: Evolution of void volume fraction at increasing strain levels in steel S2 (ε_f =4.2) and micrographs showing different examples of void formation and coalescence

Fig. 134: Evolution of void volume fraction at increasing strain levels in as-cast steel LFCS 1/05 ext (CEIT)

The damage evolution function of strain is drawn-up in Fig. 135.

108
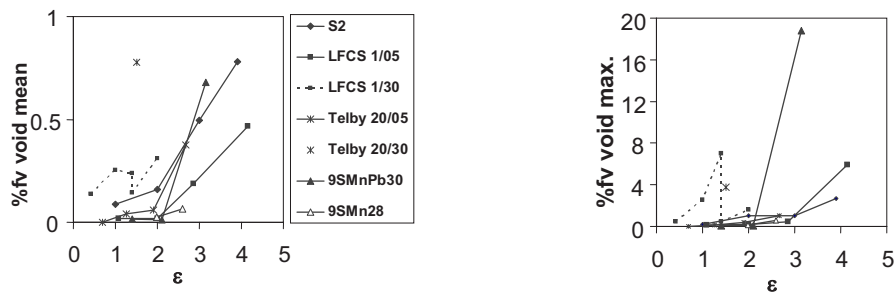
Fig. 135: Comparison of damage evolution at different strain levels (CEIT)

Characterisation of damage between as-cast and wrought structures (corner) is shown in Fig. 136. The specimens machined from the as-cast materials take failure at lower strain values than in the case of wrought conditions. In order to study the damage evolution some tests were interrupted at strain levels close to failure and the microstructure was observed in the subsurface section. This analysis showed that at a normalised strain of $\varepsilon/\varepsilon_f \sim 0.8$ there are some differences in the void volume fraction between samples from as-cast and from wrought materials. In the case of LFCS steel, the specimens machined from the corner of the wrought material (long. section), tested at $\varepsilon/\varepsilon_f = 0.7$ (total applied strain = 4.5), show elongated inclusions but there are not voids associated with these. When the applied strain increases to $\varepsilon/\varepsilon_f = 0.77$, the mean void fraction remains very small and close to 0.1% inclusions, as can be observed in Fig. 136.

As-cast ext. $\varepsilon/\varepsilon_f = 0.78$,
$\varepsilon = 3.75\%$fv void = 0.7

Wrought corner. Long $\varepsilon/\varepsilon_f = 0.77$,
$\varepsilon_{0.9R} = 4.5\%$fv void = 0.1
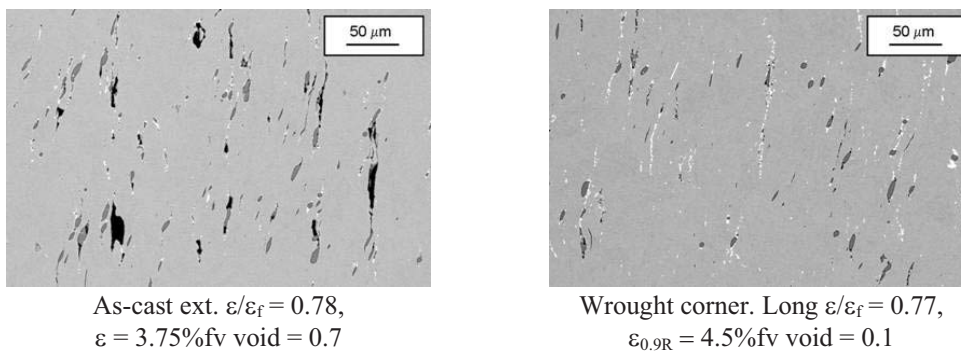
Fig.136: LFCS steel as-cast – wrought at corner (CEIT)

In contrast, for a similar $\varepsilon/\varepsilon_f$ relationship the damage is significantly higher when the as-cast material is considered and the majority of the inclusions have voids associated. These differences remain if the nominal applied strain (instead $\varepsilon/\varepsilon_f = 0.8$) is taken into account. On the other hand, the samples machined from the transversal section show large cracks, similar to those observed in the as-cast condition, but the fraction of voids associated with inclusions is smaller.

- 3-point bending (Sidenor) inc. oscillation marks

Figure 137 shows crack formation in the hot three point bending test corresponding to specimens with the three types of oscillation marks identified. Only in the case of hook type oscillation marks cracks appear, starting in the notch and following the welding line.

109
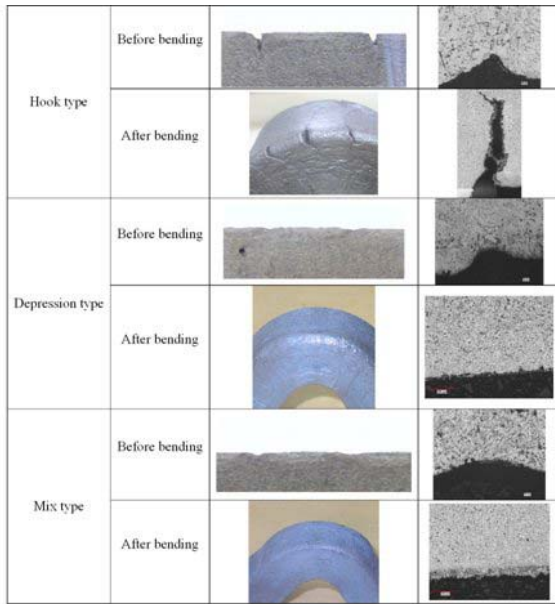
Fig. 137: Oscillation marks behaviour. Before and after hot three point bending testing (Sidenor)

Figure 138 shows the distribution of inclusions corresponding to the oscillation marks (surface, inner zones, etc.) Smaller inclusions near the surface than in the inner zone are observed. however the oscillation has a larger distribution of inclusion size in a very short space (around 30 μm) with no apparent reduction in the number of inclusions. This will weaken further the structure with respect to damage nucleation and growth.

a) Surface   b) Oscillation mark surrounding   c) Half radius
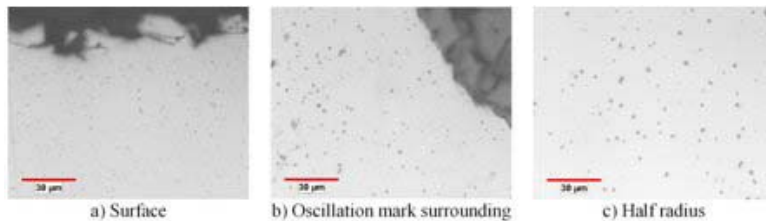
Fig. 138: Inclusions distribution near oscillation marks (Sidenor)

- **RPS testing inc. double hit (Corus)**

More than 150 tests were carried out using the RPS specimen setting. Main mode of cracking has been shown in Fig. 4 of the Extended summary. Key characterization has involved tracking nucleation, growth and coalescence function of reduction, temperature and strain rate for the various steels studied (Te-FCS, LFCS and Telby+). It can be observed that nucleation/initial decohesion around inclusions occur at 15%, through damage acting at surface specimen and internal decohesion (Fig. 139). The surface damage is promoted with larger inclusions close to surface (~50 microns from surface, s/d <2.7 where s is inclusion interspacing distance or distance from surface to inclusion, d inclusion diameter), but also secondary network of smaller inclusions (see a). Small cracks are developed (6 – 7 microns in width, 60 microns in depth). At 20% reduction, cracking (0.2 mm. max depth) is developed. This is consistent with previous findings where during this test (over 17%, the two principal stresses are tensile). Growth is accelerated from 20 to 25% reduction, finally coalescence takes place rapidly as can be observed at 30% reduction. Internal decohesion is also promoted at 25% reduction. Observation of nucleation/initial growth around MnS for samples where macrocracking has been induced show that nucleation can be triggered 2 mm below external surface of sample within the damage affected area. This has been observed irrespective of grade and temperature (Acquisitions 25 and 22 (Telby), 31 and 34 (Te)). The nucleation/damage growth around inclusions reduces as macrocracking increases towards the triaxiality inversion critical depth. For instance acquisition 27 shows a 1.8 mm macrocrack with nucleated site/internal decohesion located up to 0.4 mm from the macrocrack tip (i.e. 2.2 mm from surface). Looking at low reduction specimens, for instance acquisitions 35 and 42, internal decohesion zones are present to a depth of 0.65 mm (15% reduction) and 0.75 mm (20% reduction), despite the

triaxiality inversion being roughly constant at 2.4 mm. This leads to the following damage schematic (see Fig. 57). Damage is initiated at both surface and subsurface via internal decohesion and growth at inclusion. Larger inclusion close to surface (where s/d < 2.7]) can act as nucleation for subsurface damage. As deformation increases, growth and coalescence becomes the more prevalent mechanism with nucleation of new sites generated ahead of the crack tip but at a lower depth. This can be explained by the hardening of the matrix which reduces damage growth at inclusion interface as well as local energy release due to crack opening. Areas affected by initial nucleation/growth are therefore up to maximum of 0.55 mm below and around the surface of the crack tip at the lowest strain. Nucleation/growth and coalescence is to be put into the context of Fig. 57, with respect to magnitude and inversion of triaxiality and principal stress/strain ratios.

Typical cracking on Te-FCS is shown in Fig. 140 below. Overall, the Te-FCS has higher crack sensitivity in orientation 4a than 1a and 3a. Position 4A at mid plane of RPS mechanical test represents a depth of 5 to 6 mm from top bloom surface and 6 to 7 mm from vertical face. Orientation 3A seems to be the most resilient to cracking as shown in Fig. 99.

(a) x50 (x60 print)
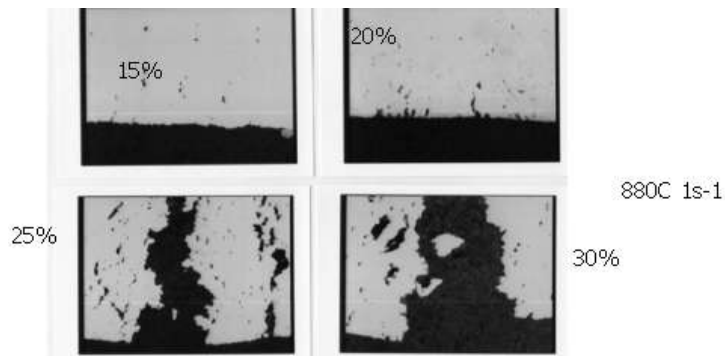
(b) x500 (x560 print exc. bottom right x930 print)　(c)
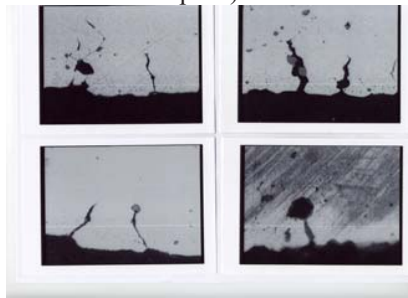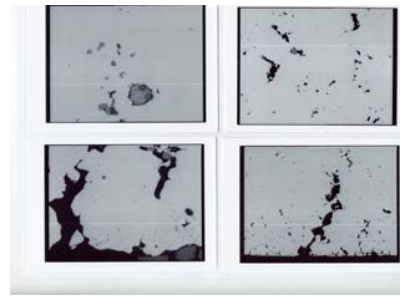
Fig. 139(a-c): Optical micrographs of (a) nucleation/growth and coalescence of ductile damage for Te as-cast corner function of deformation (b) nucleation/growth around Mn particles Aq 35 (15% deformation x500 optical, x560 print) (c) decohesion around MnS Aq 22, limit of internal decohesion Aq 31, Telby Aq 25 both surface and internal decohesion

111
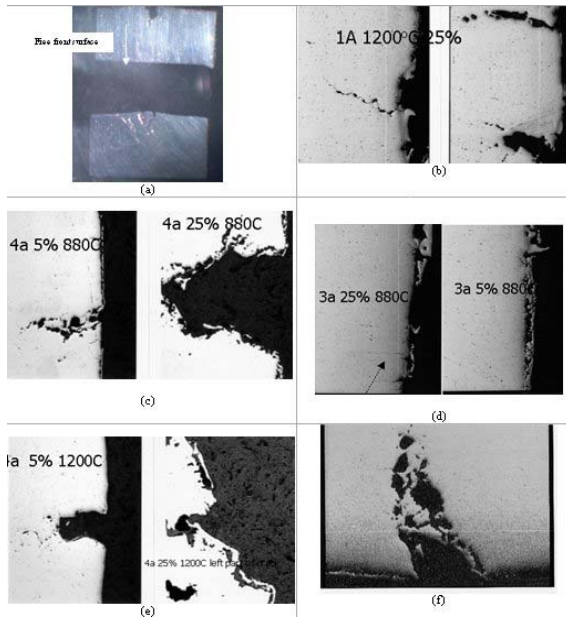
Fig. 140(a-d): (a): Macro-photograph of mid horizontal plane of RPS deformed samples at 0.1 and 10s⁻1 – 880°C – Te-FCS – 25% - Orientation 4a (Plan view) (b) example of cracking orientation 1A, 25%, 1200°C (c) cracking orientation 4a, 5 and 25% at 880°C (d) cracking orientation 3a at 880°C, 5 and 25% (e) cracking orientation 4a 1200°C, 5 and 25% (f) Acquisition 39, 3A 5% reduction, 0.1 s⁻¹, 5%

- **PSC testing (Ascometal)**

Metallographic characterisation has been performed on 32MnS5Bi and 32MnS5Pb deformed PSC samples. Figure 141 shows presence of an oxidation layer on all the samples, presence of micro-cracks (grain boundary cracking) (typical length 10 and 30 μm) and finally some deep cracks (up to 1 mm depth) when the deformation exceeds significantly the critical deformation. More cracking is present on Bi specimen.   The micro-cracks seem to be correlated with the presence of the deep cracks. Characterisation of surface/subsurface at undeformed but reheated location shows a rough surface profile with presence of oxidation. Similarly the CSM 9SMn28 grade shows intergranular cracking at the four temperature tested (See page 80).
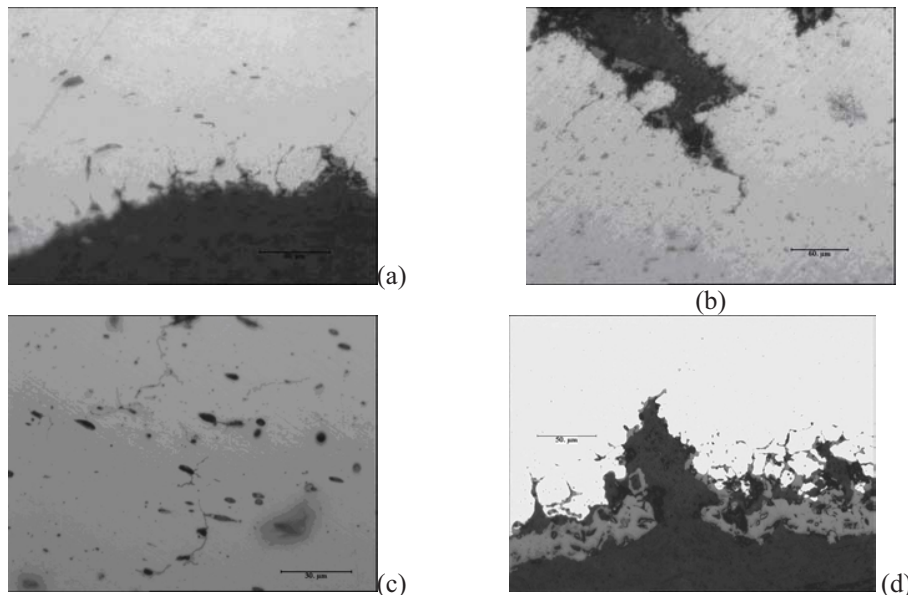
Fig. 141(a-d): (a) PSC characterisation 32MnS5Pb -1100°C (b) PSC characterisation 32MnS5Bi -1100°C (c) grain boundaries cracked at the tip of a fissure (x400) 32MnS5Bi (d) 9SMn28 final height 10.1mm reheated @ 1200°C

The influence of oscillation marks was also studied during PSC testing of CSM 9SMN28 grade. The profilometric curves on the samples before the tests show oscillation marks which depth are of about

300 μm (Fig. 142). The average spacing between the oscillation marks is about 5 mm. After the deformation, they are attenuated. The measurements has allowed the detection of cracks but no clear correlation could be observed between the cracks and the oscillation marks (see Fig. 82(h)).

(a)   (b)
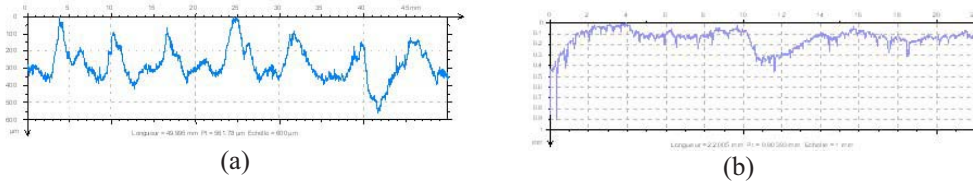
Fig. 142(a and b): (a) Profilometric curve of sample 3a (a) before deformation - 900°C - final height 15.73 mm (9MnS28) (b) after deformation (Ascometal)

- **Other mechanical tests inc. thermal etching dilatometer testing (Corus)**

Characterisation of damage for double collar test, U-bend, hexagon and flying saucer has been carried out and correlated to the mechanisms found in RPS testing. These involve Telby+ and Bi FCS material. Figure 143 shows various damage states from surface/subsurface from the flying saucer test. Damage extends to 0.4 mm from equatorial plane where SPR>1, STR~0.5. Damage growth through inclusion cluster can be seen. Intergranular cracking at both outer and inner ring occurs during double collar testing has been found again with similar conditions of SPR and STR extending up to 0.7 mm from outer ring external mid plane surface. Limited cracking occurs for hexagon compression due to triaxiality inversion (see Fig. 143(f)).
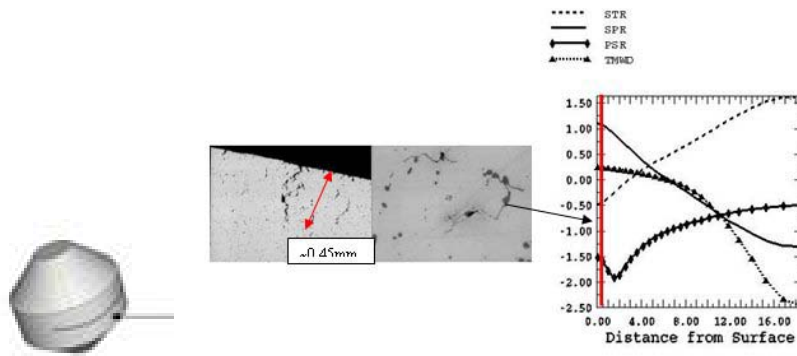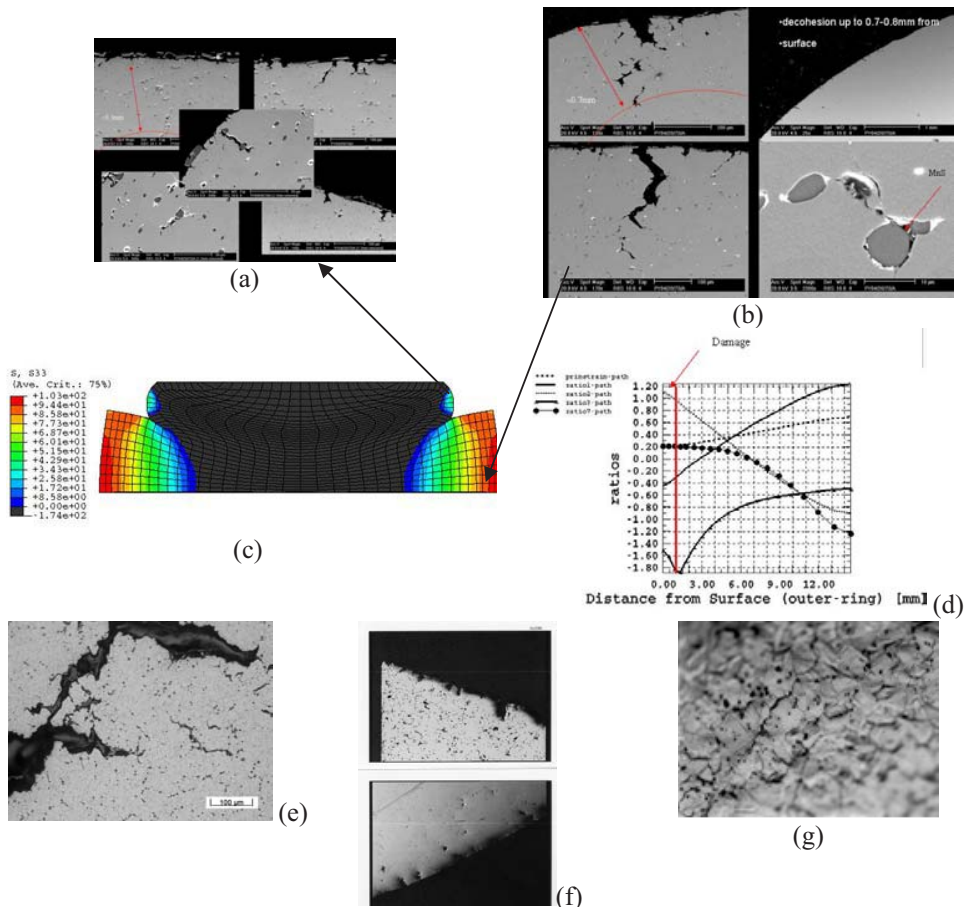
Fig. 143(a-g): (a) Double collar inner ring (b) double collar outer ring – Telby+ (c) FEM simulation of hoop stress (d) path plot of STR, SPR and PSR at mid outer ring plane (e) U-bend cracking Bi FCS (f) hexagon cracking Bi-Steel (g) thermal etching dilatometer double collar testing showing austenite grain boundary and cracking

No cracking could be found by shear during PSC testing of Bi-steel (Fig. 144).
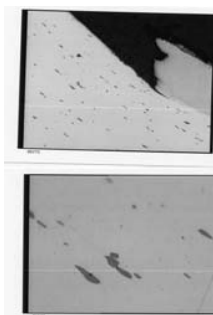
Fig. 144: Bi-steel PSC test – Shear deformation under anvil (no cracking) (Corus)

- **Upsetting testing (Mefos)**

Mefos has quantified both state of oxidation, decarburisation and precipitation on ball bearing steel. This was shown in Fig. 32. After 3.5 h in 1100C a high concentration of chromium was detected (Fig. 145(a)). Grain structure is also shown in Fig. 146(b) for the rock drill steels.
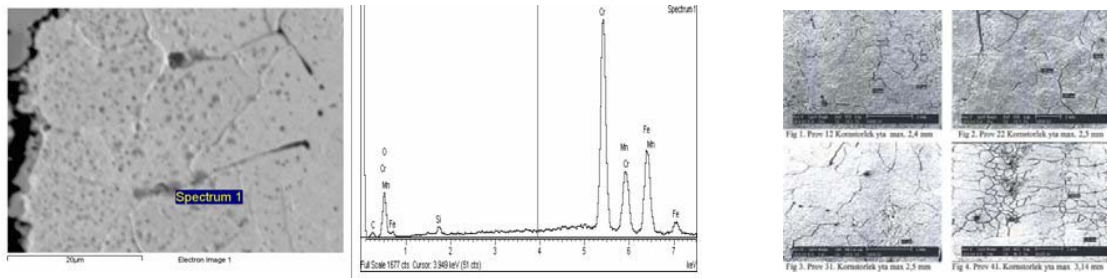
Fig. 145(a and b): (a) Cr precipitation ball bearing steel (b) Grain structure (Mefos)

- **Analysis of as-cast surfaces: presence of FeS inclusions (CEIT)**

The laboratory tests provide a better ductility behaviour in the samples machined from zones close to the surface of the as-cast material than that from the inner regions. This has been assigned to the more deleterious effect of coarser inclusions, usually associated with smaller solidification and post-solidification cooling rates. In contrast, industrial experience evidences the crucial influence of the as-cast surface in promoting defects that propagate during rolling passes. This could suggest that other factors than MnS inclusions can also contribute to deteriorate hot ductility. An analysis of as-cast surfaces was done following a procedure based on a smooth polishing of the surface in order to eliminate the oxide layer (but avoiding a complete cleaning of the surface). Following this procedure, it was possible to identify continuous networks of oxides in the case of as-cast 9SMn28 steel (see Fig. 146). Their distribution is not homogeneous along the surface: while some zones are completely free, in other regions their presence is well identified. Inside the network it is possible to distinguish the following three different regions: Fe oxides (black colour; they probably are part of the oxide layer as a consequence of a selective oxidation at grain boundaries), MnS inclusions (grey) and FeS inclusions (grey-brown). The form and size of the contours defined by the networks suggest that they can be located at as-cast austenite grain boundaries. In the matrix globular MnS inclusions are present, but in some cases it is possible to clearly identified inclusions free regions close to the boundaries of the networks (an example is shown in Figs. 146-147) corresponds to the qualitative analysis of the network. **The lack of Mn in some zones with high concentration of S is clearly identified**. It is also possible to identify some enrichment of Ni and Cu around the network. In the case of 9SMnPb30 billet, the presence of networks with MnS and FeS was confirmed (not shown). In this case the work was mainly focused on a possible combination of oscillation marks and FeS inclusions. Several transverse cuts in the depression regions were done. Although it was possible to identify defects rich in FeS in the depression region (Fig. 148), their size and quantity was not different to those observed in other zones outside the oscillation marks. Summarising, in all the cases it has been possible to identify regions with FeS inclusions (in a higher quantity in the heat **with lower Mn/S relationship) that probably have been formed as a consequence of Mn loss by oxidation (in the region close to the surface).** They propagate into the steel matrix (although in all the observed sections they are smaller than **200 μm**). Depending on the surface temperature during curving and straightening operations in the continuous casting, these regions can act as a small cracks (the presence of the oscillation marks can enhance this problem as a consequence of strain concentration effect). The high density of MnS inclusions located at grain boundaries can also favour an easy propagation into the steel.

Fig. 146: Example of oxide and inclusions network on the surface of 9SMn28 (left) and LFCS steel (middle) and 9SMnPb30 (right) (FeS inclusions are clearly identified in the network) (CEIT)
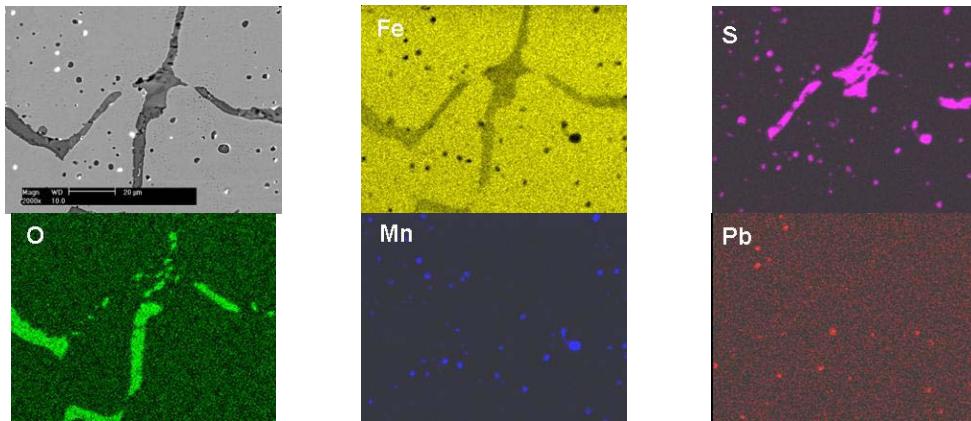
Fig. 147: Mapping of polished surface corresponding to steel LFCS 1/05 (CEIT)
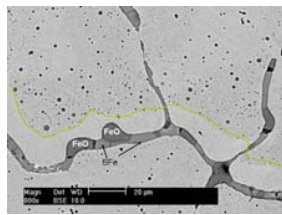
Fig. 148: MnS inclusion free region close to the network (CEIT)

3.3.5.5 Characterisation of ductile damage Rolling (as-cast, wrought) (CSM)

This was detailed in WP4 and explanation of figures 54 and 57.

3.3.6 WP6: Determination of the influence of key parameters sensitivities and establishment of regime maps

Sensitivities are described in Table 5 of the extended summary. In addition the following points can be made.

(a) Inherited from steelmaking/casting/reheating/rolling:

- As-cast surface conditions (oscillation marks) (Sidenor I+D). Hook type oscillation marks (1 to 2 mm in depth) will create nucleation sites for crack opening. This defect is also linked with potential changes of the local microstructure (shift from small to large inclusions with high density) and presence of FeS/embrittlement elements.
- Cortical zone (CSM) (Fig. 149(a)) with thickness ranging from 7 to 10 mm. Laboratory rolling has proven that the cortical zone can be used as an effective barrier against opening of sub-cortical pre-existing casting defects, however more work is required to check if micro-cracking is still being developed. Uniformity and thickness are therefore important parameters. Thinning of this protective layer through oxidation and reduction is to be studied in more detail. Sub-cortical zone with pre-existing defect may give rise to defect opening during rolling if conditions of tensile triaxiality, low temperature, and tensile principal stress prevail.
- Solidification structure (inclusion size, distribution, clustering, type, mean spacing, prior-existing incipient cracking, grain boundary precipitation, etc.). The use of the SKIZ technique (see CEIT WP5) has allowed to predict the influence of ductility function of mean local inclusion area. Wrought structures have higher ductility and smaller mean local area fraction (see CSM results on 9SMn28). Corus has also assessed the diameter to spacing ratio function of ductility. This parameter is taken into account in the damage equations and is not dissimilar to the Cocks and Ashby relationship for damage void growth rate at inclusion interface which depends on ability of material to redistribute deformation within the matrix. This of course depends on inclusion spacing. Closer inclusion spacing will lead to stress and strain network.

- Steelmaking process route (BOS v EAF) with respect to tramp elements (Cu, Sn, etc. content) and likeliness for enhancing hot shortness/embrittlement after reheating due to grain boundary diffusion.
- Level of de-oxidation (rimmed/semi-killed v killed steels) depending on level of Al. For steels studied, Type I MnS are expected (high O_2 content, with low S solubility). Pure and duplex MnS can however be formed with expected different plasticity properties. Silicate and alumina can be present. The MnS inclusion often has varying amounts of other elements, for instance Cr. Calcium often added to melt will modify MnS inclusions and generate CaS which is less ductile than MnS inclusions.
- Chemistry: the LS30-Bi contains 0.26 S with a MSC=1.48. This compares with the 0.42 S and lower MSC=0.98 for the 9SMn28. The industrial experiments confirmed the known trend of increasing ductility with MSC and its criticality below 1.0 [10]. The comparison, however, is masked by the opposite effects of the as-rolled state of the LS30-Bi steel increasing its ductility and its Bi content inducing embrittlement.
- Mn/S ratio plays a significant role in increasing ductility and avoiding phases such as FeS. The critical MnS index as calculated by Alvarez et al [10] should be greater than 1.
- Pb, Te, Bi precipitates often at inclusion tip, lowering cohesive strength. These are low melting phases (350°C for Pb) and microscopic behaviour at high temperature is not clear. What is the role of metallic Pb as Pb will become liquid/gas, enhancing the capillarity effect and influence the bonding strength of the steel matrix/inclusion interface? Could MnS inclusions be assumed fully voided or associated with a low interfacial strength? Does the presence of Pb changes the local tribology of rolling by Pb exuding to surface? A contradictory behaviour is therefore present by adding Pb to improve machinability at room temperature, whilst deleterious effect occurs at high temperature due to the low melting phase.

At microscopic scale:

- Inclusion type. MnS can be take three different types, but type I is mostly expected for this type of steel. Pure or duplex (Oxide-Sulphide) can be precipitated and will have opposite plasticity properties. In general, MnS have larger plasticity than other inclusions such as Silicates, but behaviour is non-linear and overall plasticity index is less than 1 (see Fig. 20). Small inclusions do not deform (less than 5 microns) in view of the increase of interfacial energy and their overall contribution to the matrix deformation (Fig. 149(b)). Larger inclusion stringer found in direction of rolling in wrought structure will change the ductility between longitudinal and transverse (anisotropy).
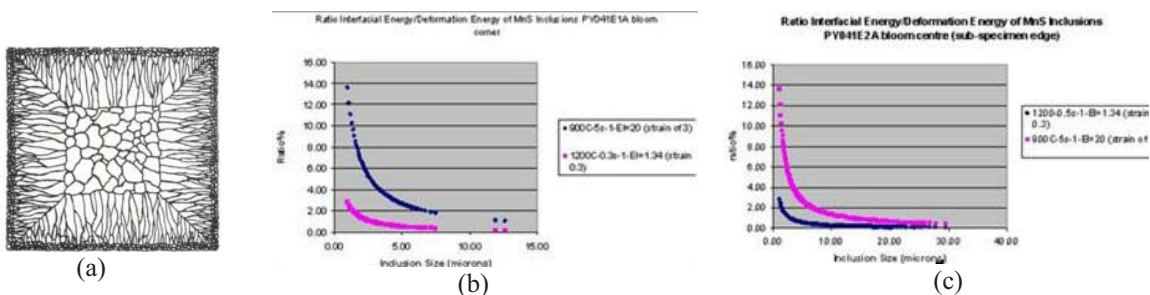
Fig. 149(a-c): (a) Chilled or cortical zone (billet skin) (b,c) Computed interfacial energy for deformation of MnS inclusions surface and bloom centre for rwo temperature and elongation (Corus)

- Clustering, mean area fraction, inclusion diameter over inclusion spacing will play a significant role from nucleation to growth/coalescence. Larger, less deformable, and closely packed will have a larger contribution to play in raising the local strain and influencing the strain partitioning. In addition depending on level of triaxiality, strain partitioning can be changed. Relation of mean inclusion area fraction v ductility, or diameter to spacing ratios have been derived. In addition according to Paliwoda [16], a minimum ratio of S/D>2.7 is required to minimise strain concentration and interaction between inclusions. Nucleation/growth can occur around inclusion without inclusion/crack impingement. In this case ductility is barely affected (see Fig. 30).

- Inclusion shape and morphology can play also a role in further enhancing strain concentration or impingement depending on direction of straining.
- Bi-modal distribution of second phase inclusions (primary sulphides and secondary oxides or carbides) can create additional strain concentration and potentially change the behaviour to void sheet mode cracking (under high triaxiality)
- Precipitation of MnS on grain boundaries. A minimum of 60% of inclusions precipitate on austenite grain boundaries. As recrystallisation proceeds, this fraction can increase. This also can be associated with triple points. This has been clearly shown by observation/experiments from CEIT and Corus with different initial grain size and use of SKIZ technique (Fig. 126). This means that dynamic recrystallisation, mainly because of the reduction on grain size, is not a mechanism able to isolate inclusions (and voids once damage is nucleated).
- Hardening of matrix. Increase of fracture strain should be expected as strain hardening of the matrix increases. This was shown by microFEM (Corus).
- A size effect in fracture due to void/inclusion. A critical strain and stress ratio will need to be achieved in relation to the inclusion/void spacing or mean area fraction.
- Localisation of flow will occur between/around inclusion tip with potential secondary oxide/inclusion playing a key role. Slight porosity (as-cast) will also contribute to decrease fracture strain. This is shown in work done by Corus.
- Reducing void/inclusion fraction at surface should increase fracture strain.

At macroscopic scale

- Mechanical solicitation with triaxiality, principal stresses (max and mid), equivalent and principal strains generated during rolling will have a marked effect through the strain path/history of the material. A "normal" ductility through exists during tensile testing for temperature around 850-900°C. There is also an inverse dependence of fracture strain on tensile stress transverse to inclusion/void. This has been demonstrated by PSC and RPS testing. The fracture strain is also dependent on the mid intermediate principal stress as demonstrated in RPS testing after 17% deformation where fracturing is accelerated (see RPS Corus).
- Rolling triaxiality operates in a regime where triaxiality is less than 1, therefore very sensitive to additional local/non-local parameters (surface/subsurface). At triaxiality greater than 1 as demonstrated by Bandstra [23], fracture strain is drastically reduced but independent of any further rise of tensile triaxiality. The curve presented in Fig. 38 is useful in positioning mechanical testing. Torsion testing is characterised by a zero or very low triaxiality and therefore damage can only be local. RPS and PSC operates in the region of 0.2 to 0.8/0.9 depending on curvature (similar to rolling) and therefore cracking can be accelerated/reduced depending on conditions. Tensile testing after necking (at maximum load, triaxiality is 0.33), triaxiality can go up to 2, therefore fracture will be rapid with minimum coalescence.
- Ductile fracture is strain and stress dependent, therefore time integral of these quantities, inversion of triaxiality, and gradient will all play a role. So far triaxiality greater than 0.5, principal stress ratio greater than 1 and strain ratio greater than 1.5 can promote fracture.
- Surface state and pre-existing defects/micro-cracks have potential to influence cracking.
- Temperature, strain rate. Increased on strain rate at high temperature should be beneficial. Ductility improves by raising the strain rate, but the gain seems to settle at steady values above 1 s-1. Lower strain rate gives rise to grain boundary sliding/cracking, which is further accelerated by the high fraction of inclusions precipitated at grain boundaries and triple point. This has been shown in Corus mechanical testing (see Fig. 140(d)).

3.3.7 WP7: Development of damage equations/constitutive models

As described in the Extended Summary, damage models applied and developed have addressed a range of length scale and coupling, ranging from simple integrated post-processing ductile damage criteria at the scale of the element (integration point) (run following completion of simulation or as a direct field variable), to more complex constitutive models coupling damage with stiffness degradation and potential element deletion, interaction between void closure and damage, viscoplastic damage model with effect inclusion spacing, and finally multiscale CAFÉ models taking into account length scale of

ductile/brittle damage with a statistical representation of second phase particle. In addition an extensive study at microscale of MnS interactions in both 2D and 3D has been carried out to supplement information of effect of triaxiality and strain partitioning. These models are summarised below.

3.3.7.1 Integrated ductile damage criteria (all except CEIT and Ovako-Imatra)

Simple integrated ductile damage criteria have their benefits in highlighting zones where damage might be initiated but most of them are either empirical or macroscopic and do not differentiate on microstructural features (inclusions, DRX, grain size, etc.). They all tend to combined effect of either triaxiality or principal stress (growth/coalescence) with the accumulated strain to predict fracture. The constants appearing on the right hand side should be material dependent and calibrated by mechanical testing (mostly uniaxial tensile test). A good review in the literature is presented by Cescotto et al [42]. Many criteria exist such as MnClintock, Rice and Tracey, Oyane, Ghosh, Brozzo, and Lemaitre to name a few. Applicability of models was assessed for the upsetting experiments carried out by Mefos (see Extended Summary). These criteria could be further developed to differentiate between different steels by for instance inclusion effect of mean inclusion spacing, etc. This was not carried out in this project.

- Cockroft-Latham : $\int_0^{\overline{\varepsilon}_f} \frac{\sigma_{max}}{\overline{\sigma}} d\overline{\varepsilon} = C_{CL}$ …(3.13) (Mefos, Ascometal, Sidenor, Corus)

This criterion was extensively used but was not calibrated. Values from 0.15-0.2 (rolling, Mefos) to 0.45 (upsetting rock drill Mefos) were calculated. The criterion does not take into account growth but is more targeted to coalescence. Zones at risk tend to be over-estimated and may not indicate the true location of initiation, for instance during tensile testing ([42]).

- Oyane: $\int_0^{\overline{\varepsilon}_f} (\frac{\sigma_m}{\overline{\sigma}} + B)\overline{\varepsilon} dt = C_{Oy}$ …(3.14) (Mefos, Ascometal)

B=0.5 was assumed (Mefos). This criterion was not calibrated with typical values of 0.45-0.5 calculated for the upsetting trial (Mefos)

- Lemaitre: $\begin{cases} \dot{D} = 0 \ if \ \varepsilon \leq \varepsilon_D \\ \dot{D} = \frac{D_c}{\varepsilon_D - \varepsilon_R}\left[\frac{2}{3}(1+\upsilon) + 3(1-2\upsilon)\left(\frac{p}{\overline{\sigma}}\right)^2\right]\dot{\overline{\varepsilon}} \ if \ \varepsilon > \varepsilon_D \end{cases}$ …(3.15) (Ascometal)

D_c : Criterion at rupture , ε_D : Strain necessary to nucleate cracks in an unixial tensile test

ε_R : Strain at rupture determined for an uniaxial test. υ : Poisson coefficient (0,33)

p : hydrostatic pressur, $\overline{\sigma}$: equivalent stress, $\dot{\overline{\varepsilon}}$: equivalent strain rate

This criterion is well accepted in the ductile damage community. Ascometal did not calibrate it for the steel studied with a typical value of 0.25. A more intense differentiation of damage localisation tends to be predicted with this criterion.

In summary, these criteria are useful for quick assessment of rolling effects such as underfill, etc., but do not in details model the 3 main mechanisms of ductile damage.

3.3.7.2 Coupled ductile damage (nucleation and coalescence) (Corus)

The damage evolution "standard" capability in ABAQUS (i.e. without use of a user material subroutine) has been used and calibrated. It is based on a damage initiation or nucleation and evolution criteria which is fully coupled in the sense that progressive degradation of the material stiffness leading to failure is modelled. The model uses mesh-independent measures either via plastic displacement (instead of strain) or energy dissipation. This model has been used in previous semester reports, but in this semester emphasis was placed on implementing more realistic physical data from mechanical testing as well as assessing its sensitivity. The RPS mechanical test has been used to that effect. Implementation with a series of selected rolling passes (WP8) has also been carried out. This model can be used with an element deletion feature to remove elements from the mesh. It is accepted that accuracy (although not specifically mesh dependent) will increase as mesh density increases in the area of damage nucleation/growth. The use of single integration point for 8-noded linear brick elements further amplifies the need for a fine mesh. Figure 150 illustrates the basic concept.
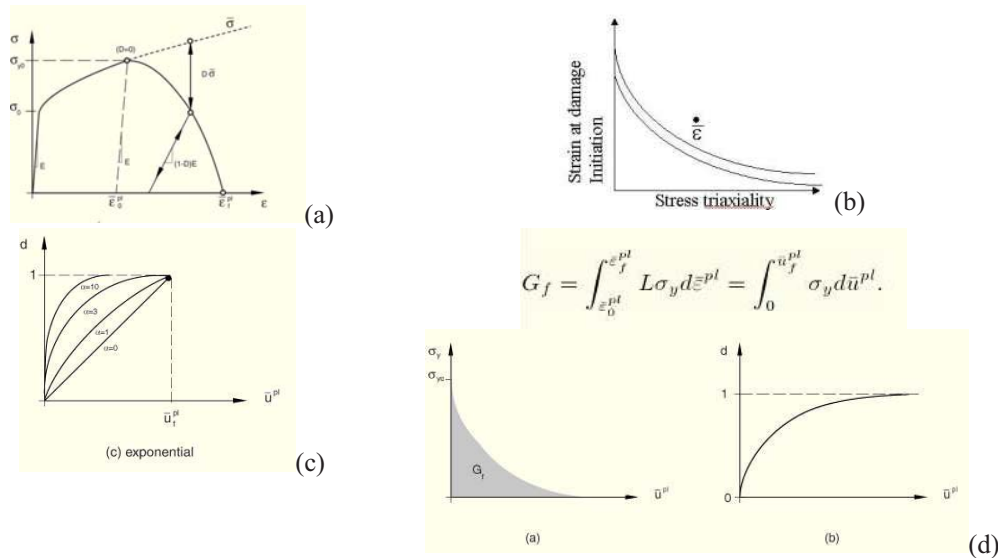
Fig. 150(a-d): ABAQUS Damage model principles (a) stress/strain to failure, (b) nucleation (c) damage versus plastic displacement following nucleation (d) fracture energy criterion [38] (Corus)

- **Damage nucleation (see Fig.38)**

Nucleation curves were constructed based on assessment of deformation and cracking for Te-FCS at 880°C (see Fig. 152). Use of the two plane of deformation (fig.97c) has been made to extract value of equivalent strain and triaxiality. The deformation threshold was 20%. In the plane normal to direction of anvil, triaxiality is high but strain is low. Fracture has only been observed on two samples so far (from more than 120 tests). From a single RPS test, two main surface data points can be extracted (at a given temperature and strain rate). These cover the range of strain and triaxiality encountered during rolling. In order to develop the full curve, ideally an extra point is required. This can be obtained from a uniaxial compression test at high friction, giving higher strain and reduced triaxiality.
The fit is based on the Rice and Tracey model [30] where:

$$\varepsilon = A.\exp(-B.\frac{\sigma_m}{\bar{\sigma}}) \ \dots \qquad \dots (3.16)$$
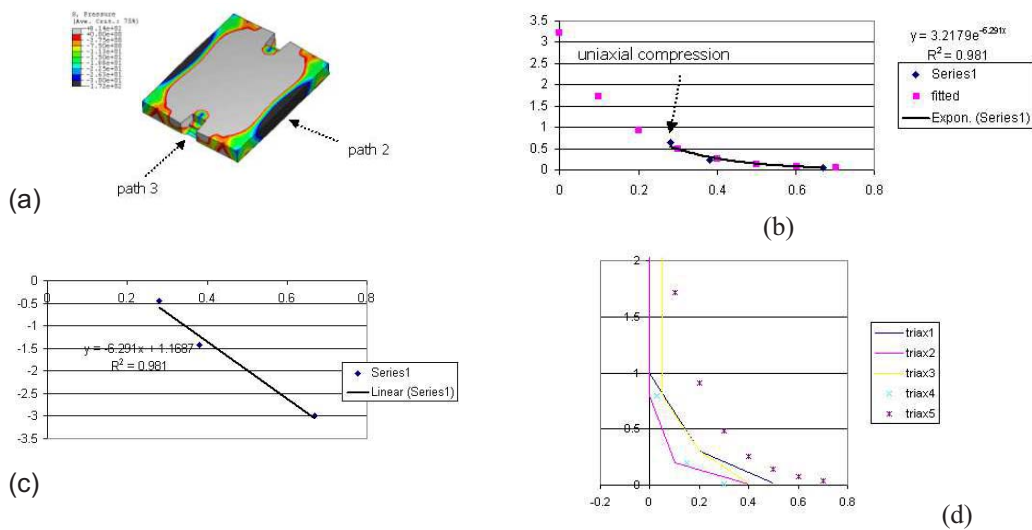
Fig. 151(a-d): Nucleation curve Te as-cast 880°C 1 s⁻¹ (a) two plane surface location for nucleation data at a given reduction (b) strain triaxiality curve using 2 data points from RPS and 1 data point from uniaxial compression high friction (high strain, low triaxiality) (c) Rice and Tracey nucleation fit (d) nucleation curves for sensitivity analysis defined below above nucleation curve (b) (defined by symbol x) (Corus)

- **Damage evolution (tensile testing)**

Stress strain data from Birmingham tensile testing (LFCS and Telby+) (Fig. 92) have been used from the point of maximum loading (start of necking with a triaxiality of 0.33) to develop stress and relative displacement data calculated from diameter at point of necking to final diameter at fracture (Fig. 152).
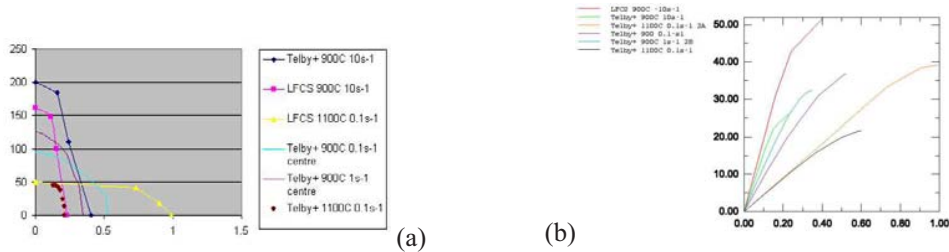
Fig. 152(a and b): (a) Stress-displacement (mm) curve used for damage evolution (b) Fracture energy Gf function of displacement (N/mm) (Corus)

The model was applied to RPS specimen (Fig.153)
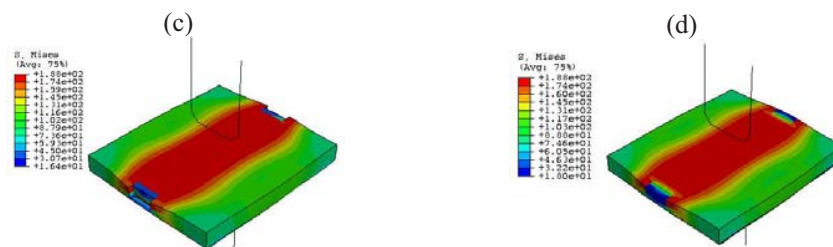
Fig. 153(a and b): (a) FEM MISES damage evolution (a) with element removal (failure) due to damage evolution (displacement) (b) and energy based (Corus)

121

3.3.7.3 Viscoplastic damage model (Corus-Birmingham) Model 1 [62]

A two-parameter viscoplastic constitutive model has been developed by Birmingham University [62] in collaboration with Corus. This model includes two types of damage parameters, which are strongly dependent on strain rate. **Both strain (though a normalised dislocation density approach), strain rate, recrystallisation, dynamic recovery, and grain size are taken into account in this approach**. The equation set is shown in Appendix 2. This model was fitted on FCS steels tensile data as presented in Fig. 92. At low strain rates, damage at grain boundary is dominant, whilst at higher strain rate (>0.1 s^{-1}), deformation by dislocation slip occurs and plasticity induced damage becomes dominant. Both damage parameters need to be integrated and the exponential rate of damage growth reduces the chance of both damage factors contributing evenly to failure. Damage evolution equations are based on nucleation and growth. By mapping damage nucleation to the rate of change of dislocation, damage healing can be taken into account. It should be noted that current implementation of damage in this model is not stress dependent; this is being currently looked at in Model 2. Figure 154 shows plasticity damage plots for the double collar test for a range of temperature conditions (1000°C (a), 727°C (b) and 1200°C (c)) and initial grain sizes (35 and 90 microns (d) at 1000°C).
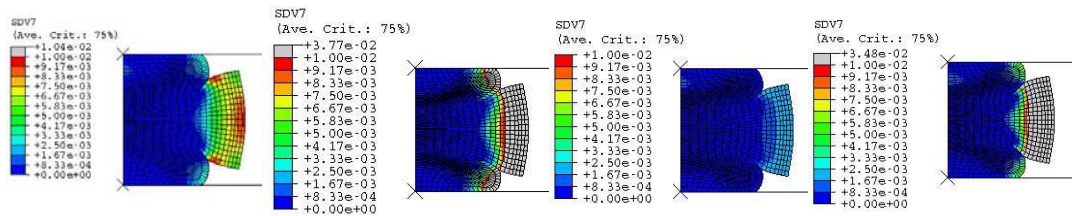
Fig. 154: Plasticity damage plots (a) 1000°C, 35 microns, (b) 727°C, 35 microns, (c), 1200°C, 35 microns, (d) 1000°C, 90 microns

3.3.7.4 Viscoplastic damage model (Corus-Birmingham) Model 2 (see [5,33,34]

A revised and somehow simplified Birmingham-Corus viscoplastic model as presented in [33, 34] has been developed to consider damage developed at inclusion and coalescence of microcrack to macrocrack due to void inclusion interaction and principal stress. The basic of the model and evolution equations which have to be integrated within a VUMAT ABAQUS framework are shown in Appendix 2. The new enhanced model has been applied to the RPS mechanical test (Fig. 155). Nucleation is not modelled only assuming that a given threshold has to be reached before growth can occur (this simulates LFCS with weak cohesive strength). Growth at inclusion (Di) is then dependent on dislocation density (strain), triaxiality based on a Cocks and Ashby model [31] and interspacing- size ratio of MnS inclusions. Coalescence (Dc) is dependent on principal stress, dislocation density and MnS spacing ratio. Model was also applied to the benchmark upsetting case presented in the extended summary (see Fig. 62).

(a)   (b)
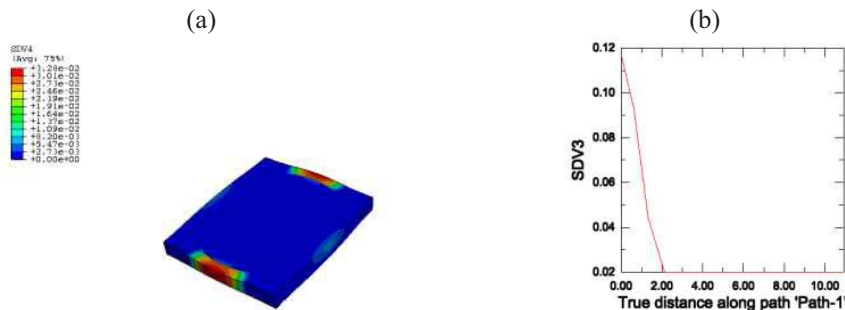
Fig. 155(a and b): (a) coalescence state variable SDV4 (b) damage growth at inclusion (path 3 of RPS specimen)

3.3.7.5 Crack growth (Modified Maire criterion [46,63]) (Corus)

The equation proposed by Maire and Bordreuil [63] using previously developed model by Thomason [18], which predicts defect radius evolution in the presence of inclusion has been further adapted (time or strain integration) to model the evolution of crack length opening during RPS testing. This model does not take into account any microstructural and surface effect (Fig. 156).

$$\dot{li} = (5/3 * n_{ii} + 0.5 \sinh(\frac{3}{2} \frac{\sigma_m}{\sigma_0})) \overline{D}_{eq}.l \quad \text{With} \quad n_{ii} = \frac{3}{2} \frac{\sigma_{ii}^D}{\sigma_0} \quad \text{and l=(l1.l2.l3)1/3} \dots(3.17)$$
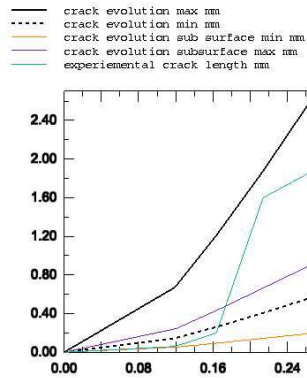
Fig. 156: Prediction of crack growth (mm) during RPS compression (path 3)

3.3.7.6 CSM constitutive model – 9SMn28 (CSM)

This model incorporates:

- isotropic hardening
- dynamic recrystallisation
- static recrystallisation at interpass/interstand
- tensile damage
- consolidation

A single state variable viscoplastic constitutive law with isotropic hardening has been developed and incorporated into a FEM rolling model of the Ori-Martin plant. The model was constructed from a set of isothermal, constant strain rate monotonic compression curves (see Fig. 103). The model is based on an inverse sinh law with a Zener Hollomon compensated strain rate, and incorporates recrystallisation kinetics via a correction (Voce approach) to the peak stress as shown in Table 17 below. An activation energy of Q_{def} 324000 J/mol with strain rate sensitivities m varying between 0.14 and 0.17 above 892°C and 0.095 for lower temperatures was obtained for that steel.

Table 18: CSM constitutive model isotropic hardening/recrystallisation

Deformation :

$$\sigma = \sigma^* + (\sigma_o - \sigma^*)e^{-\varepsilon/\varepsilon^*} - \Delta\sigma, \qquad \sigma^* = \widetilde{S}.\sinh^{-1}\left(\frac{Z}{A}\right)^{ms}, \qquad \sigma_o = So.\sinh^{-1}\left(\frac{Z}{A}\right)^{mo},$$

$$\varepsilon^* = \frac{\sigma^*}{ho\left(\frac{Z}{A}\right)^{nh}}; \qquad\qquad Z = \dot{\varepsilon}.e^{\frac{Q_{def}}{8.31(T[°K])}}; \qquad\qquad \varepsilon_{dyn.} = k_1.d^{k_2}Z^{k_3}$$

$$\Delta\sigma = \mathcal{H}(\varepsilon - \varepsilon_{dyn}).k_4.Z^{k_5}.[1 - e^{-k_6\left(\frac{\varepsilon - \varepsilon_{dyn}}{\varepsilon_{dyn}}\right)^{k_8}}] \qquad\qquad \mathcal{H}(\varepsilon < \varepsilon_{dyn}) = 0, \qquad \mathcal{H}(\varepsilon > \varepsilon_{dyn}) = 1$$

Interpass recrystallisation $T > 870\,°C$ $X = 1 - e^{-0.69(t/t_{50})^n}$ $\qquad n,_{SRX}=1.15 \qquad n,_{MDRX}=1.0$

$\varepsilon < \varepsilon_{dyn.}: SRX \qquad t_{50} = B\varepsilon^p\dot{\varepsilon}^q d^s e^{Qapp.,srx/RT} \qquad ; \qquad \varepsilon > \varepsilon_{dyn.}: MDRX \qquad t_{50} = C\dot{\varepsilon}^r e^{Qapp.,mdrx/RT}$

$$s = k_9 d^{-k_{10}}$$

Interpass softening is incorporated via Avrami's type of equations to compute recrystallised volume fraction at interpass times. The expression for the reference time t_{50} under SRX or MDRX regime was obtained from the stress relaxation experiments. The reported energies for recrystallisation values were 219 kJ for SRX and 311 kJ for MDRX (see [9]).

- **Tensile damage**

Four different models of damage have been investigated: Gurson model f^G, Stress ratios based models f^σ and f^{Gm} and finally characteristic strains-based damage model f^ε.

All of these models are linearly coupled with the flow stress (Tables A.3 Appendix 3 and Figs. 103 and 157). Although Gurson model f^G is already coded in the Abaqus, its application to non-monotonic loading as resulting during the alternate tensile-compressive cycles in a rolling line is not straightforward, because it relies in the total equivalent strain that also increases under compression. The other models were designed to be more flexible on this issue by incorporating the reduction of damage using either a void crushing model (f^ε and f^σ) or a symmetric consolidation under compressive triaxiality f^{Gm}.

Gurson damage model f^G

Assumes that a diluted distribution of voids with volume fraction f^G develops in the metal matrix by nucleation and growth. Its nucleation rate $\dot{f}_n$ evolves with the plastic strain rate around a mean value of a nucleation strain ε_N, shown in the insert for 9SMn28 steel (Figure 15), with a normal Gauss distribution. Its growth rate $\dot{f}_g$ is related to the volumetric strain rate. The total void volume fraction rate resulting from these two contributions is bounded as $0 < f^G < 1$ and is related to the flow stress by a pressure-dependent yield criterion, with coefficients q_1, q_2, q_3 for 'ordered' voided materials as introduced by Tvergaard [28].

Coupling damage-flow stress: $(1-f)\sigma_y \, \dot{\bar{\varepsilon}}_m^{pl} = \sigma : \dot{\varepsilon}^{pl}$

Yield condition for a dilute concentration of spherical voids:

$$\phi = \left(\frac{q}{\sigma_y}\right)^2 + 2q_1 f \cosh\left(-\frac{3}{2}q_2 \frac{p}{\sigma_y}\right) - (1 + q_3 f^2) = 0$$

with p = pressure and q = deviatoric stress invariant

Total rate of damage: $\dot{f} = \dot{f}_{growth} + \dot{f}_{nucleation}$ with the new voids nucleation rate: $\dot{f}_{nucleation} = A\dot{\bar{\varepsilon}}_m^{pl}$ and a normal distribution of the nucleation strain:

$$A = \frac{f_N}{s_N \sqrt{2\pi}} \exp\left[-\frac{1}{2}\left(\frac{\bar{\varepsilon}_m^{pl} - \varepsilon_N}{s_N}\right)^2\right]$$

Where ε_N is the mean value of nucleation strain, for the 9SMn28 related to temperature as in the graph, s_N its standard deviation and f_N volume fraction of new voids.

Growth of existing voids: $\dot{f}_{growth} = (1-f)\dot{\varepsilon}^{pl} : I$

Fig. 157: Gurson's damage model for the 9SMn28 steel (CSM)

Table 19: CSM damage stress and strain based model

Stress-based model f^σ This variable is a strain measure based on the Latham-Cockroft [35] damage criteria. This ratio is linked to the bulk modulus (see Appendix 3)	$f^\sigma = \int\limits_{tension\ cycle} \frac{\sigma_{max.\ principal}}{\overline{\sigma}}$
Triaxiality-based model f^{Gm} This is used for void growth where the integrand increases under tension (positive pressure) and reverses under compression. f^{Gm} cannot be reduced further than zero (corresponding to full consolidation) and is coupled to the constitutive material strength and bulk modulus. At roll bite exit, f^{Gm} increases more rapidly (See Appendix 3)	$Gm = \int \frac{pressure}{\overline{\sigma}} d\overline{\varepsilon}$
Strain-based model f^ε (see Appendix 3) predicts evolution of damage from onset of damage ε_{ond} to fracture. Damage in this model starts somewhat later than in the previous cases, because it requires not only tensile triaxiality but also that a critical strain is reached for the onset of damage. The strain-based damage variable f^ε was originally developed for flat rolling of a 2304 duplex stainless steel in a previous ECSC project [64]. This model therefore accounts for nucleation and growth. Critical strains (as per Fig.91b) are related to temperature in this model. Best fit to the tensile curve (see fig 158a) was achieved with $\alpha = 2.5$	$f^\varepsilon = \left(\frac{\varepsilon - \varepsilon_{ond}}{\varepsilon_{fract} - \varepsilon_{ond}} \right)^\alpha$ $f^\varepsilon(\varepsilon_{ond}) = 0 < f^\varepsilon < f^\varepsilon(\varepsilon_{fracture})$

The behaviour of the damage model f^ε with temperature and strain is shown in Figs. 158(b) and 158(c).
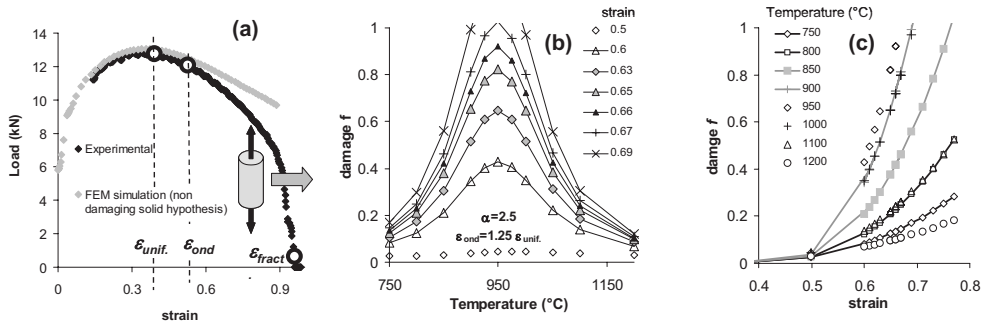
Fig. 158(a-c): Strain-based tensile damage model f^ε for the 9SMn28 steel (a) characteristic strains definition; (b) damage as a function of temperature for several strains; (c) damage as a function of strain for several temperatures (CSM)

3.3.7.7 MicroFEM (Corus)

2D MicroFEM models of inclusions and steel matrix have been developed to assess influence of biaxial testing with various triaxiality setting (from 0.7 to 1.7), inclusion plasticity, morphology and spacing. The objective is to predict strain increase due to inclusion impingement compared to far field strain (no inclusion interaction). Influence of inclusion hardness v matrix has also been studied. Debonding and crack growth has also been studied by incorporating a Gurson type porosity model (nucleation and growth) within the microFEM either at the MnS inclusions to represent low nucleation site for debonding (for instance assuming Pb is precipitating). Strain tends to concentrate around hard inclusion at tip of MnS inclusions with small interaction between different clusters (see Fig. 159). The closer the inclusions, the greater the strain concentration is developed (up to x3). When inclusions are softer than the matrix (taking into account matrix hardening), more interactions between the various inclusion clusters is developed, i.e. less strain concentration is predicted. The triaxiality has a greater effect when

126

the interspacing of inclusion increases to a given threshold with an inverse predicted behaviour between hard and soft inclusion. As triaxiality increases, strain tends to be less concentrated at soft inclusions which are less closely spaced. For closely spaced inclusions s/d<2, the interdistance between inclusions is the most significant parameter affecting strain concentration, as triaxiality and hardness of inclusion have little effect.

A two-3D inclusion sub-volume microFEM model has also been constructed to assess influence of straining, hardening and inclusion/matrix interaction (Fig. 160). Cases shown represent deformation experienced by surface/subsurface of RPS specimens. Hard inclusion/soft matrix promotes strain concentration between inclusions mostly as inclusion spacing is reduced (same behaviour as in 2D biaxial test). The 3D case shows also the importance of the matrix hardening in reducing strain localisation (Fig. A160(b)).

A relation between strain concentration and plasticity index (i.e. ratio between inclusion plasticity and matrix, assuming no recrystallisation (if ratio less than 1, inclusions are less deformable)) has also been derived as shown in Fig. 161.
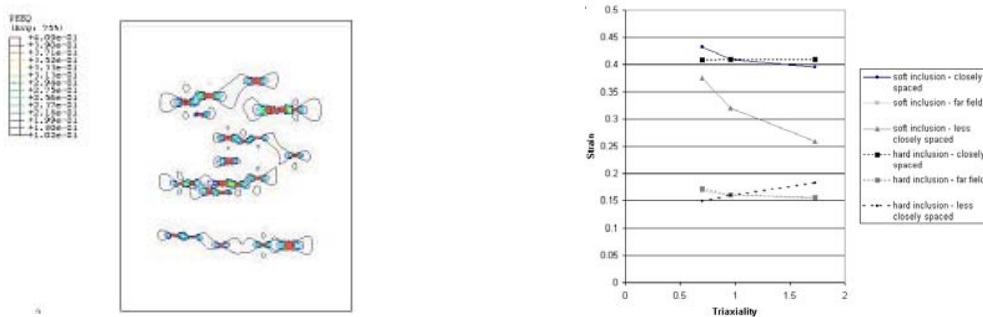
Fig. 159: 2D MicroFEM (biaxial test) to study influence of triaxiality, pacing and plasticity of inclusion (Corus)

(a)   (b)
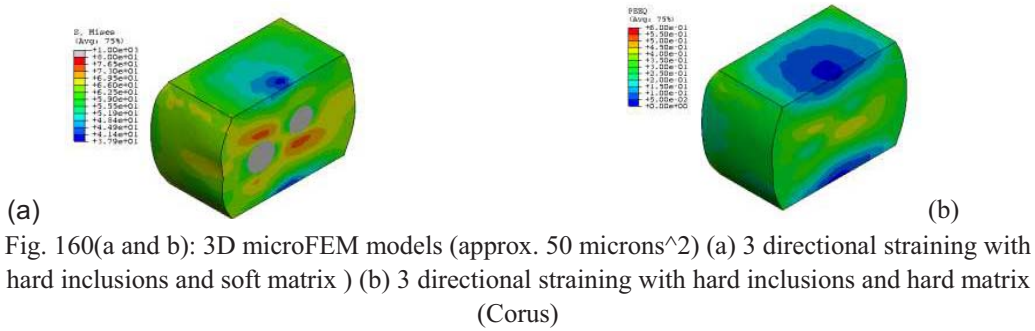
Fig. 160(a and b): 3D microFEM models (approx. 50 microns^2) (a) 3 directional straining with hard inclusions and soft matrix) (b) 3 directional straining with hard inclusions and hard matrix (Corus)

(a)   (b)

127

(c)   (d)

(e)
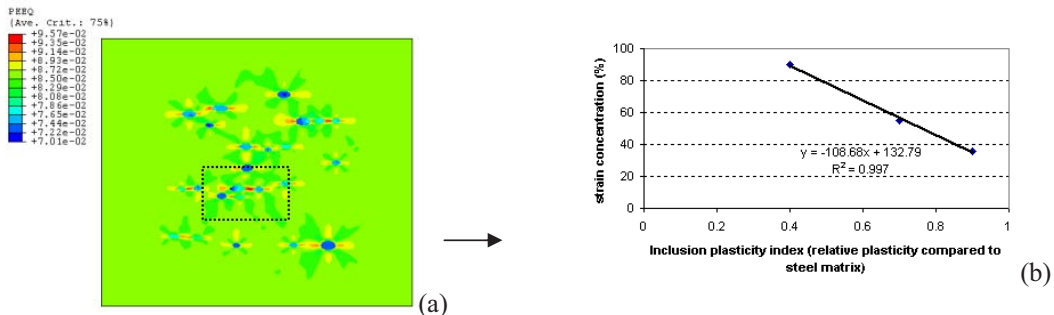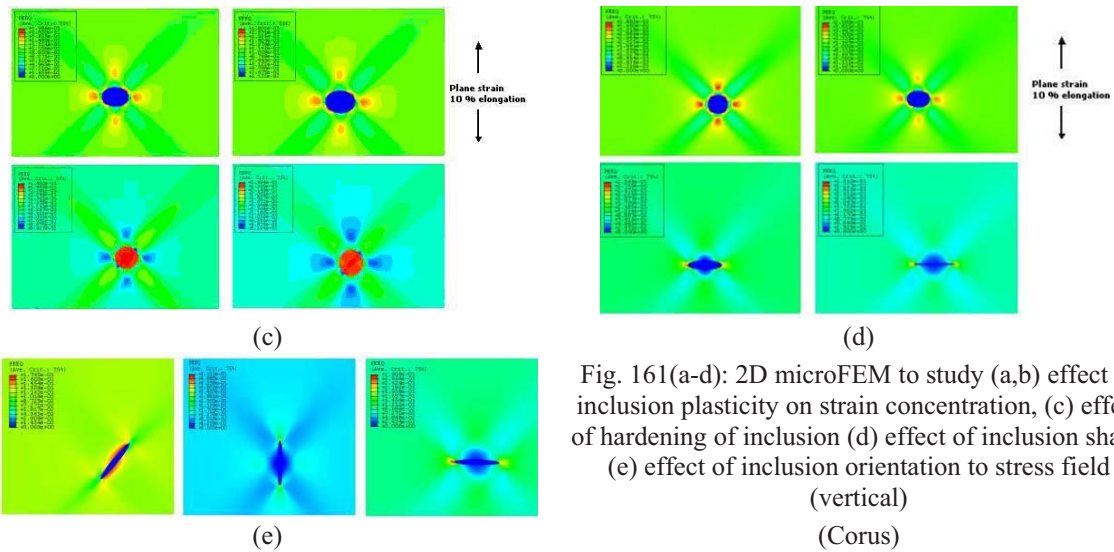
Fig. 161(a-d): 2D microFEM to study (a,b) effect of
inclusion plasticity on strain concentration, (c) effect
of hardening of inclusion (d) effect of inclusion shape
(e) effect of inclusion orientation to stress field
(vertical)
(Corus)

3.3.7.8 CAFÉ multiscale modelling (Corus)

The Birmingham Viscoplastic-Damage Constitutive Equations Model 1 and the CAFE Framework taken from [40] are now fully integrated into one single VUMAT user subroutine. For a given set of elements, users have the option of using the user subroutine to describe the material response by either (a) the constitutive equations alone or (b) the constitutive equations within the CAFE Framework in an advanced hybrid mode. The sophistication in using the user subroutine in the hybrid mode is that it allows for layers of damage mechanisms to be incorporated seamlessly into the modelling. At present, 2 categories of damage mechanisms are implemented: (1) ductile damage based on the Birmingham Viscoplastic-Damage Constitutive Equations; and (2) brittle damage based on fraction stress. The CAFÉ model has been applied (ductile regime only) to the RPS and Uniaxial upsetting tests with a central network of CAFÉ cells located in the region of interest (mid plane). The damage and stress state predicted by the viscoplastic model at the FEM integration point of each relevant element (associated to the CA set) is transferred (single integration point in Explicit) to the CA cells to update their state. The CA cells state is then updated according to specific rules (ductile damage, state of cell (live, dead), maximum number of dead cells) and the solution dependent variables related to the CA cells are then transferred back to the FE element, allowing element to be removed if the number of deal CA cells is greater than a pre-determined value. The model which incorporates the Birmingham-Corus viscoplastic damage equations based on Model 1 (see Appendix 2) shows correct behaviour of damage initiation during RPS and upsetting testing (see Fig. 62(n) and (o), 162), but in view of the complexity of the approach and the number of statistical parameters, more work is required to further test the sensitivities of the model to ductile damage.
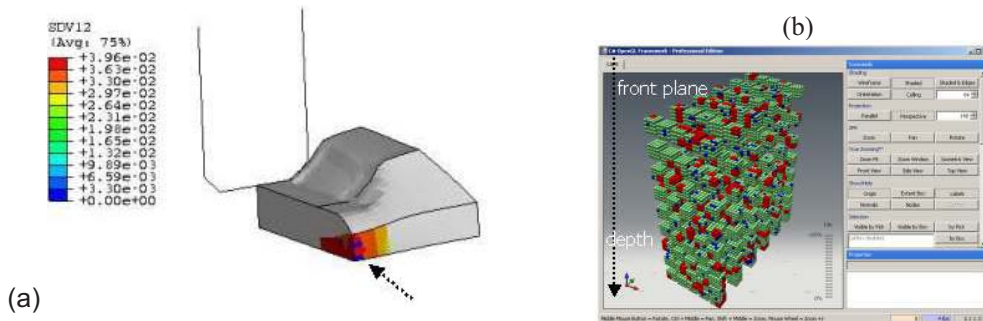
Fig. 162(a and b): CAFE model (CA arrays associated with 270 elements with 64 (4x4x4) cells)
(Corus)

128

3.3.8   WP8: Incorporation of constitutive models in multipass rolling FEM models (CSM)

Rolling develops tensile regions on the stock entering and exiting the roll gap, as well as on lateral surfaces, and these alternate with heavy compressive pressures during direct drafting (see Figs. 33 and 165). As mentioned above, the approach adopted combined consolidation rate obtained from the Gurson simulations with the more flexible procedure of user-defined tensile damage functions f^{ε} and f^{σ} (see Appendix 3).

The constitutive model was applied to single pass rolling matching set- conditions (See Appendix 1) with the stress state compared to mechanical testing (Gleeble compression of 46x46mm cylindrical specimen (see modelling benchmark Fig. 62) and tensile testing) for 3 temperatures and an equivalent strain of 0.6. Figure 163 shows the FEM distribution of the damage parameter f^{ε}. Corresponding values of the index G_m and damage variables f^{Gm} and f^{σ} at critical locations are also indicated. The Gm value is a comparative index, available in some commercial codes, while the f 's are full damage variables coupled to the material hot strength. Comparison of the 3 deformation mechanisms show:

- f^{ε} (characteristic strains based damage) predictions for tension and flat rolling follows well the trend with temperature obtained for the experimental values (see Fig. 66) for the worst case (removed hc=13 mm), but the numerical results are higher. The development of f^{ε} damage in cylindrical compression with frictional dies follows the opposite trend, due to the increasing bulging and hence bigger hoop strain as temperature increases.
- f^{σ} (based on Latham-Cockrost criterion) predictions are higher than f^{ε} for tension and rolling. For tension, f^{σ} departs from the tensile experiments (Fig. 92(b)) better represented by f^{ε}. Compression and rolling f^{σ} values almost overlap each other at the three temperatures examined.
- f^{Gm} (triaxiality based) predictions are higher than f^{ε} for rolling and about the same than its respective f^{σ} predictions for compression and tension.
- The comparison shows that for edge cracking in flat rolling the damage variable f^{ε} gives the best results.
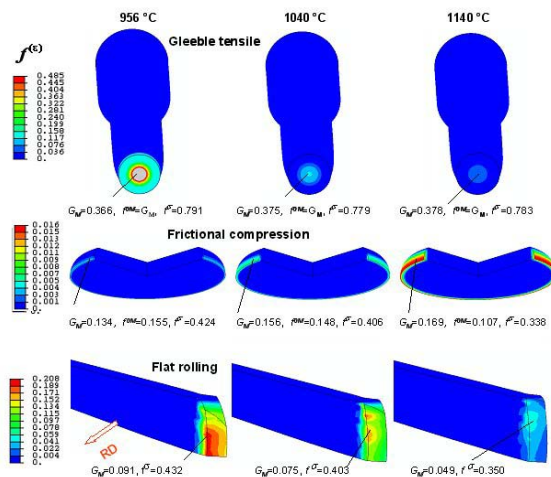
Fig. 163: Damage predictions from simulation: effects of temperature and past stress states after 0.6 plastic strain (CSM)

Figure 164 shows the application of the criteria developed to single pass rolling R0. A quadrant of the rolling stock is modelled and the rolls are assumed rigid. Two scenarios were examined by monitoring points A-E on the bloom cross-section:

- Growth and consolidation of an incipient defect (point A)
- Nucleation and growth of new cracks, these also undergoing consolidation (points B-E).

An initial condition near to failure ($f(0) = 0.9$) was attributed to this incipient defect. This can be attributed to either weak regions of dendritic porosity in the as-cast bloom (see Figure WP5) or to debonding of the recrystallised matrix from the larger subcortical MnS particles (see Fig. 54(b)).

The results for the monitoring points A-E shows:

(a) At the tip of the incipient defect (point A), all models predict a small increase in damage on crossing the tensile region at the roll-gap entry (positive pressure in Fig. 165(b)), followed by incomplete consolidation under the rolls. The larger damage raise on entry corresponds to the predictions of the f^ε and f^σ models, followed by f^G and f^{Gm} (Fig. 165(c)). The reduction of damage by consolidation within the roll gap is the same for f^G, f^σ and f^ε models, but lower than from the f^{Gm}. The next effect of the whole pass on the original damage value is a small rise for f^ε and f^σ, a small reduction for f^G and a 50% void closure for the f^{Gm}.

(b) New damage at the stock edges (point B and E) and rolled surface (point C) is of very low magnitude. Their peak value reached at the tensile region on entering the gap is crushed under the rolls but there is an upsurge of damage at the exit, with the highest predictions corresponding to the f^σ model.

(c) New damage at the bulging free surface (point D) is non negligible only for the Gurson model.

(d) The conceptual difference between the index G_m and the damage function f^{Gm} in their relation to pressure is apparent in Fig. 165(b): f^{Gm} diminishes under compression only as far as zero and increases under tension starting to rise simultaneously with the inversion of trend in G_m. Such f^{Gm} definition, however, allowed to couple damage with the material strength as in Appendix3.

A single coupled multipass rolling imposes a heavy penalty on computing turnaround for simulations owing to the mesh discretisation that become unnecessarily small for simulating the thermal and recrystallisation evolution, mostly during interpass time. Therefore it becomes imperative to split the analysis throughout the rolling schedule by repeated application of deformation and interpass modules with intermediate mapping of relevant fields. This simulation strategy developed by CSM involves a process of extraction of steady state profile and remeshing with field solutions transferred to the new mesh. The application of this technique is shown in Figs. 55 and 59.
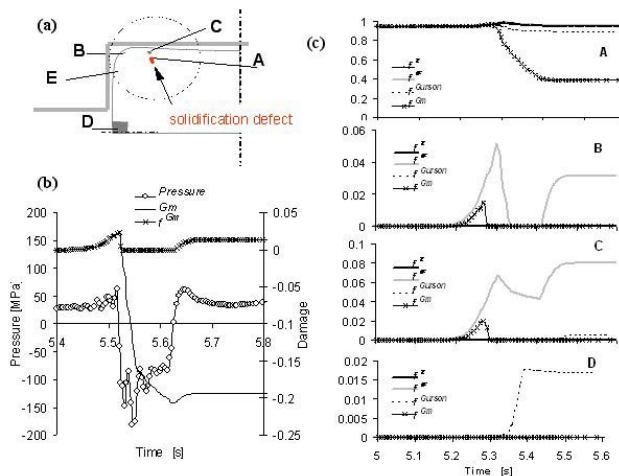
Fig. 164(a-c): Damage-consolidation predictions for R0 roughing of a 9SMn28 as-cast bloom(CSM):
$T_o = 1040$ °C, $T_{surface} = 980$ °C :
(a) monitoring points with internal incipient defect($f_o = 0.9$) placed as experimentally observed;
(b) Pressure, G_m index and damage function f^{Gm} at point E on crossing the roll gap;
(c) comparison of results from the four models investigated

3.3.9   WP9: Further development of detection device for hot metal application

The on-line Ori-Martin production system has been described in the Extended summary and therefore will not be further detailed.

3.3.9.1 On-line surface defect detector at Ovako Imatra medium bar mill

An Eddy Current surface defect detection system was trialled at Ovako Imatra's medium bar mill in May 2007. The system was a commercial application called Defectotherm T60 by German company Institut Dr. Förster GmbH & Co. KG. The medium mill in Imatra produces round bars from ø 21.85 mm up to ø 92 mm. The detection system could however only be used with bars of diameter ø 21,85 – 33.7 mm, i.e. using a mill based on six rolling stand configuration due to effect of front end bending when mill is set-up on two or four stand configuration. The detection arrangement consisted initially of two roller guides on both sides of the detection coil (Fig. 165(a)). This makes the bar both enter the coil and keep it stable during rolling. However the finished product required very careful adjustment of the rollers. With this arrangement one 24-hour test period was carried out in normal production. A total of 340 tons with diameters 21.85 – 25.0 mm bars were inspected. The system was adjusted with different setups but no bars were found defective. However it was later on observed that the roller guide rolls on the exit side of the detection coil caused some scratches, in addition a bar failed in entering the roller guide causing a cobble in the rolling line which had to be stopped for 65 minutes and the detector removed from the line. In the next trial the roller guides were removed and replaced with tube guides (Fig. 165(b)). In total, 54 hours mill time with a production of 727 tonnes was realised.
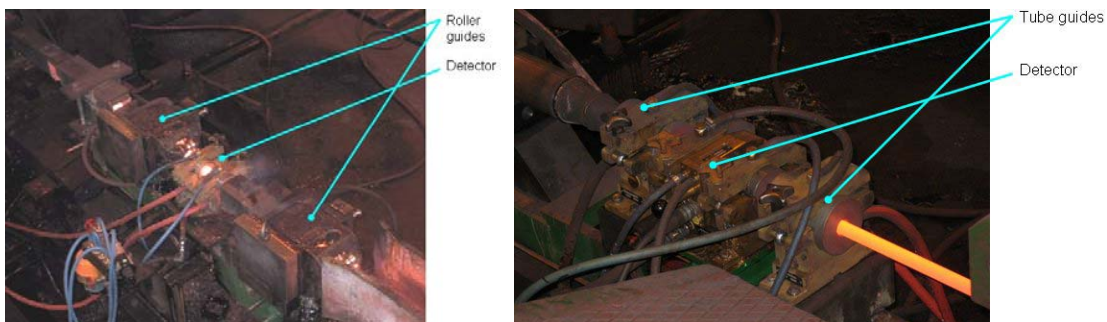
Fig. 165(a and b): Ovako Imatra Eddy Current trial system Defectotherm Förster GmbH & Co
(a) initial roller guide system (b) tube guide

During the detector trial, tail end overlapping was detected as being induced by the tension free control. Detection of roll groove wear was also made. This did not affect production as tail ends are cut off by the finishing shear (Fig. 166).
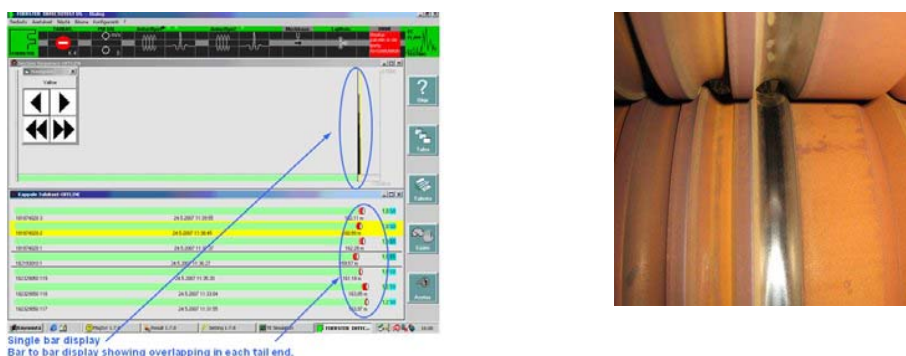
Fig. 166(a and b): Ovako Imatra Eddy Current trial system Defectotherm Förster GmbH & Co
(a) Detector display revealing overlapping (b) roll wear

3.3.9.2 Hybrid laser-Emat Ultrasound defect detection prototype (Corus)

As stated in extended summary, the work carried out in this project was done in parallel to the main developments initiated in [4]. It looked at applicability of a pulsed laser beam to detect defects on a cold moving billet and hot fixed feedstock (above Curie point). The work also involved comparing different laser systems, each of which had different wavelengths and output energies. A laser-EMAT system can find any type of defect that conventional Ultrasonics can. The successful detection of defects is dependent upon a variety of different factors (laser type and beam diameter, EMAT type, (number of coil, width, and magnetic strength), type of hardware filter, surface roughness, etc.). For instance, the location of the laser and EMAT with respect to the sample is important. A very small defect close to the laser beam would effectively block the path between the laser and EMAT. However, if the laser was further away, the same size of defect would not be detected. Therefore, for an industrial system, it would be advantageous to have an array of EMAT sensors (not developed in this project) to cover the main areas where defects typically arise (i.e. the edges and centre of the product). EMATs can also be positioned to find internal defects with a stand-off distance of less than 3 mm. The advantage of an ultrasonic inspection system is that closed cracks and cracks subsurface can be found – as can inclusions and segregation so it is a system if compared with other alternative technologies such as optical cameras and eddy current probes that can find both surface and internal defects. Ultrasound can also be used to gauge the depth of defects and calculate the defect size. Signals are not affected by scale (optical and eddy current are) and closed cracks can also be found. As will be demonstrated further in this report, ultrasound can be generated both above and below the Curie point of steel, whereas Eddy currents must be designed to work either well above or well below it.

A laser will create a plasma from ablation of the surface and breakdown of air. The shape of the impact point is roughly circular and is dependent on the laser beam. From the knowledge developed in [4], it is believed that the smallest defect at high temperature is of the order of 1 mm.

Three laser systems were available for use in this project and their specifications can be seen in Table 18.

Table 20: Specifications of laser systems used (Corus)

Wavelength (nm)	Output energy (mJ)	Portability
10064	4000	Bulky, but could be moved from Warwick University
1064	700	Not movable without significant costs from Corus
532	200	Can be moved in small van

Each of the lasers was targeted onto the same part of the steel and fired and the ultrasonic waveform data was recorded on an oscilloscope. The results can be seen in Fig. 167. Despite the weaker output energy of the 532 nm laser, the signal amplitudes and signal-to-noise ratio were very high. This is because at lower wavelengths, the more energy is absorbed into the steel in the form of ultrasound. Because this was also the most portable laser system, it was decided to use this laser as part of the trial work.
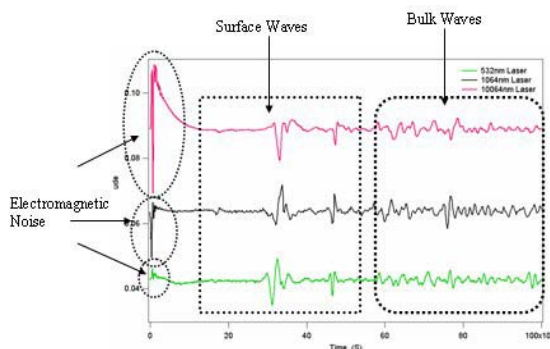
Fig. 167: Comparison signals between the 3 different laser systems (Corus)

- **Cold detection (moving billet)**

132

A side and plan view of the experimental arrangement can be seen in Fig. 168. Here, it can be seen that the laser beam was contained inside metal trunking, which housed a prism allowing the horizontal laser light to be fired vertically. The water-cooled EMAT was housed in a specially designed holder which was developed as part of another EMAT project [4] that allowed the EMAT to be kept at a near constant stand-off, approximately 2 mm above the surface of the steel. The billet being tested was 1m long, with a 100 mm square cross section. There was a transverse defect in the billet. The billet was moved back and forth under the fixed Laser-EMAT inspection point at a variety of different roll speeds, from 0.1 m/s to 1.0 m/s. The faster the rolled product moves, the less number of times the laser hits the steel and subsequently the lower the resolution of the inspection system. The 532 nm laser can be used at both 20 Hz and 40 Hz, and the number of signals that can be generated for every meter the product moves can be seen in Table 19. Because of the slow speed of the GPIB link, the laser was configured to operate at 20 Hz.

The billet was moved using the electrically driven rollers through a set of side guides, which steered the billet through the fixed inspection point. The electrical noise from the motors was reduced by ensuring the EMAT sensors and oscilloscope were electromagnetically screened and isolated. A laptop, with GPIB link to the oscilloscope was used to record the data for later analysis. LabVIEW software was written to acquire the data from the oscilloscope and save the data to disk. The software was analysed post trial, (also using LabVIEW) and the results can be seen in Fig. 168c, which shows how the defects can be found.

Table 21: Resolution function of speed and repetition rate (Corus)

Rolling speed	Laser pulse repetition rate		
m/s	1 Hz	20 Hz	40 Hz
	Distance product moves between laser pulses (mm)		
0.016 (1m/min)	16	0.8	0.4
0.1	100	5	3
0.2	200	10	5
0.4	400	20	10
0.5	500	25	13
0.6	600	30	15
0.8	800	40	20
1.0	1000	50	25

• **Hot detection (static billet)**

After the success of the cold moving trial, a later test was scheduled whereby the same billet (with the surface defect) would be heated to over 1000°C in the furnace before being positioned and moved backwards and forwards under the fixed Laser-EMAT inspection point. Trials were conducted at Swinden Technology Centre, as shown in Fig. 169(b) but it was found that the protection of the EMAT probes was not sufficient and it became damaged. Therefore, the billet was left stationary underneath the inspection point and ultrasonic measurements were taken at elevated temperatures. These results can be seen in Fig. 168(d).
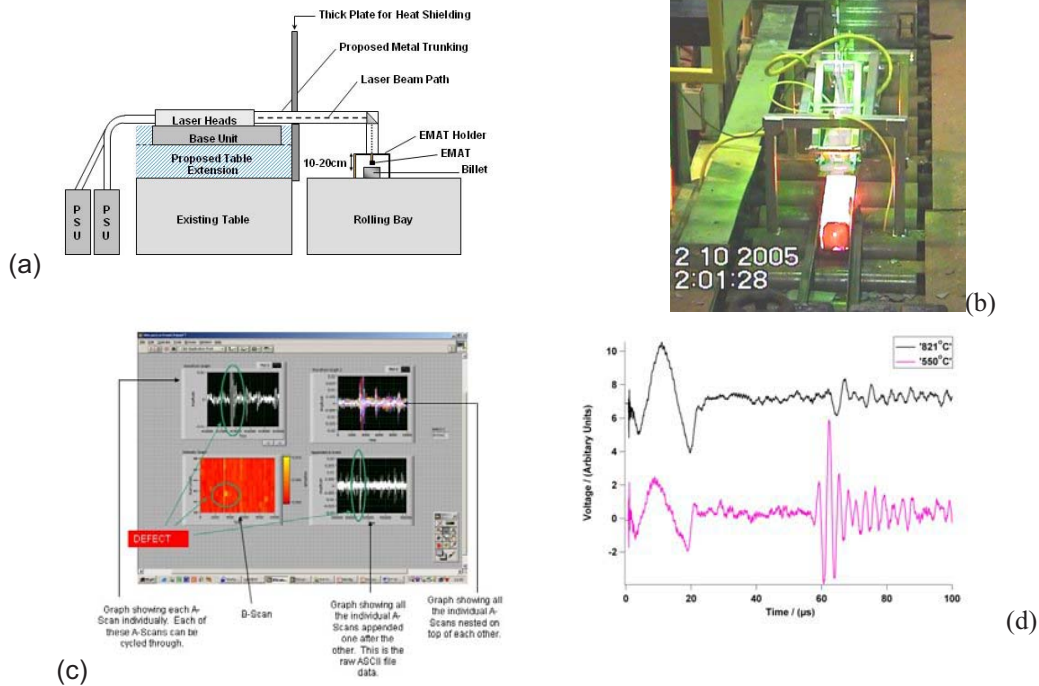
Fig. 168 (a-d): (a) Side view of prototype (b) plan view of the laser inspection facility being built.
(Corus) (c) A screen shot of the LabVIEW software
(d) Example of ultrasonic data recorded at elevated temperatures (Corus)

3.3.10 WP10: Application of improved reheating and rolling practices to industry

These are described in Extended Summary.

3.3.11 WP11: Development of set of guidance for hot rolling without generation of significant defects

These are described in Extended Summary (see page 45 onwards- Table 5).

3.4 Main conclusions

These are described in Extended Summary (see page 52 onwards).

3.5 Exploitation and impact of the research results

These are described in Extended Summary (from page 44 -55).

List of References

1. RFCS PACROLP project proposal RFS-PR-02009 – July 2003
2. Farrugia, D C J et al: 'PACROLP: The prediction and avoidance of cracking in long product hot rolling', RFCS Contract no. RFS-CR-03002, Report no. 10267-3/042, Reference Source no. 113764, Technical report no. 3, Mid-term report, Corus Research Development & Technology, Swinden Technology Centre, March 2005.
3. Krajcinovic D, 2000, Damage mechanisms: accomplishments, trends and needs, Journal of Materials Processing Technology, 62. pp180-184.
4. Baillie, I: " SURFQUALDEV: The measurement and prediction of surface quality by new developments in EMATs and scarfing and the effect of scarfing on surface defects through the mills", RFCS Agreement No. RFS-CR-03047.
5. LIU, Y, LIN, J, DEAN, T A and FARRUGIA, D C J: (2005) A numerical and experimental study of cavitation in a hot tensile axisymmetric testpiece. Journal of Strain Analysis, 40, pp571-586.
6. Wang, E G and He, J C: "Finite element numerical simulation on thermomechanical behaviour of steel billet in continuous casting mold", Scien. Technol Advan. Mat., vol.2, 2001, p257.
7. Wolf and Kurz, Metall Trans. B, 1981, vol. 12B, ppp85-93.
8. Ochoa, B et al: 2002, Effect of matrix/MnS particle interaction on hot workability of S free cutting steels, 44th Mechanical working and steel processing conf., Orlando, Sept 2002.
9. Somani, M, Pentti Karjalainen, L and Bianchi, J H: 'On the Recrystallisation Characterisitics and Kinetics of a 9SMn28 Free Cutting Steel', Materials Science Forum,Trans. Tech Publications, Switzerland, (2007), Vols. 558-559, pp333-338.
10. Alvarez de Toledo, F, Campos, O and Lainez, E: 'Influence of sulfur and Mn/S ratio on the hot ductility during continuous casting' Steel research, 1993, Vol. 6, pp292-299.
11. Nicholson, A et al (1968) Hot workability testing at united steel companies. ISI Publication 108. The Iron & Steel Institute.
12. Baker, T J and Charles, J A: 'Deformation of MnS inclusions in steel', Journal of the Iron and Steel Institute, Sept. 1972, pp680-690.
13. Kiessling, R: 'Non-metallic inclusions in steel', Parts I-IV, The Metals Society, London, 1976.
14. Sims, C E and Dahle, F B: Trans AFA, 1938, 46, pp65-132.
15. Spitzig, W A, Kelly, J F, et al. (1985). "Quantitative characterization of 2nd-phase populations", Metallography, 18, p235.
16. Paliwoda, G. and Wilson, W: Conf on mechanical working on f steel. Proc AIME 1963, 21, pp126-142.
17. Edelson et al TransASM, 1962, vol. 55 p230.
18. Thomason, P F: 1990, Ductile Fracture of Metals, Pergamon Press, UK.
19. Argon, A S: (2001), Mechanics and physics of brittle to ductile transitions in fracture, Journal of Engineering Materials and Technology 123, pp1-11.
20. Le Roy, G, et al, A model of ductile fracture based on the nucleation and growth of voids, Acta metal, 1981, vol. 29, pp1509-1522.
21. Morozov, A, et al., Journal Metal Science and Heat Treatment, Publisher Springer New York ,ISSN 0026-0673 (Print) 1573-8973 (Online) Subject Chemistry and Materials Science and Russian Library of Science, Issue Volume 22, Number 11 / November, 1980 DOI 10.1007/BF00779424 pp779-783.
22. Eshelby JD Proc R Soc 1957, vol A241, p376.
23. Bandstra, J P, et al. (2004) Modeling void coalescence during ductile fracture of a steel. Materials Science & Engineering, A336, pp269-281.
24. Rice, J R and Tracey, D M: 1969, On the Ductile Enlargement of voids in triaxial stress Field, J.Mech.Phys.Solids 17, pp201-217.
25. Bridgman, P: Studies in large plastic flow and fracture with special emphasis on the effect on hydrostatic pressure, McGraw-Hill – New York (1952).
26. McClintock, F A: A criterion for ductile fracture by the growth of holes, Journal of applied mechanics June 1968, 363-369 Transations of the ASME.
27. Oh, S I and Kobayashi, S: 'Workability of Aluminium Allow 7075-T6 in upsetting and rolling', transaction of ASME: Journal of Engineering for Industry, 1996, pp800-806.
28. Tvergaard, V: Influence of Voids on Shear Band Instabilities under Plane Strain Conditions, International Journal of Fracture Mechanics, 1981, vol. 17, pp389-407.

29. Banks, T and Gladman, T: Sulphide shape Control, metals Technology march 1979, p81.

30. Rice, JR and Tracey, D M: 1969, On the Ductile Enlargement of voids in triaxial stress Field, J.Mech.Phys.Solids 17, pp201-217.

31. Cocks, A C F and Ashby, M F: 'On creep fracture by void growth', Progress in materials science, 1982, 27, pp189-244.

32. NICOLAOU, P D and SEMIATIN, S L: (2003) An experimental and theoretical investigation of the influence of stress state on cavitation during hot working. Acta Materialia, 51, pp613-623.

33. Lin, J, Liu, Y, Farrugia, D C J and Zhou, M: 2005, Development of dislocation based-unified material model for simulating microstructure evolution in multipass hot rolling, Philosophical Magazine A, Vol. 85, No. 18, pp1967-1987. ISSN 1478-6435.

34. Foster, A: PhD, 2007, modelling of damage evolution under complex strain path and stress-states in hot deformation, Birmingham University.

35. Cockroft, M G and Latham, D J: A simple criterion of fracture for ductile metals, National Engineering Laboratory, report No240, July 1966.

36. Oyane, M: Criteria of ductile fracture strain, Bulletin of JSME, 1972, 15, pp1507-1513.

37. ABAQUS v 6.6 ® manuals

38. Hillerborg, et al, Analysis of crack formation and crack growth in concrete by means of fracture mechanics and finite elements, Cement and Concrete Research 1976, vol. 6 pp773-782.

39. LIN, J, FOSTER, A D, LIU, Y, FARRUGIA, D & DEAN, T A: (In Press) On micro-damage in hot metal working Part 2: Constitutive modelling. Engineering Transactions.

40. Shterenlikht, A: '3D CAFE Modeling of Transitional Ductile – Brittle Fracture in Steels', PhD Thesis, University of Sheffield, Sheffield, 2003.

41. Lemaitre J, 1984b, How to use damage mechanics, Nuc.Eng & Des, Vol 80, pp233-235

42. Cescotto, S and Zhu, YY: Modelling of ductile fracture initiation during bulk forming, in Complass 95 Owen et al meds, Pineridge Press 1995, pp987-997.

43. Moroli V. and Piancaldini, R. 'Apparatus and methods for control of surface quality of elongated products'. CSM-ORI MARTIN Joint International Patent Application N° PCT/IB2004/052383, 11 November 2004. Italian Patent Application Number RM 2003A000524, 12 November 2003.

44. Farrugia, D: Prediction and avoidance of high temperature damage in long product hot rolling, Journal of Materials Processing Technology 177 (2006) pp486-492.

45. MAIRE, E, BORDREUIL, C, BABOUT, L and BOYER, J-C: (2005) Damage initiation and growth in metals. Comparison between modelling and tomography experiments. Journal of the Mechanics and Physics of Solids, 53, pp2411-2434.

46. Orti,z M: A facility for simulating dynamic response of materials, http://aero.caltech.edu/~ortiz/talks/2006_07%20talks/MO_Pisa_Sept_2006_Lecture2.pdf

47. Farrugia, D C J, et al: 'PACROLP: The prediction and avoidance of cracking in long product hot rolling', RFCS Contract no. RFS-CR-03002, Report no. 10267-3/042, (Reference Source no. 113764), Technical report no. 3, Mid-term report, Corus Research Development & Technology, Swinden Technology Centre, March 2005.

48. Farrugia, D C J, et al: 'PACROLP: The prediction and avoidance of cracking in long product hot rolling', RFCS Contract no. RFS-CR-03002, Report no. 10267-2/041, (Reference Source no. 112533), Technical report no. 2, Semester report, Corus Research Development & Technology, Swinden Technology Centre, September 2004

49. Farrugia, D C J, et al: 'PACROLP: The prediction and avoidance of cracking in long product hot rolling', RFCS Contract no. RFS-CR-03002, Report no. 10267-4/051, (Reference Source no. 114803), Technical report no. 4, Semester report, Corus Research Development & Technology, Swinden Technology Centre, September 2005.

50. Farrugia, D C J, et al: 'PACROLP: The prediction and avoidance of cracking in long product hot rolling', RFCS Contract no. RFS-CR-03002, Report no. 10267-5/052, (Reference Source no. 120456), Technical report no. 5, Semester report, Corus Research Development & Technology, Swinden Technology Centre, March 2006.

51. Farrugia, D C J, et al: 'PACROLP: The prediction and avoidance of cracking in long product hot rolling', RFCS Contract no. RFS-CR-03002, Report no. 10267-6/052, (Reference Source no. 131117), Technical report no. 6, Semester report, Corus Research Development & Technology, Swinden Technology Centre, Aug 2006.

52. Tormatic, Orion AZZIS Développement d'un logiciel d'analyse des essais de torsion des métaux à chaud Rapport de stage. Mastère en Matériaux et Mise en Forme de l'ENSMP, septembre 1999.

53. Fields, Backofen, Determination of strain hardening characteristics by torsion testing, proc ASTM, (1957), vol. 57, pp1259-1271.
54. Davenport, S B and Higginson, R L: (2000). "Strain path effects under hot working: an introduction", Journ. Mater. Proc. Technol., 98, p267.
55. Badiola, D J and Gutierrez, I: (2004). "Study of the strain reversal effect on the recrystallization and strain-induced precipitation in a Nb-microalloyed steel", Acta Mat., 52, p333.
56. Bartolome, R, Jorge-Badiola, D, et al. (2003). "Flow stress behaviour, static recrystallisation and precipitation kinetics in a Nb-microalloyed steel after a strain reversal", Mater. Sci. Eng. A, 344, p340.
57. Christodoulou, N, Woo, O T, et al. (1986). "Effect of stress reversals on the work hardening behaviour of polycrystalline copper", Acta Met., 34, p1553.
58. Vincze, G, Rauch, E F, et al. (2005). "A comparison of the mechanical behaviour of an A1050 and a low carbon steel deformed upon strain reversal", Acta Mat., 53, p1005.
59. Thakur, A, Vecchio, K S, et al. (1996). "Bauschinger effect in Haynes 230 Alloy: Influence of strain rate and temperature", Metall. Mater. Trans. A, 27A, p1739.
60. Leden, B: "Mathematical reheating furnace models in STEELTEMP®", Proceedings International Conference SCANHEATING '85, Paper no. 2, MEFOS, Luleå, June 1985.
61. Riaz, S and Ludlow, V: "IMPROVEMENTS TO BILLET SURFACE QUALITY", ECSC Agreement No. 7210.PR/333.
62. Foster, A D, Lin J, Liu Y, Farrugia, D C J and Dean, T A: 'Constitutive modelling of damage accumulation during the hot deformation of free-cutting steels', Proceedings of the 8th ESAFORM Conference on Material Forming, ESAFORM 2005, 27th-29th April 2005, Romania, Vol. 1, pp201-204.
63. Bordreuil, et al 2004, A specific orthotropic damage model at finite strains, J >Mater Proc Technol 69 pp119-138.
64. Zhou, M, Wiklund, O, Karjalainen, L P, Bianchi, J H, Gutierrez, I and Peura, P: 'The effect of strain reversal and strain-time path on constitutive relationships for metal rolling/forming processes', Technical Steel Research Final Report EUR 19891, Official Publications of the EU, Luxembourg (2001).
65. Tinet, H, Klocker, H, et al. (2004). "Damage analysis during hot deformation of a resulfurised stainless steel", Acta Mat., 52, p3825.
66. Bianchi, J H and Karjalainen, L P: 'Modelling of dynamic and metadynamic recrystallisation during bar rolling of a medium carbon spring steel', Journal Materials Processing Technologies, (2005), 160, pp267- 277.

List of Figures

143

List of Tables

Appendix 1: CSM

Table A1-Process conditions and cracking observed during the pilot mill flat rolling experiments; T=top, B=bottom, L=lateral surfaces of the bloom

ID	initial thickness [mm]	removed layers from original surfaces [mm]	Temperature [°] reheating T [°C], t [hh:mm]	rolling core	rolling surface	rolling reduction %	cooling	cracking rolled surface	cracking edges
LS30-Bi medium C free cutting steel									
Bi1	70	T=0,B=70,L=0	1200-01:00	1120		30	a.c.	No	No
Bi12	49	T=0,B=90,L=0	1200-01:00	1018		30	a.c.	No	No
Bi2	70	T=0,B=70,L=70	1200-01:15	1120		40	a.c.	No	No
Bi13	49	T=0,B=90,L=70	1200-01:15	1120		50	a.c.	No	No
Bi20	70	T=0,B=70,L=70	1200-01:45	1120		40	a.c.	No	No
Bi21	70	T=0,B=70,L=70	1200-02:00	1027		40	a.c.	No	No
Bi22	70	T=0,B=70,L=70	1200-05:10 + 1170-00:30	1092		60	a.c.	No	Yes
Bi23	70	T=0,B=70,L=70	1200-05:10+ 1130-00:50	1048		60	a.c.	No	Yes
Bi14	70	T=0,B=70,L=70	1100-00:50	1025		70	a.c.	No	Yes
9SMn28 Low-C Free cutting steels with high S									
Set 1: several medium reduction consecutive passes, hc=0 (with as-cast cortical zone)									
R11	36	T=0,B=104,L=0	1187	1171	1096	36.1	a.c.	No	No
R12	36	T=0,B=104,L=0		1110	1023	23.9	a.c.	No	No
R13	36	T=0,B=104,L=0		1011	921	20.0	w.q.	No	No
R21	36	T=0,B=104,L=0	1187	1173	1098	36.1	a.c.	No	No
R22	36	T=0,B=104,L=0		1061	976	23.9	a.c.	No	No
R23	36	T=0,B=104,L=0		964	875	20.0	w.q.	No	No
R31	36	T=0,B=104,L=0	1187	1044	969	36.1	a.c.	No	No
R32	36	T=0,B=104,L=0		963	878	23.9	a.c.	No	No
R33	36	T=0,B=104,L=0		901	809	20.0	w.q.	No	No
R41	36	T=0,B=104,L=0	1115	1058	984	40.3	a.c.	No	No
R42	36	T=0,B=104,L=0		1014	927	39.5	w.q.	No	No
R51	36	T=0,B=104,L=0	1111	999	925	40.3	a.c.	No	No
R52	36	T=0,B=104,L=0		925	838	39.5	w.q.	No	No
Set 2: several reduction single passes, several hc									
6.21	22	T=4,B=114,L=4	1050	960	900	15	a.c.	No	No
6.22	22	T=7,B=111,L=7	1050	960	910	15	a.c.	No	No
6.23	22	T=4,B=114,L=4	1050	960	890	25	a.c.	No	No
6.24	22	T=7,B=111,L=7	1050	960	893	25	a.c.	No	No
6.25	22	T=7,B=111,L=7	1190	1110	1060	25	a.c.	No	No
Set 3: low reduction consecutive passes, hc=15 mm									
F31	70	T=15,B=55,L=15	1086 – 2:00 h	1030	930	15	a.c.		
				1020	940	15	a.c.		
			1080 –1:00 h	1035	928	15	a.c.		
				1027	923	15	a.c.	Yes	No
F32	70	T=15,B=55,L=15	1090 – 1:56 h	1058	970	15	a.c.		
				1043	960	15	a.c.		
			1080 – 1:00 h	990	925	15	a.c.		
				983	920	15	a.c.	Yes	No
F33	70	T=15,B=55,L=15	1088 – 2:00 h	1042	945	15	a.c.		
				1005	920	15	a.c.		
			1080 –1:05 h	1030	936	15	a.c.		
				1027	920	15	a.c.	Yes	No
Set 4: partial rolling high reduction, several hc and temperatures									
6.13	29	T=7,B=104,L=7	1100 – 1 :00	963	901	max. 46	a.c.	No	1
6.14	29	T=7,B=104,L=7	1190 – 1 :00	1110	1045	max. 57	a.c.	No	3
6.32	29	T=10,B=101,L=10	1100– 1 :00	960	900	max. 58	a.c.	No	8
6.12	20	T=13,B=107,L=13	1100– 1 :00	956	897	max. 57	a.c.	19	13
6.31	29	T=13,B=98,, L=13	1150 – 1 :00	1041	980	max. 57	a.c.	3	3
6.11	16	T=13,B=111,L=13	1190 – 1 :00	1146	1043	max. 59	a.c.	2	5
6.12R	20	T=30,B=90,L=30	1100– 1 :00	956	897	max. 57	a.c.	1	12
6.11R	16	T=30,B=94,L=30	1190– 1 :00	1146	1043	max. 59	a.c.	No	2
6.31R	29	T=70,B=41,L=30	1150 –1 :00	1041	980	max. 57	a.c.	1	11

Appendix 2: Corus - Birmingham Viscoplastic model

Model 1:

$$\dot{\varepsilon}_p = A_1 \cdot \sinh\left[A_2 \cdot \left(\frac{\sigma}{1-D_{GB}} - (R+k)\cdot(1-D_{Pi})\right)\right] \bigg/ \left(\frac{d}{d_0}\right)^{\gamma_1} \tag{1}$$

$$\dot{S} = H_1 \cdot (x \cdot \bar{\rho} - \bar{\rho}_c \cdot (1-S))\cdot(1-S)^{\gamma_4} \tag{2}$$

$$\dot{x} = X_1 \cdot (1-x)\cdot\bar{\rho} \tag{3}$$

$$\dot{\bar{\rho}} = \left(\frac{d}{d_0}\right)^{z_1} \cdot (1-\bar{\rho})\cdot|\dot{\varepsilon}_p|^{z_3} - C_r \cdot \bar{\rho}^{z_3} - \frac{C_s \cdot \bar{\rho}}{1-S}\dot{S} \tag{4}$$

$$R = 0.5 \cdot B \cdot \bar{\rho}^{-1/2} \cdot \dot{\bar{\rho}} \tag{5}$$

$$\dot{d} = \left(\frac{G_1}{d}\right)^{\gamma_s} - G_2 \cdot S \cdot \left(\frac{d}{d_0}\right)^{\gamma_6} \tag{6}$$

$$\sigma = E\cdot(\varepsilon_T - \varepsilon_p) \tag{7}$$

$$\dot{D}_{GB} = \eta \cdot \left[[a_4 \cdot (1-D_{GB})\cdot\bar{\rho}] + \left[\left(\frac{1}{(1-D_{GB})^{n_1}} - (1-D_{GB})\right)\cdot|\dot{\varepsilon}_p|\right]\right] \tag{8}$$

$$\dot{D}_{Pi} = a_5 \cdot \left[[(1-D_{Pi})\cdot\bar{\rho}] + \left[a_6 \cdot \frac{D_{Pi}\cdot d}{(1-D_{Pi})^{n_2}}\cdot|\dot{\varepsilon}_p|^{n_4}\right]\right] \tag{9}$$

$$\dot{D}_T = \dot{D}_{GB} + \dot{D}_{Pi} \tag{10}$$

where

$$\eta = a_1 \cdot \exp\left(-a_2 \cdot \left(1-\frac{d}{d_c}\right)^2\right) \tag{11}$$

$$d_c = a_3 \cdot (\dot{\varepsilon}_p)^{-n_s} \tag{12}$$

Model 2: (17 constants to be determined via GA)

$$\dot{\varepsilon}_p = \left\langle \frac{\dfrac{\sigma_e}{1-D_C} - (k+R)}{K} \right\rangle_+^{n} \qquad R = B\sqrt{\bar{\rho}}$$

$$\dot{\bar{\rho}} = k_1 \cdot (1-\sqrt{\bar{\rho}})\cdot\dot{\varepsilon}_p - c_1\bar{\rho}^{c_2}$$

$$\dot{D}_i = z_1\omega\dot{\varepsilon}_p^{\gamma} \cdot \frac{\sinh\left(2\dfrac{(n_d - 1/2)}{(n_d + 1/2)}\dfrac{\sigma_H}{\sigma_e}\right)}{\sinh\left(\dfrac{2}{3}\dfrac{(n_d - 1/2)}{(n_d + 1/2)}\right)}$$

$$\dot{D}_C = z_2 \cdot \left\langle \frac{\sigma_1}{1-D_C}\right\rangle_+ \cdot \omega\cdot\sinh\left(z_3 \cdot \sqrt{\bar{\rho}}\cdot D_i\right)\cdot\dot{\varepsilon}_p$$

$$\sigma = E(\varepsilon_T - \varepsilon_e)$$

Dc: Damage coalescence
$\sigma_1/(1-D_C)$ maximum principal stress acting on the non-damaged area

$\bar{\rho} = \dfrac{\rho - \rho_0}{\rho_{max} - \rho_0}$ normalised dislocation density

$\dot{\bar{\rho}} = k_1 \cdot (1-\sqrt{\bar{\rho}})\cdot\dot{\varepsilon}_p$ dislocation storage and dynamic recovery

$\dot{\bar{\rho}}_{STATIC} = c_1\bar{\rho}^{c_2}$ static recovery

$R = B\sqrt{\bar{\rho}}$ isotropic hardening

$k = k_0\exp\left(\dfrac{Q_p}{\kappa T}\right)$ $\quad c_1 = c_0\exp\left(\dfrac{-Q_R}{\kappa T}\right)$

Di: Damage at inclusion
ω: spatial variation of spacing to diameter ratio

$E = \dfrac{E_0}{\cosh^2(K_1(T-T_0))}$

$B = \dfrac{B_0}{\cosh^2(K_1(T-T_0))}$

$z_2 = z_{2(0)}\exp\left(\dfrac{Q_C}{\kappa T}\right)$

Appendix 3: Table A.3 - CSM damage model

STRAIN AND STRESS BASED MODELS

<u>TENSION</u>

Strain-based damage: $f_i^{\varepsilon} = \int df^{\varepsilon} = f_{i-1}^{\varepsilon} + \int\limits_{tension\ cycle} \frac{d}{d\varepsilon}\left[\frac{(\varepsilon tensile - \varepsilon ond\,(T))}{(\varepsilon\ fracture\,(T) - \varepsilon ond\,(T))}\right]^{\alpha} \cdot d\varepsilon$

$f^{\varepsilon}(\varepsilon ond) = 0 < f^{\varepsilon} < f^{\varepsilon}(\varepsilon fract.) = 1$

$\varepsilon_{tensile} = \overline{\varepsilon} - \varepsilon_{exit\ from\ compression} + \varepsilon_{equivalent\ from\ residual\ damage\ f}$

$\varepsilon_{equivalent\ from\ residual\ damage} = f^{1/\alpha}.\left[\varepsilon_{fr}(\dot{\varepsilon},T) - \varepsilon_{ond}(\dot{\varepsilon},T))\right] + \varepsilon_{ond}(\dot{\varepsilon},T)$ for $f^{\varepsilon} > 0$

$\varepsilon_{equivalent\ from\ residual\ damage} = 0$ for $f^{\varepsilon} = 0$

The initial condition $f(0)$ **is also considered as a residual damage.**

For 9SMn28: α = 2.5 and: ε_{ond} = 1.25 (-0.0000021926 T^2 +0.0041052 T -1.5753),

$\varepsilon_{fracture}$ **= 0.0000097484** T^2 **– 0.018499** T **+ 9.4438**

Stress-based damage: $f_i^{\sigma} = f_{i-1}^{\sigma} + \int\limits_{tension\ cycle} \frac{\sigma_{max.\ principal}}{\overline{\sigma}}\ d\varepsilon$

<u>COMPRESSION</u>

(a) From Tanaka's (1987) void crushing procedure applied to rolling:

$f_i^{\varepsilon\ and\ \sigma} = f_{i-1}^{\varepsilon\ and\ \sigma}{}_{previous\ tensile\ cycle}\ (1 - Pc)$

$P_c = \sum\limits_{i=0}^{2}\sum\limits_{j=0}^{2-i} c_{ij}\cdot[ln(1+\varepsilon_c)]^i\cdot[ln(1-Gm_c)]^j$

$Gm_c = \int\limits_{compression\ cycle} \frac{\sigma_m}{\overline{\sigma}} d\varepsilon_c$

$\varepsilon_c = \overline{\varepsilon} - \varepsilon_{exit\ from\ tension}$

	$C_{0,0}$	$C_{0,1}$	$C_{0,2}$	$C_{1,0}$	$C_{1,1}$	$C_{2,0}$
Tanaka (upsetting test)	0	0.71	2.66	11.79	1.65	-7.22
(CSM R0 bar rolling)	0.0003	-1.03	0.05	-0.0004	4.25	0.13

(b) From Gurson's model rolling simulations:

$f_i^{\varepsilon\ and\ \sigma} = f_{i-1}^{\varepsilon\ and\ \sigma}{}_{previous\ tensile\ cycle} - 0.08\,(\overline{\varepsilon} - \overline{\varepsilon}_{previous\ tensile\ cycle})$

Triaxiality-based damage: <u>TENSION AND COMPRESSION</u>

$$f^{Gm} = \max(\int \frac{pressure}{\overline{\sigma}}\ d\varepsilon, 0)$$

DAMAGE-THERMOMECHANICS COUPLING

Flow stress	**Bulk modulus**
$\sigma(\overline{\varepsilon},\dot{\overline{\varepsilon}},T,f) = \sigma(\overline{\varepsilon},\dot{\overline{\varepsilon}},T,0).[1 - f(1-a)]$ $a = 10^{-2}$	$\kappa(T,f) = \frac{E}{3\{1 - 2v_o[1 - f(1-c)]\}}[1 - f(1-b)]$ $b = 10^{-4}$ $c = 10^{-2}$